ISSN 0915-6348

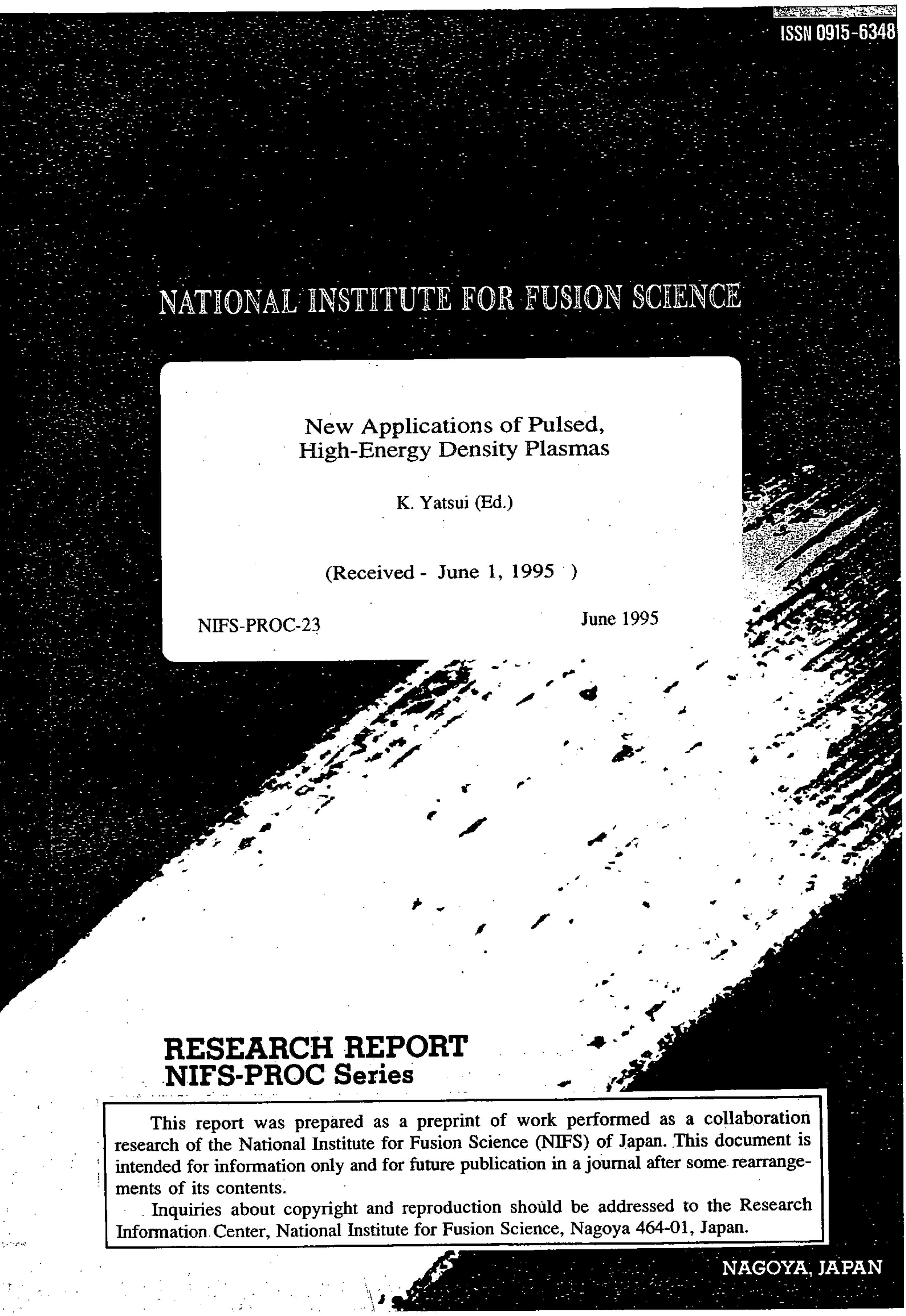

NATIONAL INSTITUTE FOR FUSION SCIENCE

New Applications of Pulsed, High-Energy Density Plasmas

K. Yatsui (Ed.)

(Received - June 1, 1995)

NIFS-PROC-23

June 1995

RESEARCH REPORT
NIFS-PROC Series

NAGOYA, JAPAN

New Applications of Pulsed, High-Energy Density Plasmas

Edited by Kiyoshi Yatsui

December 12 ~ 13, 1994
National Institute for Fusion Science
Nagoya, Japan

Abstract

This is the collected article of papers presented at the symposium on "New Applications of Pulsed, High-Energy Density Plasmas", held at NIFS on Dec. 12 ~ 13, 1994. Various topics on new applications of pulsed, high-energy density plasmas are summarized including the following subjects:

- Recent progress of pulsed power technology
- Generation and focusing of intense pulsed ion beam
- Applications of relativistic electron beam
- Fundamental research of inertial confinement fusion
- Recent progress in Z-pinch
- Physics of particle beam-target interaction
- Development of X-ray lasers

Keywords: High-Energy Density Plasma, Pulsed Power, High Power Ion Beam, Intense Relativistic Electron Beam, High Power Microwave, Z-Pinch

PREFACE

This is the collected article of papers presented at the collaborative research symposium on "New Applications of Pulsed, High-Energy Density Plasmas" which was held at National Institute for Fusion Science, Nagoya, on Dec. 12 ~ 13, 1994. The main interests were concerned on the characteristics and associated new applications of the high density plasmas produced mostly by intense, pulsed, charged particle beams. The topics covered R & D on pulsed power technology, pulsed ion beam, relativistic electron beam, inertial confinement fusion, Z-pinch, plasma focus, high-power microwave, switches, target interaction, X-ray lasers, materials science, and so on.

At the symposium, 27 papers were presented, and totally 81 scientists (in two days) attended from universities, institutes or private companies.

Great achievements were obtained by this symposium through fruitful discussions among attendees.

Kiyoshi Yatsui
Symposium Chairman
Nagaoka University of Technology

CONTENTS

Metal Surface Modification by Irradiation of an Intense Pulsed Ion Beam ··········· 1

M. Yatsuzuka, Y. Hashimoto, T. Yamasaki, and H. Uchida

Study of YBCO Thin Films Deposited by Intense Pulsed Light Ion Beam Evaporation ··········· 10

C. Grigoriu, E. P. Achmad Chamdani, T. Sonegawa, K. Masugata, K. Yatsui

Dynamics of Z-Pinch Plasma Target for Beam-Plasma Interaction ··········· 18

T. Hosokai, M. Nakajima, T. Aoki, K. Horioka, and M. Ogawa

Evaluation of the Mechanism Ion Source Production in LIB Diode ··········· 27

E. Chishiro, K. Masugata, and K. Yatsui

Space Charge Effects on the Characteristics of Grid-Controlled Vacuum Arc Ion Sources ··········· 35

J. Hasegawa, M. Nakajima, and K. Horioka

Numerical Simulation of Spherical Plasma Focus Diode ··········· 43

W. Jiang, K. Masugata, and K. Yatsui

Property Measurements of Light Ion Beams for Inertial Confinement Fusion ··········· 53

K. Yasuike, T. Yamashita, T. Ochi, H. Urai, S. Miyamoto, and S. Nakai

X-Ray Emission and Energy Input into a Gas-Puff Z-Pinch ··········· 63

T. Fujimi, K. Takasugi, T. Shibuya, and T. Miyamoto

Optically Coupled Voltage Measurement on a Z-Pinch ··········· 72

T. Shibuya and K. Takasugi

Improvements of Surface Discharge Switch ··········· 80

N. Hamana, K. Takasugi, and T. Miyamoto

Transformer-Type Pulse High Voltage Generator ··········· 90

J. Irisawa, S. Takano, and K. Terao

Development of Inductive Energy Storage Pulsed Power Generator with Output of MV Class ··········· 101

K. Hasegawa, H. Akiyama, S. Katsuki, S. Maeda, F. Kinoshita, and H. Kuribayashi

Characteristics of High Current Pulsed Arc Discharge ··········· 108

K. Masugata, M. Yoshida, T. Suzuki, and K. Yatsui

Power Flow in a Resistive Micro-MITL ···································· 118

K. Horioka, K. Hiraoka, M. Nakajima, and T. Aoki

Numerical Study of Coaxial Double Z-Pinch for Resonant Photopumping X-Ray Laser ···································· 124

T. Aoki, K. Horioka, and M. Ogawa

A Time Resolved 1D Soft X-Ray Camera System for an Impulsive Source and Its Application to a Plasma Focus Experiment ···································· 136

T. Yanagidaira, H. Kurita, T. Koshimizu, J. Mikami, T. Yamamoto, K. Shimoda, and K. Hirano

Hot Spots Characterization in Gas Puffed Z-Pinch Experiment ···································· 146

J. Du, H. Oba, T. Ohata, Y. Takahama, K. Shimoda, and K. Hirano

Enhanced Stability and Increased Soft X-Ray Generation in a Dense Plasma Focus by Additional High Z Gas Puff ···································· 156

H. Kitaoka, A. Sakurai, A. Nonaka, T. Yamamoto, K. Shimoda, and K. Hirano

Metal Vapor Puff Z-Pinch Plasma and 1D MHD Simulation ···································· 166

K. Arai, S. Furuya, E. Goto, K. Hanazawa, and S. Ishii

Creation and Measurements of Fine Particles Z-Pinch Plasma ···································· 176

Q. Ai, D. Itagaki, O. Tsuboi, and S. Ishii

An Experimental Study of Pulse Beam-Excited Strong Langmuir Turbulence ······ 182

R. Ando, M. Masuzaki, H. Morita, K. Kobayashi, M. Yoshikawa, H. Koguchi, and K. Kamada

An X-Band Gyro-BWO Experiment with an Intense Relativistic Electron Beam ···································· 189

K. Kamada, H. Igarasi, K. Nawashiro, S. Kawasaki, R. Ando, and M. Masuzaki

Cascaded High-T_c Bulk Superconductor Lenses (Supertrons) for Intense Electron Beams ···································· 198

A. Ohshima, H. Matsuzawa, Y. Mizutani, K. Shoji, E. Ikawa, Y. Chino, and S. Suganomata

PROGRAM

Symposium on New Applications of Pulsed, High-Energy Density Plasmas
Dec. 12 (Mon)~ Dec. 13 (Tue), 1994
National Institute for Fusion Science

Dec. 12 (Monday)

13:30	Metal Surface Modification by Irradiation of an Intense Pulsed Ion Beam	M. Yatsuzuka, Y. Hashimoto, T. Yamasaki, and H. Uchida (Himeji Institute of Technology)
13:55	Application of Pulsed Power Discharge to Gas Process	A. Kawachi, S. Adachi, and Y. Nakagawa (Osaka City University)
14:20	Study of YBCO Thin Films Deposited by Intense Pulsed Light Ion Beam Evaporation	C. Grigoriu, E. P. Achmad Chamdani, T. Sonegawa, K. Masugata, K. Yatsui (Nagaoka University of Technology)
14:45	Dynamics of Z-Pinch Plasma Target for Beam-Plasma Interaction	T. Hosokai, M. Nakajima, T. Aoki, K. Horioka, and M. Ogawa (Tokyo Institute of Technology)
15:10	Evaluation of the Mechanism Ion Source Production in LIB Diode	E. Chishiro, K. Masugata, and K. Yatsui (Nagaoka University of Technology)
15:30 ~ 15:45	Break	
15:45	Space Charge Effects on the Characteristics of Grid-Controlled Vacuum Arc Ion Sources	J. Hasegawa, M. Nakajima, and K. Horioka (Tokyo Institute of Technology)
16:10	Numerical Simulation of Spherical Plasma Focus Diode	W. Jiang, K. Masugata, and K. Yatsui (Nagaoka University of Technology)
16:30	Pulsed Power Fusion and High Energy Density Plasma	S. Miyamoto, K. Yasuike, and S. Nakai (Osaka University)
16:55	Property Measurements of Light Ion Beams for Inertial Confinement Fusion	K. Yasuike, T. Yamashita, T. Ochi, H. Urai, S. Miyamoto, and S. Nakai (Osaka University)
17:20	X-Ray Emission and Energy Input into a Gas-Puff Z-Pinch	T. Fujimi, K. Takasugi, T. Shibuya, and T. Miyamoto (Nihon University)
17:45	Optically Coupled Voltage Measurement on a Z-Pinch	T. Shibuya and K. Takasugi (Nihon University)

Dec. 13 (Tuesday)

9:00	Improvements of Surface Discharge Switch	N. Hamana, K. Takasugi, and T. Miyamoto (Nihon University)
9:25	Transformer-Type Pulse High Voltage Generator	J. Irisawa, S. Takano, and K. Terao (Nagaoka University of Technology)
9:50	Development of Inductive Energy Storage Pulsed Power Generator with Output of MV Class	K. Hasegawa, H. Akiyama, S. Katsuki, S. Maeda, F. Kinoshita, and H. Kuribayashi (Kumamoto University)

10:15	Characteristics of High Current Pulsed Arc Discharge	K. Masugata, M. Yoshida, T. Suzuki, and K. Yatsui (Nagaoka University of Technology)
10:35 ~ 10:50	Break	
10:50	Repetitive Generation of High Power Pulses by Optically Activated Semiconductor Switches	U. Katschinski*, H. Akiyama and H. Meiev (Kumamoto University, Technical University of Braunschweig*)
11:15	Power Flow in a Resistive Micro-MITL	K. Horioka, K. Hiraoka, M. Nakajima, and T. Aoki (Tokyo Institute of Technology)
11:40	Numerical Study of Coaxial Double Z-Pinch for Resonant Photopumping X-Ray Laser	T. Aoki, K. Horioka, and M. Ogawa (Tokyo Institute of Technology)
12:05	A Time Resolved 1D Soft X-Ray Camera System for an Impulsive Source and Its Application to a Plasma Focus Experiment	T. Yanagidaira, H. Kurita, T. Koshimizu, J. Mikami, T. Yamamoto, K. Shimoda, and K. Hirano (Gunma University)
12:30 ~ 13:30	Lunch	
13:30	Hot Spots Characterization in Gas Puffed Z-Pinch Experiment	J. Du, H. Oba, T. Ohata, Y. Takahama, K. Shimoda, and K. Hirano (Gunma University)
13:55	Enhanced Stability and Increased Soft X-Ray Generation in a Dense Plasma Focus by Additional High Z Gas Puff	H. Kitaoka, A. Sakurai, A. Nonaka, T. Yamamoto, K. Shimoda, and K. Hirano (Gunma University)
14:20	Metal Vapor Puff Z-Pinch Plasma and 1D MHD Simulation	K. Arai, S. Furuya, E. Goto, K. Hanazawa, and S. Ishii (Tokyo Institute of Technology)
14:45	Creation and Measurements of Fine Particles Z-Pinch Plasma	Q. Ai, D. Itagaki, O. Tsuboi, and S. Ishii (Tokyo Institute of Technology)
15:10 ~ 15:25	Break	
15:25	An Experimental Study of Pulse Beam-Excited Strong Langmuir Turbulence	R. Ando, M. Masuzaki, H. Morita, K. Kobayashi, M. Yoshikawa, H. Koguchi, and K. Kamada (Kanazawa University)
15:50	An X-Band Gyro-BWO Experiment with an Intense Relativistic Electron Beam	K. Kamada, H. Igarasi, K. Nawashiro, S. Kawasaki*, R. Ando, and M. Masuzaki (Kanazawa University, Saitama University*)
16:15	Measurement of Pulsed Microwave Power Generated by Virtual Cathode Oscillator	M. Nakayama, M. Yatsuzuka, I. Ohta, and S. Nobuhara (Himeji Institute of Technology)
16:40	Cascaded High-T_c Bulk Superconductor Lenses (Supertrons) for Intense Electron Beams	A. Ohshima, H. Matsuzawa, Y. Mizutani, K. Shoji, E. Ikawa, Y. Chino, and S. Suganomata (Yamanashi University)

List of Participants

S. Adachi	Osaka City University
Q. Ai	Tokyo Institute of Technology
R. Ando	Kanazawa University
T. Aoki	Tokyo Institute of Technology
K. Arai	Tokyo Institute of Technology
E. Chishiro	Nagaoka University of Technology
J. Du	Gunma University
M. Fukao	Shizuoka University
T. Fujimi	Nihon University
S. Furuya	Tokyo Institute of Technology
C. Grigoriu	Nagaoka University of Technology
N. Hamana	Nihon University
J. Hasegawa	Tokyo Institute of Technology
K. Hasegawa	Kumamoto University
K. Hirano	Gunma University
K. Hiraoka	Tokyo Institute of Technology
K. Horioka	Tokyo Institute of Technology
T. Hosokai	Tokyo Institute of Technology
J. Irisawa	Nagaoka University of Technology
W. Jiang	Nagaoka University of Technology
K. Kamada	Kanazawa University
T. Kamo	Mitsubishi Ind. Co.
S. Kato	Nisshin Elec. Co.
U. Katschinski	Kumamoto University
S. Katsuki	Kumamoto University
N. Kimura	Shizuoka University
H. Kurita	Gunma University
Y. Lui	Tokyo Institute of Technology
K. Masugata	Nagaoka University of Technology
H. Matsuzawa	Yamanashi University
S. Miyamoto	Osaka University
T. Miyamoto	Nihon University
K. Naito	Nisshin Elec. Co.

Y. Nakagawa	Osaka City University
M. Nakayama	Himeji Institute of Technology
N. Nishino	Hiroshima University
T. Ohata	Gunma University
A. Sakurai	Gunma University
T. Shibuya	Nihon University
K. Takasugi	Nihon University
A. Tominaga	Shizuoka University
T. Yamamoto	Gunma University
T. Yanagidaira	Gunma University
K. Yasuike	Osaka University
K. Yatsui	Nagaoka University of Technology
M. Yatsuzuka	Himeji Institute of Technology

Metal Surface Modification by Irradiation of an Intense Pulsed Ion Beam

Mitsuyasu YATSUZUKA, Yoshiyuki HASHIMOTO,[1] Tohru YAMASAKI,[2]
and Hitoshi UCHIDA[3]

Department of Electrical Engineering,
[2]Department of Materials Science and Engineering,
[3]Department of Mechanical and Intelligent Engineering
Faculty of Engineering, Himeji Institute of Technology,
2167 Shosha, Himeji, Hyogo 671-22
[1]Department of Electronics, Kobe City College of Technology,
8-3 Gakuen-Higashimachi Nishiku, Kobe, Hyogo 651-21

Abstract

Metal surface modification by irradiation of intense pulsed ion beams (IPIB) has been studied experimentally. A mixed carbon and fluorine IPIB with power density of 32 MW/cm^2, pulse duration of 25 nsec was irradiated to titanium, aluminum, copper and $Ni_{65}Cr_{15}P_{16}B_4$ alloy. Surface temperature of titanium was estimated to exceed its boiling point (3550K) by IPIB irradiation, resulting in removing of machining roughness of titanium surface. For $Ni_{65}Cr_{15}P_{16}B_4$ alloy, an amorphous layer on the substrate surface within 0.66 μm in depth was formed by IPIB irradiation. Ion range, heating temperature and cooling rate for a nickel substrate are estimated to be 0.23 μm, 3150K and 3.8×10^5 K/sec, respectively.

1 Introduction

Recently, an intense pulse ion beam (IPIB) with a high power density (~GW/cm^2) and a short pulse width (~10nsec) is attracted as a new heat-source instead of laser in a material development field.[1-5] As ion ranges are extremely shorter than electron ones,

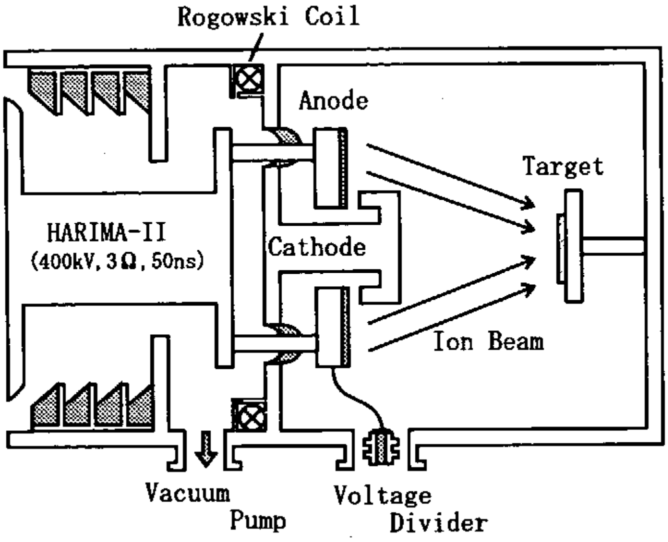

Fig.1 Schematic configuration of experimental setup.

the beam energy is deposited to a surface layer, typically, within a few μm. As a result, a target surface is heated up to several thousand degrees centigrade in a short time of several nanosecond, and is immediately followed by rapid cooling and resolidification. Solidification of metals at the rapid cooling rates results in the production of amorphous or nano-crystalline phases and the smoothing of metal surfaces.

In this paper, we report on the smoothing of titanium surface and the formation of an amorphous layer on a $Ni_{65}Cr_{15}P_{16}B_4$ alloy by irradiating of the IPIB. The apparatus and methods are introduced in §2. Experimental results and some discussion are presented in §3, and some conclusions are described in §4.

2 Apparatus and Methods

2.1 Experimental Setup

A drawing of an experimental setup is shown in Fig. 1. The IPIB was generated with an inverse pinch ion diode (IPD)[6,7] using the pulsed power generator "HARIMA-II" (400 kV, 3 Ω, 50 ns) at Himeji Institute of Technology. The IPD was consisted with a ring anode and an annular cathode. The IPD was located at the end of the "HARIMA-II" generator. The outer diameters of the anode and the cathode were 50 mm and 16 mm, respectively. A Teflon plate 2 mm in thick was attached to the anode as an ion source. The anode-cathode (A-K) gap length was 3 mm. A target material was located at 120

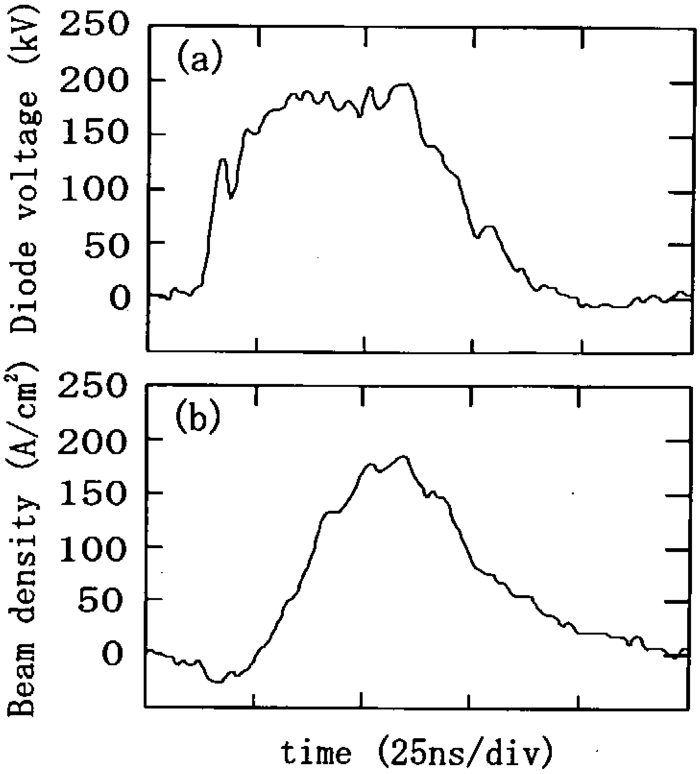

Fig.2 The typical time history of (a) a diode voltage and (b) a current density of ion beams, respectively.

mm downstream the anode. The typical pressure for diode operation was in the range of 2.0×10^{-5} to 8.0×10^{-5} Torr. The diode voltage was measured with a resistive divider placed close to the anode plate. The diode current was measured with a Rogowski coil at the output of the pulsed power generator. The ion current was estimated using a biased ion collector (BIC) located on the downstream side of the diode.

2.2 Properties of the IPIB

Figure 2 shows the typical time history of (a) a diode voltage, (b) a current density of an ion beam was measured with the BIC located at 120 mm behind the anode. As seen in Fig. 2, the diode voltage reaches the maximum value of 180 kV in 10 nsec, and the pulse width is 70 nsec (full width at half maximum: FWHM). The current density of the ion beam has maximum value of 180 A/cm^2. A pulse duration of the ion beam was found to be 25 nsec. From these values, a power density of the ion beam was estimated to be 32 MW/cm^2. The main components of the ion beam were confirmed carbon (C^{2+}, C^{3+}, C^{4+}) and fluorine (F^{+}, F^{2+}) ions in another experiment.[8)]

3 Results

3.1 Surface Smoothing

IPIBs were irradiated to an aluminum, copper and titanium plates (15mm × 15mm × 0.5mm), respectively. These targets were polished with emery paper (#1000) and annealed in a vacuum as the heat treatment. The target was located at 120 mm behind the anode and was irradiated with the IPIB at 5 times. Figure 3 shows the topography of the target surfaces before and after IPIB irradiation. The machining roughness produced by polishing is found on the surface of each target before IPIB irradiation. As seen in Fig. 3, the machining roughness on the titanium and aluminum surfaces almost disappears after IPIB irradiation. However, the smoothness on the treated aluminum surface is not sufficient compared with the titanium surface. Furthermore, there are some new defects such as a crater on the treated aluminum surface. On the other hand, the machining roughness on the copper surface is not removed by IPIB irradiation.

By irradiating IPIB to a target material, the target surface is heated in a short time of several nanoseconds. Neglecting radiation loss, the temperature rise of the target surface is written as

$$T_{\mathrm{S}} = \frac{2p}{K}\left(\frac{\kappa\,\Delta t}{\pi}\right)^{1/2} \qquad \mathrm{(K)} \tag{1}$$

where κ is the thermal diffusion rate, K is the thermal conductivity, p is the power density of the uniform beam, and Δt is the beam pulse width. Substituting the present parameters (p=32MW, Δt=25 nsec) into eq.(1), a temperature rise of each target material is estimated. The results obtained are shown in Table 1 together with the melting point and boiling point of each target material. From this result, the temperature rise of titanium surface is found to sufficiently exceed the boiling point. Thus, some of the titanium surface might be evaporated by IPIB irradiation. The estimated surface temperature of the aluminum exceeds its melting point, but is less than its boiling point. For a case of copper, the estimated surface temperature is less than its melting point. From these studies above, the surface temperature rise more than a boiling point might be a necessary condition for production of surface smoothing by IPIB irradiation.

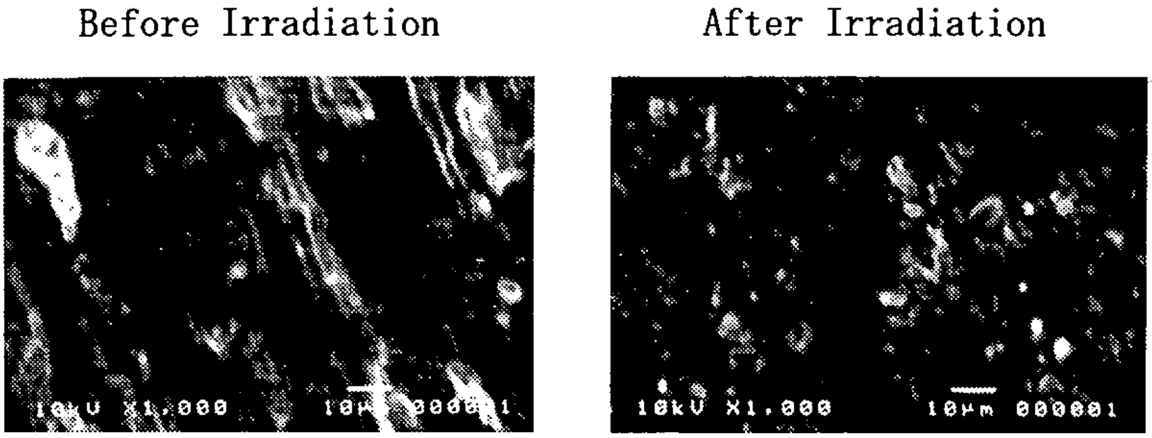

Before Irradiation

After Irradiation

(a) Aluminum

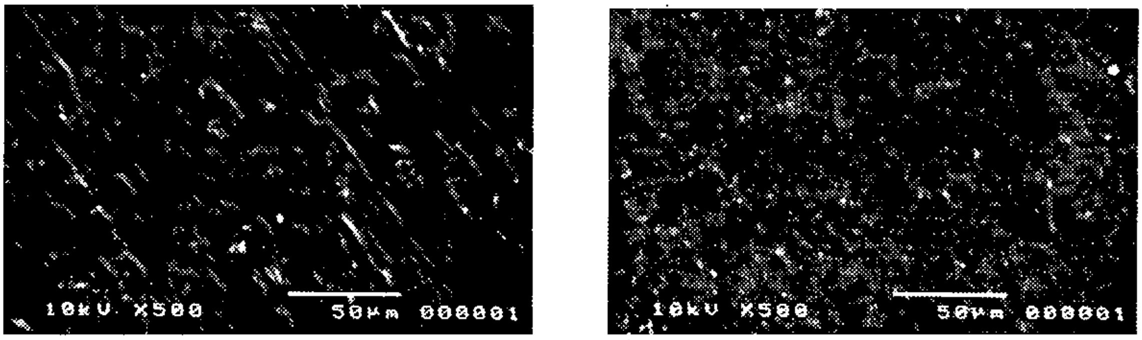

(b) Titanium

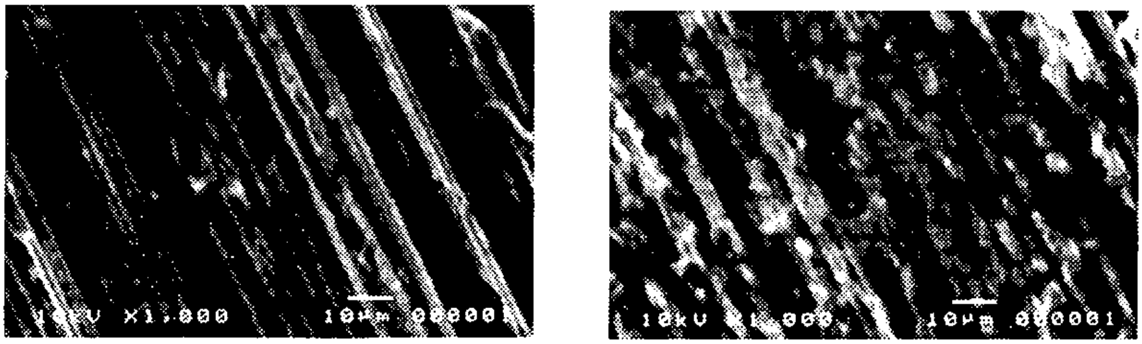

(c) Copper

Fig.3 The topography of the target materials before or after irradiation of a 32 MW/cm^2, 25 nsec mixed carbon and fluorine beam.

Table 1 The surface temperature of target materials by irradiating to IPIB of power density, 32MW/cm^2 and pulse width, 25nsec.

Target	Temperature rise T_S (K)	Melting point T_M (K)	Boiling point T_B (K)
Al	2,773	873	2,723
Ti	8,373	1,933	3,550
Cu	1,773	1,356	2,853

3.2 Amorphous layer formation

A shot of mixed carbon and fluorine IPIB was irradiated on a $Ni_{65}Cr_{15}P_{16}B_4$ alloy to make amorphous structure. The amorphous nature of the IPIB-processed surface was examined by the X-ray diffractometry (CuKα, 50 kV, 200 mA).

The typical X-ray diffraction pattern of the IPIB non-irradiated $Ni_{65}Cr_{15}P_{16}B_4$ alloy is shown in Fig. 4(a), where the maximum X-ray diffraction depth is estimated to be approximately 1.3 μm. Figure 4(b) shows the X-ray diffraction patterns of the IPIB irradiated $Ni_{65}Cr_{15}P_{16}B_4$ alloy for various incident angle α of the X-ray to the target, where $\alpha = 1.0°$, 1.5°, and 2.0° correspond to the maximum X-ray diffraction depth from the surface, d=0.6, 0.99, and 1.3 μm, respectively. As shown in Fig. 4, the diffraction pattern of the non-processed substrate reveals the crystalline phase which is characterized by the narrow spectrum. While the IPIB-processed $Ni_{65}Cr_{15}P_{16}B_4$ alloy surface exhibits the typical diffraction pattern of the amorphous structure. The diffraction patterns for $\alpha = 1.5°$ and 2.0° reveal the formation of a mixture of a major amorphous and a minor crystalline phase. For $\alpha = 1.0°$, however, the narrow spectrum indicating the crystalline phase disappears, suggesting that a shot of IPIB irradiation to the $Ni_{65}Cr_{15}P_{16}B_4$ alloy produces amorphous structure within the surface layer less than 0.66 μm.

To make a rough estimate of temperature rise and cooling rate of the target surface by a IPIB irradiation, we assume that a single species of carbon or fluorine ions is injected into the nickel target. Since the ion beam energy is typically 180 keV in the present experiments, the ion beam velocity is less than Bohr electron speed ($v_B \sim 2.2 \times 10^8$ cm/sec). For this low energy region, total ion ranges in a target are given by Lindhard, Scharff and Shiϕtt (LSS) theory.$^{9)}$ Using LSS theory the total range of the carbon or fluorine ions

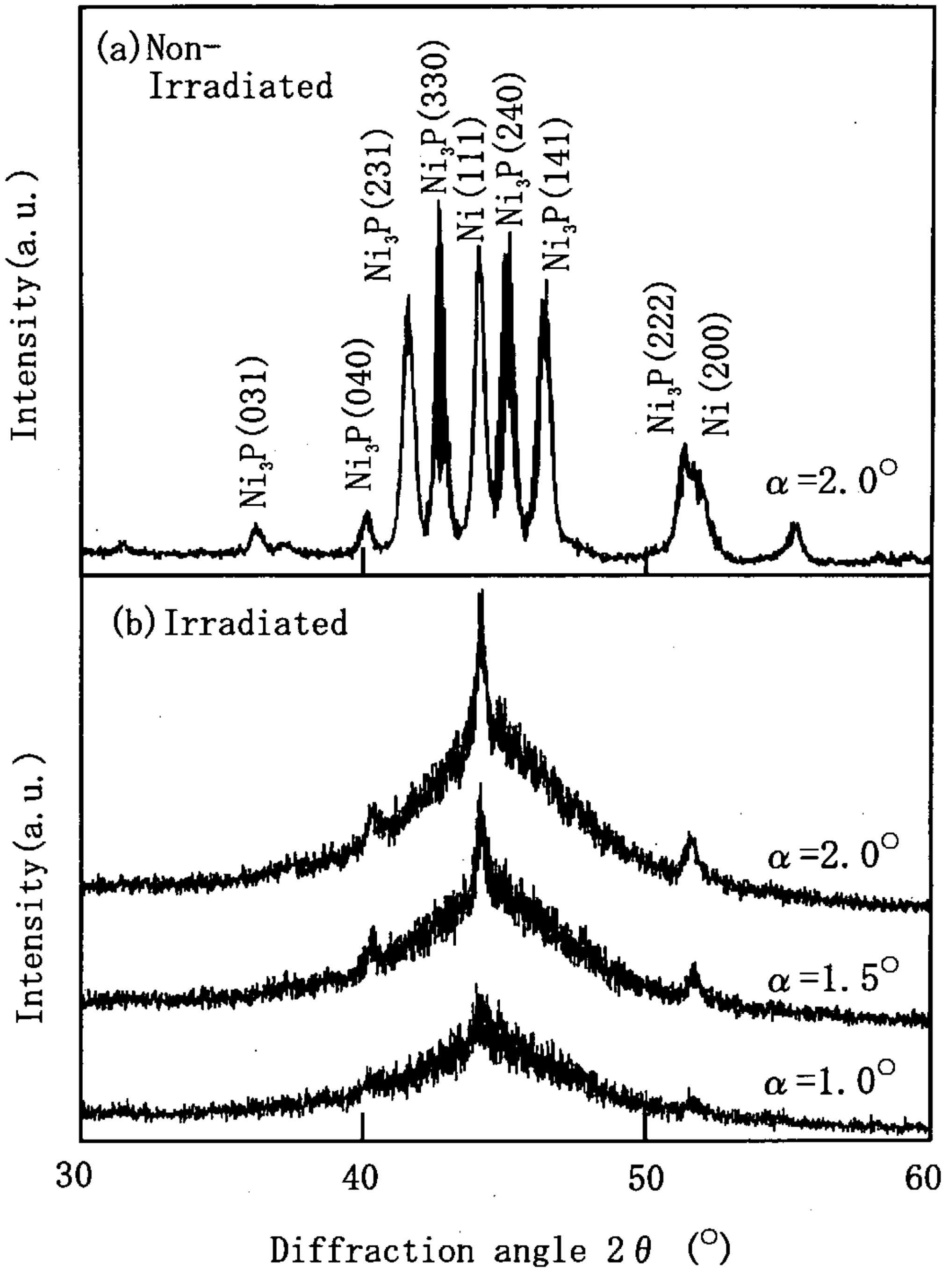

Fig.4 X-ray diffraction patterns of (a) a non-processed $Ni_{65}Cr_{15}P_{16}B_4$ alloy and (b) the IPIB irradiated $Ni_{65}Cr_{15}P_{16}B_4$ alloy where α indicates the angle of the incident X-ray to the target. The smaller value of α indicates the smaller depth from the surface.

with the beam energy of 180 keV is estimated to be 0.23 or 0.17 μm, respectively. On the other hand, the thermal diffusion time for the distance of an ion range R is approximately given by $\tau_d = R^2/\kappa$. Using $\kappa = 0.13$ cm^2/sec and $R = 0.23$ μm for nickel, we obtain $\tau_d = 4$ nsec that is less than the beam pulse duration (τ_d=25 nsec). This implies that the temperature of the target is given by the solution of thermal diffusion equation shown in eq.(1). For the present conditions (p=32MW/cm^2, Δt=25nsec, K=0.67 W/cm/K), we obtain $T_S = 3150$ K with eq.(1). Then the near surface of the target is heated up to more than boiling point of nickel, i.e. 3004 K. The cooling rate for amorphous formation is written as

$$\frac{dT}{dt} = \frac{h\,(T_m - T_g)}{\rho\, c_p\, z} \qquad \text{(K/sec)} \tag{2}$$

where T_m is the melting point, T_g is the glass transition temperature, h is the heat transfer coefficient from the high temperature region to the initial temperature region, ρ is the solid density, c_p is the specific heat of target, and z is the depth of high temperature region. With $T_m = 1728$ K, $\rho = 8.85$ g/cm^3, and $c_p = 0.57$ J/g/K for nickel eq.(2) yields $dT/dt \sim 3.8 \times 10^5$ K/sec, where we used $z = 0.57$ μm (thermal diffusion length), $h = 0.1$ J/sec/cm^2/K, and $T_g = 690$ K for the $Ni_{65}Cr_{15}P_{16}B_4$ alloy. The cooling rate estimated above is enough for producing amorphous structure of nickel alloys.

4 Conclusion

A mixed carbon and fluorine IPIB with the power density of 32 MW/cm^2 was irradiated to the target materials. The machining roughness on titanium surface was removed sufficiently by IPIB irradiation. A surface smoothness is dependent on the temperature rise of target surface by IPIB irradiation. The irradiation of IPIB results in amorphous structure on $Ni_{65}Cr_{15}P_{16}B_4$ alloy surface within 0.66 μm in depth.

References

[1] A .D.Pogrebnjak, I. F. Isakov, M. S. Opekunov, Sh. M. Ruzimov, A. E. Ligachev, A. V. Nesmelov and I. B. Kurakin : Phys. Lett. **A123** (1987) 410.

[2] Y. Shimotori, M. Yokoyama, S. Harada, H. Isobe, K. Masugata and K. Yatsui : J. Appl. Phys. **63** (1988) 968.

[3] K. Yatsui : Laser & Particle Beams **7** (1989) 733.

[4] G. E. Remnev and V. A. Shulov : Laser & Particle Beams **11** (1993) 707.

[5] E. L. Neau : IEEE Trans. on Plasma Science **22** (1994) 2.

[6] Y. Hashimoto, M. Sato, M. Yatsuzuka and S. Nobuhara : Jpn. J. Appl. Phys. **31** (1992) 1922.

[7] Y. Hashimoto, M. Yatsuzuka and S. Nobuhara : Jpn. J. Appl. Phys. **32** (1993) 4838.

[8] Y. Hashimoto, M. Yatsuzuka and S. Nobuhara : Jpn. J. Appl. Phys. **33** (1994) 5094.

[9] J. Lindhard, M. Scharff and H. E. Shiϕtt, Kgl. Danske Videnskab Selskab, Mat. Fys. Modd **3**, No.14(1963).

STUDY OF YBCO THIN FILMS DEPOSITED BY INTENSE PULSED LIGHT ION BEAM EVAPORATION

C.Grigoriu, E.P.Achmad Chamdani, T.Sonegawa, K.Masugata, K.Yatsui
Laboratory of Beam Technology
Nagaoka University of Technology, Nagaoka, Niigata 940-21, Japan

Preparation of thin films of YBCO on MgO (100) by means of intense, pulsed ion beam evaporation is reported. The films have been characterized by X-ray diffraction and electron probe microanalysis. We investigated the dependence of the film composition on target stoichiometry, substrate temperature and number of shots. The study reveals possibility of production of high quality films, c-axis perpendicular on the substrate surface, from 123 YBCO target, 700 ^{0}C substrate temperature, single shot, vacuum deposited. Multishot depositions create off-stoichiometric films, Cu and Ba depleted, approximately by 43%~67% less than the target content in Cu or Ba. This could be explained as a reevaporation of the lower boiling temperature elements (Cu, Ba), by every new high temperature and energy ablated plume.

1. Introduction

Extensive efforts have been devoted to the growth of superconducting oxide films. A number of film deposition techniques as thermal evaporation by electron beam evaporation or molecular beam epitaxy, pulsed laser deposition, sputtering, sol-gel method, have been successfully used for growth of superconductive films. High quality epitaxial films with sharp resistive transitions and high critical current densities now are being routinely produced using such deposition techniques.

An intense, pulsed, light ion beam (LIB) is a possible candidate to be applicable to materials deposition.(1) The intense, pulsed, light ion beam evaporation technique (IBE), can provide high quality films on large area substrates, with a fast deposition rate and at a lower substrate temperature, even without heating the substrate, to prevent the interface from degradation.

If we irradiate the LIB on a target, an extremely high-power density will be achieved near the surface of the target, resulting a high density, high temperature ablation plasma. The beam power density for LIB is typically 10^9 W/cm^2 with the pulse duration of 50~70 ns. This process seems to be similarly to pulsed laser ablation, but total energy/shot, the diameter of LIB-target interaction, are higher by many orders of magnitude than the laser ablation method. All the above characteristics are very attractive, and hence the IBE technique seems to be very promising.

There now exists a considerable amount of literature describing processes and parameters governing the deposition. Some studies have been carried out on the IBE physics.(2-5) However, IBE technique used for the preparation of thin superconductive film requires an understanding of the mechanism of the growth of the film and at the same time to provide practical and technological aspects such as design and optimization of the deposition system.

Our research effort focuses on the development of thin superconductive films deposition, $YBa_2Cu_3O_{7-\delta}$ (YBCO), by IBE technique. In this sense, we carried out a systematic investigation for understanding of specific aspects.

In this article, we investigated the deposition of thin YBCO film on MgO (100) substrate. The fundamental task has been to elucidate dependence of the film composition upon the target composition, number of the shots, substrate temperature. In obtaining a multielement thin film by the evaporation from a single compound target a substantial deviation of composition of film material from its source target is often recognized.(6) For preparation of good YBCO thin films by IBE, this aspect is fundamental, that is why, our work focused on the analysis of the film composition and its optimization by the adjustment of target composition, number of shots.

2. Experimental

Figure 1 schematically illustrates the experimental setup.

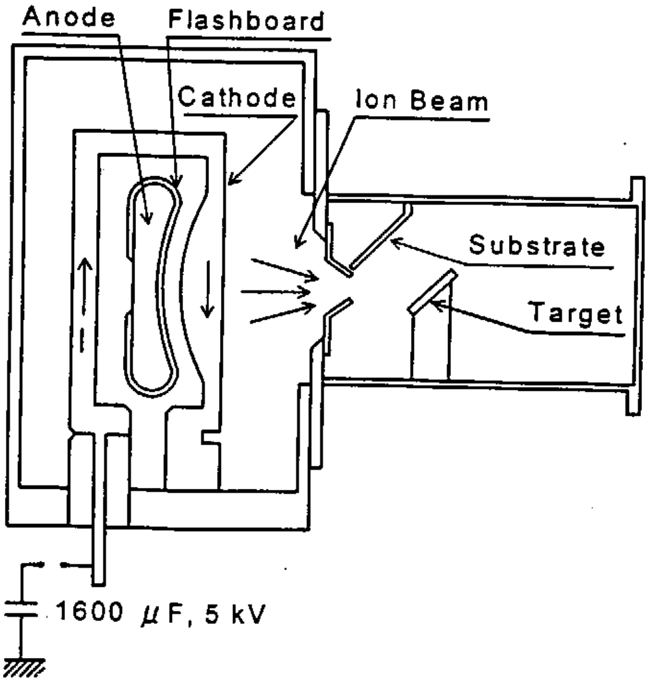

FIG. 1 Experimental setup of IBE system

The experiment has been carried out by the LIB accelerator, ETIGO-II.(1) The LIB is produced by a magnetically insulated ion diode with a geometrically focused configuration. A polyethylene sheet is attached to the anode. The ion species are mainly protons. To achieve geometric focusing of the LIB , both the anode and cathode are spherically shaped. Typically we have operated the magnetically insulated ion diode at V_d (diode voltage) ~1.1 MV, I_d (diode current) ~80 kA, pulse width of I_d ~70 ns and ion current density ~0.5 kA/cm^2. The ion beam is focused onto a 2 cm diameter YBCO target. An intense luminous plume of material is ejected normal to the target surface and is deposited on a parallel placed MgO (100) substrate, of 1.5×1.5×0.05 cm^3. The target position could be varied (3~10 cm) for optimization of target to substrate distance. In contrast with laser ablation method, it is not necessary the target to be rotated , because the ion beam irradiates uniformly the surface of target. The targets were prepared by mixing an appropriate amount of Y_2O_3, $BaCO_3$ and CuO powders, firing at 900 ^{0}C and pressing them into a 2 cm disk at a pressure of 0.8 tons/cm^2, followed by sintering at 950 ^{0}C in flowing oxygen at atmospheric pressure, for 10 hours, and slowly cooled in the furnace.

The polished MgO (100) substrates were cleaned by degreasing procedure involving acetone. Prior deposition, the MgO substrate was annealed for 6 hours at 1000 ^{0}C in flowing oxygen in order to improve the surface crystalinity. It was cemented on a heater block with a silver adhesive for a very good thermal contact, and at the same time, to have a good impact resistance (because of the important impulse value of the ablation plasma on the substrate(4)). The heater block was made of stainless steel and the temperature was measured by means of a thermocouple positioned in a hole under the substrate. The temperature was between 680 ^{0}C and 750 ^{0}C.

Deposition was made in vacuum (3×10^{-2} Pa), and because *in situ* growth is predominantly limited by the incorporation of oxygen atoms into the cell of superconductor oxide, we also deposited in oxygen (2.7 kPa). This phenomenon could be very significant, if we take into account that the deposition is made for a very short duration, 1~5 shots means microseconds, in comparison with hours for other methods. Following deposition , the layers were amorphous as revealed by X-ray diffraction. They were annealed in flowing oxygen using an annealing cycle as follows: heated to 950 ^{0}C /6 h , cooled 6 ^{0}C /min to 600 ^{0}C , 600 ^{0}C /3 h, and cooled to the room temperature in the oven.

The microstructure of the deposited samples was examined by scanning electron microscope (SEM). X-ray diffraction analysis and electron probe microanalysis (EPMA), were carried out to examine cristalinity and composition. The films deposited in vacuum could be up to 0.3 μm thick for one shot, 6 cm target-substrate distance, depending on target-substrate distance, the oxygen pressure and beam energy; thinner films are obtained for longer target-substrate distances , lower beam energy, and higher oxygen pressure.

3. Results

Firstly, we investigated the films deposited from a 123 YBCO target, substrate being at room temperature, in vacuum or 2.7 kPa oxygen pressure. The X-ray-diffraction patterns for these films are inadequate, with many extra-peaks of unidentified phases; for example Fig. 2 shows XRD pattern for a film deposited in vacuum, at room temperature. These results, correlated with preliminary EPMA[(8)], suggest that our layers are off-stoichiometrically.

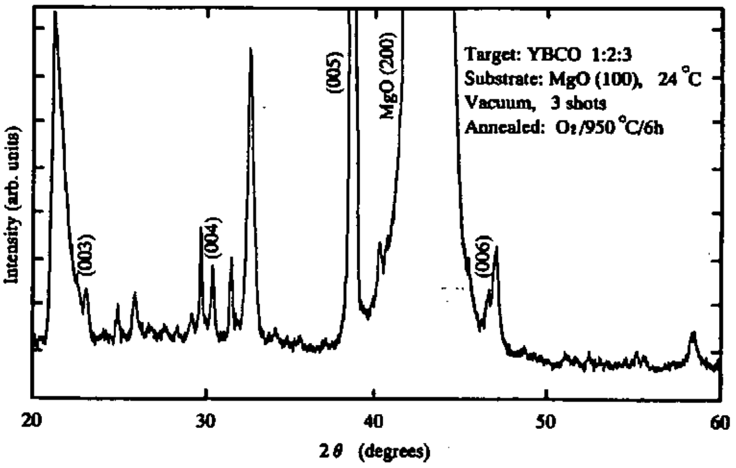

FIG. 2 The XRD pattern of a film deposited in vacuum, 24 °C, 3 shots, annealed; 1:2:3 target.

In order to achieve an improved film composition, we used different target compositions, enriched in barium and copper: Y:Ba:Cu 1 : 2.7~3.5 : 3~5.5, (targets being prepared in the same way). In the case of deposition in vacuum, the best XRD pattern, (Fig. 3), have been obtained with a 1:3.5:5.5 target. When deposition was made in 2.7 kPa oxygen, the best XRD was for 1:3:4 target.

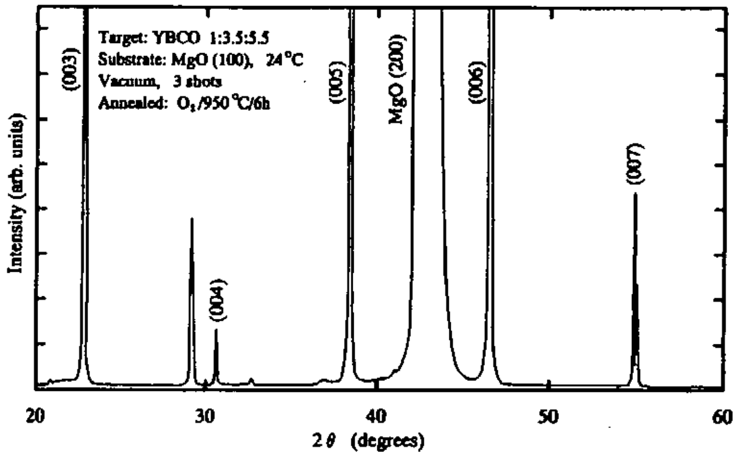

FIG. 3 The XRD pattern of a film deposited in vacuum, 24 °C, 3 shots, annealed; 1:3.5:5.5 target.

Briefly, we can draw the following conclusions: a) the deposition mechanism in vacuum and oxygen is different, and hence we can not obtain the same film quality with the same target composition; b) Ba and Cu enriched targets substantially improve the XRD patterns.

For a better understanding of deposition by IBE , we also investigated the role of the substrate temperature. It is known that in other methods the substrate temperature is an important parameter for optimizing the film growth, influencing nucleation processes and the mobility of the deposit across the substrate.

In Fig. 4(a) is shown a single shot film XRD pattern, for which have been used 123 target and the substrate temperature have been 700 ^{0}C.

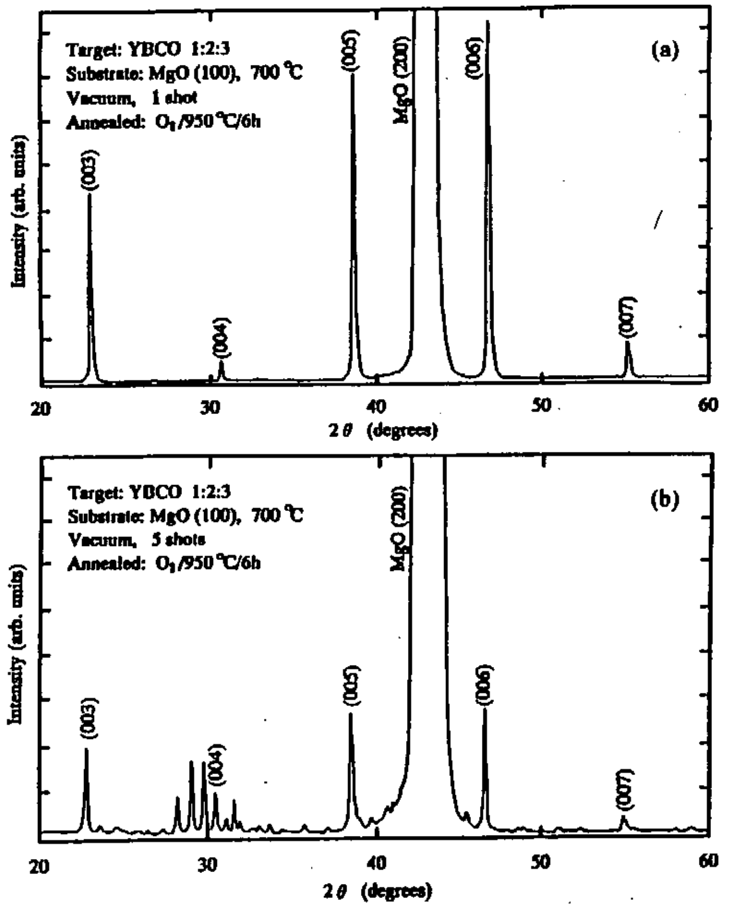

FIG. 4 The XRD patterns of the YBaCuO films (a) deposited in vacuum,700 ^{0}C, 1 shot, annealed, target 1:2:3, and (b) deposited in vacuum,700 ^{0}C, 5 shots, annealed, target 1:2:3.

One can notice that the film deposited by a single shot , shows very pronounced intensity (00*l*) lines, indicating the highly textured structure with the c–axis oriented perpendicular to the substrate surface. It is clear, that the substrate temperature play a very important role in IBE deposition technique, having an optimal value of approximately 700 ^{0}C.

In the case of films deposited by three and five shots , for example five shots case illustrated in Fig. 4(b) , appear many extra peaks which can be associated with the deviation from the film optimal stoichiometry.

In order to elucidate the film stoichiometry we used EPMA, namely energy-dispersive X-ray spectrometer (EDS).

Before to present the experimental results, we must emphasize complexity of the analysis related to the accuracy of the quantitative EDS technique. It is known that the X-ray intensities are not linear with composition because of matrix absorption and enhancement, or of variation in absolute X-ray yield with the atomic number. Therefore, the matrix effects necessitate the use of comparison standards which have to be in the same form as the sample to be analyzed. The accuracy of the analysis is dependent on the standards and the operating conditions (current, operating voltage, x-ray line, etc.) .

On the other hand, the analysis of the thin film is more complicated because the electrons may cross the film, and the X-ray emission now is affected by both film and substrate. A possible method for multielement composition analysis of the thin films(9) could not be used, because of standard thin films that are necessary, particularly because of the barium thin film which create very complex problems.

We adopted correction factor approach, "ZAF" procedure(9,10). For calculation of the composition of the specimens have been sufficient two iterations. In this procedure we used pure yttrium, barium and copper standards. A special attention has been paid to barium manipulation, a very reactive element, sensitive to oxygen, water and common cleaning means, as alcohol. Also we limited our analysis procedure to the films with thickness greater than electron penetration depth, i.e. the films obtained by three or five shots, in vacuum. Fortunately, they are just the films which shows inadequate XRD patterns and therefore we are especially interested to know their composition.

The EDS analysis was performed in an integrated or "windows" mode.

The stoichiometric ratios are listed in Table I.

TABLE I. YBCO thin film composition dependence on target composition. Deposition conditions are: LIB energy density 50 J/cm^2, power density 1 GW/cm^2; the distance between the target and MgO substrate (d) 6 cm; deposited in vacuum, ~3×10^{-2} Pa.

Target Y:Ba:Cu	Substrate temperature [^{0}C]	Number of shots	Ba / Y	Cu / Y
1:2:3	24	3	1.14	1.33
1:2:3	700	5	0.88	0.98
1:2.7:3.8	24	3	1.26	1.62
1:3:4.5	24	3	1.32	1.75
1:3:5	24	3	1.36	1.80
1.3.5:5.5	24	3	1.51	2.19

The EDS results reveal that in the case of multishot deposition, in vacuum, the film is barium and copper depleted; in comparison with initial target stoichiometry, we noticed 43~56% less barium and 56~67% less copper. These results confirm the inadequate XRD patterns for multishot depositions, and suggest utilization of higher Ba and Cu concentration targets.

If we compare IBE with pulsed laser ablation, apparently a similar deposition technique, where it is used pulsed laser beams (typically 30 ns pulses with the energy of 10~100 mJ/pulse, 0.1~5 J/cm^2, and a repetition rate around 10 pps), our case is very different. The target is irradiated with LIB of approximately 50 J/cm^2, 1 GW/cm^2, and maximum 5 pulses. The plume that impinges the substrate, consists of huge amount of very energetic particles. In consequence, the substrate suffers instantaneously a strong bombardment, occurring a selective reevaporation, particularly valid for barium and copper, which in comparison with yttrium, have lower boiling points, by 1698 ^{0}C and 770 ^{0}C, respectively, less. Of course, at the same time, the environmental gas pressure, is a very important parameter, that influences both incident LIB, and the ablated plume, and thus influences the reevaporation process.

The thin films deposited in oxygen being thinner, we could not get reliable data, concerning the film stoichiometry. Additional work on this subject is in progress.

4. Conclusions

In conclusion, we investigated the deposition possibility of the YBCO films by intense, pulsed, light ion beam evaporation on MgO substrates. The single shot deposited film, from the 123 target, at an optimal temperature of 700 ^{0}C, reveals typical XRD pattern for high quality epitaxial YBaCuO films which have a high degree of orientation, c-axis perpendicular on the substrate. The films deposited by multiple shots, show many extra-XRD peaks, owing to off-stoichiometry composition. Improved XRD patterns have been obtained using Ba and Cu enriched targets. Electron probe microanalysis has shown that during the successive irradiations, the composition of the film is Ba and Cu depleted, about by 43%~67% less than the Ba and Cu concentration of the target. This phenomenon could be explained by the reevaporation of the Ba and Cu from the previous deposited film, every time when it is bombarded by the high temperature energetic plume. Furthermore, we concluded, that for multishot deposition , the target has to be enriched in Ba and Cu, in accordance with the deposition conditions.

References

(1) K. Yatsui, Laser Part. Beams 7,733 (1989)

(2) Y. Shimotori, M. Yokoyama, H. Isobe, S. Harada, K. Masugata and K. Yatsui, J. Appl. Phys. **63**, 968 (1988).

(3) Y. Shimotori, M. Yokoyama, S. Harada, K. Masugata and K. Yatsui, Jpn. J. Appl. Phys. **28**, 468 (1989).

(4) X.D. Kang, K. Masugata and K. Yatsui, Jpn. J. Appl. Phys. **33**, Pt. 1, 1155 (1994).

(5) K. Yatsui et al, Phys. of Plasmas **1**, Pt. 2,1730 (1994).

(6) Y. Kageyama and Y. Taga, Appl. Phys. Lett. **55** (10) 1035 (1989).

(7) K. Yatsui et al, Laser Part. Beams **5**, 495 (1987).

(8) M. Oh-hashi, Master thesis (Nagaoka University of Technology), (1992).

(9) J.I. Goldstein, D.E. Newbury, P. Echlin, D.C. Joy, C. Fiori and E. Lifshin, Scanning Electron Microscopy and X-ray Microanalysis, (Plenum Press, N.Y.), 359 (1981).

(10) L.S. Birks, Electron Probe Microanalysis, ed. E.Krieger, (N.Y.), (1979).

Dynamics of Z-pinch Plasma Target for Beam-Plasma Interaction

Tomonao HOSOKAI, Mitsuo NAKAJIMA, Takayuki AOKI,
Kazuhiko HORIOKA and Masao OGAWA

Department of Energy Sciences, Tokyo Institute of Technology
Nagatuta 4259, Midoriku Yokohama 226 Japan

Abstract

In order to get stable, long life and high density targets for beam-plasma interaction experiments, the dynamics of Z-pinch hydrogen plasma was investigated under intermediate discharge conditions (drive current < 100kA , initial gas density < 10^{18}cm^{-3}). It was confirmed that there was a structure in the Z-pinch plasma column. As initial gas pressure increases, the current sheet in the column separated from the shock front. The interaction between the current sheet and the reflecting shock wave was observed. Those behaviors were well explained by a 1D-MHD simulation. If we can optimize the discharge condition, we can obtain the long life and high density plasma target.

1. Introduction

The experimental research on the interaction process of heavy ion beams with plasma is of great interest for heavy ion fusion (H.I.F.) and accelerator technology.[1],[2] Theoretical calculations predict that stopping power and charge state of heavy ions increases in plasma effect as compared to in cold gas. Furthermore, the effects of dielectronic and three-body recombination are becoming important in the high density plasma. They are strongly dependent on the electron density.[3]

Typically, there are two types of conventional Z-pinch plasma whose behaviors are well understood. One is the so-called dynamic Z-pinch. The discharge is generally driven by large-sized pulse power generator under conditions of high drive current (> 1MA) and low initial gas density (< 10^{17}cm^{-3}). Its behavior is well explained by the application of snow plow model. Another is the spark channel. It is typically observed in high pressure gap switches, and is characterized by the expanding plasma column; inverse Z-pinch discharge. Usually it has been operated under conditions of low drive current (< 10kA) and high initial gas density (> 10^{18}cm^{-3}). Their qualitative behavior can be explained by the strong shock approximation [4]. However, under intermediate ranges between the dynamic Z-pinch and the spark channel (drive current < 100kA, initial gas density < 10^{18}cm^{-3}), there is not clear explanation for dynamics of the Z-pinch plasma. Because of complex structure in the plasma column, it is almost impossible to express the plasma dynamics by the simple analytical models.

In order to realize beam plasma interaction experiment, we try to get stable high density plasma target by Z-pinch discharges. We investigate the dynamics of Z-pinch hydrogen plasma column in the intermediate operational range. The formation and the pinch phase of plasma column have been observed with its visible light emission. To explain the plasma dynamics, numerical simulations using a simple model and a one dimensional, single fluid, two temperature MHD model have been carried out.

The purpose of the present investigation is to make clear the dynamics of Z-pinch discharge by comparison of the experimental results with simulations.

2. Target Requirements

In the beam-plasma interaction experiment, ion beams are injected into a cylindrical plasma. Theoretical prediction indicates that the electron area density above 10^{19} cm^{-2} of hydrogen plasma are required for the appearance of the plasma effect. To attain such high electron density with well defined condition it is necessary to produce a neutral free plasma.

Plasma parameters and their geometry must be matched to the ion beam features. The requirement for the target diameter comes from the ion beam spot size. At least, the life time of the target should be much greater than the transit time of the interacting projectiles traversing the interaction region. Therefore, the uniformity and stability are the critical factors for the target plasma; that means the column is homogeneous and free from instabilities over the whole interaction region and duration.

For our beam-plasma experiment, heavy ion beams ranging from C^{12+} to Ar^{18+} with a fixed energy of 6MeV/u will soon be available in the accelerator facility HIMAC (Heavy Ion Medical Accelerator in Chiba) at the NIRS (National Institute of Radiological Sciences).

Several kinds of plasma sources have been considered as targets. Although, dynamic Z-pinch discharges driven by large sized pulse power generators can produce dense plasmas, the whole system is too large for the beam line structure of the accelerator. From the point view of geometrical adaptability to the beam line, a Z-pinch device using moderate sized capacitor is the most favorable candidate.

Requirements for the hydrogen plasma target are listed as follows.

[1] Electron area density > 10^{19} cm^{-2} (fully ionized).
[2] Diameter > 5mm
[3] Life time > 0.5μsec
[4] Uniform and instabilities free
[5] Adaptable to the beam line of accelerator

3. Experimental Setup

3-a. Z-pinch Device

We produced the Z-pinch plasma driven by a simple LC circuit with a peak current level up to 60kA and initial gas pressure of 20 torr. Parameters of the Z-pinch device are as follows.

Bank energy < 800J

Charging voltage 10 - 20kV
Capacitance 4.4μF
Inductance(including circuit inductance) 100nH
Maximum current < 60kA
Current rise < $3 * 10^{10}$ A/sec
Filling pressure 0.4 - 20 torr (H_2)
Plasma length 10 cm
Pyrex tube radius 3.5cm

Figure 1 shows a schematic of the Z-pinch device. The symmetric and coaxial arrangement is necessary for a homogenous plasma ignition and its stability. The arrangement of the components of the devices, (capacitor, spark gap switch and Pyrex tube filled with hydrogen gas) were piled up coaxially in this order. The return path of current, consisting of twelve copper rods from anode to the capacitor, was also constructed coaxially. A knife edge on the cathode electrode close to the inner wall of Pyrex tube helps homogenous ignition and discharge on the surface of the inner wall. The discharge current and the voltage between electrodes were monitored by a Rogoswki coil and a high voltage probe.

3-b. Diagnostic Systems

Figure 2 shows a schematic of the experimental set up. The discharge dynamics and the electron densities at the center of Z-axis were diagnosed by visible light emission of the hydrogen plasma. The discharge dynamics was observed with a streak camera (HAMAMATSU C-2830). The slit of the camera was aligned perpendicular to the Z-axis, which cut out the image from center portion of the column. The focal depth of this optical system is about 5mm from the center of Z-axis.

The electron density was estimated from the Stark broadening of hydrogen Balmer-α (656.3nm). The line broadening of Hα is analyzed using a 25cm-monochromator with gratings of 1200 lines per millimeter(Japan Spectroscopic Co.Ltd. CT-25C). It is coupled with the streak camera, which is arranged behind exit slit of it. The slit was aligned parallel to the Z-axis of the column. The spatial and the temporal resolution of this system were about 0.1nm and 20 nsec respectively. They were calibrated using a He-Ne laser(632.8nm).

4. Numerical Simulation

We have done numerical calculations on the dynamics of the Z-pinch plasma using 1D-MHD code; MULTI-Z [5] .

We assume that the plasma channel has been formed initially by the first discharge. The initial condition of the simulation is as follows; The gas has uniform density in the Pyrex tube. The gas temperature has a coaxial double layer profile, the outer shell of 5 mm thickness with T = 0.04 eV and the core of 3 cm thickness with T = 0.0026 eV.

The interface of the layers determined from the observed streak images. The outer shell of 0.04 eV has high electrical conductivity, so that it plays a role of initial current sheet. The discharge current is mainly determined by the parameters of the external circuit. Therefore we set the discharge current of the experiment as an input parameter in the simulation.

Figure 3 shows the calculated X-t diagram. Figure 4 shows spatial-time distributions of electron density. Figure 5 shows spatial-time distributions of electron temperature. These results lead to the following picture of the plasma dynamics in the Z-pinch discharge. The current flow starts from the area where close to the wall (r > 3cm), leaves the wall and goes inside to the axis as time evolution. A shock wave is driven by the pressure of the current sheet and propagates ahead of the current sheet and reflects at the center. As initial gas pressure increases, the velocity of the current sheet decreases compared to that of shock front, so the current sheet separates from the shock front. The electron density is increased behind the shock front. There are a lot of neutrals between the shock front and the boundary of current sheet. When the cylindrical shock wave converges to the axis, the electron density and temperature increase rapidly and gas is fully ionized only in the central narrow region with thickness about 2mm. At the peak, the electron density is about $\fallingdotseq 1.8 * 10^{18} cm^{-3}$ and the electron temperature is $\fallingdotseq$1.5eV, when we drive the hydrogen gas of 0.4torr with peak current of 60kA.

In the current sheet the electron temperature and the electron density are increased by Joule heating. As shown in Fig.3, the interaction appears between the reflecting shock and the imploding current sheet.

5. Discussion; Comparison with MHD Simulations

Figure 6 shows the typical streak image of the plasma column where Z-axis denotes luminous intensity of the image. As shown in figure 6, the cylindrical plasma was formed at the inner wall of the Pyrex tube in the beginning of discharge and the current sheet converged to the center.

Figures 7 shows the comparison of experimental results with calculated results on pinch time as a function of initial gas pressure. The pinch time was experimentally determined from the streak images as the time when width of luminous region takes minimum value at the first stage of convergence. On the other hand, from the snow plow calculation, we can define the pinch time. In the similar way, from the MHD simulation, pinch time of the shock wave and the current sheet boundary was also defined. The snow plow estimation agree with observed ones only at low pressure region. The motion of observed luminous region can be explained well by the motion of the calculated current sheet boundary on the MHD simulation for all initial conditions.

Figure 8 shows comparison of the X-t diagram obtained by the MHD simulation with observed luminous profiles on the center. A strong correlation was observed between them. As shown in Fig. 8, the luminous profile keep a peak value from the arrival time of shock front till the arrival time of the current sheet boundary on the axis. The time duration corresponds to the life time as the plasma target. The time evolution of electron density (Fig.4) on the axis is shown in Fig.9. We can find a structure in the plasma column. A shock wave driven by the pressure of current sheet implodes ahead of the current sheet. The shock wave reflects on the axis and interact with the imploding current sheet. The interacted shock wave reflects back to the axis. The high electron density is maintained for time duration of the processes (see Fig.9). The interaction process is also observed in the results of MHD simulation. When we drive the discharge with a peak current of 60kA at 0.4 torr (H_2 gas), the observed maximum electron density and the life time of it reached $1.5*10^{18}cm^{-3}$, 500 nsec respectively on the axis. These values are consistent with the simulations shown in Section 4.

These results lead to following picture for the Z-pinch discharge. The magnetic pressure produced by the current, Z-discharge is usually greater than the gas pressure in compression processes. In the compression phase, the pressure drives an imploding shock wave. In case of a dynamic Z-pinch, magnetic pressure is far greater than the gas pressure. So, the current sheet can travel with almost the same velocity of the shock front. But when the magnetic pressure decreases and the effective mass of the current sheet increases, it can't move with the shock front. As a result, the separation between them increases with decrease of the driving current and increase of the initial gas pressure. If we can optimize the interaction process between the shock wave with the current sheet, we can obtain high density and long life plasmas at the center axis.

6. Conclusions

Under the intermediate discharge conditions (drive current < 100kA , initial gas density < $10^{18}cm^{-3}$), a structure was observed in the plasma column. In the discharge column, the converging current sheet drove an imploding shock wave in front of it, and the separation of them increased with the initial pressure. The correlation between them was assured by streak images of visible light emission from the plasma column. Utilizing this structure, we can expect high density and long life plasma targets.

With the peak current of 60kA and the initial gas pressure of 0.4torr, we could make a Z-discharge plasma of 2mm diameter, $1.5*10^{18}$ cm^{-3} electron density, and 500 nsec life time on the center.

7. Acknowledgment

We are grateful to Professor S.Ishii for providing us the storage capacitors and giving us valuable comments on this work.

8. References

[1] D.Gardes, R.Bimbot *et al.* ; Journal de Physique, 49, C7-151 (1988)

[2] C.Deutsch, P.Fromy, X.Garbet and G.Maynard; Fusion Technology, vol.13 , 362 (1988)

[3] T.Peter and J.Meyer-ter-Vehn; Phys. Rev. A 43, 2015 (1991)

[4] G.Vlases and D.Jones; Phys. Fluids, 9, 478, (1966)

[5] T.Aoki; this proceeding.

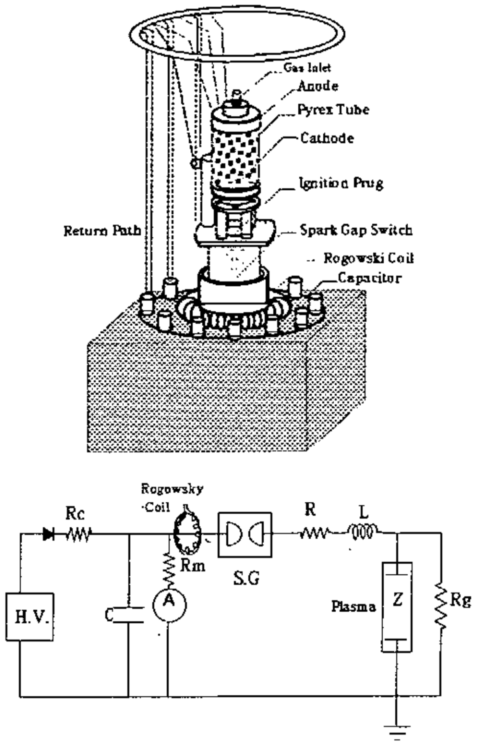

Figure 1 A schematic of the Z-pinch device.

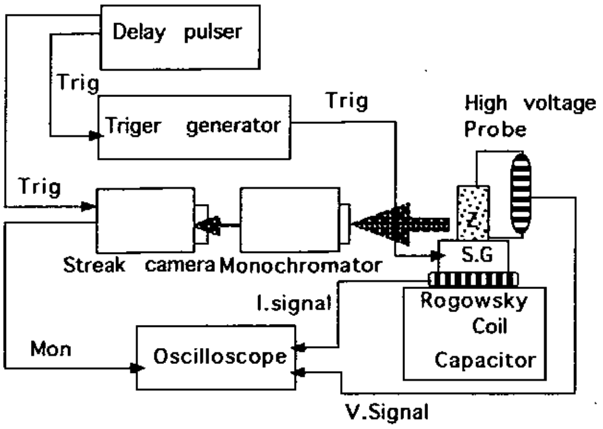

Figure 2 Schematic of the experimental set up.

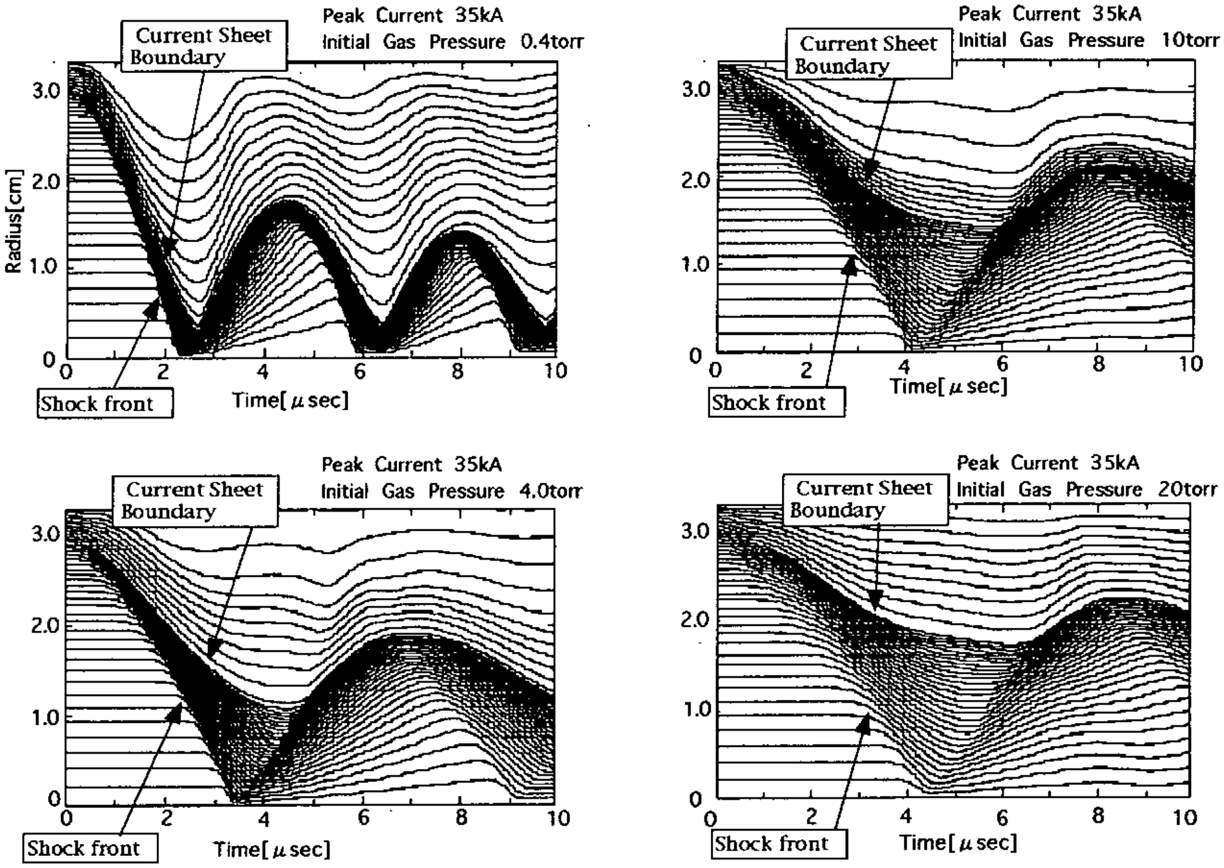

Figure 3 X-T diagram obtained by MHD simulation.

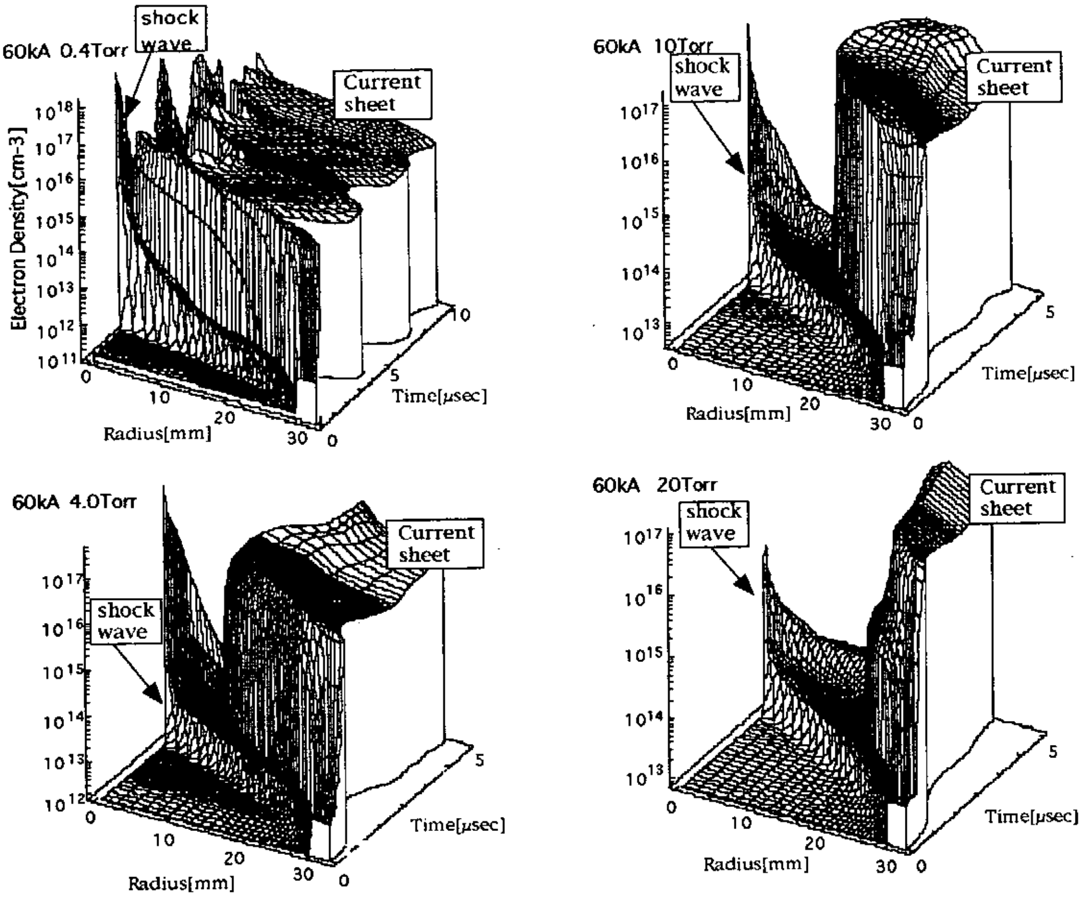

Figure 4 Spatial-time distribution of electron density.

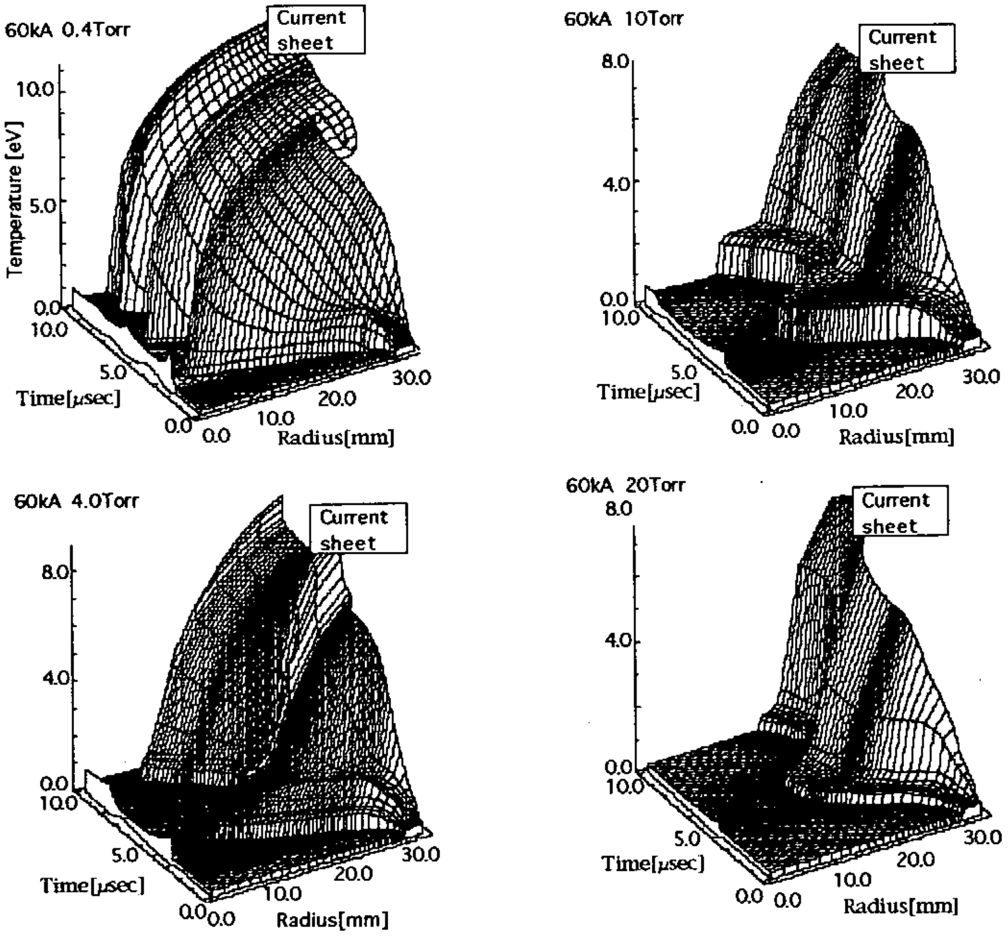

Figure 5 Spatial-time distribution of electron temperture.

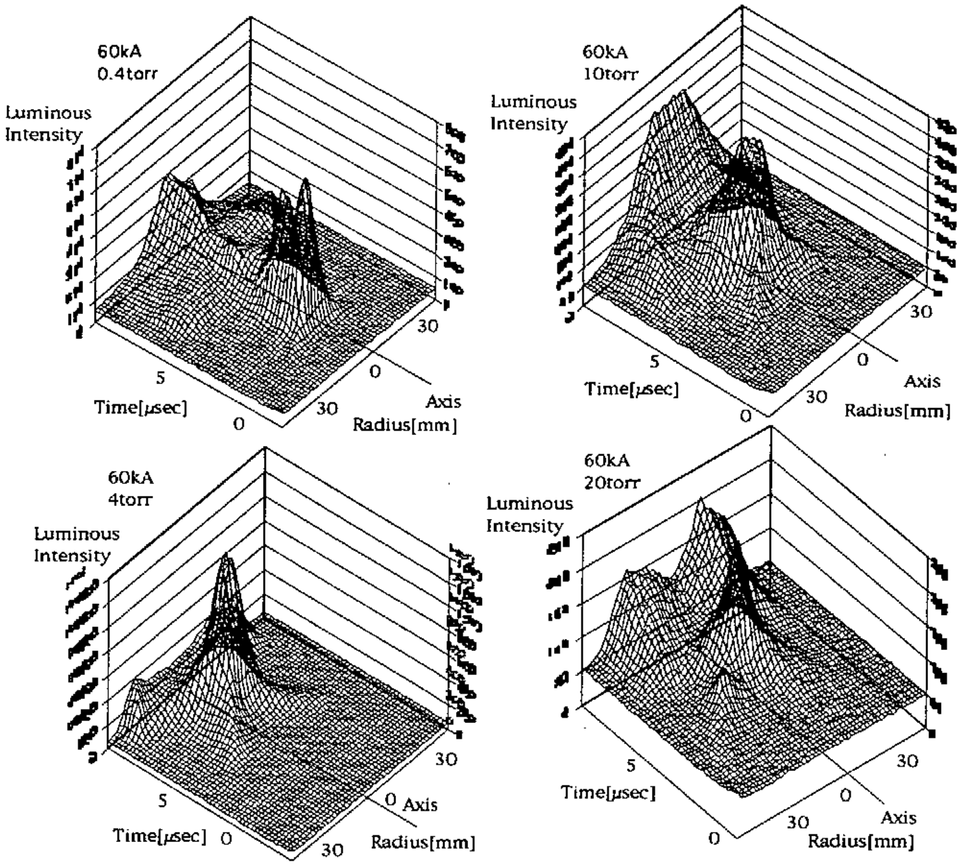

Figure 6 The typical streak image on the plasma column.

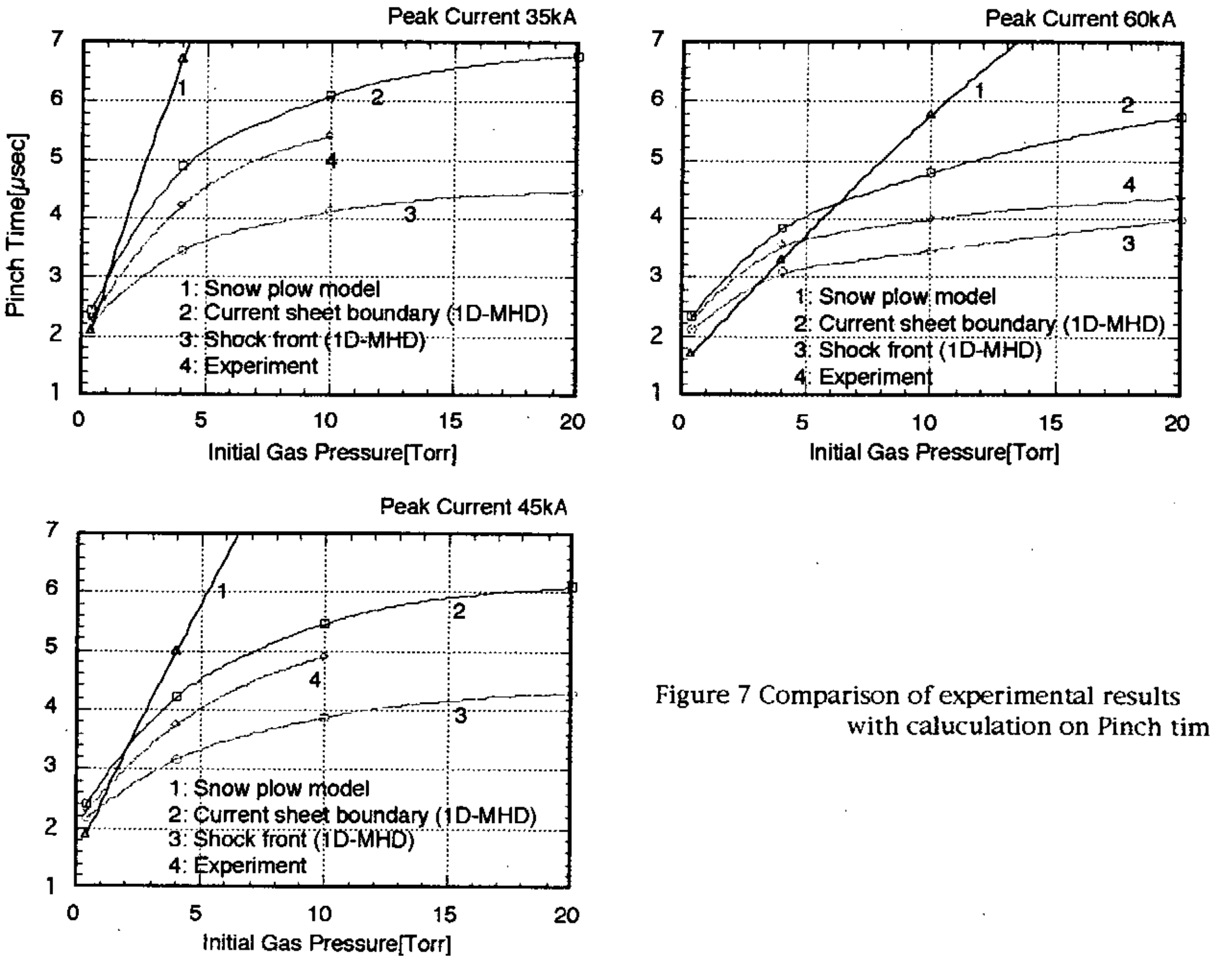

Figure 7 Comparison of experimental results with caluculation on Pinch time

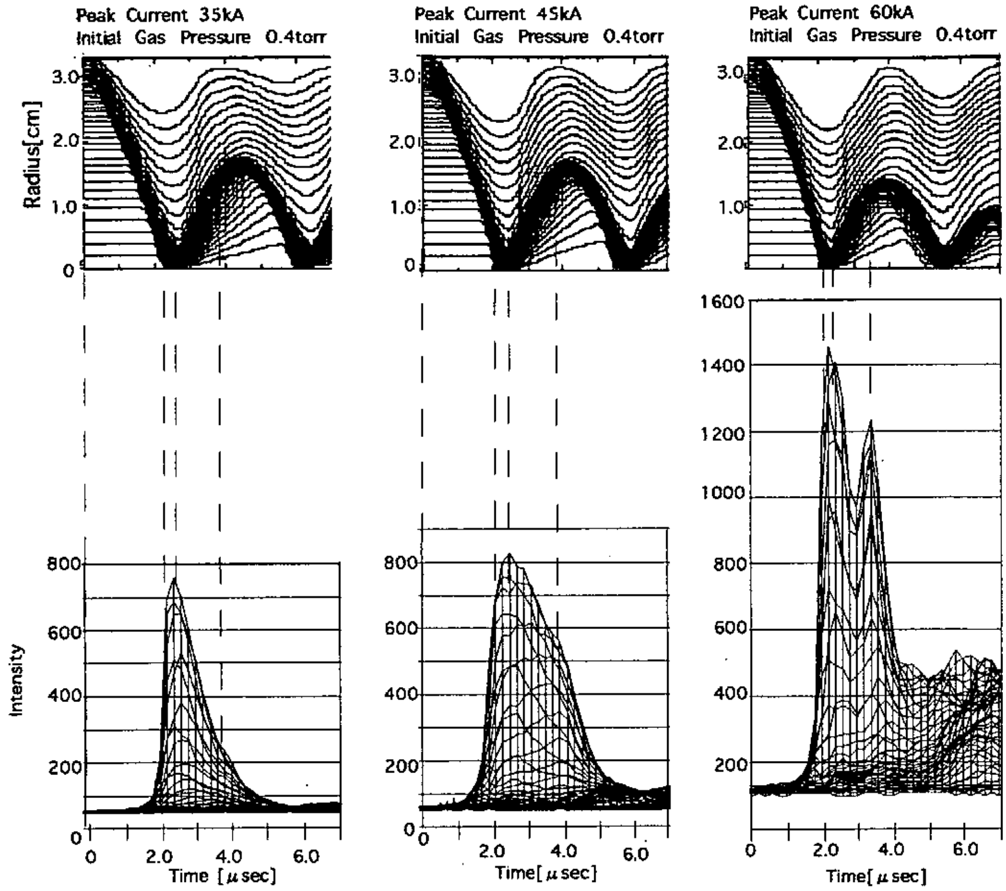

Figure 8 Comparison of X-t diagram
with observed luminous profiles on the axis.

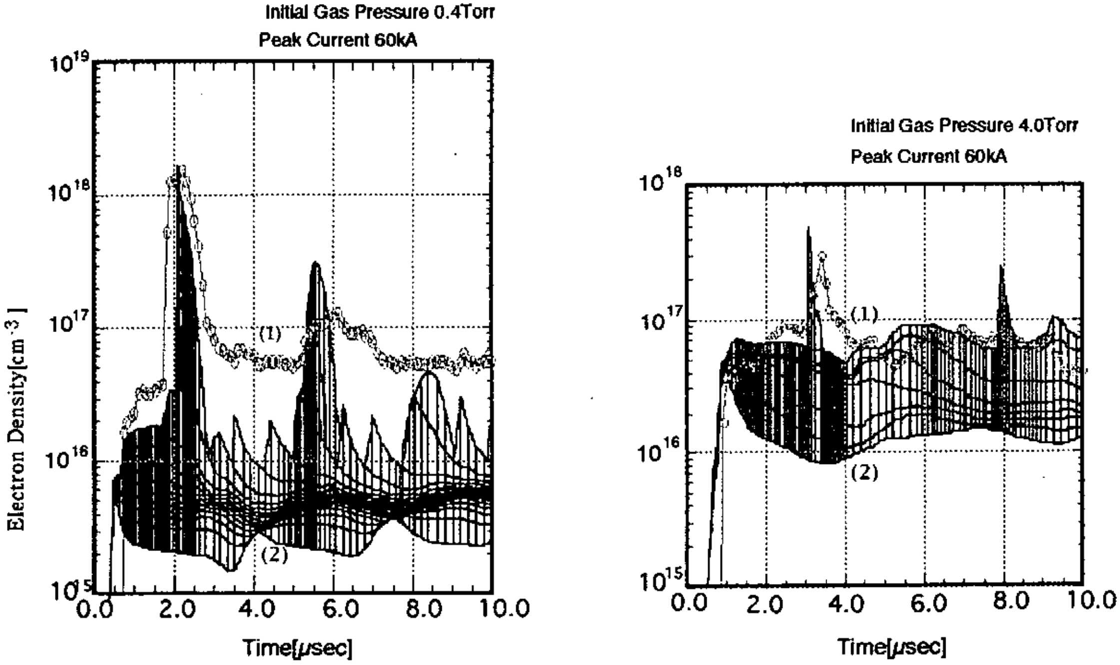

Figure 9 The evolution of electron density at Z-axis.
(1) show the observed electron density
(2) Cross section of spatial-time distribution (by MHD Simulation)

Evaluation of the Mechanism Ion Source Production in LIB Diode

Etsuji Chishiro, Katsumi Masugata and Kiyoshi Yatsui

Nagaoka University of Technology,
Nagaoka, Niigata 940-21

abstract

The characteristic of a magnetically insulated diode in a multi-shot operation is investigated. An ion current density (J_i) decrease with increasing number of shot both in high current mode (short gap) and low current mode (long gap) operation. The value of J_i in the first shot is space charge limited with an enhancement factor against space charge limiting current of 1.6. It becomes lower than 1 after several shot of operation. To evaluate the effect of the sorption of gas in the anode surface, desorption characteristics of insulator is evaluated. The outgased sample is found to have a higher surface breakdown voltage and rare desorption. From the experiment, we see that the sorbed gas in the flashbord strongly affect the production of LIB.

1. Introduction

An intense, pulsed, light-ion beam (LIB) is considered as a hopeful candidate for an energy driver of inertial-confinement fusion. Furthe-rmore, it has been successfully demonstrated to be applied for materials science.

A magnetically insulated diode (MID) has mainly been used to generate LIB. In the MID, a magnetic field is applied parallel to the surface of electrodes to inhibit electron flow to the anode. Thereby anode has rare damage in MID, which enable the multi-shot operate without replacing anode. However, when the MID is successively operated without braking the vacuum, J_i decrease with increasing number of shot.

In the diode, ions are considered to be extracted from an anode plasma produced by a surface-flashover. The surface flashover in vacuum is considered to be occur in the expanding cloud of gas described from insulator1). The main source of desorbed gas prior to the flashover is considered to be the molecules adsorbed on the insulator2). Consequently, the molecules adsorbed on the anode has a important role on the production of LIB.

There is two types of absorption, sorption or dissolution of gas in the solid, and adsorption on the surface. The absorption is a short range phenomena, for example, for a vacuum of 10^{-3} Pa, the adsorbed molecules produces 3-10 mono-layers in one fifth of a second.[3)] Since the partial gas pressures (H_2, N_2, H_2O etc.) of residual gas have no remarkable dependence on the number of shot, and that the interval of the shot of MID is in the order of 10^3 sec, quantity of the adsorbed molecules just before the shot is considered to be saturated, and independent on the shot number.

On the other hand, sorption is a long range phenomena in the order of days. When the insulator is exposed to the atmosphere, a certain amount of molecules permeate into the insulator. The quantity of sorbed gas can be controlled by heating the insulator after the evacuation, or change the environment where the insulator is exposed. The continuous shot without breaking vacuum will reduce the quantity of sorbed gas.

In the paper we concentrates to investigate the effect of sorption on the production of LIB. At first, the investigation is described of the dependence of ion current density (J_i) on the number of shot. Secondly, the desorption characteristics is investigated when the surface flashover is produced. Finally we discusses the effect of sorbed gas on the production of LIB

2. Successive operations of MID

The characteristics of MID in the multi-shot operation has been measured to investigate the effect of sorbed molecules on the anode surface. To evaluate the effect of sorbed gas on the production of LIB, anode is baked to reduce the sorbed gas. Since the condition of absorbed is not affected by a low temperature baking of 85 °C. Furthermore, the absorption is a shorter time range phenomena, condition of absorption is not expected to be affected by a multi-shot operation.

2.1 Apparatus and methods

Fig. 1 shows the schematic of the experimental set-up. In the MID, an insulating magnetic field (B) is produced by an external current through a one-turn coil, which also acts as a cathode. Inside the cathode, aluminum anode is placed, which is connected to the output of pulse-power system. The anode have thirteen of polyethylene-filled, 70-mm-long groves on the surface. The grooves has a width and pitch of 3 and 6 mm, respectively, and they are oriented parallel to the magnetic field. In the experiment, low-density polyethylene (LDPE) is used, the density of which is 0.92 g/cm^3.

In the extraction side of the MID, a brass vanes are installed on the cathode to extract LIB. Inside the anode a heater of resistive metallic wire is equipped to bake the anode. The baking temperature in the experiment is controlled to ~ 85 °C. It is lower than softening temperature of LDPE[4] (~ 90 °C) and higher than the boiling temperature of vacuum oil (~ 75 °C) at 10^{-2} Pa.

Diode current (I_d) and inductively corrected diode voltage (V_d) are monitored by a magnetic prove and capacitive divider, respectively. Ion current density (J_i) is monitored by a array of biased ion collectors (BIC's). The BIC's are biased at a voltage of -1.0 kV to remove accompanying electrons. The array is located at 34-37 mm downstream from the anode surface. The measured points of BIC's are described in Fig. 1. The signals of BIC's are averaged to obtain J_i.

Table I lists the experimental condition. In each gap length, ratio of applied B-field to critical insulated field (B_c)[7] is larger than 1. Operating process is as follows; First shot is operated at 90 minutes after the started of evacuation. After the 1st shot, 6 shot of successive shots are done with a interval of 15 minutes. After the shots, vacuum was broken to replace the anode.

The pressure in the experiment is in the range of $1\text{-}2\times10^{-2}$ Pa. Four set of experiments are done for each conditions and the results are averaged.

Table I Operating condition.

Gap length (mm)	Peak Volt. (MV)	B-field (T)	B/B_c
9.5	1.1-1.3	0.71	1.2-1.3
6.5	1.1-1.3	0.94	1.1-1.2

2.2 Experimental results

Typical wave forms of V_d, I_d and J_i are shown in Fig. 2. As seen in the figure, V_d has a pre-pulse of 150 kV, with duration of 150 ns. I_d and J_i rises at about 30 ns after the main voltage pulse. All through the experiments, the delay time ranges from 20 to 50 ns and it is independent on the baking condition or shot number. Considering the time-of-flight from anode to BIC's (~ 8 ns for proton of 150 keV), turn-on delay time is estimated to be 10-40 ns.

Fig. 3 shows the variation of J_i on the number of shot. For each conditions, J_i decrease with increasing the number of shot. In case of shorter gap, strong reduction of J_i is observed. In all conditions, the value of J_i seems to approach to the value of 100-150 A/cm^2. On the other hand, in case of $d = 6.5$ mm, the baking caused a slight decrease of J_i, whereas no difference is observed in case of $d = 9.5$ mm.

Fig. 4 (a) shows the charge density of ion beam (Q_i) extracted from MID as a function of the number of shot. Here Q_i is given by integrating J_i. As seen in the figure, Q_i has a similar behavior as J_i.

Enhancement factor of Q_i over the space charge limiting value (Q_{CL}) for proton is calculated to evaluate the limiting mechanism of ion current. In the evaluation, following equation is used to evaluate Q_{CL}.

$$Q_{CL} = \frac{4\varepsilon_0}{9d^2}\sqrt{\frac{2e}{m_p}}\int V_d^{\,1.5}dt, \qquad (1)$$

Here, d is the gap length of each operating condition. Fig. 4 (b) shows the result. As seen in the figure, for the 1st shot, enhancement factor of ~ 1.6 is observed for 3 conditions, whereas ~ 1.2 for the case of d = 6.5 mm with baking. Those values suggest that for the 3 conditions, Q_i is limited by a space charge effect, whereas in case of d = 6.5 mm and with baking, the Q_i is source limited.

The enhancement decreases for all conditions, however, after several shots, the values become less than 1 when anode is baked.

3. Desorption of sorbed molecules by a surface flashover

To evaluate the effect of sorbed gas on the process of the production of ion source, desorption characteristics of LDPE is investigated. The effect of sorbed molecules on the process of flashover, relation of a concentration of sorbed molecules in the LDPE and a quantity of desorbed molecules by flashover.

3.1 Apparatus and methods

Fig. 5 shows the experimental apparatus. It consist of a vacuum chamber and a pressure measurement system which is connected the chamber by a connecting tube of lower conductance. A sample material of LDPE sheet is placed inside the chamber. On the sample, pair of pin electrodes (gap length = 5 mm) are equipped to make a surface flashover. Four types of differently pre-treated samples are prepared, the treatments of which are listed as follows;

(a) no pre-treatment (allowed in the 1 atm of air)
(b) outgased in the vacuum of 10^{-5} Pa for 7 days,
(c) treated in a pressurized air (7 atm) for 10 days to absorb it,
(d) treated as (c) and allowed in the vacuum of 10^{-5} Pa for 20 hours.

Pre-treated samples are installed in the chamber and make a following process:

1. Install the sample in the chamber.

2. Keep the pressure of the chamber at 10^{-4}- 10^{-5} Pa for 90 minutes.
3. Close the gate valve (V_1) and wait until the pressure rises up to 10^{-3} Pa.
4. To make a surface flashover, shots a sires of 5-pulses (34 kV, 1 Hz)
5. Measure the pressure at P_2 and evaluate the quantity of desorbed gas.
6. With a interval of 1 minute next sires of pulse is applied to the electrodes.

Figure 6 shows the pressure at P_2. Since V_1 is closed, the vacuum chamber is evacuated by a pump 2 through the connecting tube, pressure at P_1 is larger than P_2. As seen in the figure, pressure at P_1 and P_2 increases by making a surface flashoever.

Since the conductance of the tube is known, the flux of gas through the tube can be evaluated from the of pressure at P_1 and P_2 and hence we can evaluate the quantity of desorbed gas (Q) by using the equation,

$$Q = \frac{N_A}{RT} C \int \left\{ P_{1(t)} - P_{1i} \right\} - \left\{ P_{2(t)} - P_{2i} \right\} dt, \qquad (2)$$

where N_A, R, T, and C are the Avogadro's constant, gas constant, the temperature of chamber wall (T=295 K), and the conductance of the connecting tube (8 ℓ/s), respectively.

3.2 Experimental results

Fig. 7 shows a quantity of desorbed gas as a function of the number of shots. As seen in the figure, for sample (a), desorbed gas is 8×10^{16} molecules at the 1st shot and it gradually decreased with increasing the number of shots. After 10th shot, it became a constant value of about $\approx 5\times10^{16}$ molecules.

On the other hand, for sample (b) we obtain almost no flashover until 25th shot due to the increase of breakdown voltage by the treatment, and Q is very low in the beginning. After 25th shot, stable flash-over is obtained and the outgas level increases up to 5×10^{16} molecules/shot. For sample (c), high vale of $Q = 1.5\times10^{17}$ molecules/shot is observed. The value of Q is stable and not decrease for 70 shot. For sample (d), a quantity of desorbed gas keeps a high level in the beginning, however, it decreases to the low level of $\approx 1\times10^{17}$ in 10 shot.

From the experiment we see that the pre-treatment of sample strongly affect the desorption characteristics and flashover voltage.

4. Discussion

As shown in §2, J_i has a strong dependence on the shot number. Here, we consider the cause of the dependence. From the absorption isotherm calculated by B.E.T., we see that absorbed molecules make a 4 or 5 layers on the insulator, which is almost independent on the temperature when it is in the range of -40–80 °C.

Which means that the quantity of absorbed gas is independent on the shot number. On the other hand, as shown in §3, the quantity of desorbed gas has a strong dependence on pre-treatment and/or the shot number. Those facts surest that J_i is affected by the sorption of gas in the flashbord.

The process of the production of surface flashover is basically considered to be as follow[1), 2)].

(i) high potential applied across insulator,

(ii) surface leakage current flows through insulator (be called *pre-flashover*)

(iii) causing the desorption of gas from insulator surface (due to the ohmic heating),

(iv) electron emission from electrodes causing ionization in gas leading to Townsend avalanche,

(v) further desorption due to stimulated electron bombardment of insulator surface,

(vi) thermal and ionic bombardment of insulator surface leading to additional desorption and vaporization of insulator molecules, adding to neutral number density in the flashover region.

(vii) further ionization in gas phase leading to fully developed flashover discharge.

In the process, absorbed and desorbed gas seems to play an important role and affect the characteristics of surface flashover. Furthermore, from the fact that the breakdown voltage is high in a outgased sample, desorption of sorbed gas by *pre-flashover* promote the Townsend avalanche.

Since the sorption is the long term phenomena and decreases in the successive shots, the decrease of J_i seems to be due to the decrease of sorbed gas and/or the difficulty of surface flashorver due to the decrease of sorbed gas.

REFERENCES

1) A. Watson: J. Appl. Phys. **38** (1967) 2019.
2) Y. Ohki and K. Yahagi: J. Appl. Phys. **46** (1975) 3695.
3) E. W. Gray: J. Appl. Phys. **58** (1985) 132.
4) Y. Ito: Kobunshi-Kagaku **63** (1960) 2016 [in Japanese].
5) R. N. Sudan and R. U. Lovelance: Phys. Rev. Lett. **31** (1973) 1174.

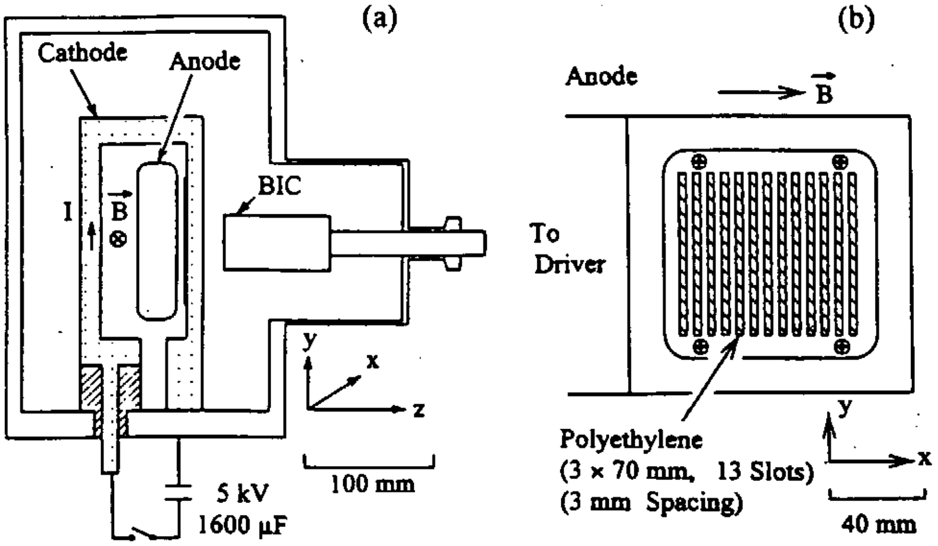

Fig. 1 Schematic of experimental set-up. (a) cross-sectional view of the MID. (b) side view of the anode.

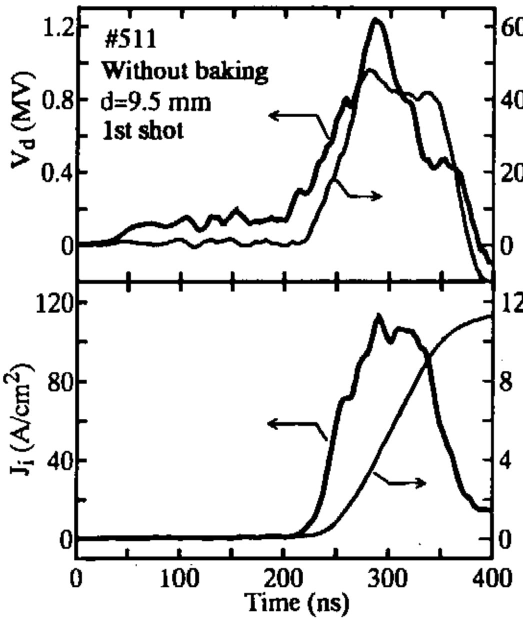

Fig. 2 Typical wave forms of the MID.

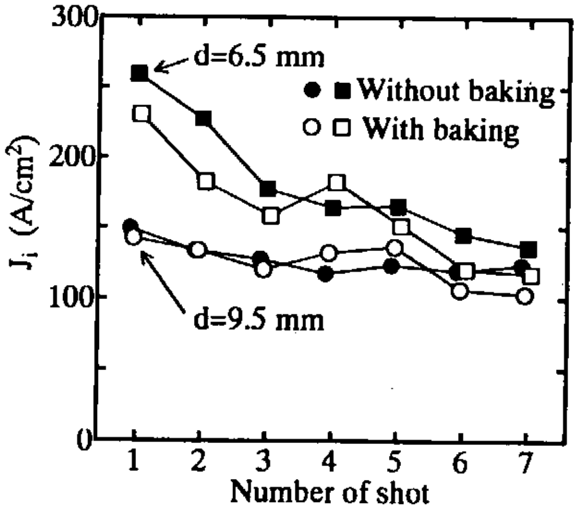

Fig. 3 J_i as a function of number of shot.

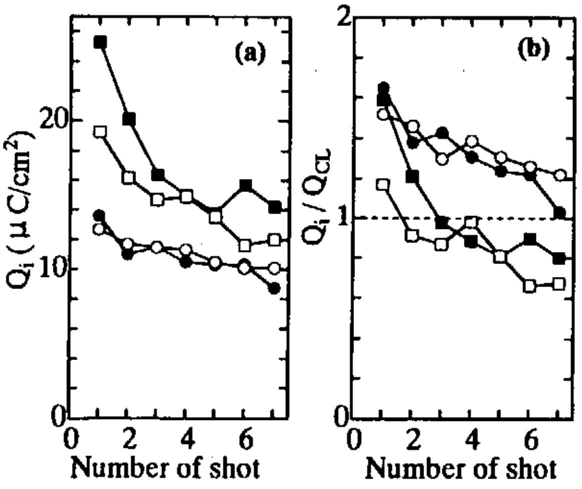

Fig. 4 (a) Q_i, (b) Q_i/Q_{CL} as a function of number of shot.

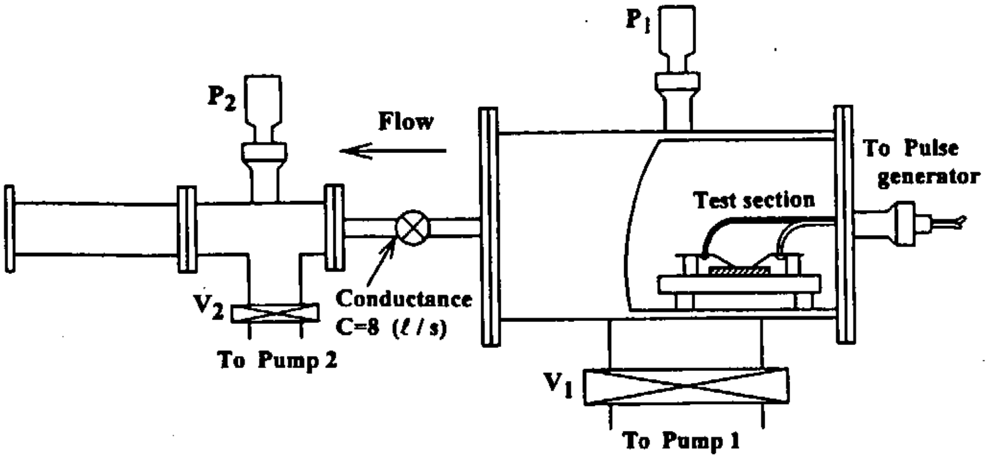

Fig. 5 Schematic of experimental apparatus to measure the desorbed gas.

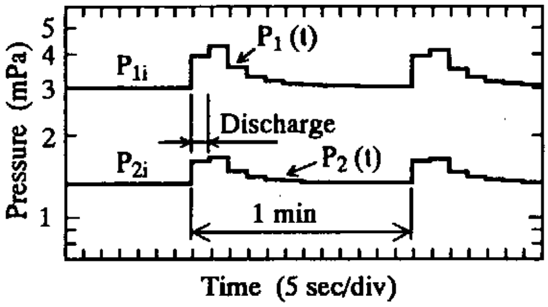

Fig. 6 Typical wave forms of both pressure.

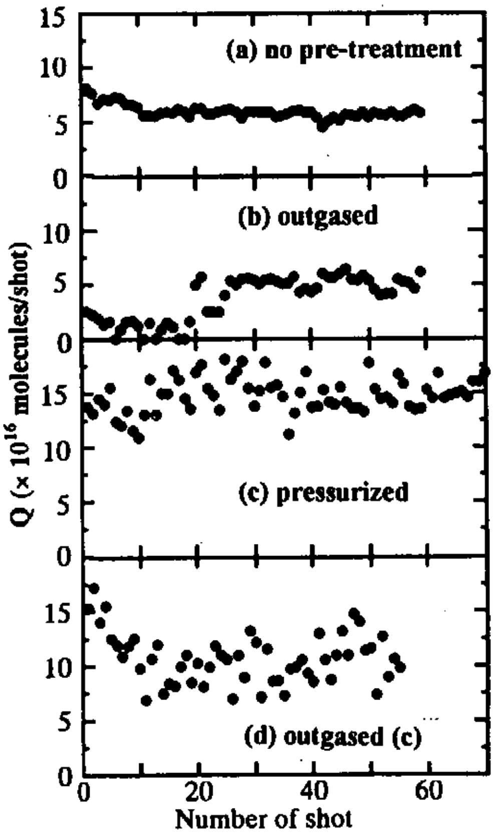

Fig. 7 A quantity of desorbed gas as a function of number of shot.

Space Charge Effects on the Characteristics of Grid-Controlled Vacuum Arc Ion Sources

Jun HASEGAWA, Mitsuo NAKAJIMA and Kazuhiko HORIOKA

Department of Energy Sciences, Tokyo Institute of Technology,
Nagatsuta 4259, Midori-ku, Yokohama 226, Japan

Abstract

We have developed a vacuum arc ion source with a new extractor structure, to investigate the space-charge effects on the dynamics of extraction gap. The fundamental concept of this ion source is based on conventional grid-controlled vacuum arc ion sources. As the first step, we operated it with single gap configuration for basic characterization of the grid-controlled extractor. We found that the ion beam gradually became unstable with increasing the shot number. This unstable behavior could be attributed to the increase of either high energy component of the electrons or lighter impurities in the arc discharge plasma.

1. Introduction

Since vacuum arc discharges can produce almost all kind of metallic ions with high flux, they have been applied to high current ion sources. However, because of intrinsic fluctuations of them, it is difficult to extract stable ion beams with conventional extractors.

In order to suppress the temporal variations of the source plasma flux, a grid-controlled extractor was proposed by S. Humphries et.al.[1]. In this extractor, an electrostatically biased anode is used to confine electrons of the source plasma. Separated ions form a potential hump in an extraction gap due to their space charge. The potential hump, which is called virtual anode, dams up the plasma ion flow, and part of the ions are extracted as an ion beam. The beam current is controlled by space-charge effects in the gap. Hence, the extracted ion beams are independent of the fluctuations of plasma sources. However, since the virtual anode defines an emission surface of ion beams, its temporal and spatial variations, i.e., virtual anode oscillation, may have deleterious effects on the beam stability and emittance.

To investigate such effects and to improve the beam quality, we proposed a new grid-controlled extractor with double acceleration gaps[2]. The first gap of this extractor is the same as a normal grid-controlled extractor. Because a well controlled ion beam from the first gap creates the virtual anode in the second gap, effects of the virtual anode on the ion beams can be systematically investigated with well defined condition.

As the first step, we operated the vacuum arc ion source in single gap mode to make the basic characterization. In this paper, we will mainly mention the results of the basic experiments on the normal grid-controlled vacuum arc ion source.

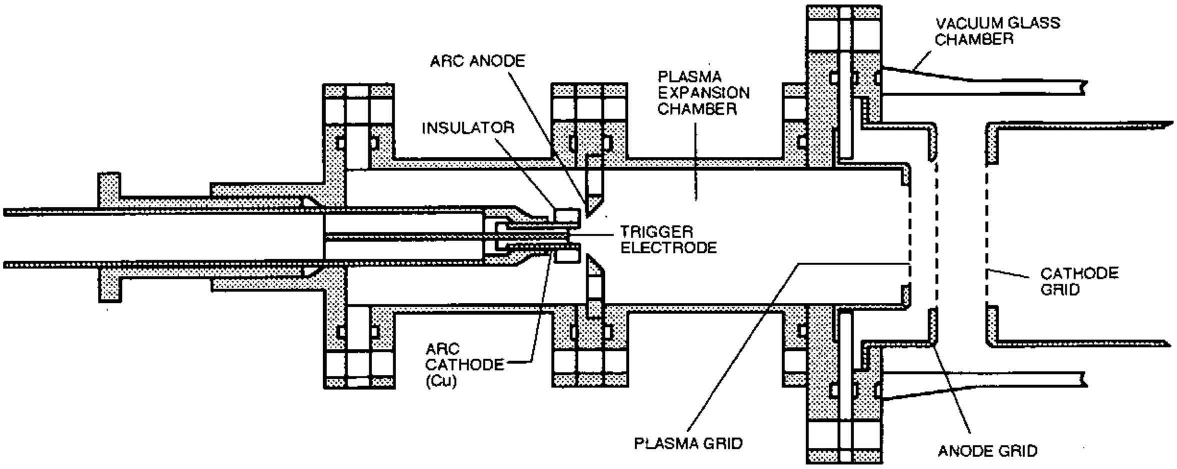

Fig. 1. Schematic diagram of vacuum arc ion source.

2. Experimental Setup and Procedures

A schematic drawing of the vacuum arc ion source is shown in Fig.1. Base pressure of the vacuum chamber is maintained at about 5×10^{-6}Torr by a turbo molecular pump. The arc discharge is initiated by a surface flashover discharge between the trigger electrode and the cathode. This flashover discharge is driven by a Krytron pulse generator through a pulse transformer. The arc discharge is driven by a LC pulse forming network (PFN) which has an impedance of 5Ω and a pulselength of 100μs. For impedance matching, a 5Ω series resister is inserted between the network and the arc discharge. The arc current is 50A to 400A, which is determined by the charging voltage of the PFN. Typically, the arc current is set to 200A in our experiments. The ion species of vacuum arc discharge plasma is determined by the cathode material. We use a ϕ10 copper pipe as the arc cathode and the plasma source of copper ions.

The produced plasma drifts into the expansion chamber of 11cm long. The chamber is electrically connected to the arc anode. The grid-controlled extractor is composed of three metallic grids. The plasma grid, connected to the plasma expansion chamber, is 100x100 tungsten mesh with 0.025mm wire. The anode grid is 100x100 tungsten mesh with 0.030mm wire. It is maintained at negative potential with respect to the plasma grid by an external bias circuit. The potential difference is high compared to the kinetic energy of most of the plasma electrons. Since the potential of the anode grid prevents plasma electrons from reaching the anode grid, a thin ion sheath is formed around the grid wire. Ions separated from the electrons in the sheath are collected by the anode grid or enter the extraction gap. When an extraction voltage is not applied, the space charge of the ions forms a virtual anode in the gap near the anode grid. Most of the ions entering the gap are reflected by the potential, collected by the anode grid, or reentering the plasma expansion chamber. Because almost all of the source plasma is confined by both the anode grid and the virtual anode, plasma prefill of the extraction gap is suppressed. When an extraction voltage is applied, the virtual anode potential is lowered and part of ions are extracted as an ion beam. The ion beam current density is

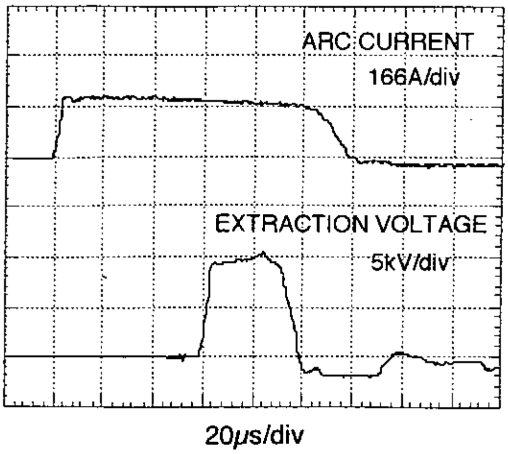

Fig. 2 Typical waveforms of arc discharge current and extraction voltage. Top: arc discharge current, 166A/div. Bottom: extraction voltage, 5kV/div, 20μs/div.

determined by the space-charge limit corrected for the initial directed ion energy.

In our experiments, the extraction gap width is typically set to 2cm. An extraction voltage is powered by a Blumlein type PFN, which has an impedance of 12Ω and a pulselength of 30μs. A 12Ω matching resister is connected to the PFN in parallel to the gap. The extraction voltage is 1-10kV, which is equal to the charging voltage of the PFN.

Typical waveforms of the arc current and the extraction voltage are shown in Fig.2. Here the arc current is about 200A, and the nominal extraction voltage is 10kV. We can arbitrarily delay the timing of the application of the voltage. In Fig.2, the delayed time from the initiation of arc discharge is set to 50μs.

3. Results and Discussions

3.1 Arc Plasma Measurements

The plasma ion flux was monitored by the anode grid in the extractor. Because most of the supplied plasma ions are collected by the anode grid after several reflective motions, signals from the anode grid approximately represents the available plasma ion flux at the extractor. Strictly speaking, the current density measured by the anode grid, which is used as an ion collector, is not equal to the available plasma flux because there is a leak flux and the effective area of the anode grid cannot be defined precisely. However, since we paid attention to fluctuations of the source plasma flux, we neglected this small inaccuracy. The merit of this measurement scheme is that we can monitor both the supplied plasma flux and the extracted ion beam simultaneously.

Typical waveforms of arc plasma ion flux at the grid position (13cm downstream from the arc anode) are shown in Fig.3. A sudden decrease in ion flux was found to happen at 30μs after the ignition of the discharge (upper waveforms). The movement of cathode spots to the outside portion of the cathode cylinder may cause this reduction. In order to prevent the movement of them, we used an insulator surrounding the metallic cathode. As a result, almost constant plasma supply was achieved over 100μs (lower waveforms). However, the supplied flux of arc plasma still fluctuates in short time scale (μs), provably because of intrinsic time-varying properties of the vacuum

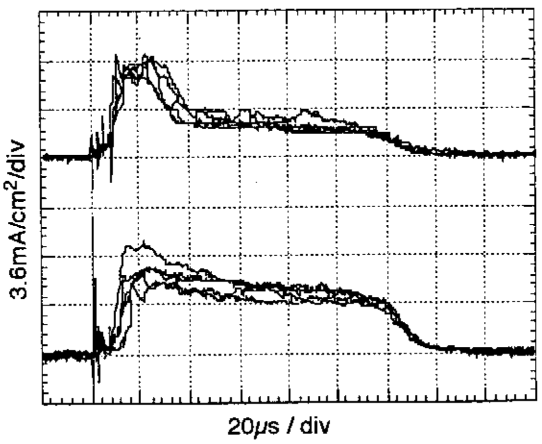

Fig. 3 Typical waveforms of arc discharge plasma ion flux. (5shots overlay) Top: without an insulator. Bottom: with an insulator.

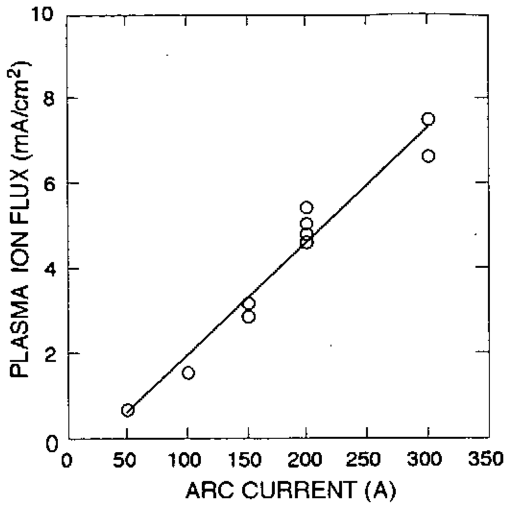

Fig. 4 Plasma ion flux at 13cm downstream from arc anode as a function of arc discharge current.

arc discharge.

Figure 4 shows available plasma ion flux as a function of the arc discharge current. The graph shows that the ion flux increases in proportion to the increase of the arc current. Higher current supply will be achieved by shortening the plasma expansion chamber or increasing the arc discharge current.

3.2 Grid-Controlled Extraction

Before extraction experiments, we measured a leak plasma ion flux to estimate a bias voltage required for the confinement of the source plasma. The arc discharge current was fixed to 200A. To measure the leak ion flux, we used a biased collector at 2cm downstream from the anode grid. The cup has an entrance aperture of $\phi 6$ and a collector cup biased to -90V. Secondary electrons from the collector is magnetically suppressed by a pair of permanent magnets.

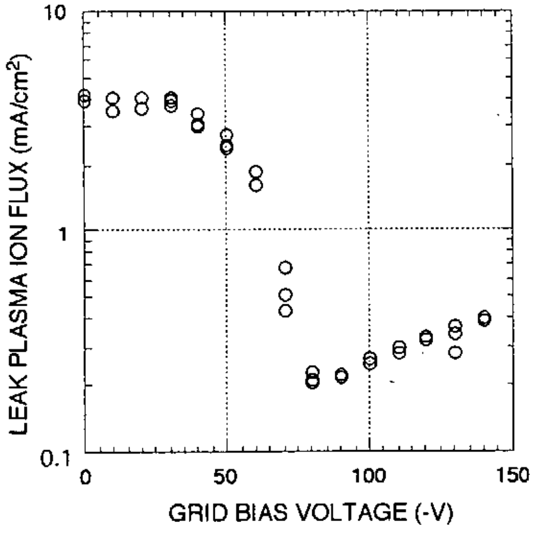

Fig. 5 Plasma ion flux downstream from anode grid as a function of bias voltage.

Figure 5 shows a plot of the measured leak ion flux as a function of the bias voltage of the anode grid. When the bias voltage is not applied (Vg=0V), the bulk of source plasma expands into the extraction gap. For the 0-bias condition, the measured ion flux was 4mA/cm^2 . The leak ion flux decreases with increasing bias voltage from -40V to -80V. At a bias voltage of -80V, the flux is reduced to about 0.2mA/cm^2 . From these results, we confirmed that the source plasma confinement is sufficiently achieved at a bias of -100V.

When the voltage exceeds -100V, the leak

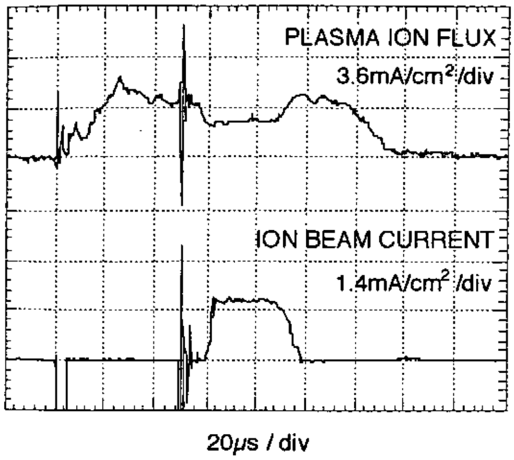

Fig. 6 Typical waveforms of plasma ion flux and extracted ion beam. Extraction voltage: 10kV. Delay: 50μs.

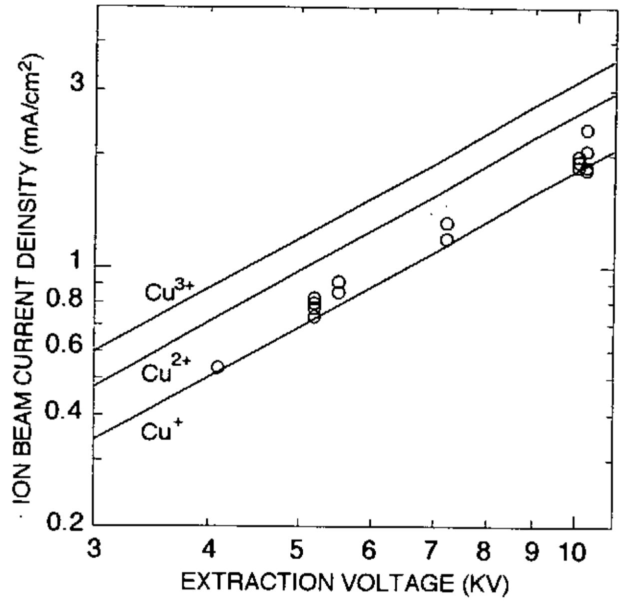

Fig. 7 Log-log plot of ion beam current density vs. extraction voltage. Gap width: 2cm.

flux begins to increase. We have not yet understood why this increase arises.

We used a Faraday cup of 9cm length to measure the ion beam downstream from the cathode grid. It has a cylindrical electron suppressor of 4cm length and a 4cm long collector cup. The suppressor was biased to -180V. The entrance aperture is 6mm in diameter.

Figure 6 shows typical waveforms of the source plasma ion flux measured by the anode grid (upper trace) and the extracted ion beam current measured by the cup (lower trace). In this case, an extraction voltage is applied at 50μs after ignition of the arc discharge, and the grid potential is -100V. The beam current is almost constant and not influenced by the fluctuations of the source plasma. As shown in Fig.6, while the extraction voltage is applied, the source plasma ion flux is reduced. This reduction implies the virtual anode formation i.e., part of source plasma ions entering the gap are extracted and the residual ions are reflected.

Figure 7 shows comparison between the available ion beam current density and the Child-Langmuir(CL) current density corrected for the initial directed ion energy. Three solid lines represent the corrected CL current density for Cu^+ , Cu^{2+}, and Cu^{3+} ions as a function of the extraction voltage. Generally, the vacuum arc discharge produces a high fraction of multiply stripped ions. It is known that copper beams from vacuum arc plasmas are typically composed of species with charge states Q=1, 2, and 3[3]. The measured ion beam current density corresponds to the CL value for Cu^+. This implies that the ion beam is extracted under the space-charge limit mode, and that Cu^+ ions are dominant in the extracted beams.

To investigate the influence of the grid bias voltage on behavior of the extraction gap, we measured the ion beam current at several different bias conditions. Figure 8 shows the waveforms of the ion beam current measured at four different bias voltages.

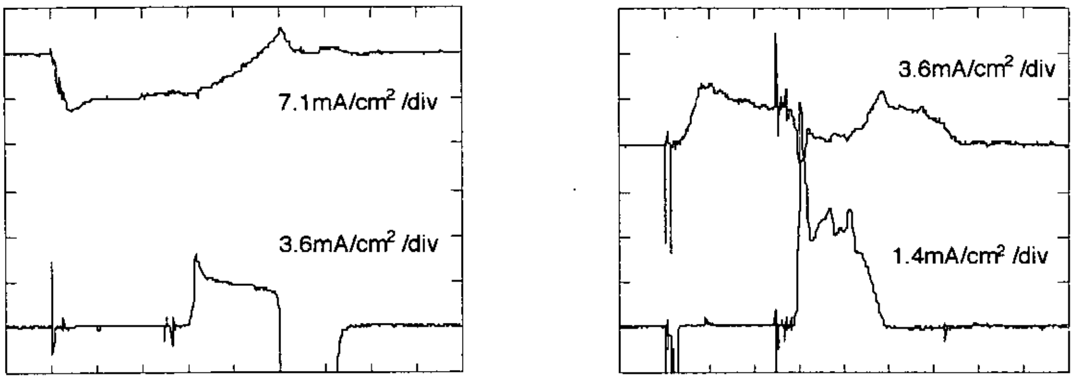

(a) Vg = 0V

(b) Vg = -60V

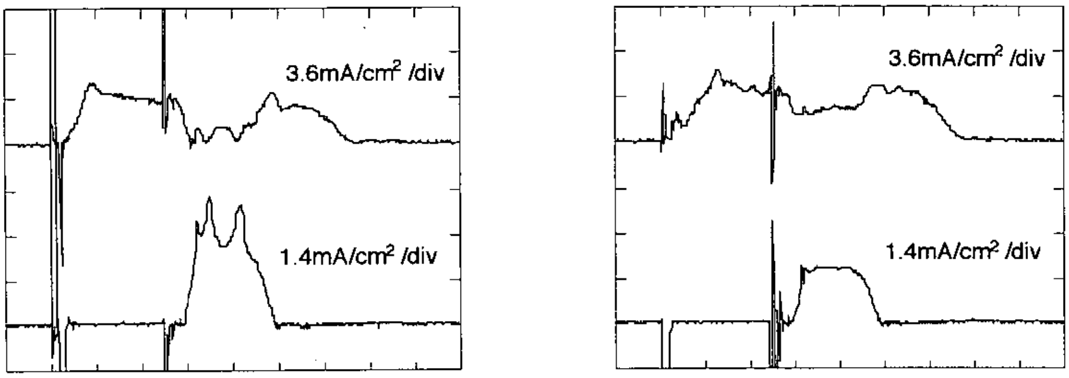

(c) Vg = -80V

(d) Vg = -100V

Fig. 8 Effects of grid bias voltage on extracted ion beams

When the grid voltage is 0V, the waveform of the ion beam has an initial peak due to plasma prefill of the gap, and the current density level is much larger than the geometrically predicted CL value. Although the initial peak becomes smaller with increasing the bias voltage, the waveforms are still unstable and have several sharp peaks at -60V and -80V. This is because the confinement of the source plasma is not perfect. When the bias voltage is -100V, the plasma confinement is enough for the grid-controlled extraction. Consequently, the waveform of ion beams becomes very stable and the current density almost corresponds to the CL value. From these measurements, we confirmed that even if the source plasma is unstable, the grid-controlled extraction has a capability of the stabilization.

3.3 Discussions

We found that the ion beam current was modulated with the successive operation of the vacuum discharge after the arc cathode was exchanged for a new one. When the number of shots exceeds about fifty, the waveforms of ion beams become very spiky and unstable (Fig.9). Furthermore, the level of current density gradually increases with

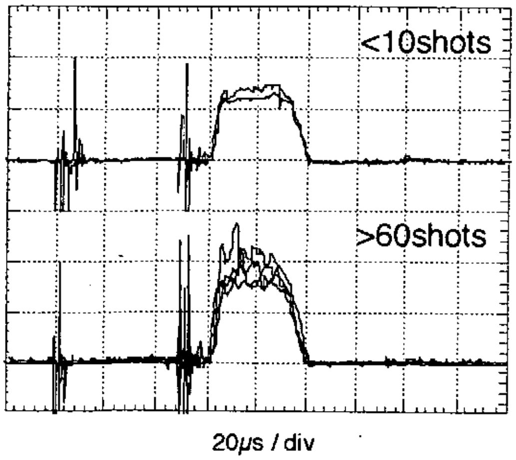

Fig. 9 Typical waveforms of stable and unstable ion beams. Top: waveforms under 10 shots. (2 shots overlay) Bottom: waveforms over 60 shots. (4 shots overlay)

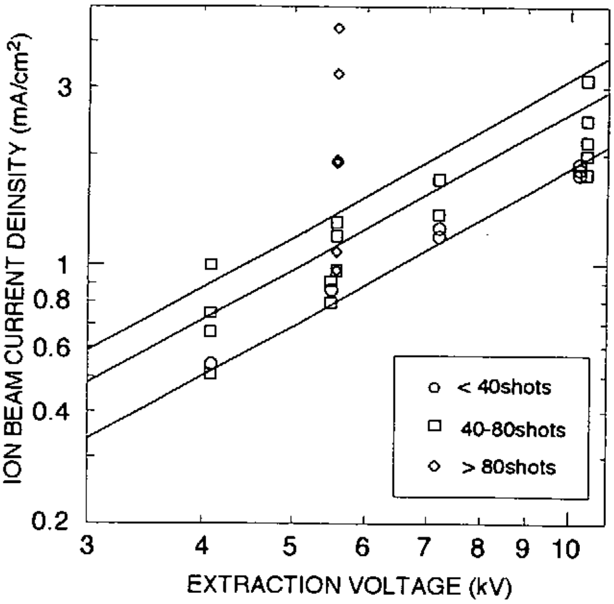

Fig. 10 Log-log plot of ion beam current density vs. extraction voltage. Beam current increases with increasing shot number of ion source.

the number of shots (Fig.10). Although we have not fully understood the mechanism of this phenomenon, there is no doubt that the change of the source plasma properties leads to this instability of the ion beams.

In order to explain the unstable behavior of the extraction gap, we have to take account of two possible factors. First one is the increase of the leak flux. As shown in Fig.11, the leak of plasma flux gradually increased with increasing the shot number. The increase of the leak plasma flux indicates that the confinement of the source plasma becomes imperfect. The insufficient confinement may lead to unstable operation of the grid controlled extractor. As a result, it is expected that the extracted ion beam becomes unstable as is shown in Fig. 8(c). There is a possibility that the increase of hot electrons in the arc plasma cause both the increase of the leak flux and the instability of the ion

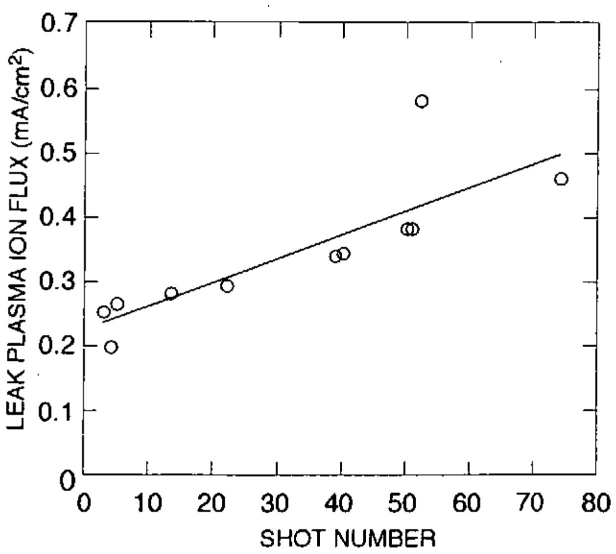

Fig. 11 Plot of leak plasma ion flux as a function of shot number of ion source.

beams. Anyway, more detailed investigation is necessary to reveal what causes the increase of the leak flux and why this increase leads to the instability of the ion beams.

Second possible factor is the increase of impurities in the arc plasma. If the impurities lighter than copper ions, e.g. proton, carbon, etc., increase with the repetitious operation of the source, the effective CL current density becomes larger than that of copper, and this causes the enhancement of the ion beam current. Furthermore, temporal variations of the flux of the impurities during an extraction pulse may lead to current peaks of the ion beam. After several tens of shots, we observed slight erosion of the insulator at the boundary between the cathode metal and the insulator. This indicates that a slight amount of impurities are created by the arc discharge. In order to confirm the impurity level of the beams, we have to perform TOF measurements.

The increase of lighter impurities cannot explain the increase of the leak flux because the lighter ions can be confined by the electrostatic grid more easily. Hence, these two factors are independent of each other.

4. Concluding Remarks

We have confirmed that the grid-controlled extraction scheme is very effective for the generation of temporally stable ion beams, as has been reported [1, 4]. The extracted ion beams were well controlled and its current density was stabilized at the Child-Langmuir limit value.

With simultaneous observation of the plasma flux to the anode grid and the extracted beam current, we confirmed virtual anode formation in the extraction gap. However, the lifetime of the stable operation was limited to about fifty shots. It is concluded that the cause of the unstable operation can be attributed to the degradation of the stable virtual anode.

High current accelerators require ion sources of good optics in the microsecond range[4]. Provably, stability of the virtual anode is one of the critical factors for the sources with good optics. Further studies including the double gap configuration will reveal more detailed information about the stable operation of grid-controlled extraction gaps.

References

[1] S. Humphries, Jr. *et al.*, "Grid-controlled extraction of pulsed ion beams," *J. Appl. Phys.*, vol. 59, no. 6, p1790, (1986)

[2] K. Horioka, J. Hasegawa and M. Nakajima, "Pulsed ion beams extracted from vacuum arc ion source with double accelerator gap," *Proc. BEAMS '94*, p447, (1993)

[3] I. G. Brown, and X. Godechot, "Vacuum arc ion charge state distributions," *IEEE trans. Plasma Sci.*, vol. 19, no. 5, p713, (1991)

[4] H. L. Rutkowski, D. W. Hewett and S. Humphries, Jr., "Development of arc ion sources for heavy ion fusion" *IEEE trans. Plasma Sci.*, vol. 19, no. 5, p782, (1991)

Numerical Simulation of Spherical Plasma Focus Diode

W. Jiang, K. Masugata, and K. Yatsui
Laboratory of Beam Technology, Nagaoka University of Technology
Nagaoka, Niigata 940-21

Abstract

A self-magnetically insulated, three-dimensionally-focused ion-beam diode, spherical plasma focus diode (SPFD), is studied by numerical simulation using a two-dimensional, electromagnetic, relativistic particle-in-cell computer code. The calculated results of the diode impedance, the ion-current efficiency, and the focusing characteristics of the ion beam are presented. These results, except the data of the ion-beam current, are in good agreement with the experimental results.

1. Introduction

An intense pulsed light-ion beam (LIB) with high power density can generate a high-temperature, high-density plasma which is interesting in researches of inertial confinement fusion (ICF) and material science. For application as an ICF driver, an ion beam with a peak power of ~ 100 TW and a pulse width of 10 ~ 15 ns will be required,[1] therefore complex ion diodes and large power supply systems are necessary. For applications in material science, on the other hand, compactness and high-efficiency of the ion-beam generator are required.

As a compact, high-efficiency ion-beam diode, we have developed a three-dimensional focusing, self-magnetically insulated diode.[2,3] Figure 1 shows the conceptual structure of this ion-beam diode, which was named as spherical plasma focus diode (SPFD). It consists of two concentric spherical electrodes. The operative principle of the SPFD is similar to that of the two-dimensional focusing, self-magnetically insulated diode we had developed before.[4-8] When a pulsed voltage is applied on the diode, electrons are emitted from the cathode and accelerated toward the anode. When the diode current increases, the azimuthal magnetic field generated by the diode current prevents most electrons from going to the anode. Meanwhile, an anode plasma is generated by electron bombardment and/or flashover on the anode surface. The ions emitted from the anode surface are accelerated in the

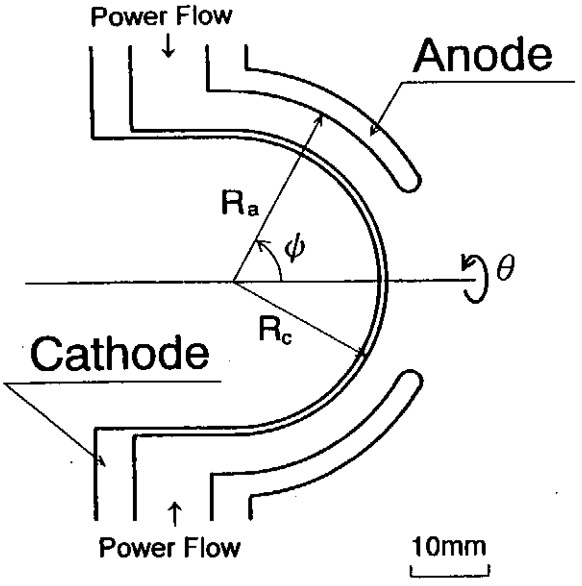

Fig. 1 Conceptual structure of SPFD.

gap and focus toward the center through the perforated cathode.

We compared the SPFD with other diodes in the following respects.

1) The SPFD is a self-magnetically-insulated type of diode. The elimination of the external magnetic field system reduces the complexity of the diode structure so that SPFD can be made very compactly.

2) The SPFD is not an extraction-type diode. The intense ion beam can only be obtained inside the cathode so that the diagnostics of the ion beam become very difficult and the application of the ion beam is relatively restricted. The advantage of this configuration is tight focusing and large irradiation angle of the ion beam. As a result, high power density can be obtained with the SPFD.

3) The SPFD has very good symmetry in the azimuthal direction. All unsymmetrical factors, including the effect of the self-magnetic field, the nonuniformity caused by the azimuthal grooves on the anode surface and the effect of the electron sheath, are in the direction perpendicular to the azimuthal direction. Therefore, the divergence angle in the azimuthal direction is very small. In the applied-B diodes, however, the applied magnetic field is usually in the direction perpendicular to that of the self-magnetic field so that no good symmetry exists in any direction.

4) Electrons do not accumulate in the gap of SPFD. In the high efficiency applied-B diodes, most electrons are prevented from reaching the anode. Since the power flow always brings electrons into the diode gap, the total electron charge in the gap increases continuously. As a result, the diode impedance drops very quickly for high-power diodes. Another problem caused by the long residence time of electrons in the gap is the development of instabilities in the electron sheath which have been found to be the major cause of ion-beam divergence in high-power applied-B diodes. On the other hand, since electrons do not accumulate in the gap of SPFD, the above problems are not serious for SPFD.

Experimentally, the radii of the cathode and the anode are 20 mm and 25 mm, respectively. In the spherical coordinate system (r, θ, ψ), the spherical diode gap covers a solid angle with $0 - 2\pi$ in the θ direction and $\pi/6 - \pi/2$ in the ψ direction.

The anode flashboard is made of azimuthal (θ) grooves (1 mm wide) filled with epoxy. The cathode is perforated with holes (with a transparency of ~ 40 %) or made by copper wire (with a transparency of > 95 %). Diagnostic results have shown that the ion beam is focused on the surface of a cylindrical volume that has a diameter of 0.5 mm in the radial direction and a length of 2.5 mm in the axial direction near the geometric center.[3] This result indicated that the ion deflection angle in the ψ direction is several times larger than that in the θ direction.

To understand the ion deflection mechanism, it is necessary to study the behavior of particles in the SPFD. However, this study can hardly be carried out in the experiments. We have performed numerical simulation to study the dynamic behaviour of the SPFD.[9)] In this paper, we present the simulation model and the initial results. From the simulation results, we give the distributions of the particles and the fields in the diode gap and the characteristics of ion beam focusing. The intent of this work is to optimize the ion-current efficiency and ion focusibility of the SPFD.

2. Simulation Model

The simulation is carried out using a two-dimensional (r, z) particle-in-cell code, which contains dynamic solutions to Maxwell's equations and relativistic particle kinematics.

Figure 2 shows the volume of simulation.

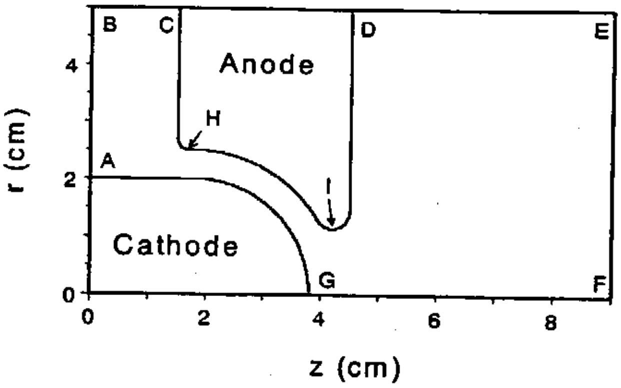

Fig. 2 Simulation area and boundaries.

Both the anode and the cathode are assumed to be perfect conductors and the space outside the electrodes is assumed to be perfect vacuum. The boundary AB is conductive which is connected with the cathode. The boundaries DE and EF are also conductive and are connected with the anode. The boundary FG is on the symmetric axis. A voltage on the boundary BC is specified to introduce electromagnetic energy into the volume of simulation. Throughout the simulation, the whole cathode surface is space-charge limited electron emitter. For the anode, however, only the surface from H to I is proton emitter and the emission is also space-charge limited. All particles arriving at any electrode or boundary are removed from the simulation, except at the boundary FG which is reflective to the particles.

To solve Maxwell's equations, the vacuum area is divided into uniform square cells with 0.2 mm in width. The radial and axial electric fields and the azimuthal magnetic field are associated with each cell. Simulation particles, each representing

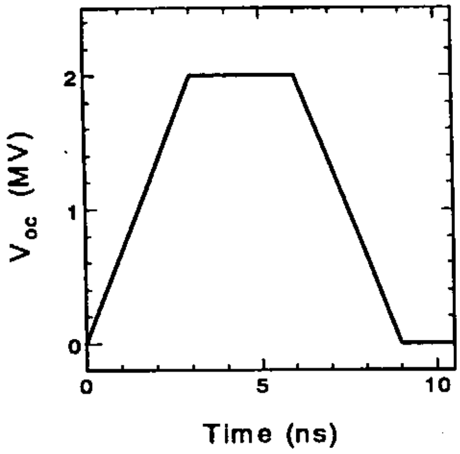

Fig. 3 Waveform of open-circuit source voltage used in simulation.

about 4.8×10^9 electrons or protons, are used to simulate the electron and ion flows and provide self-consistent sources for the field equations. The radial and axial velocities of each particle are obtained by solving the relativistic (for electrons) and nonrelativistic (for ions) equations of motion. Since there is no force on the azimuthal direction, the azimuthal velocity of each particle is not considered. The fields and the particle velocities are calculated once for each time step of 0.3 ps.

The voltage on the boundary BC is determined by applying an open-circuit voltage (V_{oc}) on the SPFD and a 6.5 Ω resistor in series. The resistor represents the characteristic impedance of the pulse-forming line of the pulsed power generator, "ETIGO-II", that was used to drive the SPFD in the experiments. Figure 3 shows the time history of V_{oc} for the simulation. In Fig. 3, the peak value is typical in the experiments but the time scale is several times reduced for saving the computer time.

3. Simulation Results

Figure 4 shows the simulation results of (a) the diode voltage (V_d) and the diode current (I_d), and (b) the total electron current (I_e) and the total ion current (I_i). Here, the diode current is obtained from the average magnetic field on the boundary BC. The diode voltage, calculated by using equation $V_{oc} = V_d + 6.5I_d$, is used to give the axial electric field on boundary BC. The total electron current is obtained by counting the number of electrons that arrive at the anode surface and the boundaries DE and EF. The

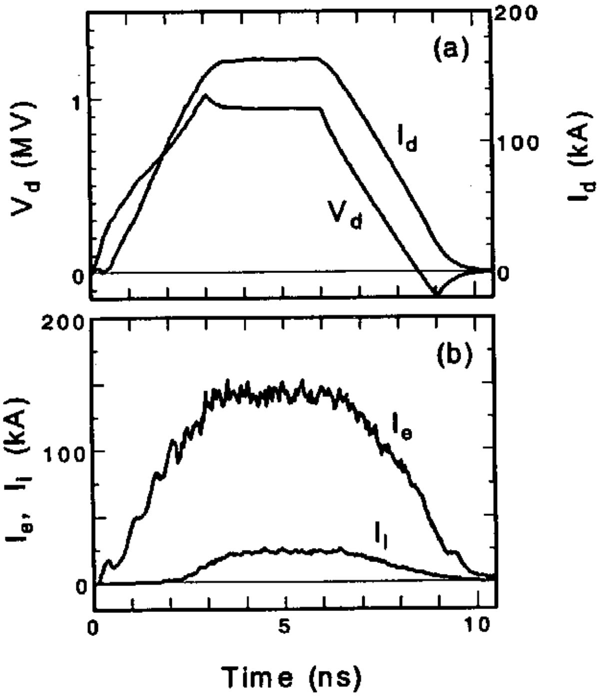

Fig. 4 Simulation results of (a) diode voltage (V_d) and diode current (I_d), and (b) total electron current (I_e) and total ion current (I_i).

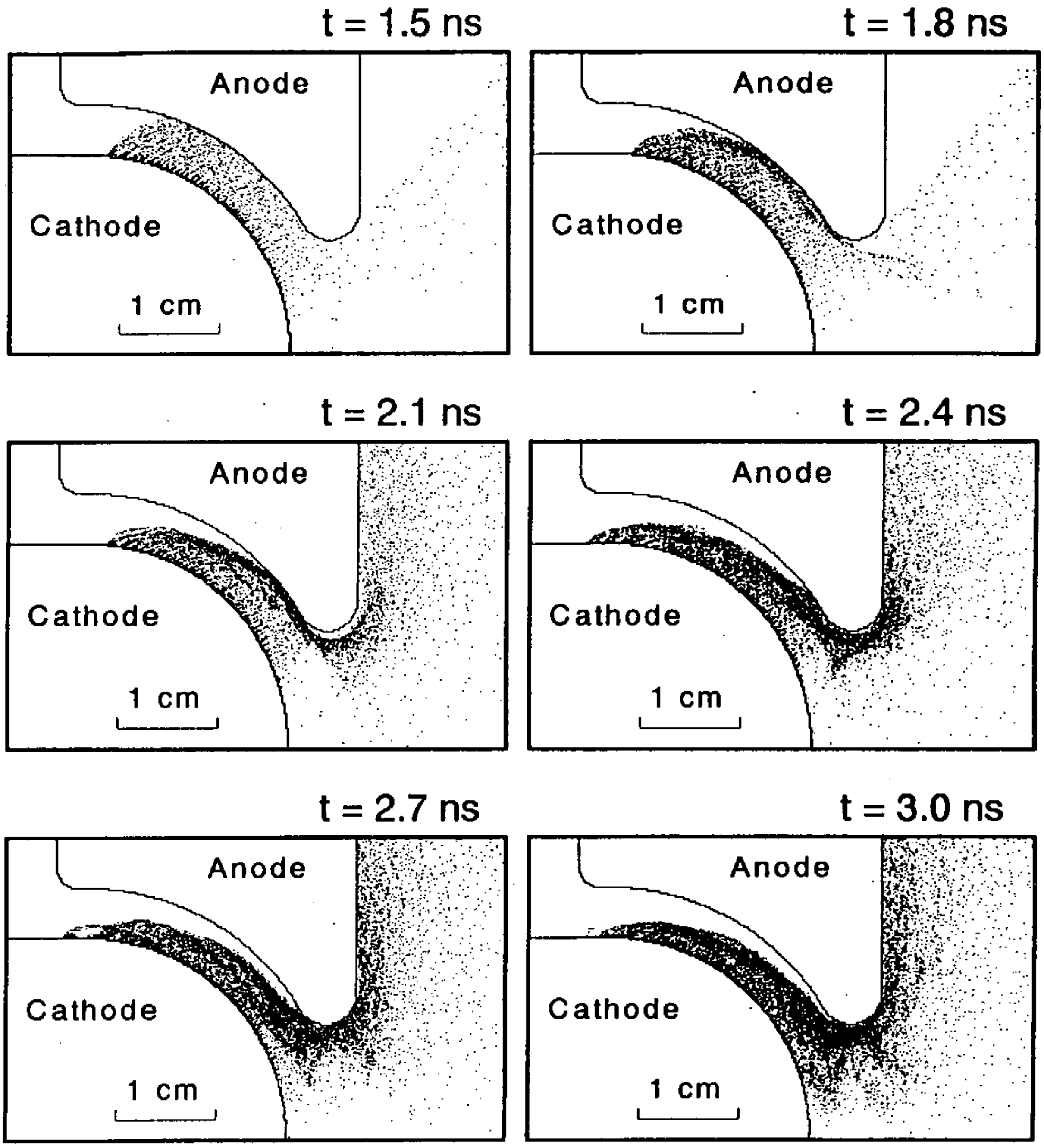

Fig. 5 Electron maps obtained from 1.5 to 3 ns.

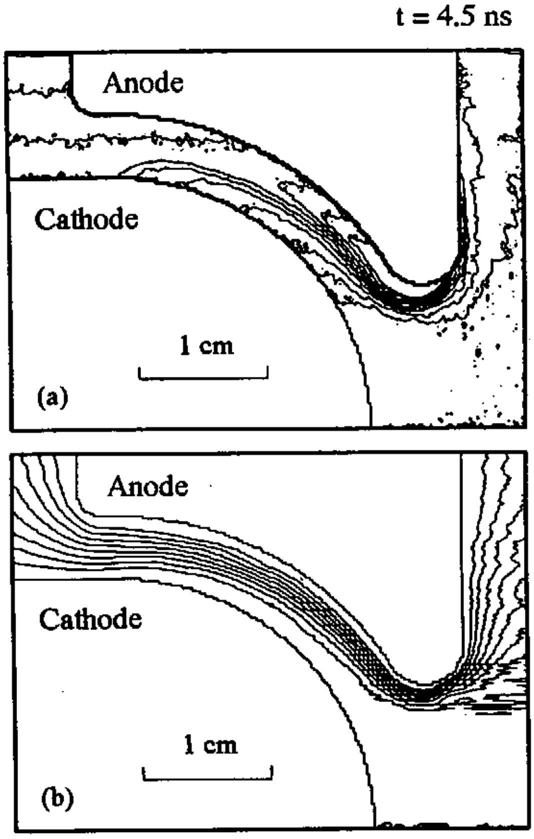

Fig. 6 (a) Equi–magnetic–flux density lines from 0.2 to 2.0 T with an interval of 0.2 T, and (b) equi–potential lines from 0.1 to 0.8 MV with an interval of 0.1 MV, obtained at t = 4.5 ns.

total ion current is obtained by counting the number of ions that arrive at the cathode surface. The diode impedance calculated from V_d and I_d is ~ 5.8 Ω during the flat–top of the diode current. The total ion current is ~ 25 kA, which is nearly 4 times higher than that obtained by the Child–Langmuir law of ion flow. The calculated ion–current efficiency $I_i/(I_e+I_i)$ is ~ 15 %, which is about 6.5 times that given by the bipolar flow.

Figure 5 shows the electron maps obtained from 1.5 to 3 ns. At the begining, the diode current is low so that the azimuthal magnetic field is too weak to bend the electron trafectories and the electrons are seen to cross diode gap to the anode. When the diode current increases, the magnetic field becomes stronger. As a result, the electron flow is gradually directed toword the downstream side of the diode gap. At t = 3 ns, when the diode voltage reaches the peak value, most part of the diode gap is well insulated by the self–magnetic field induced by the diode current.

Figure 6 shows (a) the equi–magnetic–flux–density lines and (b) the equi–potential lines obtained at $t = 4.5$ ns. In Fig. 6(a), ten equi–B_θ lines are from 0.2 to 2 T with an interval of 0.2 T. In Fig. 6(b), eight equi–potential lines are from 0.1 to 0.8 MV with an interval of 0.1 MV. It is noticed that the highest magnetic field appears at the downstream side of the diode gap. This is an important feature of the SPFD. The spherical diode gap compresses the electron sheath at the downstream side so that the magnetic field on the surface becomes stronger than that of the upstream side. On the other hand, since the electron sheath expels the electric field, the equal potential lines are compressed toward the anode at the downstream side, indicating strong electric field on the anode surface and therefore high ion–beam current density.

Figure 7 shows (a) the electron currents and (b) the average ion–current densities obtained in different regions on the anode

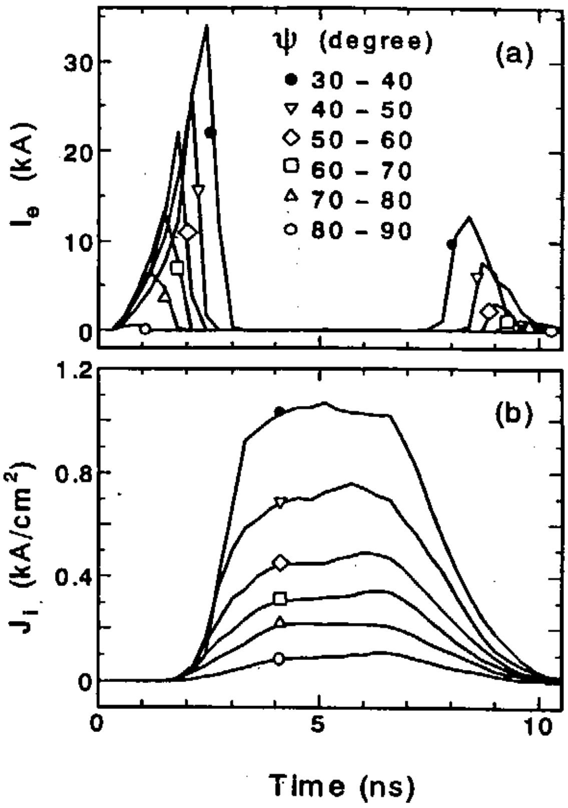

Fig. 7 (a) Electron currents and (b) average ion-current densities, obtained in different regions on the anode surface.

surface. The coordinate ψ is that shown in Fig. 1. In each region, the electron current is obtained by counting on the anode surface and the ion current is obtained on the cathode surface. The ion-current densities are obtained by dividing the ion currents with the associated area of the anode surface. From Fig. 7(a), we see that, when the diode current is low, the electron irradiation is observed in most regions on the anode surface. As the current rises, the electron currents drop to zero one after another from the large-ψ (upstream) regions to the small-ψ (downstream) regions. The gap is well insulated during most part of the power pulse. From Fig. 7(b), it is obtained that the ion-current density varies from ~ 0.1 kA/cm^2 in the upstream regions to ~ 1 kA/cm^2 in the downstream regions. It is noted that the Child-Langmuir space-charge limited ion-current density is ~ 0.2 kA/cm^2. Compared with this value, the ion-current densities in the downstream regions are clearly enhanced by the space-charge effect of the electron sheath. In the region $80° \le \psi \le 90°$, however, the ion-current density is probably lowered by the edge effect, since the ion currents are obtained on the cathode surface.

4. Characteristics of Ion Beam Focusing

In the simulation, ions are removed from the simulation when they reach the cathode. However, their velocity vectors are used to extend their trajectories into the cathode to give the profiles of the ion-number density along the axis and on several cross-section planes. In the following, we use the cylindrical coordinate system (r, θ, z), with the origin on the geometric center of the SPFD.

Figure 8 shows (a) the extended ion trajectories and (b) the time-integrated profile of the relative ion-number density along the central axis. Figure 8(a) is obtained by taking the average ion velocity vector throughout the simulation. Since the azimuthal velocity of each particle is zero, the trajectories of all the ions cross with the central axis (r = 0). Data shown in Fig.

8(b) are obtained by counting the ion numbers along the axis. Figure 8(b) shows that the maximum ion-number density appears at z ~ 1.5 mm with the value several times higher than that at z = 0. The full width of half maximum (FWHM) of the profile is about 3 mm in the z direction.

Figure 9 shows the time-integrated profile of relative ion-number density on the planes of z = 0 and z = 1.5 mm. The numbers of ions are counted in discrete annular regions with Δr of 0.1 mm. Data shown in Fig. 9 are obtained by dividing the ion number with the area of the associated ring. From Fig. 9, we see that both curves show sharp peaks at r = 0 indicating high ion-current density at the center. The FWHMs are less than 0.3 mm and the peak value at z = 1.5 mm is about 5 times as large as that at z = 0.

Due to the two-dimensional nature of the simulation code, the azimuthal deflection of the ions cannot be evaluated. Actually, fluctuations in the anode plasma or the electron sheath may cause asymmetry in the azimuthal direction, resulting in the azimuthal deflection of the ions. Instead, we prefer to obtain the average ion-current density within a certain radius. As an example, the average ion-current densities obtained within the radius of 0.5 mm are shown in Fig. 10. The maximum value obtained at z = 1.5 mm is ~ 330 kA/cm^2.

5. Comparison with Experimental Results

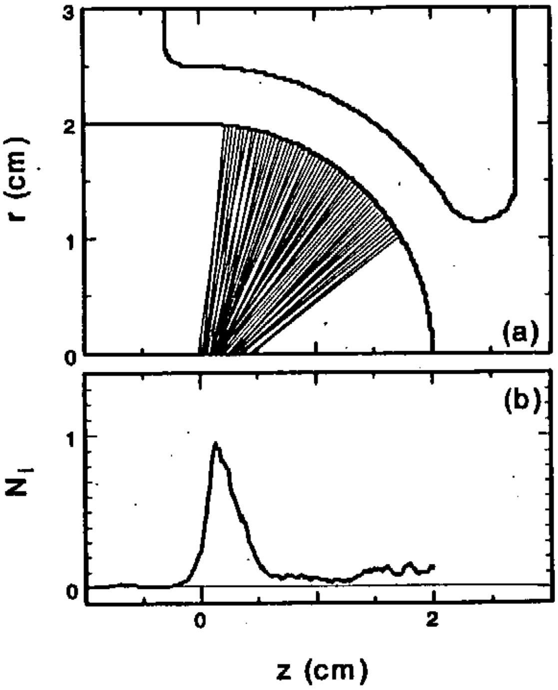

Fig. 8 (a) Ion trajectories averaged in time and (b) time-integrated profile of relative ion number density obtained on the axis.

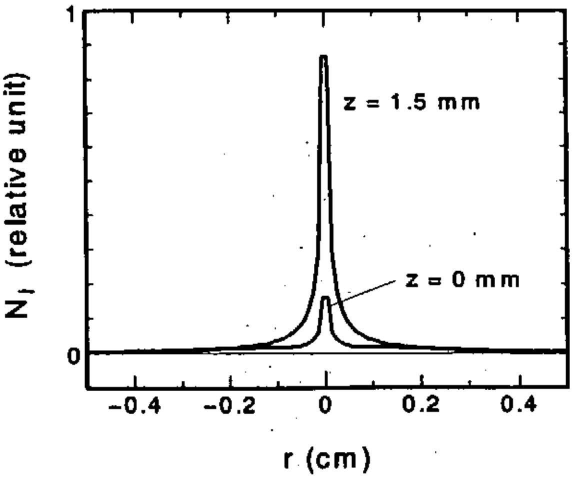

Fig. 9 Time-integrated ion density profiles obtained on cross-sectional planes z = 0 and z = 1.5 mm.

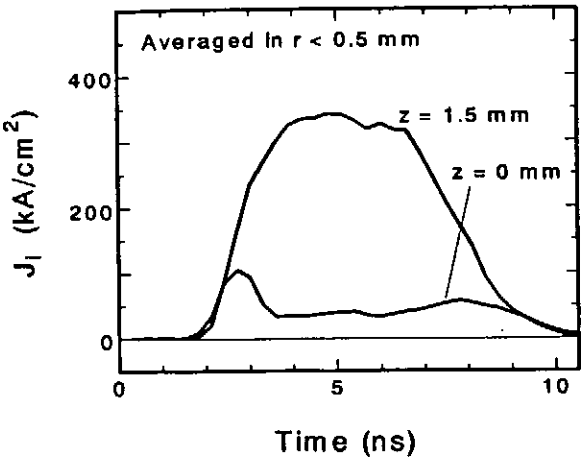

Fig. 10 Ion–beam current density averaged within r = 0.5 mm obtained on planes z = 0 and z = 1.5 mm.

The simulation results are compared with the experimental data.[3] For the experimental results, the diode voltage and the diode current are obtained at the peak diode power. Experimental ion–beam current density is the peak value averaged on the anode surface. The focusing area is given by the FWHMs of the ion–current density profile in the axial and radial directions.

The diode impedance is seen to be in good agreement. For the total ion current, however, the experimental result is ~ 68 kA, about 2.7 times as large as the simulation result. Since the accuracy of the experimental result is within a factor of 2, it is obvious that the experimental ion current is higher than that given by the simulation. The ion current is possibly enhanced by anomalous access of electrons to the anode surface. Experimentally, the anode damage by electron bombardment was observed in the downstream region, contrary to the simulation result shown in Fig. 5.

The experimental results showed the line focusing of the ion beam and gave a cylindrical focusing area with the length of ~ 2.5 mm and the diameter of ~ 0.5 mm. The axial length of the focusing are is in good agreement with the simulation results.

6. Conclusions

Using a two–dimensional, electromagnetic, relativistic particle–in–cell computer code, we have obtained the following simulation results for the SPFD.

1) With the source voltage of 2 MV and the source impedance of 6.5 Ω, the impedance of the SPFD is ~ 5.8 Ω.

2) The total ion current is ~ 25 kA, giving an ion–current efficiency of ~ 15 %.

3) The ion–current density on the anode surface varies from ~ 0.1 kA/cm² at the upstream side to ~ 1 kA/cm² at the downstream side.

4) Line focusing of the ions is obtained on the central axis. The profile of the number density on the axis shows a FWHM of ~ 3 mm.

5) On the cross–sectional plane at z = 1.5 mm, the ion–current density averaged in r < 0.5 mm shows the maximum value of 330 kA/cm².

References

1) P. L. Dreike, E. J. T. Burns, S. A. Slutz,

J. T. Crow, D. J. Johnson, P. R. Johnson, R. J. Leeper, P. A. Miller, L. P. Mix, D. B. Seidel, and D. F. Wenger: *J. Appl. Phys.* **60**, 878 (1986).

2) W. Jiang, T. Sakagami, K. Masugata, and K. Yatsui: *Proc. 9th Int. Conf. High-Power Particle Beams*, ed. D. Mosher and G. Cooperstein (Washington, D. C.), **II**, 859 (1992).

3) W. Jiang, K. Masugata, and K. Yatsui: *Jpn. J. Appl. Phys.* **32**, L752 (1993).

4) K. Yatsui, Y. Araki, K. Masugata, M. Murayama, M. Ito, E. Sai, M. Ikeda, Y. Shimotori, A. Takahashi, and T. Tanabe: *Proc. 6th Int. Conf. High-Power Particle Beams*, ed. C. Yamanaka (Osaka Univ., Osaka), 329 (1986).

5) K. Yatsui, Y. Shimotori, Y. Araki, K. Masugata, S. Kawata, and M. Murayama: *Proc. 11th Int. Conf. Plasma Phys. & Controlled Nuclear Fusion Res.* IAEA, **3**, 177 (1987).

6) K. Masugata, H. Isobe, K. Aga, M. Matsumoto, S. Kawata, W. Jiang, and K. Yatsui: *Laser and Particle Beams* **7**, 287 (1989).

7) K. Yatsui, K. Masugata, Y. Sekimoto, W. Jiang, H. U. Karow, H. Bluhm, D. Rusch, W. Bauer, and G. Kessler: *Proc. 8th Int. Conf. High-Power Particle Beams*, eds. B. N. Breizman and B. A. Knyazev (World Scientific, Novosibirsk, USSR), I, 535 (1990).

8) W. Jiang, K. Masugata, and K. Yatsui: *Laser and Particle Beams* **10**, 53 (1992).

9) W. Jiang, T. Sakagami, K. Masugata, and K. Yatsui: Phys. Plasmas, 2, 325 (1992).

Property measurements of light ion beams for Inertial Confinement Fusion

Kazuhito YASUIKE, Takayuki YAMASHITA, Tohru OCHI, Hiromitsu URAI, Shuji MIYAMOTO, Sadao NAKAI

Institute of Laser Engineering, Osaka University

Abstract

There are assumed that the divergence growth origin from an ion transit time coupling to dioctron instability in the electron sheath is different in directions parallel (azimuthal) and perpendicular (radial) to ExB drift direction. In order to observe divergence change with time in parallel and perpendicular to the ExB drift direction, the two-dimensional APC are developed. The two-dimensional APC method enable observing divergence and intensity distributions simultaneously with ~10 ns time resolution. Measured ion beam by the APC is a hollow beam, generated from the two-stage applied-B type ion diode with passive ion source driven by Reiden-SHVS pulsed power machine. Experimental results show that the divergence in parallel to ExB growth with time in contrary that the divergence in perpendicular to ExB show nearly constant values with time changes.

In order to improve spatial uniformity of ion beams, changing the magnetic field configuration of the first stage of the diode are tried. The evaluation of the beam uniformity is done by the APC measurements. A more uniform condition is found at reduced inner magnetic field that means non-uniform-B condition at the anode surface.

1. Introduction

The low divergence, spatially uniformity are necessary for the high brightness beam and beam focusbility especially in ion beam fusion. Ion beams for inertial confinement fusion requires the high intensity beams more than 5000 TW/g on a target for achievement of a cavity temperature about 300 eV[1-10]. Figure 1 shows an example configurations for ion beam fusion. An estimated beamlet parameters in fig. 1 are energy of 30 MeV, ion current of 0.3 MA Lithium beam with divergence of 7 upto 4 mrad for the hollum target of radius 1.5 cm. In order to achieve high intensity focus, lower the beam divergence and improvement of beam uniformity are important.

The beam non-uniformity in the diode restrict total extracted current from the diode due to the Child-Langmuir limit. Origins of the beam divergence are from the source divergence and are generated in the ion diode. Computational simulation of ion extraction from a diode predict that the beam divergence may grow with time as results of an ion transit-time instability initiated by coupling with a diocotron instability in the electron sheath in the diode[12-15]. Theoretical studies also predict that non-uniformities in the beam degrades the beam quality due to filamentation[16]. There are high radial applied magnetic field for insulate electron current in the diode. There are assumed that growth of the beam divergence in parallel and perpendicular to the ExB drift directions, are not identical due to the radial applied magnetic field. Figure 2 shows the concept of radial and azimuthal divergence $\Delta\theta_r$ and $\Delta\theta_\theta$ respectively. The measurement of radial and azimuthal beam divergences in and intensity with time and spatial resolution are necessary in order to understand the physics in the diode A-K gap, to understand the origin of beam angular divergence, to verify the scale low of the ion diodes and to generate high brightness ion beams.

2. Experiment

The radially applied-B type two-stage ion diode driven by Reiden-SHVS induction adding system which have 4+4 MV, 50+50Ω and 100 ns duration capability are used. Figure 3 shows experimental set-up. The diode A-K gap of first and second stage are respectively 10 and 11 mm. The diode insulating magnetic field is about 0.5 T which corresponds to diode critical voltage ~ 2.2 MV. The aluminum grooved epoxy filled passive anode is used for the ion source. Typical beam parameters are diode voltage of 700 keV, ion current density of 2 - 10 A/cm^2 which are limited under the Child-Langmuir current and the applied pulse duration of 100 ns. The particle types form the diode are proton and carbon. We intended to observe time evolutions of divergence and intensity distributions in both radial and azimuthal direction which are parallel and perpendicular to ExB drift respectively. We have designed a time resolved APC, which used gated micro channel plate (MCP) as a ion detector. The two-dimensional APC are constituted of pinhole array made from 100 μm thickness Tantalum plate having 7 columns x 7 rows φ 100 μm pinholes and a time gated MCP. A minimum pinhole separation of the observation angle is 20 mrad. The APC observes the anode with spatial resolution of 1 mm on the anode, the divergence angle resolution of less than 20 mrad and time resolution of 10 ns. The Aluminum 1 μm thickness filter on the 1 μm mylar film is located in 0.5 mm front of the MCP. The 1 μm Al filter have 70 keV and 500 keV stopping power for proton and carbon particles, respectively. Thus, the detected image at the MCP are mainly in proton.

First, we observe time evolutions of beam divergence by two-dimensional APC and then the beam uniformity improvement by changing magnetic field configuration are performed.

Figure 4 shows results of the two-dimensional APC testing, the time evolution of radial and azimuthal divergence $\Delta\theta_r$ and $\Delta\theta_\theta$, respectively. The radial divergence changes as time goes on.

The azimuthal divergence changes little with time and start from rather high value than $\Delta\theta_r$ in spite of parallel direction to the grooves on the anode.

We intended to improve an uniformity of the beam intensity along to the radial direction by changing magnetic field configuration in the first stage of the diode. We change a proportion of diode magnetic field winding current at the inner I_{inner} and at the outer I_{outer} of the first stage of the diode. The proportion of the second stage is fixed to 1 throughout the experiment. A condition I_{inner}/I_{outer} = 1 is a uniform-B condition along the radial direction at the cathode edge. At the uniform-B condition, the magnetic field pressure distributions are not uniform[18]. Thus, a formation of the plasma on the passive source is not uniform and there will be non-uniform beam from that ion source. Figure 5 shows improvement by changing a proportion of the inner and the outer of the first stage magnetic field winding (a) I_{inner}/I_{outer} = 0.5, (b) 0.67. These results show that the uniformity of the intensity are improved, however the value of the intensity are reduced.

3. Conclusion

The two-dimensional APC are developed and tested. Measurements the applied-B diode beam with time evolution using the APC shows that the beam has different divergence in radial and azimuthal directions. This APC measurement will be applied to unveil the mechanism of the divergence growth in the diode.

Improvement of beam uniformity was achieved by changing the proportion of the diode field winding current. These results shows the direction for the beam uniformity improvements.

Reference

[1] K. Imasaki, S. Miyamoto, S. Higaki, T. Ozaki, S. Nakai and C. Yamanaka, Jpn. J. Appl. Phys., **23** L83(1984).

[2] D.L. Cook, R.G. Adams, J.H. Aubert, L.D. Bacon, J.E.Bailey, D. D.Boolmquist, J. D.Boyes, G.A. Chandler, et al., "LIGHT-ION-DRIVEN INERTIAL CONFINEMENT FUSION," 14th Int'l Conf. on Plasma Phys. and Controlled Nuclear Fusion Research, Würzburg, Germany.

[3] D.D.-M. Ho, J.A. Harte and M. Tabak, "Radiation-Driven Targets for Heavy-Ion Fusion," IAEA 15th Int'l Conf. on Plasma Physics and Controlled Nuclear Fusion Research, Seville, Spain, 1994.

[4] M.K. Matzen, G.O. Allshouse, J.E. Bailey, G.A. Chandler, D.L. Cook, M.S. Derzon, R.J. Dukart, D.J. Johnson, R.J. Leeper, A.R. Moats, E.J. Mcguire, T.A. Mehlhorn, T. Nash, R.E. Olson, J.L. Porter, J.P. Quintenz and C.L. Ruiz, "PROGRESS IN ION BEAM

TARGET DESIGN AND EXPERIMENTS", 15th Int'l Conf. on Plasma Physics and Controlled Nucl. Fusion Research, Sevile, Spain, IAEA-CN-60/B-P-14, 1994.

[5] R.R. Peterson, "Ballistic Focus Light Ion Beams for an Inertial Confinement Fusion Reactor," Proc. of 9th Int'l Conf. on High-Power Particle Beams, 1992, Washington D.C., **II** 909.

[6] R.R. Peterson, D. Bruggink, R.L. Engelstad, G.L. Kulcinski, E.G. Lovell, J.J. MacFarlane, E.A. Mogahed, G.A. Moses, S. Rutledge, M.E. Sawan, I.N. Sviatoslavsky, G. Sviatoslavsky and L.J. Wittenberg, "LIBRA-LiTE, A BALLISTIC FOCUS LIGHT ION INERTIAL CONFINEMENT FUSION REACTOR," Proc. of 9th Int'l Conf. on High-Power Particle Beams, 1992, Washington D.C., **III** 1901.

[7] J.P. Quintenz, R.G. Adams, G.O. Allshouse, J.H. Aubert, L.D. Bacon, J.E. Bailey, D.D. Bloomquist, J. Boyes, G.A. Chandler, R.S. Coats, D.L.Cook, J.T. Crow, M.E. Cuneo, M.S. Derzon, M.P. Desjarlais, et al., "PROGRESS IN THE LIGHT ION DRIVEN INERTIAL CONFINEMENT FUSION PROGRAM", 15th Int'l Conf. on Plasma Physics and Controlled Nucl. Fusion Research, Sevile, Spain, IAEA-CN-60/B-1-I-6, 1994.

[8] M.G. Mazarakis, D.L. Smith, L. Bennett, J.W. Poukey, R.E. Olson, T.R. Lockner and J.J. Ramirez, "PBFA-II Modification for High-Power High-Convergence Implosion Experiments," Proc. of 10th Int'l Conf. on High-Power Particle Beams, 1994, San Diego, CA.

[9] S. Miyamoto, A. Zakou, S. Yasumura, K. Takitani, T. Akiba, K. Imasaki, C. Yamanaka and S. Nakai, "TWO STAGE DIODE FOR LIGHT ION FUSION DRIVER", IAEA Technical Committee Meeting on Drivers for Inertial Confinement Fusion, 15-19 April 1991 Osaka Japan, 1991.

[10] S. Miyamoto, K. Yasuike, N. Shirai and K. Imasaki, IEEE trans. on Plasma Science, **21** 567(1993).

[11] S. Miyamoto, K. Yasuike, M. Murakami, K. Nishihara, S. Nakai, K. Imasaki, C. Yamanaka, K. Yatsui, K. Masugata, S. Kawata, K. Kasuya, K. Horioka and T. Aoki, "FUSION ENERGY RESEARCH BY LIGHT ION BEAMS IN JAPAN", 15th Int'l Conf. on Plasma Physics and Controlled Nucl. Fusion Research, Sevile, Spain, IAEA-CN-60/B-P-10, 1994.

[12] S.A. Slutz and M.P. Desjarlais, J. Appl. Phys., **67** 6705(1990).

[13] M.P. Desjarlais, T.D. Pointon, D.B. Seidel, R.S. Coats, M.L. Kiefer, J.P. Quintenz and S.A. Slutz, Phys. Rev. Lett., **67** 3094(1991).

[14] T.D. Pointon, M.P. Desjarlais, D.B. Seidel, S.A. Slutz, R.S. Coats, M.L. Kiefer, and J.P. Quintenz, Phys. Plasmas, **1(2)** 439(1994).

[15] S.A. Slutz and J.W. Poukey, "SIMULATIONS OF MULTISTAGE INTENSE ION BEAM ACCELERATION," Proc. of 9th Int'l Conf. on High-Power Particle Beams, 1992, Washington D.C., **III** 1801.

[16] S.A. Slutz, Phys. Fluids B, **4** 2645(1992).

[17] J.D. Jackson, "Classical Electrodynamics 2nd ed.", John Wiley & Sons, Inc., New York (1975).

[18] D. L. Hanson, et al., "Improved Field Geometries for SABRE Extraction Ion Diode Operation with Passive Ion Sources", the proceeding of the 10th International Conference on High Power Particle Beams, San Diego CA.

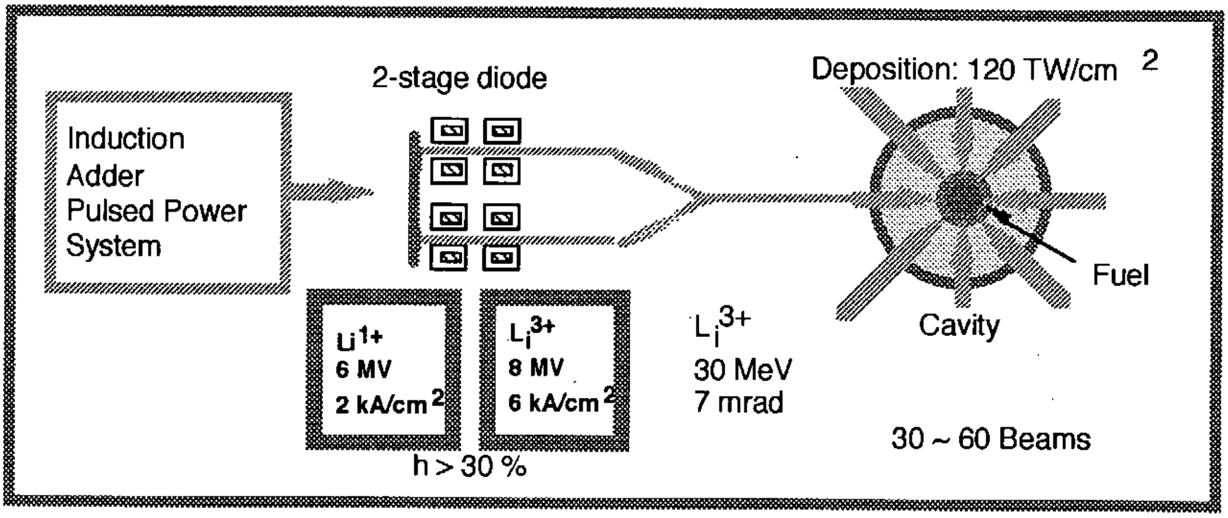

Fig. 1 An example of ion beam fusion using 30 to 60 beamlet modules. Each module is constituted of a two-stage diode fad by induction adding system. At the first stage of the diode, 6 MeV, 2kA/cm^2 Li^{1+} beam are generated and injected to the second stage. The injected beam from the first stage are charge striped by means of stripping structure such as charge stripping foil into Li^{3+} from Li^{1+}, thus the beam current and the post-accelerated energy are tripled.

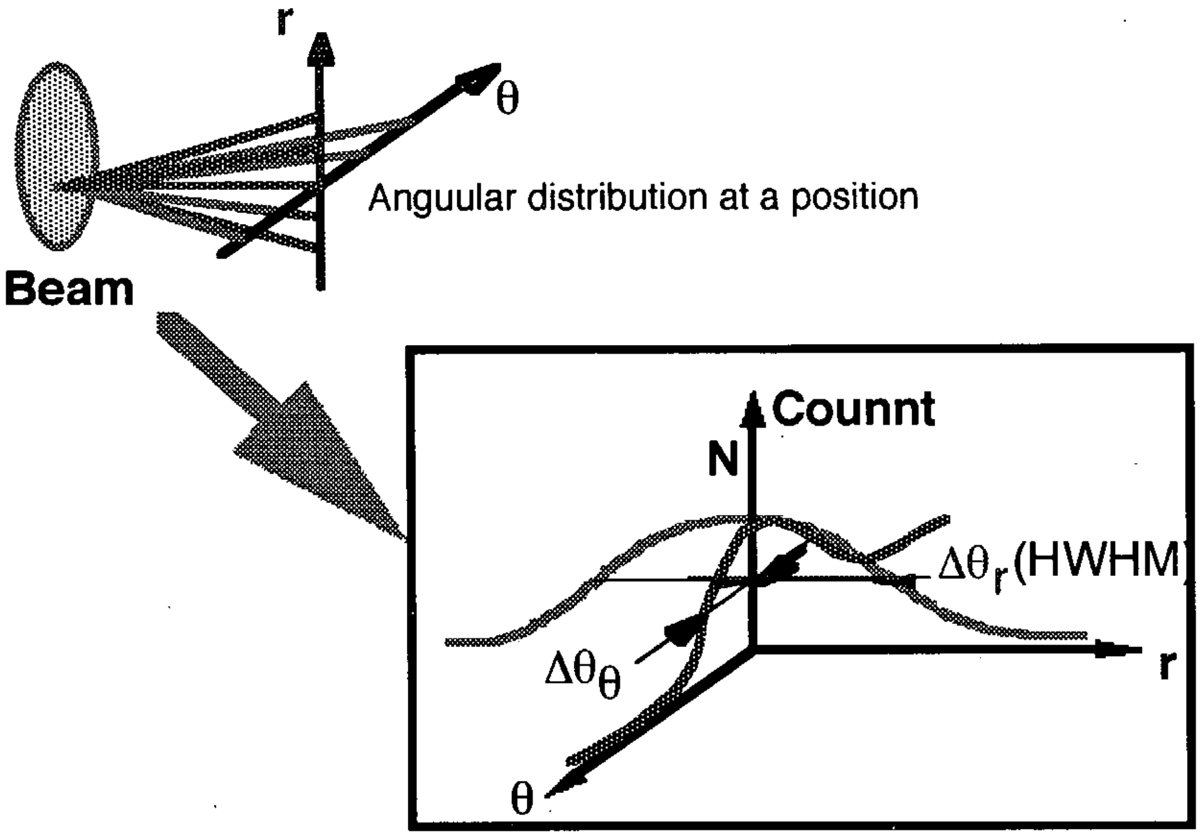

Beam divergence in θ and r directions ($\Delta\theta_r$ and $\Delta\theta_\theta$).

Fig. 2 Definition of beam divergence in radial r and azimuthal θ directions at a point is shown. The half width in the direction r or θ of half maximum of the angular distributions from a point are defined as beam divergence $\Delta\theta_r$ or $\Delta\theta_\theta$ at that point. The angular distributions are assumed as a Gaussian[17].

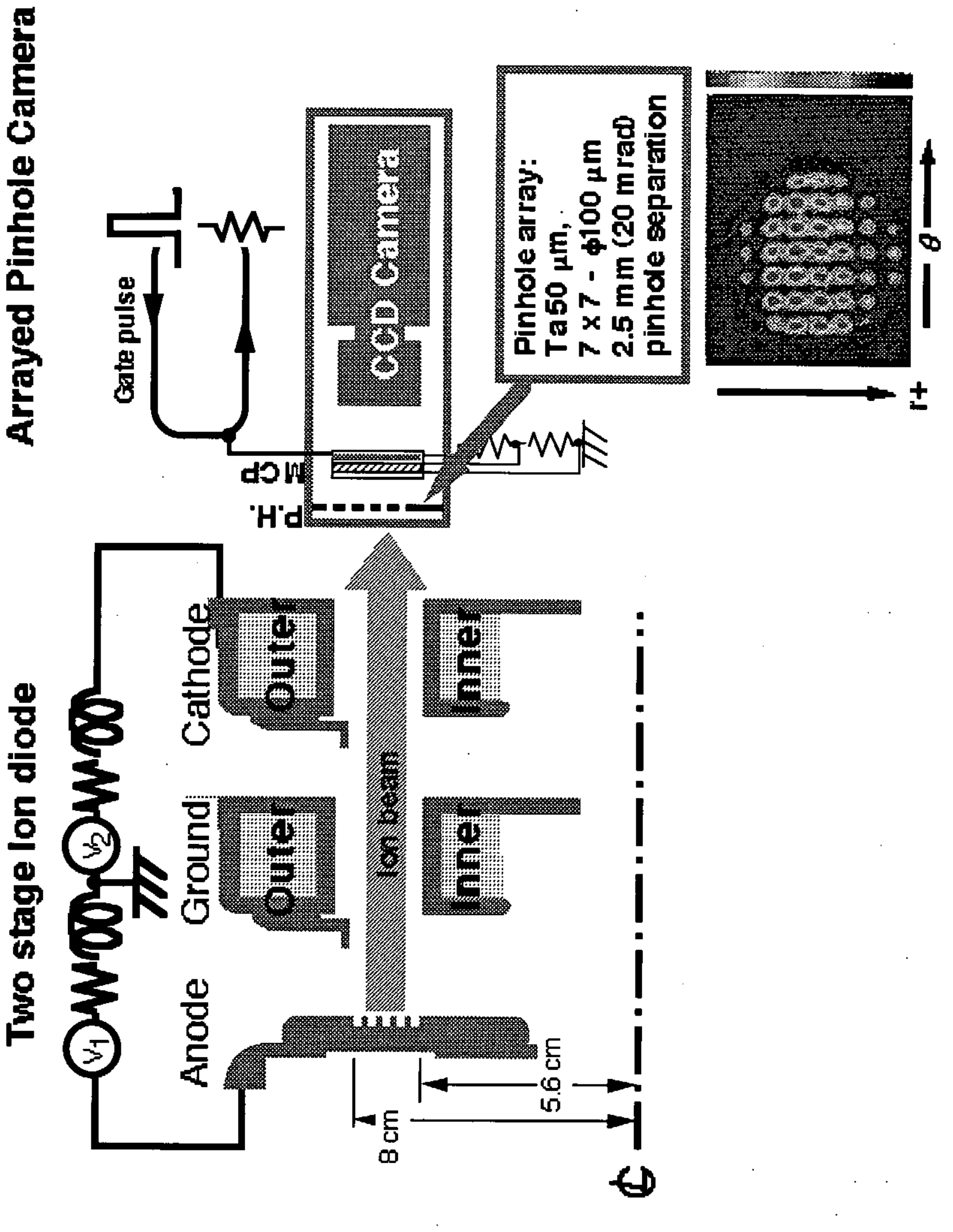

Fig. 3 Experimental set-up are shown. A hollow beam from two-stage ion diode fed by the Reiden-SHVS induction adding system was diagnosed by the two-dimensional arrayed pinhole

camera (APC). **Diode:** A Passive aluminum grooved epoxy filled anode was used as an ion source. In order to improve spatial uniformity of the beam, magnetic field configurations of the first stage were changed by means of changing a proportion of the inner and the outer of the first stage magnetic field winding I_{inner}/I_{outer} **APC:** The APC was constitute of a pinhole array and gated micro channel plate (MCP) as an image detector. The pinhole array of the APC has 7 columns x 7 rows pinholes.

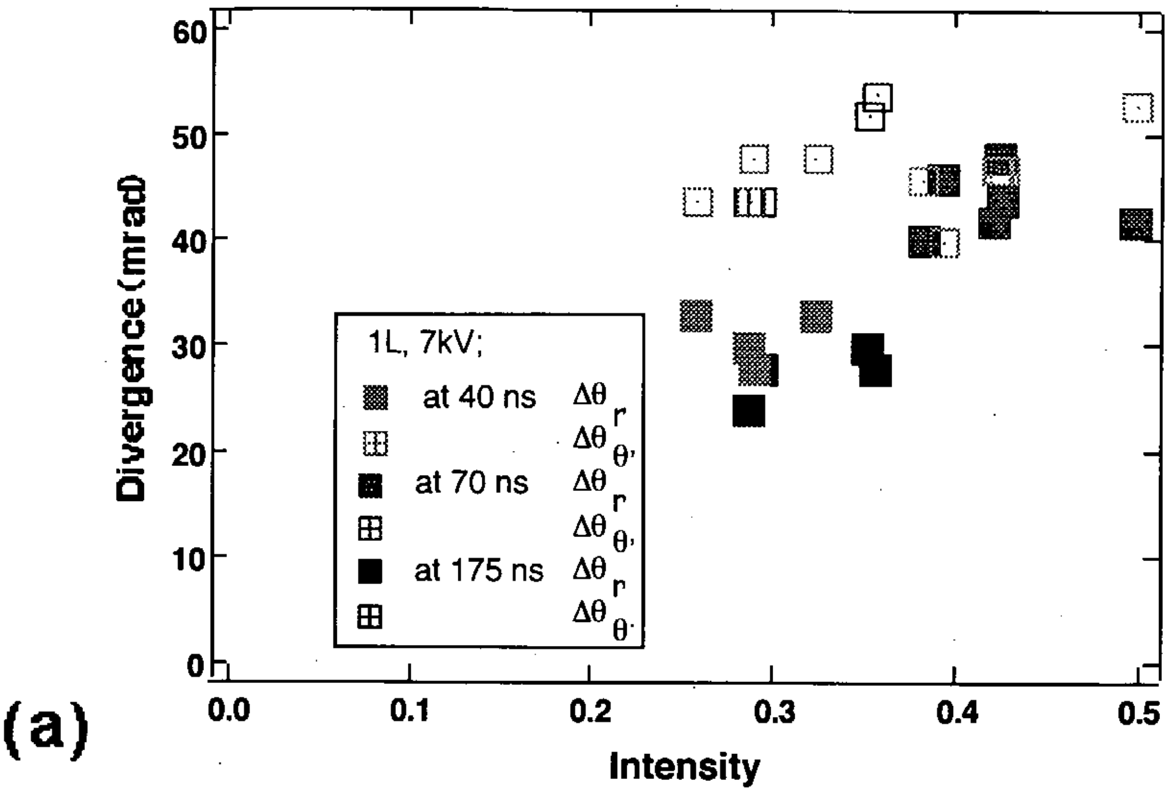

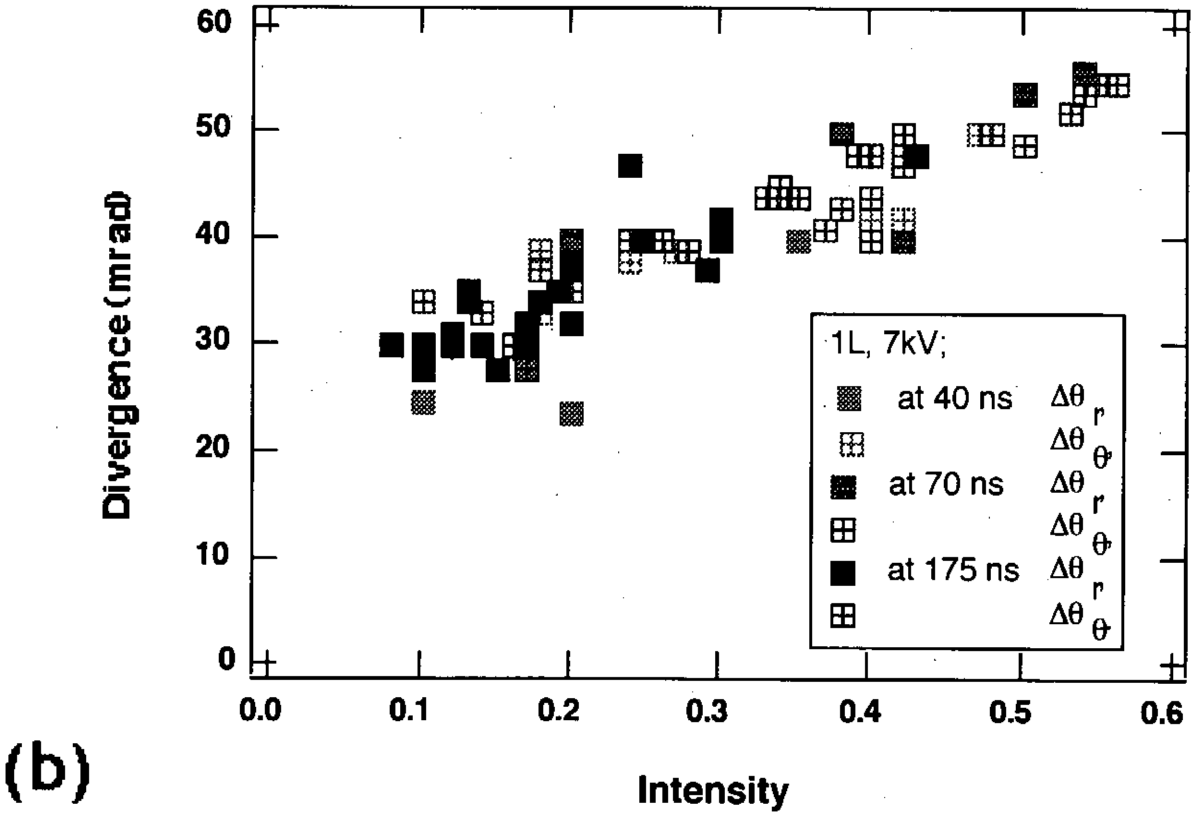

Fig. 4 Time evolution of divergence $\Delta\theta_r$ and $\Delta\theta_\theta$ are shown (a). There is a tendency that the divergence depends on intensity distributions (b).

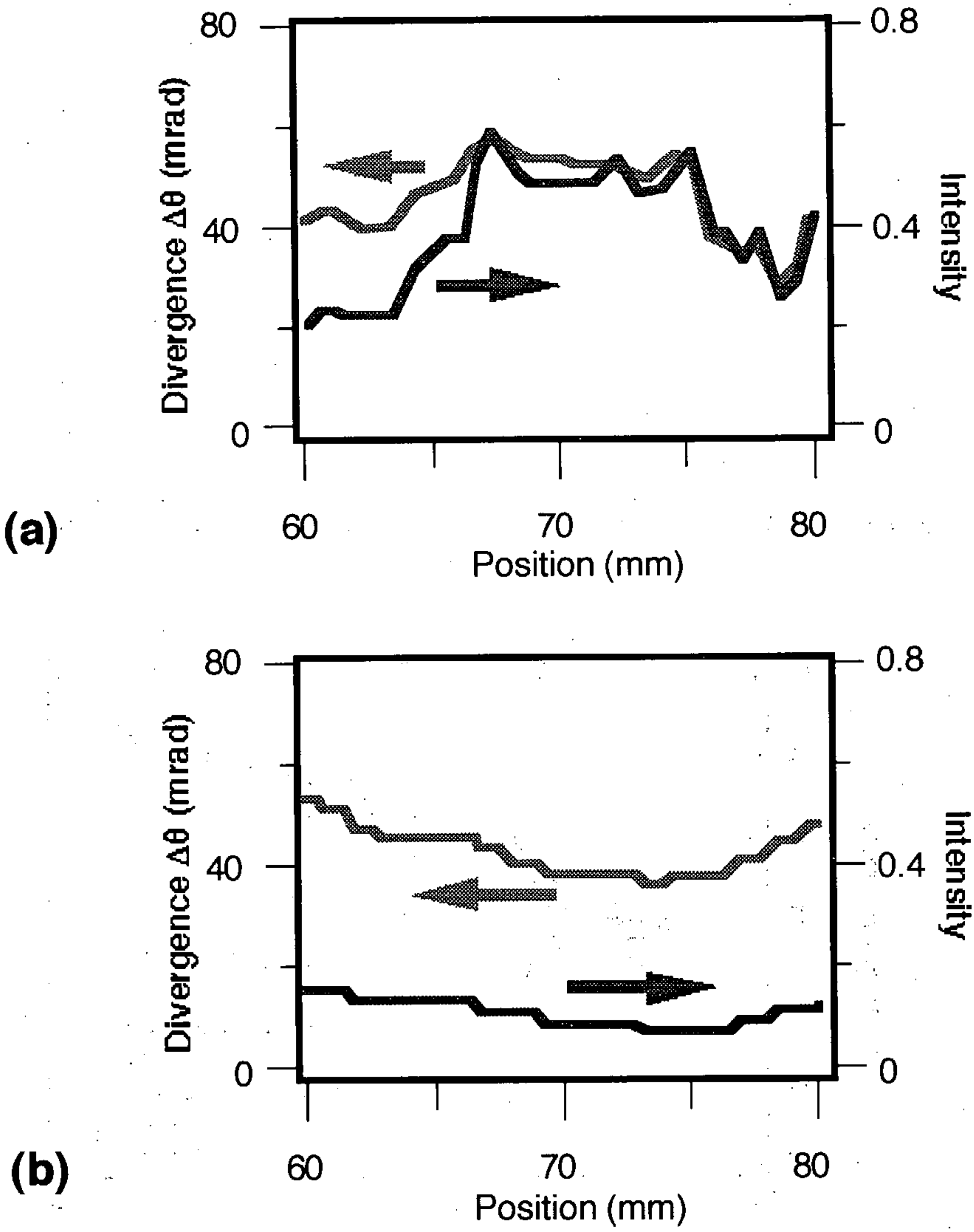

Fig. 5 Beam uniformity in radial direction is improved by changing a proportion of the inner and the outer of the first stage magnetic field winding (a) $I_{inner}/I_{outer} = 0.5$, (b) 0.67.

Xray Emission and Energy Input into a Gas-puff Z-Pinch

Tatsuya Fujimi,+, Keiichi Takasugi,
Takuji Shibuya+ and Tetsu Miyamoto

Atomic Energy Research Institute, Nihon University
+*College of Science and Technology, Nihon University*

Abstract

The x-ray emission character of a gas-puff z-pinch plasma and the energy input into the plasma were investigated. With increasing the amount of gas, the input energy increased due to increment of the pinch current, but the radiation temperature decreased. By using Ne, Ar and Kr gas, the energy increased with atomic number of the gas, and the temperature also increased. These are attributed to the smallness of the average pinch radius.

I. Introduction

Z-pinch is a contraction phenomenon caused by self-magnetic feild produced by high speed and high current discharge. In an annuler gas-puff z-pinch[1] the gas shell is formed between the electrodes and a solitary annuler plasma is created at the onset of discharge. The plasma is known as an intense pulsed soft x-ray sourse.[2]

We measured x-ray intensity with absorption method, and radiation temperature was evaluated for z-pinches with different initial gas density and atomic number of the gas.

The efficiency of energy input into z-pinch has been evaluated assuming constant magnetic flux.[3] We investigated the energy by directly analyzing circuit parameters using measured plasma current.[4,5] The plasma inductance and the averaged radius were also evaluated temporally.

II. Experimental Device and Measurements

Figure 1 is sectional plan of the SHOTGUN z-pinch device.[6] A gas nozzle is mounted on the anode to which a high speed gas valve is connected. The prenum pressure is fixed to 5 atm in the experiment. The storage section consists of 24 μF capacitor bank. The charged voltage is 25 kV and the energy is 7.5 kJ.

To mesure discharge currents we used Rogowskii coils. The anode current shows that entered into the discharge chamber, and the cathode current shows that flows throgh both electrodes. XUV signal from the bulk plasma was detected by a vacuum x-ray diode utilizing photoelectronic effect. X-rays from localized hot spots were detected by scintillation probes with absorption filters. Here we used 10 μm Be, 50 μm Al and 200 μm Al to get spectral information of the x-ray.

III. Analyzing Method

a. Circuit Analysis

A dip in discharge current is caused by radial change of inductance, which correspond to average radius of the plasma colmun.[5] We treat discharge system as LCR equivalent circuit shown in Fig. 2. Plasma resistance R_p is negligibly small except at the onset of discharge. So that we assume $R_p = 0$ in the analysis. The total inductace $L(t)$ is expressed as follows,

$$L(t) = L_c + L_p(t) = -\frac{1}{I(t)} \int_0^t (R_c I(t) + V(t))dt. \tag{1}$$

where R_c is circuit resistance, L_c is circuit inductance and L_p is plasma inductance. The capacitor voltage V is obtained by integrating the current I.

If discharge current flows surface of cylindorical plasma, the change in the inductance ΔL is related to the minimum contraction radius r,

$$\frac{r_0}{r} = \exp\left(\frac{2\pi\Delta L}{\mu_0 l}\right). \tag{2}$$

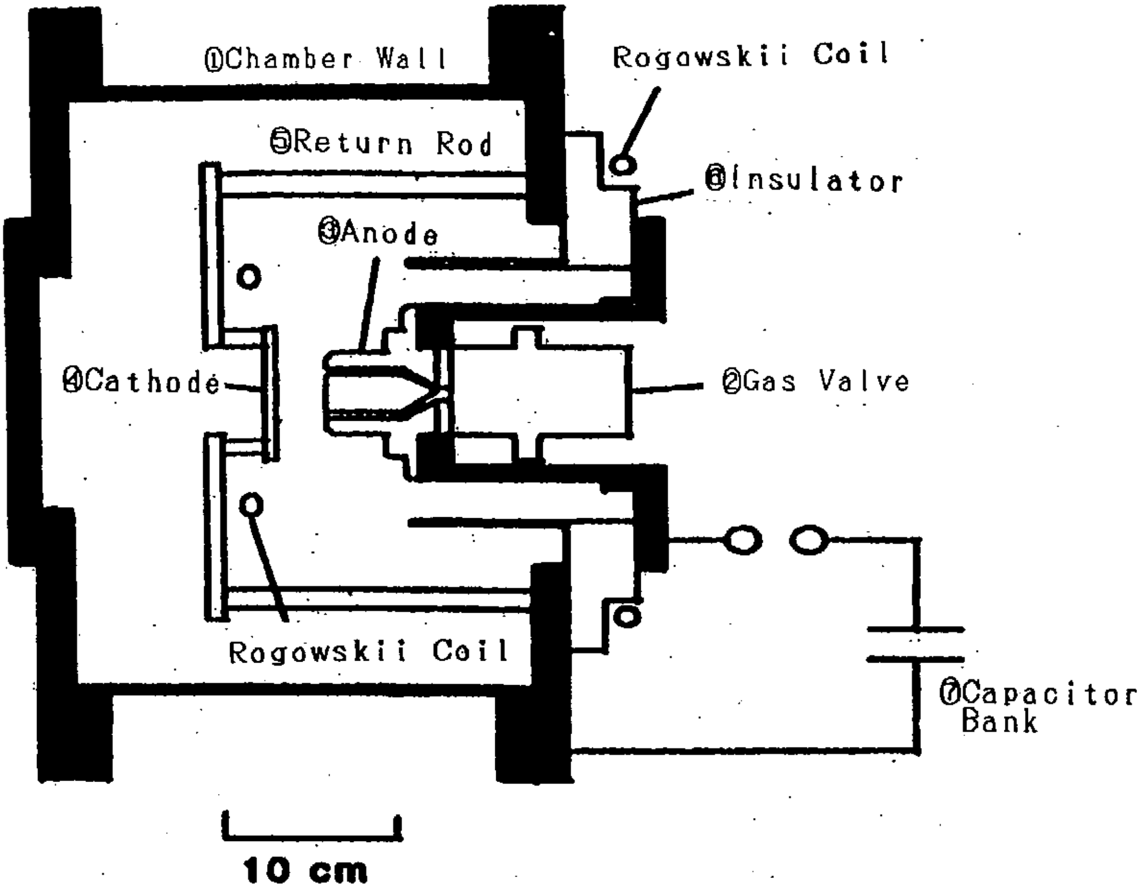

Fig. 1. SHOTGUN z-pinch device.

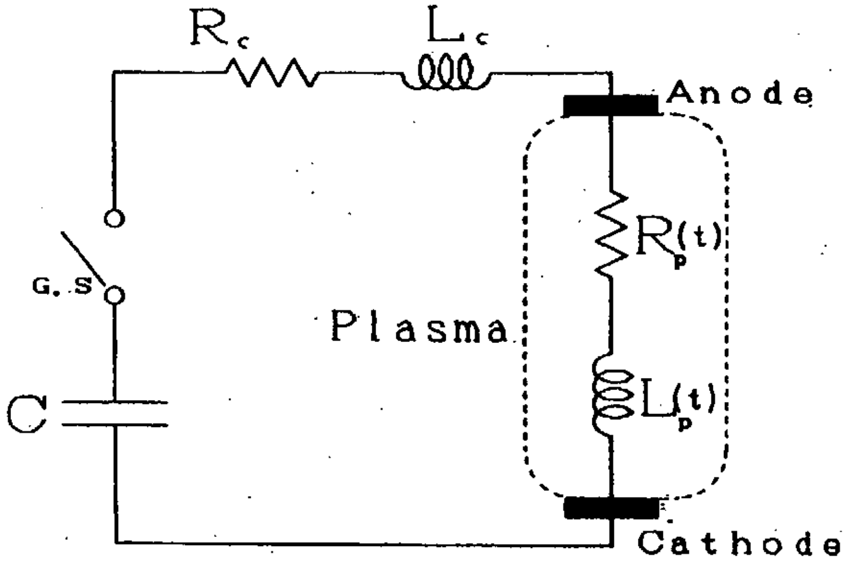

Fig. 2. LCR equivalent circuit.

where l is the length of plasma column.

Input energy into plasma is expressed as,

$$E(t) = \int_0^t V(t)I(t)dt - \int_0^t R_c I(t)^2 dt - \frac{1}{2}L(t)I(t)^2. \tag{3}$$

The first term is the energy that flows out of the capacitor, the second term is circuit loss, and the third term is inductive enrgy.

b. Radiation Temperature

In order to characterize x-ray emission, we used radiation temperature to express energy distriction of photons. The detector intensity is expressed as follows,

$$I(l,T) = \int_0^\infty \beta E \exp\left(\frac{-l}{\lambda(E)}\right) N_0(E,T)dE. \tag{4}$$

where βE is efficiency of the detector, and N_0 is number of photons emitted according to Planck's formula. The term $\exp(-l/\lambda)$ is filter's transmission. The temperature is not the plasma temperature unless the plasma is optically thick in this energy range.

IV. Experimental Results

The top two traces of Fig. 3(a) shows typical anode and cathode currents. A dip is observed in the current waveform, which is due to rapid increase in the plasma inductance. The bottom traces in the figure shows soft x-ray signals. The pulsed x-ray emission produced by contraction of the plasma corresponds to the current dip. The current level is about 200 kA. We can estimate the inductance, the average radius and the net input energy from the current. The width of the x-ray pulse becomes narrow as the thickness of the filter increases. Figure 3(b) shows the radius and radiation temperature as a function of time. The radius rapidly decreases to about 0.1 mm at the current dip. The net energy input is about 700 J. The temperature rapidly increases up to 1.5 keV.

Next we investigated the dependence of delay time of discharge from gas-puff detection T_d. The z-pinch discharge between the electrodes occurs between T_d = 0.2 ms and 0.45

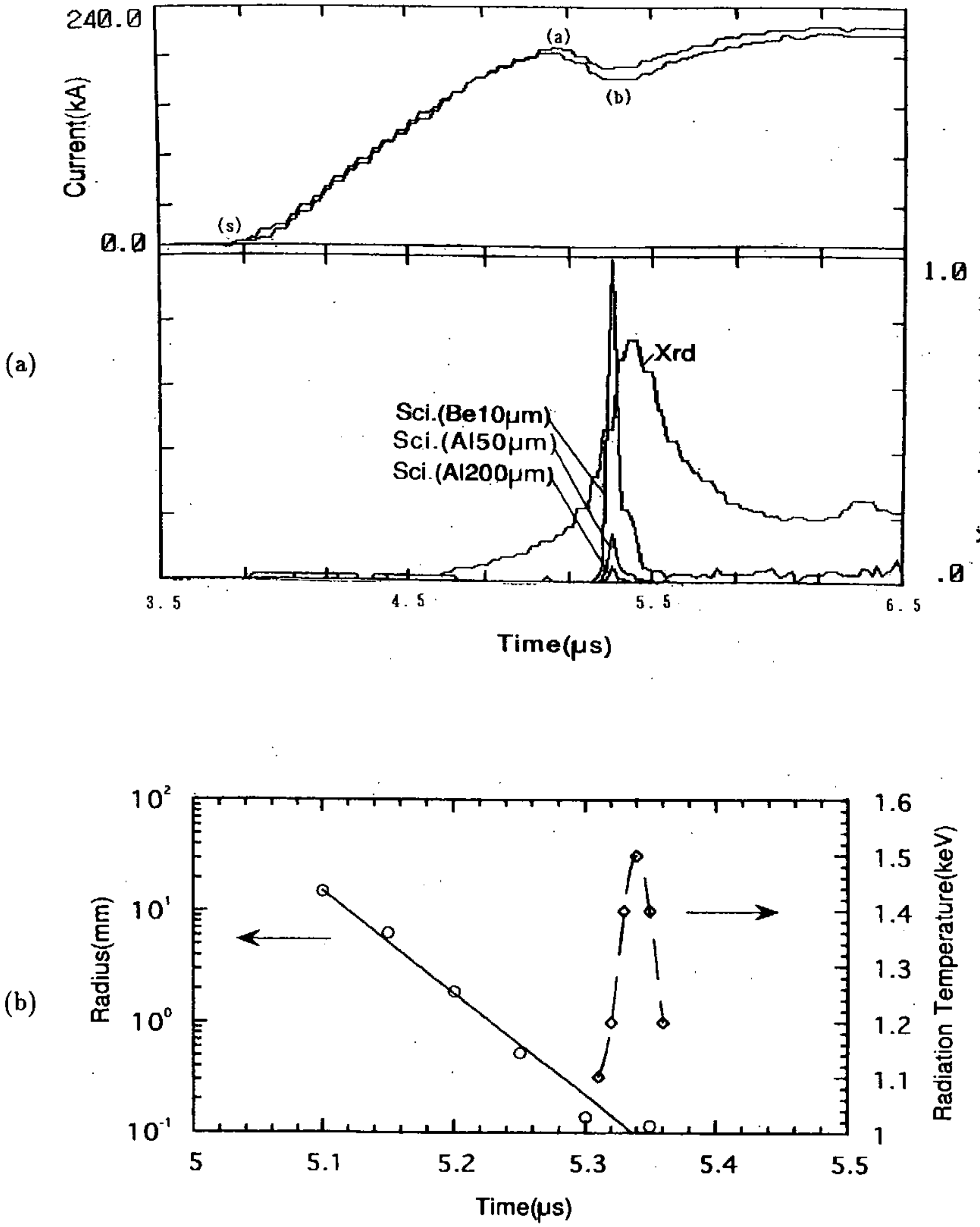

Fig. 3. (a) Typical current and soft x-ray waveforms.

(b) Temporal behaviors of the average plasma radius and the radiation temperature.

ms. Figure 4(a) shows x-ray intensities as a function of T_d. X-ray with high photon energy decreaces more rapid than that with low photon energy. The radiation temperature T_{rad} also decreaces with T_d. The temperature T_{rad} is about 1.2 keV at $T_d = 0.2$ ms, T_{rad} is about 1.1 keV at $T_d = 0.3$ ms, and T_{rad} is about 1.0 keV at $T_d = 0.4$ ms. The net input energy ΔE and the change of inductance ΔL are shown in Fig. 4(b). The energy ΔE increaces with T_d, because the time required for pinch increases and the current at the pinch also increases. The inductance decreases with T_d due to increase in plasma density. The gas pressure increases with T_d as shown in Fig. 4(c). The input energy normalized by the pressure, which decreases with T_d, is also shown in the figure.

We found that input energy into plasma depends on the current value at the maximum pinch, and the energy can be controled by T_d. In z-pinches with different operating gases, the current and the pinch time are almost the same by fixing T_d. Figure 5(a) shows atomic number dependence of x-ray intensities. The hard component of x-ray increases much with atomic number. The result agrees with that of x-ray pinhole photographs.[5] The temperatures $T_{rad} = 1.1$ keV for Ne, $T_{rad} = 1.1$ keV for Ar and $T_{rad} = 1.5$ keV for Kr. The energy ΔE and the inductance ΔL are shown in Fig. 5(b). Both increases with atomic number. As the current level is fixed, the energy ΔE is converted from magnetic energy due to rapid change in the inductance. The average pinch radius r calculated from ΔL is shown in Fig. 5(c). The radius dicreases with atomic number. The change in the inductance is direct result of the change in plasma radius.

V. Summary

The x-ray emission character of a gas-puff z-pinch plasma were investigated and the radiation temperature of emitted x-ray was evaluated using absorption method. The circuit parameters and the net input energy into the plasma were obtained by analyzing the plasma current.

The average plasma radius decreased rapidly near the current dip. The radiation temperature was shown to increase with radial collapse. With increasing the amount of gas, the net

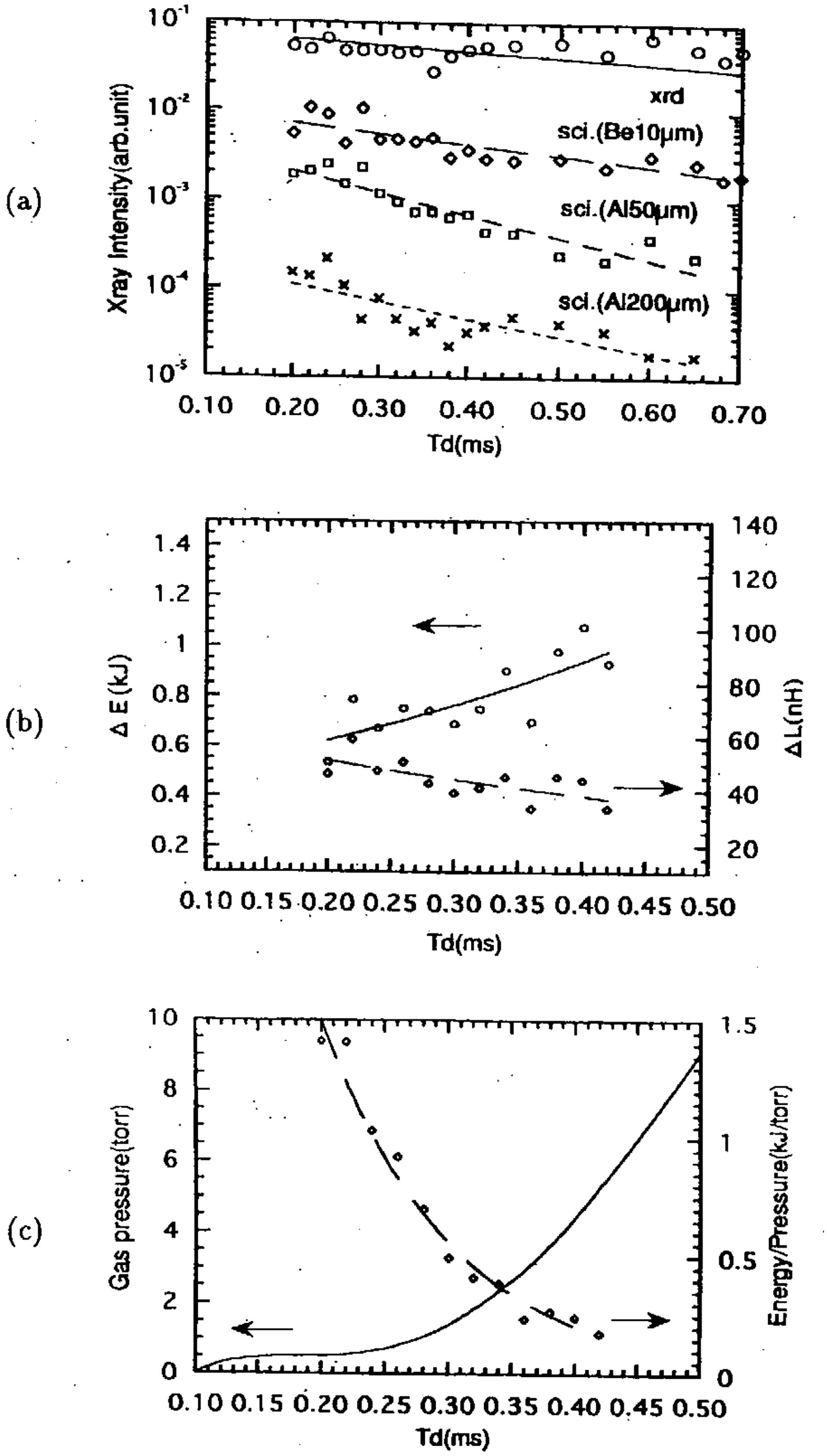

Fig. 4. (a) X-ray intensities with different detectors vs delay time of discharge T_d.

(b) The net energy input ΔE and the change in inductance ΔL vs T_d.

(c) Gas pressure and the normalized input energy vs T_d.

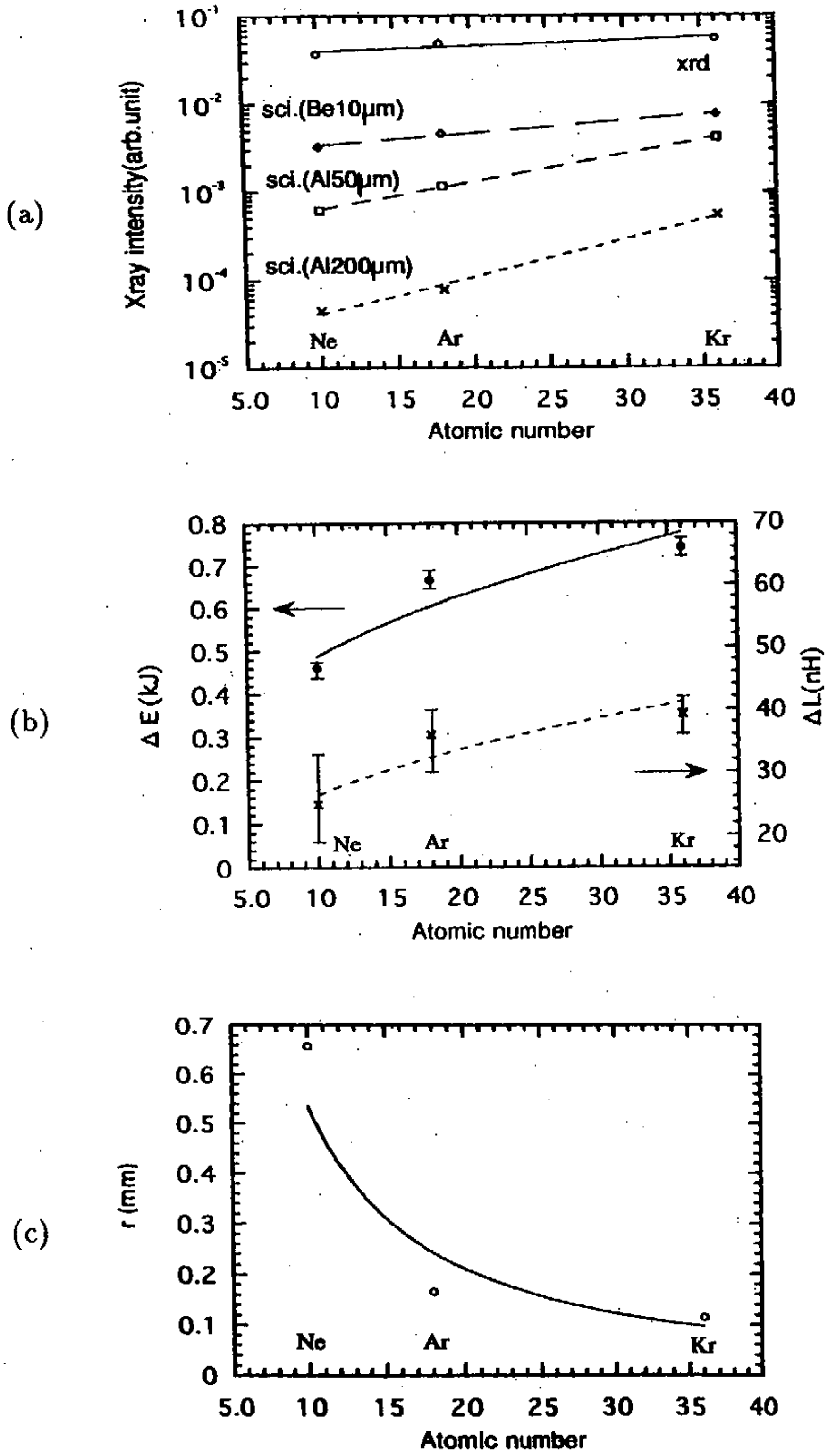

Fig. 5. (a) X-ray intensities with different detectors vs atomic number of the gas.

(b) The net energy input ΔE and the change in inductance ΔL vs atomic number.

(c) Pinch plasma radius vs atomic number.

input energy increased due to increment of the pinch current, but the radiation temperature decreased. The energy increased with atomic number of the gas, and the temperature also increased. The conversion of magnetic energy to the kinetic energy of the plasma is caused by the rapid change in the inductance, hence the plasma radius. The increments in the energy and the temperature are attributed to the smallness of the pinch radius. Radiative and ionizing energy loss should occur in high atomic number z-pinche, which causes strong radial collapse of the plasma.

References

[1] P.G. Burkhalter, J. Shiloh, A. Fisher and R.D. Cowan : J. Appl. Phys. **50**, 4532 (1979).

[2] R.B. Spielman, D.L. Hanson, M.A. Palmer, M.K. Matzen, T.W. Hussey and J.M. Peek : J. Appl. Phys. **57**, 830 (1985).

[3] J. Bailey, Y. Ettinger, A. Fisher and N. Rostoker : Appl. Phys. Lett. **40**, 460 (1982).

[4] K. Imasaka, H. Akiyama and S. Maeda : NIFS-PROC-14, 20 (1993).

[5] K. Takasugi, H. Suzuki, K. Moriyama and T. Miyamoto : NIFS-PROC-18, 163 (1994).

[6] K. Takasugi, A. Takeuchi, H. Takada and T. Miyamoto : Jpn. J. Appl. Phys. **31** 1874 (1992).

Optically Coupled Voltage Measurement on a Z-pinch

Takuji Shibuya+ and Keiichi Takasugi

Atomic Energy Research Institute, Nihon University

+*College of Science and Technology, Nihon University*

Abstract

Capacitive voltage divider with optical signal transmitter was constructed for the SHOTGUN z-pinch experiment. Temporal power input into the plasma was calculated from the voltage and the current signal, and the Spitzer resistivity at the onset of discharge was evaluated. The Joule input energy was 150 J and the inductively input energy was 400 J. The total energy input efficiency was about 20 %.

I. Introduction

Z-pinch is an easy means of producing high energy density plasma, and the electrically stored energy can be fed into the plasma quite efficiently[1]. In order to estimate the efficiency, the measurement of discharge voltage and current is essential to get power feed into the plasma. In a z-pinch plasma the change of plasma inductance during contraction plays important role in power input, because the plasma is radially accelerated with converting the magnetic energy into the kinetic energy. The net power input can be calculated from voltage, current and circuit resistance.

The measurement of discharge voltage is quite difficult in electromagnetically noisy environments. To avoid this difficulty, optical signal transmission technique is valid such as

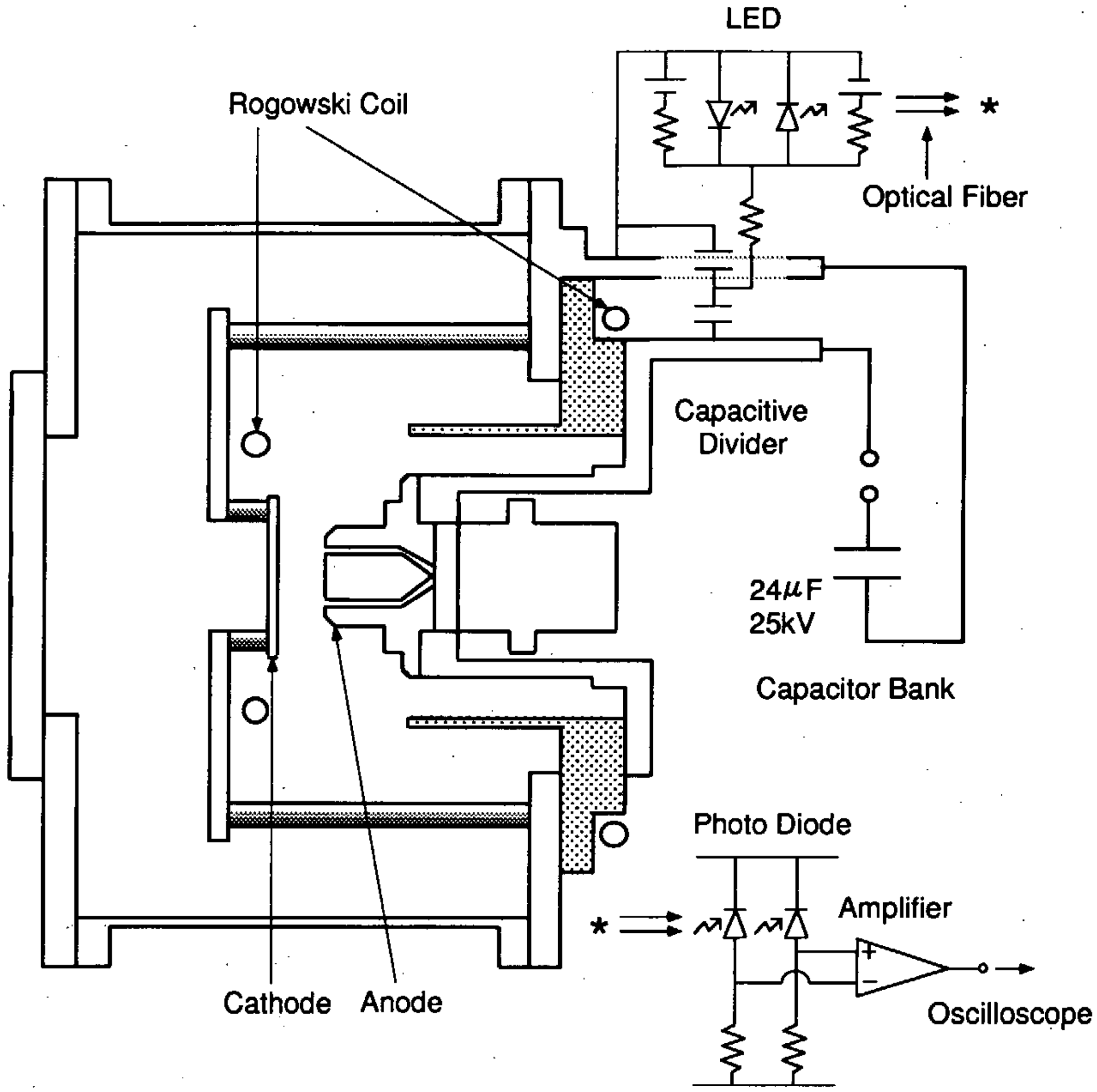

Fig. 1. Schematic configuration of the SHOTGUN z-pinch device and the voltage measurement system.

the use of LED[2] and Pockels cell[3]. In this paper the measurement of discharge voltage that used the technique, and the temporal power input into the plasma calculated from the discharge voltage and current are reported.

II. Experimental Setup

Figure 1 shows the schematic configuration of the SHOTGUN z-pinch device[4]. The 24 μF capacitor bank was used. The charge voltage and energy were 25 kV and 7.5 kJ. The anode consists of a gas nozzle and it spout out hollow-shaped gas. The diameter of the nozzle is 36 mm. The electrodes are made of carbon, and the spacing of the electrodes is 40 mm. The gas used here is Ar whose plenum pressure is 5 atm.

The anode and the cathode currents were measured by Rogowski coils. The voltage was measured near the discharge chamber with a capacitive divider. Capacitive divider has been installed on a strip line between the vacuum chamber and the capacitor bank. It consists of two part, a capacitive divider and an optical transmitter. In order to reduce circuit inductance the capacitive divider has a coaxial structure. Optical transmitter uses resistance and LED, and this translate an electric signal to an optical signal. A translated optical signal was transferred to optical receiver by optical fiber. This technique was useful in decreasing electromagnetic noises. Because of keeping liner response, some bias current was applied by a set of batteries. Frequency response of the optical transmitter/receiver system can be up to 7 MHz at -3 dB. This frequency response is limited by the capacitance of the LED, but satisfies the requirements of the experiments.

III. Input Energy into The Plasma

Figure 2 shows the waveforms of the discharge voltage and currents. The voltage is dropped to about one half of the capacitor voltage due to the circuit (feeder) inductance. A wedge in the voltage and a hollow in the current were observed due to the rapid change of plasma inductance in the contraction of plasma. The power, shown in Fig. 3, was calculated from the voltage and the currents. This shows that the input of the power into the discharge

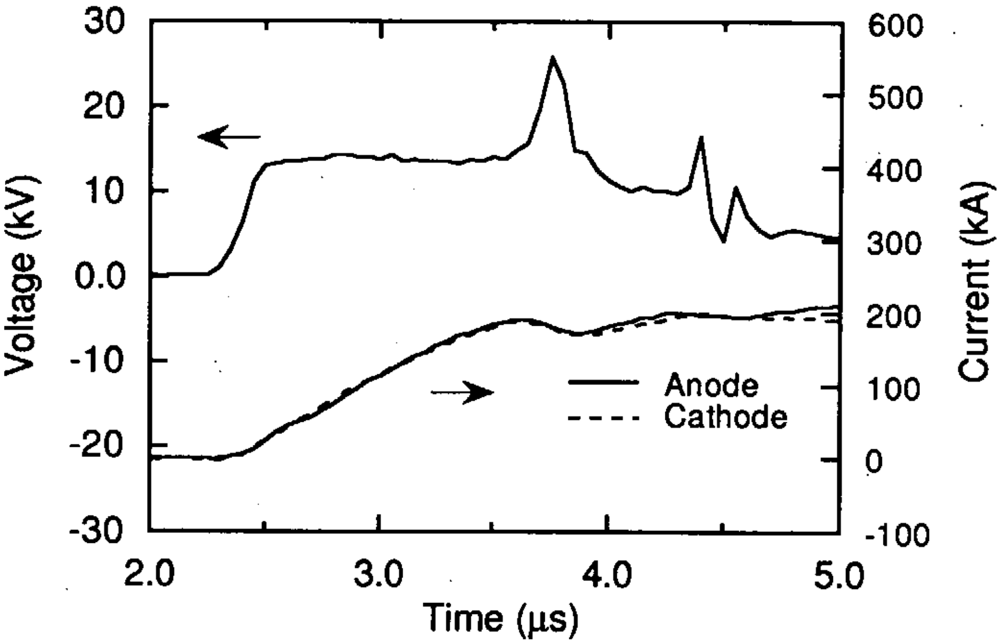

Fig. 2. The measured voltage and current waveforms of typical z-pinch discharge.

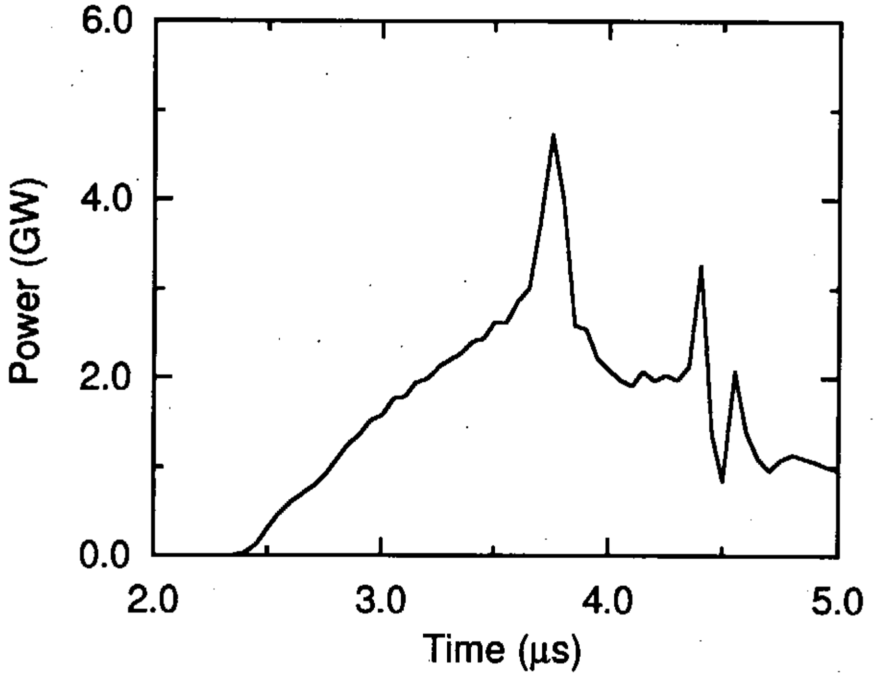

Fig. 3. Power input calculated by the voltage and current waveforms.

chamber was up to 4.5 GW instantaneously.

From an observation of the plasma in visible light by a Kerr-cell camera[5], a radius of plasma was kept constant at the beginning of discharge. So we suppose that the plasma radius hence the inductance is fixed and that the resistance is variable in this phase. The resistance $R(t)$ is written as

$$R(t) = \frac{V(t) - L\frac{d}{dt}I(t)}{I(t)}, \tag{1}$$

where $V(t)$ is the voltage, $I(t)$ is the current, L is the inductance. The inductance is sum of plasma inductance and chamber inductance, and these were 16 nH and 20 nH respectively. Figure 4 shows the resistance and electron temperature calculated assuming Spitzer resistivity. The waveform of the resistance consists of plasma resistance and chamber resistance. The chamber resistance is approximately 50 mΩ and is assumed to be constant. Plasma resistance decreases rapidly as the current increases. The waveform of the electron temperature shows rapid ohmic heating immediately before a contraction of the plasma.

A radius of plasma keeps constant for a moment, but it starts to shrink as the current increases. Then the plasma inductance is no more constant and should change. The plasma resistance becomes small and is neglected now. The inductance $L(t)$ is written as

$$L(t) = \frac{1}{I(t)} \int (V(t) - RI(t))dt. \tag{2}$$

Now we suppose that the resistance is equal to the chamber resistance. Figure 5 shows calculated inductance and average plasma radius. The waveform of the inductance consists of plasma inductance and chamber inductance. Because we assumed the chamber inductance was constant, an increment of inductance was caused by the change of plasma inductance. The average plasma radius was calculated from plasma inductance. The radius at the maximum pinch was 1.0 mm for this shot.

The net input energy into the plasma $E_p(t)$ is calculated as follows,

$$E_p(t) = E_1(t) - E_R(t) - E_{Lc}(t) - E_{Lp}(t), \tag{3}$$

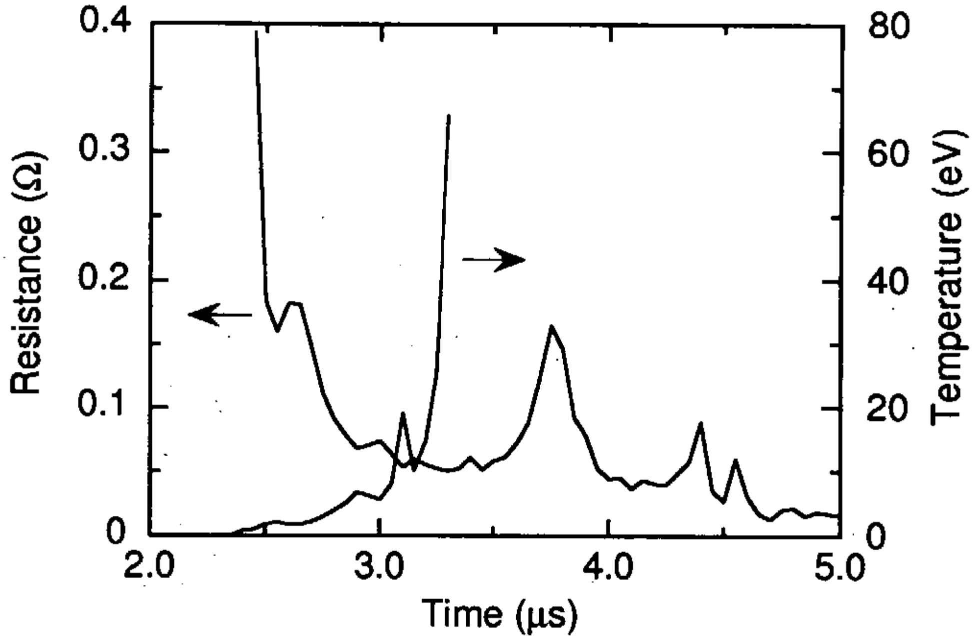

Fig. 4. The resistance and the electron temperature calculated assuming Spitzer resistivity.

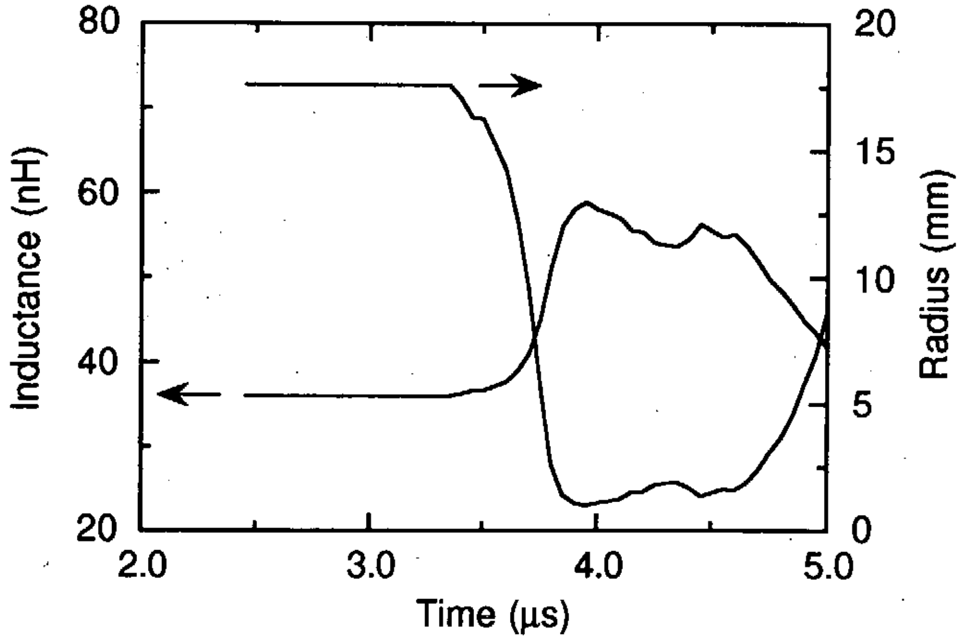

Fig. 5. The calculated inductance and the average plasma radius.

and

$$\begin{aligned} E_1(t) &= \int I(t)V(t)dt, \\ E_R(t) &= \int R(t)I(t)^2dt, \\ E_{Lc}(t) &= \frac{1}{2}L_cI(t)^2, \\ E_{Lp}(t) &= \frac{1}{2}L_p(t)I(t)^2, \end{aligned}$$

where L_c and $L_p(t)$ are the chamber inductance and the plasma inductance, respectively. $E_1(t)$ is the energy input into the discharge chamber, $E_R(t)$ is the resistively consumed energy by the circuit, and $E_{Lc}(t)$ and $E_{Lp}(t)$ are the inductive energies stored in the circuit and the plasma. The calculated energies are shown in Fig. 6. Here $E_2 = E_1(t) - E_R(t)$, $E_3 = E_2(t) - E_{Lc}(t)$ and $E_4 = E_3(t) - E_{Lp}(t)$. The energy E_p shows increment of plasma energy by contraction of plasma column and increase of plasma inductance at that time.

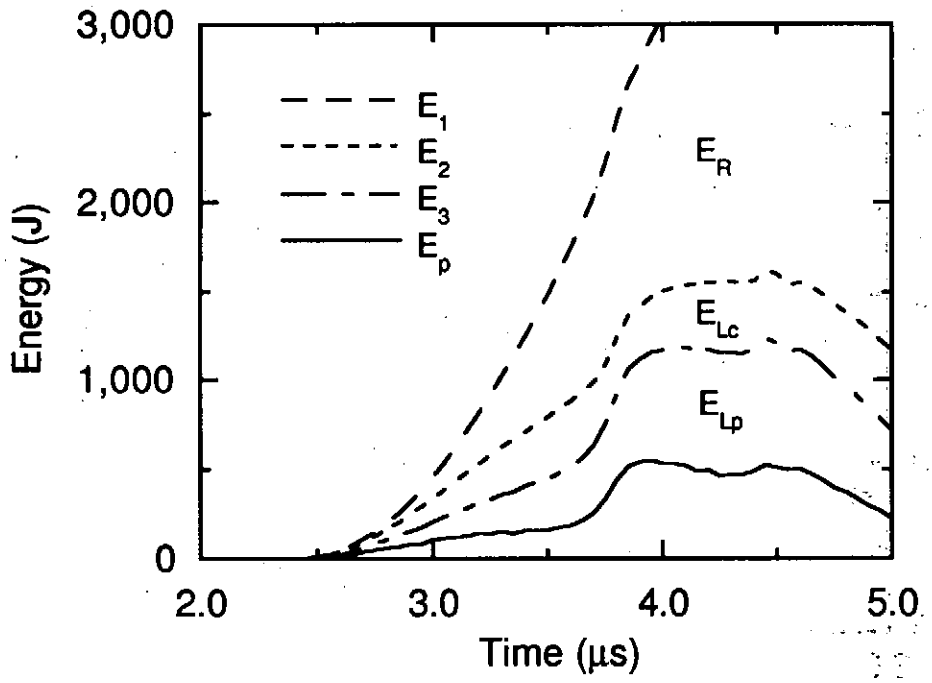

Fig. 6. The total input energy E_1, the resistive consumed energy E_R, the inductive stored energies E_{Lc} to the circuit and E_{Lp} to the plasma, and the net input energy E_p to the plasma.

IV. Summary

Capacitive voltage divider with optical signal transmitter was constructed for the SHOTGUN z-pinch experiment. The electromagnetic noise was significantly reduced, and the voltage was measured near the discharge chamber.

The temporal power inputs into the discharge section and the plasma were calculated from the voltage and the current signal. The Spitzer resistivity at the onset of discharge was evaluated. The Joule input energy was 150 J.

After the plasma resistance became negligible the plasma inductance changed. The inductively input energy was 400 J. The total net input energy was 550 J, while the energy input into the chamber was 2930 J. The energy conversion efficiency was about 20 %.

References

[1] K. Takasugi, H. Suzuki, K. Moriyama and T. Miyamoto : NIFS-PROC-18, 163 (1994).

[2] K.H. Finken and U. Ackermann : J. Appl. Phys. **53**, 226 (1982).

[3] M.R. Osborne and M.H.R. Hutchinson : Rev. Sci. Instrum. **57**, 2353 (1986).

[4] K. Takasugi, A. Takeuchi, H. Takada and T. Miyamoto : Jpn. J. Appl. Phys. **31**, 1874 (1992).

[5] K. Moriyama, K. Takasugi, T. Miyamoto and K. Sato : NIFS-PROC-18, 90 (1994).

IMPROVEMENTS OF SURFACE DISCHARGE SWITCH

N. Hamana, K.Takasugi and T. Miyamoto

College of Science and Technology, Nihon University
Kanda-Surugadai, Chiyoda-ku, Tokyo, Japan

ABSTRACT

Several improvements on a surface discharge switches were investigated. It was demonstrated for the new triggering method based on both corona discharge and field distortion to be more reliable and more excellent than for that by only the field distortion or multiple triggers. It was shown that optimum values, in which the switch impedance decreased without losing the features of the surface discharge switch, existed for the thickness and width of the electrodes. The effects of floating elctrodes were also investigated for further decreasing the switch impedance. The damage of the insulator surface was diminished remarkably by decreasing the switch resistance.

1. INTRODUCTION

Recently, requirements for fast rising, high current pulses (pulsed power devices) are increasing in many fields. The gap switches, which are one of important components in these pulsed power devices, are often a main source of the inductance that limits the characteristics of the devices. Hence, it is important to diminish the switch inductance. Surface discharge gap switches, in which the electrodes are separated from the return current conductor by a thin insulator, have often been used in the fast rising high current circuits, because of low inductance. When the current flows through only a few current channels, however, the inductance is limited in a relatively high value, so the triggering method is important in this switch. Buzzi et.al. showed that multichannel surface switch using multiple trigger-pins was useful to decrease the inductance (1) . The surface discharge switches have, however, other drawbacks --high resistivity and damage of the discharge surface. In this paper, it is demonstrated that the triggering method based on corona discharges & field distortion is simpler and more effective. Several improvements are also proposed and examined to diminish the above drawbacks.

2. EXPERIMENTAL ARRANGEMENTS

Transmission lines consisted of two Al foils sandwiching polyester sheets were used as capacitors with C = 17.0, 22.7, 34.0 and 45.4 nF. The inductance of the circuit resulted from the connection region between the capacitor and the switch, and from the switch. The inductance of the capacitors itself is negligible in comparison of them. A capacitor with 70.0 nF was also used, which was consisted of several pairs of the above ones connected in parallel, so the inductance is higher by 30 nH than the others. The capacitors were charged to the voltage 17 − 29 kV, and connected to the surface switch. The current profiles were measured by magnetic probes.

We can obtain the half period t_h, that is, the period between two adjacent phases where the current is zero, and the ratio of the adjacent peak currents, for example, the ratio of the first one to the second I_1/I_2 from the current profile. We can expect that the circuit inductance L is nearly constant during the discharge. When the resistance R is also assumed to be constant except the early, short period of discharges, we can determine the circuit parameters from the current profile.
The angular frequency ω and the time constant τ are given as

$$\omega = \pi / t_h \quad \text{and} \quad \tau = t_h / \ln(I_1/I_2) . \tag{1}$$

In the present experiment, the switch resistance is not necessarily negligible, so the current decays fast. The frequency ω_0 for the ideal case corresponding to $\tau = \infty$ is given as

$$\omega_0 = (\omega^2 + \tau^{-2})^{1/2} = \omega [1 + \pi^{-1} \ln(I_1/I_2)] . \tag{2}$$

The inductance L and the resistance R are given as

$$L = \frac{1}{C \omega_0^2} \qquad R = \frac{2L}{\tau} , \tag{3}$$

The first maximum current and the phase corresponding to it are given by

$$I_1 = \frac{V_0}{\omega_0 L} \exp \left[- \frac{1}{\omega \tau} \right] \sin^{-1} \left[\frac{\omega}{\omega_0} \right] \tag{4}$$

$$t_1 = \frac{t_h}{\pi} \frac{\omega_0}{\omega} \sin^{-1} \left[\frac{\omega}{\omega_0} \right] . \tag{5}$$

The high voltage pulse for triggering was fed to the triggering electrode by three stages Marx bank, each stage of which was charged to 27.5 kV.

3. TRIGGERING METHODS

Several triggering methods have been applied to the surface switch. In this experiment, three types of triggering methods were examined.

(a) Triggering by multiple pins (1)

The trigger discharges are fired between the cathode and a lot of trigger pins arranged in parallel to and near the cathode, as shown in Fig.1 (a). The switch is closed by arc channels induced between electrodes by the trigger discharge. The inductance and resistance decrease with increasing a number of the arc channels. High triggering voltage is needed in order to fire reproducibly a lot of arc channel.

(b) Triggering by field distortion

An Al foil is inserted between the discharge surface (and electrodes) and the return current as the triggering electrode (Fig.1(b)). The field between the electrodes is distorted, when a triggering voltage is applied to the triggering foil. As a result, the discharge starts between the electrodes.

(c) Triggering by corona discharge and field distortion

An Al foil is arranged on the ceiling of the discharge area and the electrodes as the triggering electrode (Fig.1(c)). When a voltage is applied to the foil, corona discharge occurs between the triggering foil and the return current feed in addition of the field distortion as well as in type (b). The discharge between electrodes starts as a result of both effects.

Typical experimental results are given for three cases in Table 1. In three cases the anode and cathode electrodes were 100 mm in width, and were arranged with separation of 50 mm from each other, and was connected to the capacitor of 70.0 nF charged at 29 kV. In type (b) only few arc channels were observed on the surface. In type (a) twelve trigger pins were used with separation of 5 mm from the cathode. The trigger discharge occurred between all pins and the cathode, but the arc current channels between the anode and cathode were formed only half in average under the above conditions. The inductance and resistance will decrease rather than the values in table 1, if the number of arc channels increases. In order to fire the arc channels corresponding to the numbers of pin, we will need higher voltage to apply to the trigger pins in addition to arrange the pins carefully. The type (a) was more complicate in the arrangement than in type (b), and not more reliable. The inductance and resistance decreased with increasing triggering voltage in the three cases. This means that a number of arc channels increased in type (a) and (b). The inductance and resistance were the lowest in type (c). This means that the discharge was more uniform in type (c). In this experiment, type (c) was adapted in all experiment as the triggering method.

In the present experiment a photo triggering, in which the switch is triggered by irradiating the discharge surface with intensive violet light, was not studied. If the irradiating light is not intensive enough, the photo triggering can not exceed the triggering by means of the corona discharge and the field distortion effect.

4. Optimization of Electrode Thickness

Influences of the electrode thickness on the inductance and resistance were examined. The definition of the parameters is given in Fig.2(a). Figure 3(a) and (b) displays the dependence of the inductance and resistance for the electrode thickness d. Both values of them were higher for thinner electrode, and decreased rapidly with increasing thickness. The inductance increased slowly with further increasing thickness after it reached the minimum value, while the resistivity decreased slowly. The current rising rate versus d is shown in Fig.2(c). Under the present conditions, the thickness for the minimum inductance (the optimum thickness) was 3 mm.

If the discharge was uniform and the current flowed along the narrow layer on the surface, the inductance should be smaller in thinner electrode. The result shows that the discharge is not so uniform in thin electrodes, but is consist of a few arc channels. Resistance decreasing with thickness means the increase of the cross section that the current passed through. The experimental results show that the cross area increased rapidly in $d < 3$ mm and gradually $d > 3$ mm. Thus, we can conclude that the discharge changes from the arc one to surface one (volume one) with increasing electrode thickness.

The damage of the discharge surface was examined for the electrode thickness 0.5, 1 and 3 mm. A Teflon sheet of thickness 200 μ m was used as the discharge surface. The damage of Teflon surface per every 15 shots is displayed in Fig. 4. The damage was remarkably weak in the electrode thickness 3 mm (that is, in low resistance discharge). The differences between thickness 0.5 mm and 1 mm were not clear in Fig.4, but appeared when a number of shots was decreased.

5. Effects of Floating Electrodes

The switch resistance depends on the separation between the electrodes, which is determined by the withstand voltage of the switch. In order to decrease the separation, that is, to increase the withstand voltage, the electrodes were separated by a small distance δ from the discharge surface, as shown in Fig.2(b). The withstand voltage increased with δ , and saturated at the voltage 13, 26 and 28 kV for the separation between electrodes ℓ = 5, 15 and 20 mm, respectively, as shown in Fig.5.

Figures 6 (a) and (b) display the dependence of the inductance and resistance versus the separation ℓ between electrodes for several values of δ , respectively. The resistance was proportional to ℓ for $\delta < 3$ mm. For $\delta > 5$ mm, however, the resistance increased with higher rate and tended to saturate in $\ell > 30$ mm. The dependence for $\delta > 5$ mm completely differed from that for $\delta < 3$ mm, and the experimental results lost reproducibility in $3 < \delta < 5$ mm. These results showed that the discharge mode changed between $3 < \delta < 5$ mm. This feature was observed for the inductance. When $\delta < 3$ mm, the inductance increased only slowly with ℓ . When $\delta > 5$ mm, however, the inductance increased rapidly with ℓ . As a result, the current rising rate is lower for $\delta = 5$ than for small δ , as shown in Fig.6(c).

The delay time and the jitter were depended on the discharge voltage V, and were 60 ns and ~ 4.4 ns at V = 29 kV, respectively. This delay time is relatively long, and it resulted from the relatively slow rising trigger pulse. If the fast risng trigger pulse is used, we will be able to achieve shorter delaytime and jitter.

If the conductivity, that is, the plasma temperature is same, the cross area of the discharge in $\delta = 5$ mm is ~ 0.57 times that of δ =3 mm for $\ell < 30$ mm. When the cross area decreases, the current density increases, and the temperature also increases, if no total current changes. As a result, the increase of the resistance due to decreasing cross area has a tendency to be canceled, because of $R \propto \ell /ST^{3/2}$. It is reasonable that the inductance increases slowly when $\delta > 3$ mm, because discharge current will have a tendency to leave a little from the return current. We conclude from the experimental results and the above consideration that the discharges kept the features of surface flashover discharge for $\delta < 3$ mm, but did not for $\delta > 5$ mm.

6. Effects of Electrode Width

6. 1 Experimental Results

The dependence of the switch parameters on the electrode width was examined using the electrodes with the width 50, 100, 200 and 400 mm and the capacities with 17, 22.7, 34.0 and 45.4 nF. In this experiments the type of Fig. 2(b) with $\delta = 3$ mm was used as a load switch. The inductance was inversely proportional to the width w for the capacities $C \leqq 34.0$ nF, but were not for C = 17.0 nF, as shown in Fig.7(a). On the other hand, the resistance decreased with increasing capacitance, and was nearly constant on the width for C > 34.0 nF, and showed the tendency to increase with the width for small capacitance. The inductance and resistance for $C = 22.7$ nF showed the tendency similar with that for $C \geqq 34.0$ nF except $w = 200$ mm, in other words, for a wide electrode. The switch was heavy load for all capacitors when the electrode with the width 400 mm was used. The current rising rate and the current versus the width are displayed for several values of capacitance in Fig.7(c) and (d), respectively.

6. 2 Discussion

In the ideal model that the current is uniform in the direction of width, both switch inductance L_s and resistance R_s are given by

$$L_s = L - L_f = \mu_0 \ell\, d/w \quad , \tag{6}$$

$$R_s = R - R_f = \eta\, \ell /wd \quad . \tag{7}$$

Hence, the inductance decreases inversely proportionally to the width of the electrodes w when ℓ d is fixed. It is satisfied for $C = 34.0$ and 45.7 nF, and nearly for $C = 22.7$ nF (see Fig.7(a)) . Figure 7(a) and (b) suggest that the current is uniform for $C =$ 34.0 and 45.7 nF, but is not uniform enough in $w = 200$ mm for $C = 22.7$ nF, and is not for $C = 17.0$ nF. We conclude that the minimum capacitance or the current density exists for uniform discharges. The floating inductance and switch one are easily obtained to be $\sim$ 10 nH and $\sim$ 5 nH for $C = 34.$ and 45. nF from Fig.7(a) using Eq.(6) .

On the other hand, the resistance depended not only on w, but also the resistivity η . If the plasma fully ionized, the resistivity η is proportional to $T^{-3/2}$ .The temperature will depend on the current density. We assume as $T \backsim i^{\alpha}$. The current is nearly proportional to $(C/L)^{1/2}$, as $(R/2)(C/L)^{1/2} << 1$ in the present experimental condition. If the current is uniform, the current density was proportional to $(C/L)^{1/2}/wd_c \backsim (\mu_0 \ell\, dd_c^{\,2})^{-1/2}(C/w)^{1/2}$, where d_c was thickness of the current. Hence, we have

$$R_s \backsim i^{-3\alpha/2} \ell /wd \backsim C^{-3\alpha/4} \ w^{3\alpha/4-1} (\ell\, dd_c)^{3\alpha/4} (\ell /d) \tag{8}$$

The resistance was independently on the width w for $C = 34.0$ and 45.7 nF. If ℓ , d and d_c are constant, we obtain $\alpha \sim 4/3$, so we obtain the relation

$$R_s \backsim C^{-1} \ . \tag{9}$$

To confirm Eq.(9), the R–C relation normalized by the value for $C = 45.7$ nF and $w =$

50 mm is drawn in Fig.8. We obtain the relation $R \propto C^{-1.23}$ from the resistance for $C = 34.0$ and 45.7 nF in which the current was presumed to be uniform. The points departing from the line in Fig.8 are corresponding to the data for which the current is considered to be not uniform from their inductance. The gradient of this line differs by the factor 0.23 from the above prediction (9). The thickness of the current layer d_c and the separation between the current layer and the return current d were assumed to be constant in deriving Eq.(9). However, they depend weakly on the current density. The small discrepancy between the experiment and Eq.(9) will result from these assumptions.

7. CONCLUSIONS

In this experiment a new triggering method for the surface discharge switch was demonstrated. It was based on the corona discharge and the field distortion effect, and was more excellent than that based only on the field distortion effect or using multiple trigger pins. In these methods the switch was closed by arc discharges, while it was closed by volume discharge in the present triggering method.

The switch resistance decreased with the electrode thickness. The damage of the insulator surface (i.e. the discharge surface) was diminished remarkably due to decreasing resistance. The switch inductance also decreased unless the electrodes were too thick. Second, the withstand voltage increased by floating the electrodes by a small distance from the discharge surface. The optimum distance was 3 mm in the present experiment. The features of the surface discharge switch vanished due to further increasing electrode thickness or further separation between the electrodes and the discharge surface. It is possible to shorten the separation between the electrodes for the same withstand voltage, and as a result, both inductance and resistance decreased.

The switch inductance decreases with the electrode width if the current flows uniformly and exceeds the critical value. On the other hand, the switch resistance is independently of the electrode width for the uniform current and decreases inversely proportionally with increasing capacitance (that is, with increasing current).

REFERENCES

1. J. M Buzzi, H. J. Doucet, W. D. Jones, Rev. Sci. Instrum. 61(2)(1990)852.

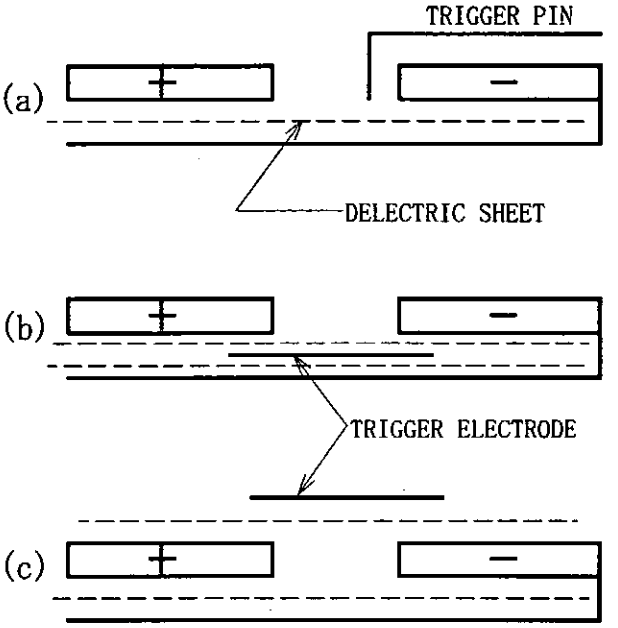

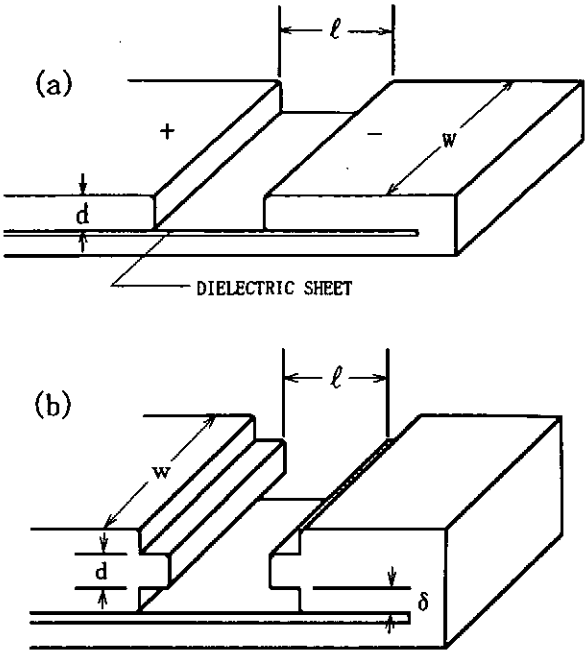

Fig. 1 Conceptual figures for triggering methods.

(a) Triggering by the multiple pins

(b) Triggering by the field distortion

(c) Triggering by the corona discharge and field distortion

Fig. 2 Schematic figures of surface discharge Switch.

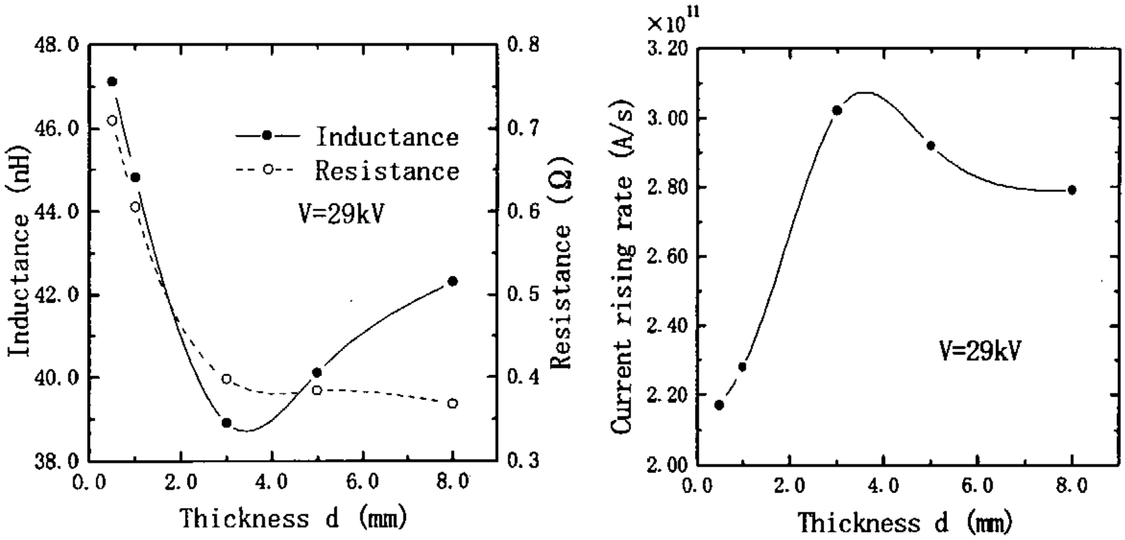

Fig. 3 Dependence of Inductance and Resistance on the electrode thickness d.

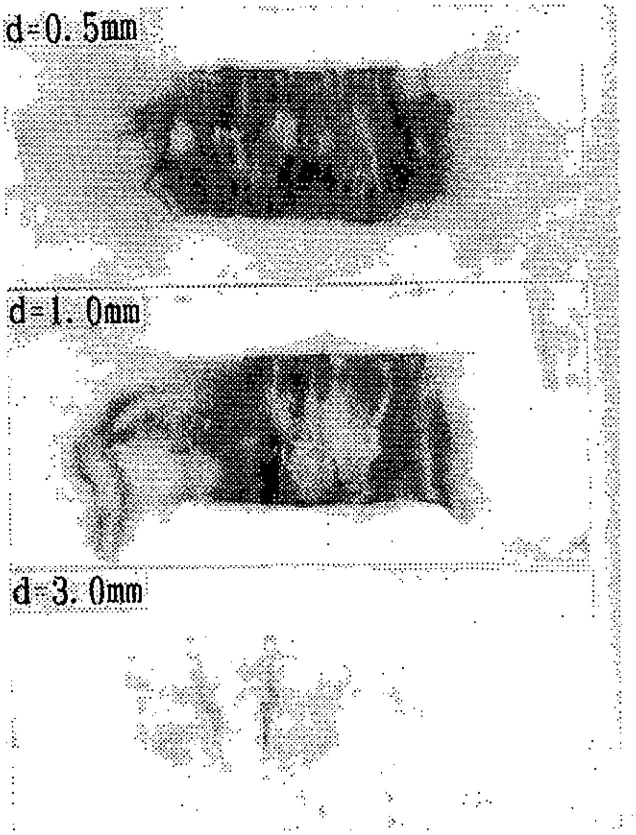

Fig. 4 Damage of the insulator surface per fifteen shots for the electrodes thickness d=0.5, 1.0 and 3.0 mm.

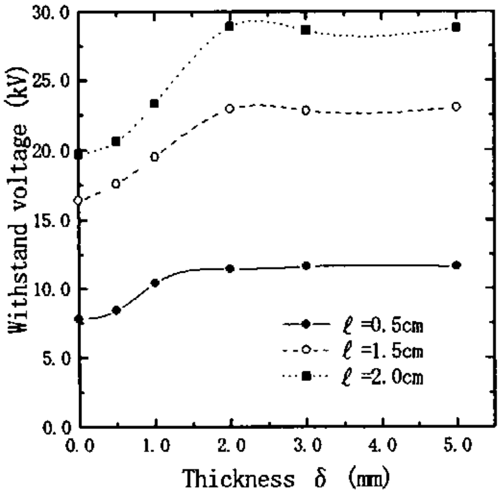

Fig. 5 Withstand voltage versus δ for several values of ℓ.

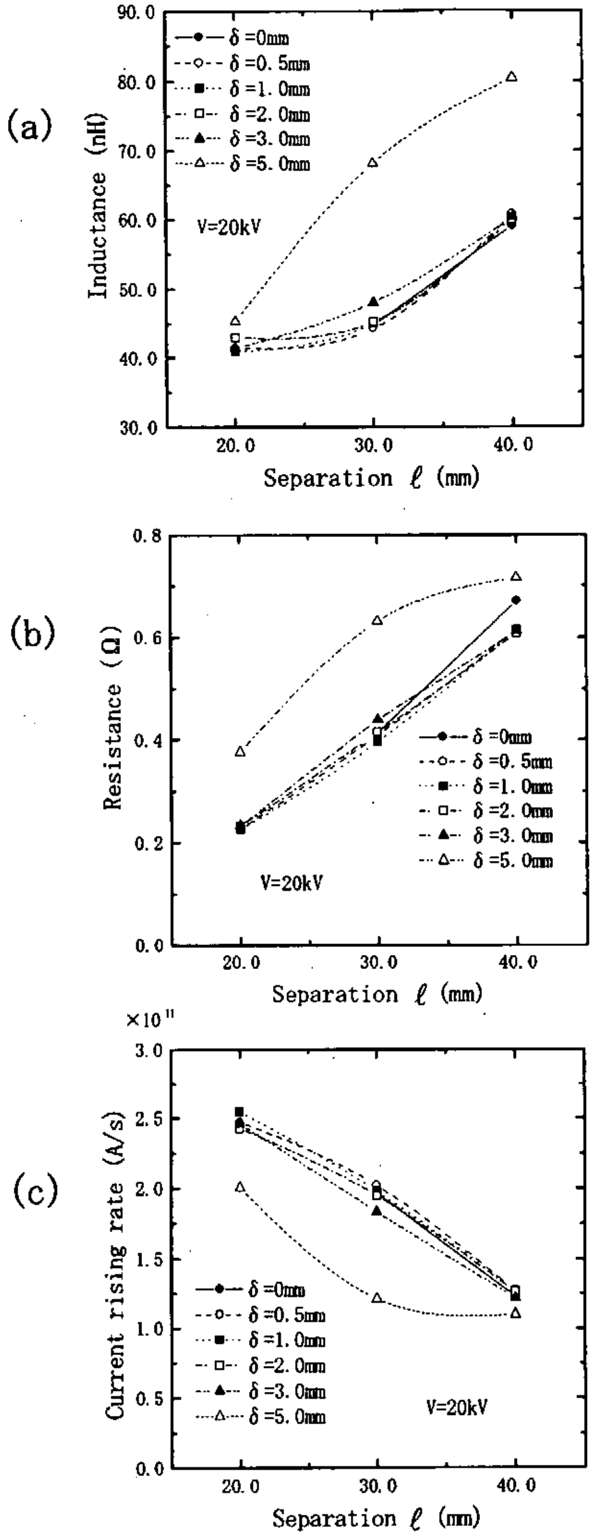

Fig. 6 The switch parameters in the floating electrodes : (a) the Inductance, (b) the resistance and (c) the current rising rate versus the electrode separation ℓ.

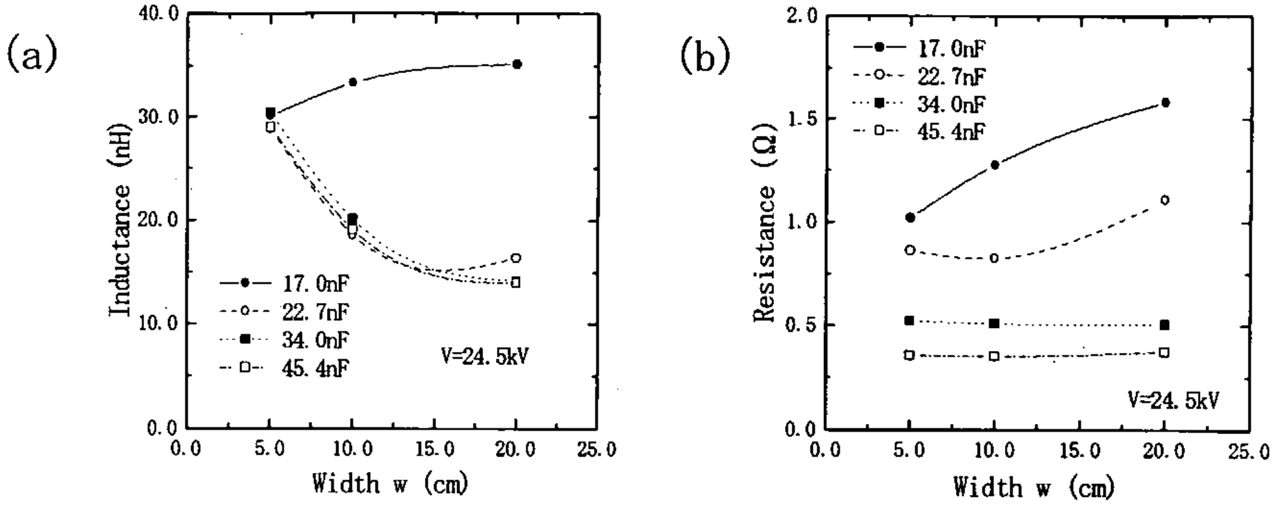

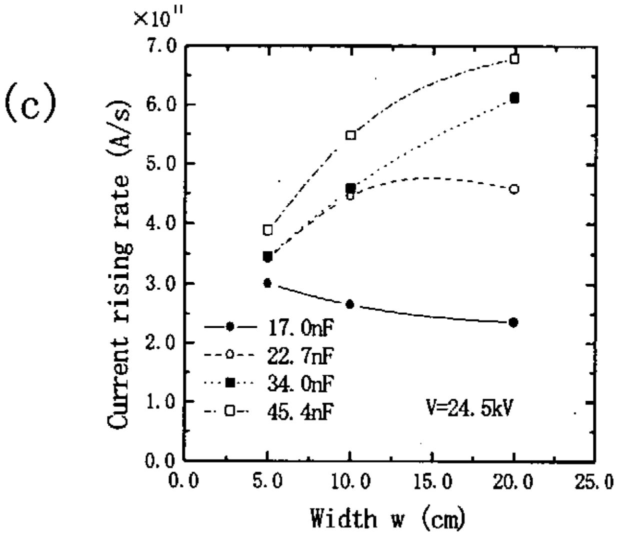

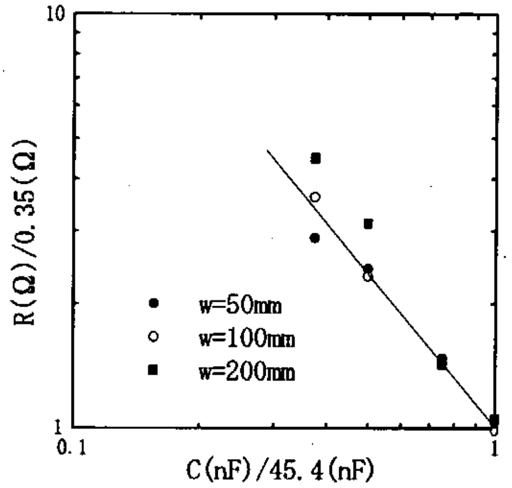

Fig. 7 Effect of the electrode width :
(a) the Inductance, (b) the Resistance
and (c) the Current rising rate.

Fig. 8 The normalized resistance versus the normalized capacitance. The normalization was carried out by the result for C=45.4nF and w=50mm.

Table 1 Comparison between three types of switches : triggering by (a) the multiple pins, (b) the field distortion , and (c) the corona discharge and field distortion.

	Inductance(nH)	Resistance(Ω)	Current rising rate(A/s)
(a)	95.0	0.94	9.85×10^{10}
(b)	61.9	0.64	1.49×10^{11}
(c)	45.1	0.58	2.48×10^{11}

Transformer-type pulse high voltage generator

J.Irisawa, S.Takano and K.Terao

Department of Electrical Engineering, Ngaaoka University of Technology,

Nagaoka, Niigata 940−21, Japan

A triple−resonance pulse transformer circuit is compared experimentally to the well−known double−resonance one. The primary circuits of each are fixed and a turn ratio of the transformer is varied from 1:10 to 1:50 by every 10 turns. The triple−resonance mode shows high voltage multiplication and high efficiency of energy transfer compared to the double resonance mode, particularly at a high turn ratio of the transformer.

1. Introduction

In pulse−power technology, a transformer−type accelerator is a good candidate for a high−voltage pulse generator suitable for repetitive operations. The well−known double resonance circuit is widely designed to operate as a transformer−type accelerator 1)~4). The maximum voltage gain of the transformer under the double resonance condition is $\sqrt{L_2/L_1}$ where L_1 and L_2 are a primary and a secondary inductance of the transformer. Reed 5) proposed the greater voltage gain for Tesla−transformer accelerator which predicted an 18% increase in voltage gain. Bieniosek 6) proposed the triple resonance pulse transformer circuit which takes into account the internal capacitance of the transformer. This paper describes an experimental study on the double and triple resonance circuit with the same primary circuit parameters at five different turn ratio of the transformer. Mainly, the voltage mutiplication and the energy transfer efficiency of the double and triple resonance are discussed.

2. Basic principle

A double resonance circuit with an internal capacitance C_{2F} of the tranceformer and with an external tuning inductance L_{2F} is shown in Fig.1. The energy transfer of 100% is completed from C_1 to C_2 when the circuit, assuming C_{2F} of Fig.1 is zero, meets the resonant conditions of $L_1 \cdot C_1 = (L_2 + L_{2F}) \cdot C_2$ and the coupling coefficient of the transformer K=0.6. Internal capacitance of transformer lowers the efficiency of energy transfer. When C_{2F} is comparable to C_2, the efficiency decrease to less than 50%.

Fig.2 shows a triple resonance circuit which introduces an external capacitance C_2 and an external turning inductance L_3 attractively into the circuit. The energy transfer of 100% is completed from C_1 to C_3 when the circuit meets the resonant conditions of $L_1 \cdot C_1 : L_2 \cdot C_2 : L_3 \cdot C_3 = 1 : 0.97 : 0.54$, $L_2 : L_3 = 5 : 6$ and the couplig coefficient of the transformer K=0.674.

3. Experimental apparatus

The detail of experimental apparatus is shown elsewhere[4]. The switching element of the primary circuit is a reverse-conducting thyristor of Mitsubishi FT100AX(1200V, 7000A). The transformer is an air-core design with a 0.2m diameter 10 to 50-turn enamel wire secondary winding surrounding a one-tune spiral-wound primary. A primary inductance L_1 of 1.05 μH and an energy storage capacitor C_1 of 0.985 μF are fixed through the experiments. The coupling coefficient K of the transformer is tuned by sliding the secondary winding relative to the primary for K to meet the resonance conditions as close as possible.

4. Circuit operation

Fig.3 shows the measured parameters of double and triple resonance circuit at a transformer turn ratio of 1:30 under the vest fit resonance conditions obtained experimentally. L_1, L_2 and C_1 are common in both double and triple resonance circuits for compairing the characteristics of the double resonance circuit with the triple resonance circuit.

The typical waveforms are shown in Fig.4 for double resonance operations and in Fig. 5 for triple resonance operations, respectively. V_1, V_2 and V_3 are the charging voltage at C_1, C_2 and C_3. A computer simulation of the circuit is performed by taking into account a resistance and a stray capacitance. Compairing the waveforms of experimental to that of simulation in both the double and the triple mode, a good quality of the waveforms has been obtained in the case of the triple mode. This comes from experimentally an easy adjustment of the resonance conditions in the triple mode compared to the double mode.

Table 1 and table 2 are parametes of double resonance circuit and triple resonance circuit at an each turn ratio, respectively. Here T is $L_2 \cdot C_2/L_1 \cdot C_1$. T_1 and T_2 are $L_2 \cdot C_2/L_1 \cdot C_1$ and $L_3 \cdot C_3/L_1 \cdot C_1$, respectively.

5. Voltage multiplication and efficiency of energy transfer

The voltage multiplication vs. the number of secondary winding under the condition of both double and triple resonance mode is shown in Fig.6. The voltage multiplication is defined as a ratio of the maximum output voltage at C_2 or C_3 to the initial charging voltage at C_1. In the case of the triple mode, the theoretical curve fits with the measured points (▲). In the case of the double mode, the measured points(·) stay below the theoretical curve and the differences are large at a high turn ratio. At the fixed turn ratio, the voltage multiplication is high in the triple resonance case compared to the double resonance case.

The efficiency of energy transfer vs. the number of secondary winding is shown in Fig.7. The efficiency of energy trasnfer is defined as a ratio of the maximum stored energy at C_2 or C_3 to the initial stored energy at C_1. The ratio of the stray capacitance C_{2F} to C_2 is also indicated in this figure. As the number of secondary winding increases, the energy transfer efficiency of both double and triple resonance circuit decreases monotonously. This comes from the monotonic increase of C_{2F}/C_2. The energy transfer efficiency of the triple resonance circuit is recognized upper the efficiency curve of the double resonance. The differencies become apparent as a turn ratio increases.

6. Conclusion

The double and the triple resonance circuits have been operated with the same parameters of a primary circuit at five different turn ratio of transformer. A reverse-conducting thyristor has been used as a switching element in a primary circuit.

Tuning the circuit parameters to meet the resonance conditions, the triple resonance circuit is preferable to the double resonance circuit.

The triple resonance circuit operates with good voltage multiplication compared to the double one at the same turn ratio of the transformer.

The energy transfer efficiency of the double and triple resonance circuit decreases monotonously as the turn ratio increases. But the triple resonance circuit is preferable to the double resonance circuit in the sense of energy transfer efficiency, particularly at a high turn ratio of the transformer.

References

1. D.Finkelstein et al., Rev. Sci. Instrum. 37, 159(1966)
2. I.Boscolo et al., Rev. Sci. Instrum. 45, 1535(1975)
3. M.T.Buttram et al., IEEE Trans. Electron Device ED-26, 1503(1979)
4. J.Irisawa et al., Laser and Particle Beams 11, 431(1993)
5. J.L.Reed, Rev. Sci. Instrum. 59, 2300(1988)
6. F.M.Bieniosek, Rev. Sci. Instrum. 61, 1717(1990)

Table 1. Parameters of double resonance circuit.

turn ratio	1 : 10	1 : 20	1 : 30	1 : 40	1 : 50
L1(μH)	1.050				→
L2 (mH)	0.110	0.330	0.610	0.980	1.370
C1(μF)	0.985				→
C2 (nF)	8.750	2.700	1.350	0.800	0.580
C2F(nF)	0.420	0.380	0.350	0.240	0.170
R1 (Ω)	0.250				→
R2 (Ω)	0.260	0.380	0.450	0.520	0.590
K	0.580	0.600	0.580	0.580	0.570
T	0.975	0.982	1.003	0.985	0.993
C2F／C2	0.048	0.141	0.259	0.300	0.293

Table 2. Parameters of triple resonance circuit.

turn ratio	1 : 10	1 : 20	1 : 30	1 : 40	1 : 50
L1(μH)	1.050				→
L2 (mH)	0.110	0.330	0.610	0.980	1.370
L3 (mH)	0.132	0.390	0.720	1.120	1.670
C1(μF)	0.985				→
C2 (nF)	8.750	2.700	1.350	0.800	0.580
C2F(nF)	0.420	0.380	0.350	0.240	0.170
C3 (nF)	4.300	1.450	0.810	0.490	0.330
R1 (Ω)	0.250				→
R2 (Ω)	0.260	0.380	0.450	0.520	0.590
R3 (Ω)	0.250	0.330	0.420	0.510	0.590
K	0.680	0.680	0.650	0.640	0.660
T1	0.975	0.982	1.003	0.985	0.993
T2	0.549	0.547	0.564	0.531	0.533
L2／L3	0.833	0.846	0.847	0.875	0.820
C2F／C2	0.048	0.141	0.259	0.300	0.293

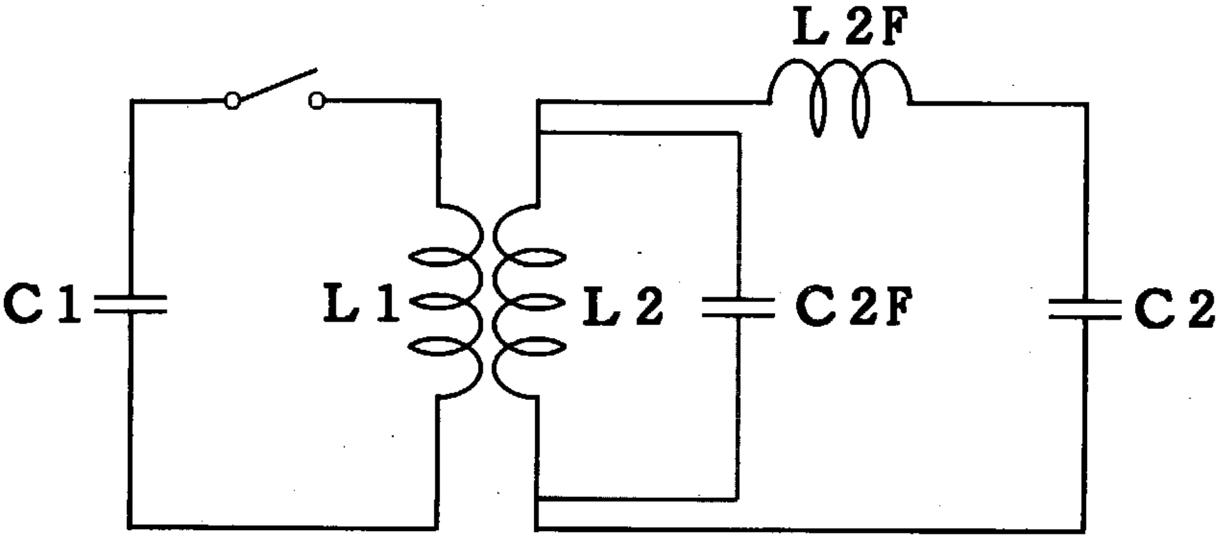

Fig. 1. Double resonance circuit.

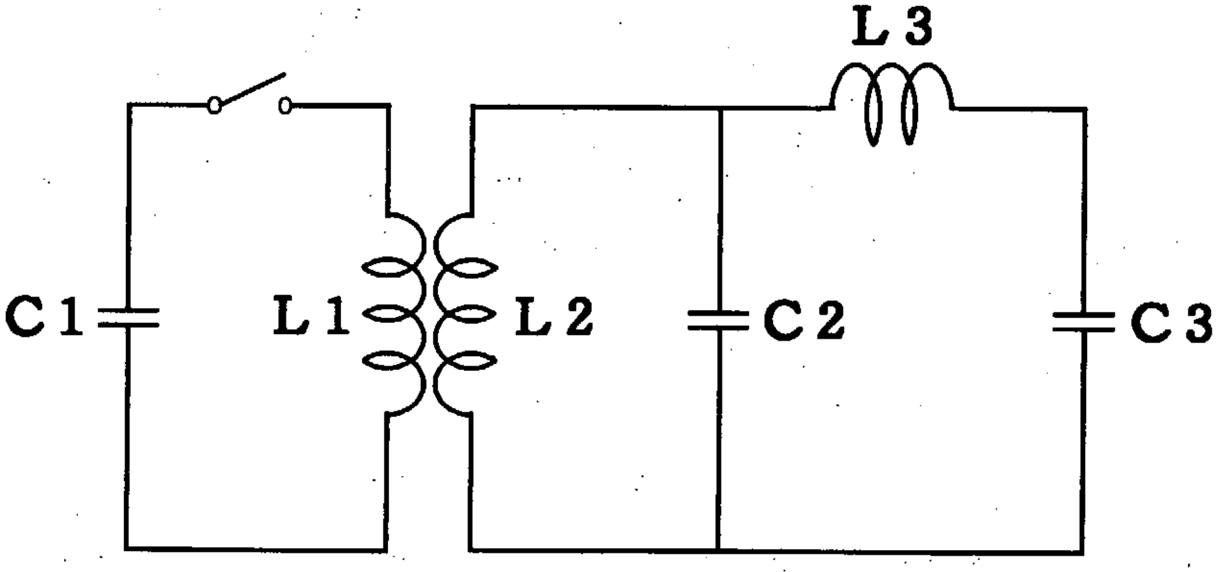

Fig. 2. Triple resonance circuit.

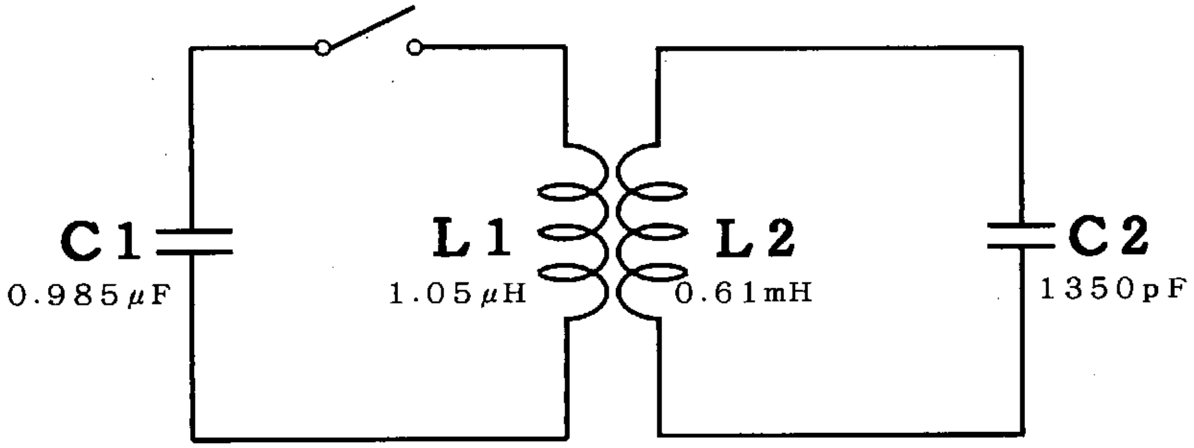

a) double resonance.

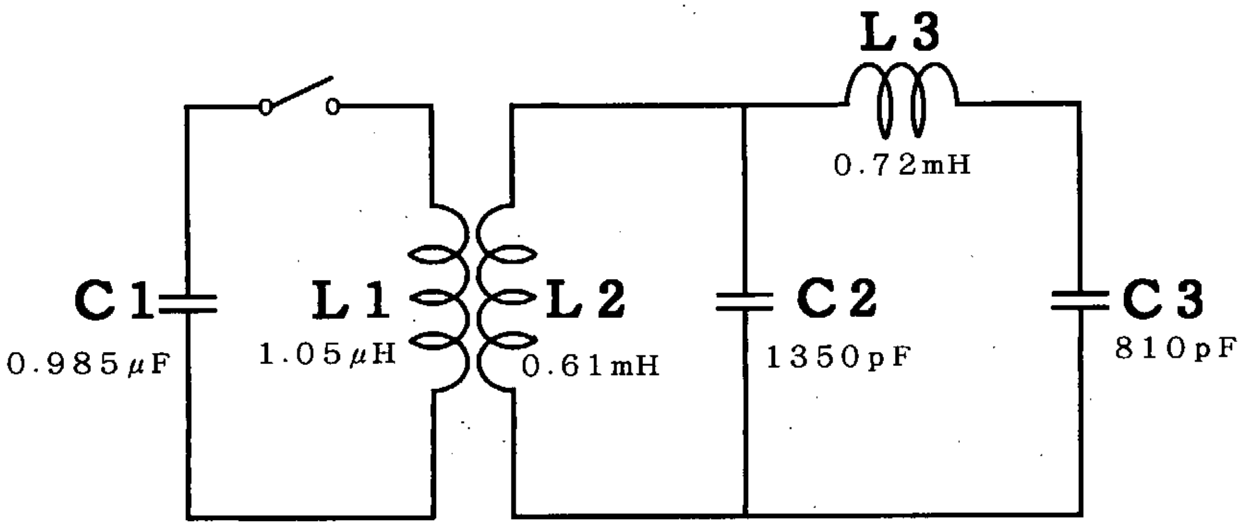

b) triple resonance.

Fig.3. Measured parameters of circuit with turn ratio 1:30.

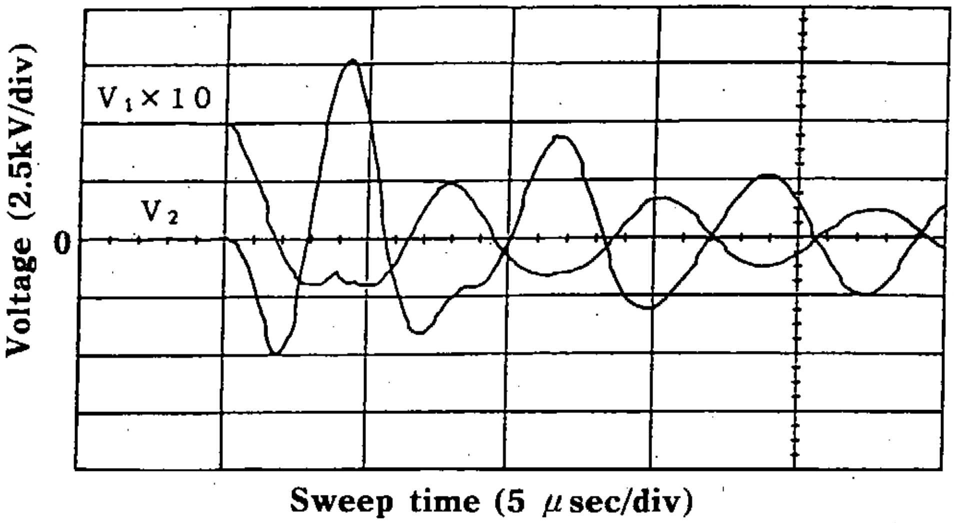

a) experiment

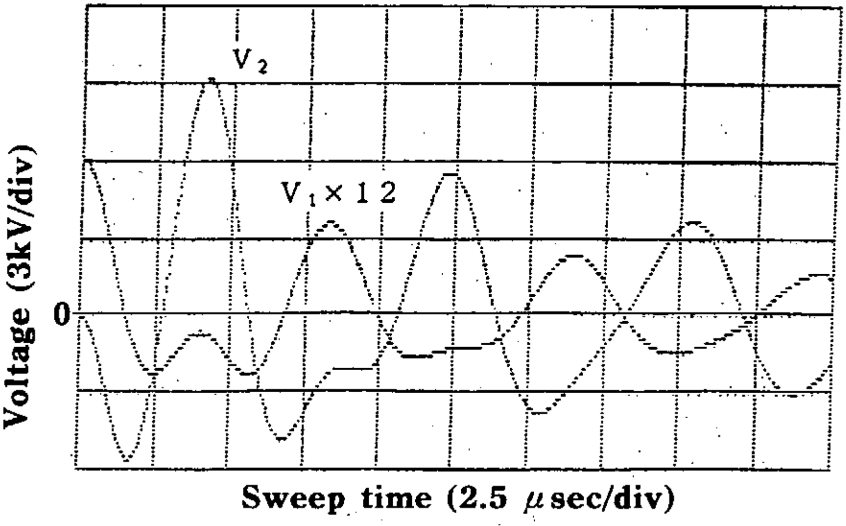

b) simulation

Fig.4.Typical waveforms for double−resonance operations.

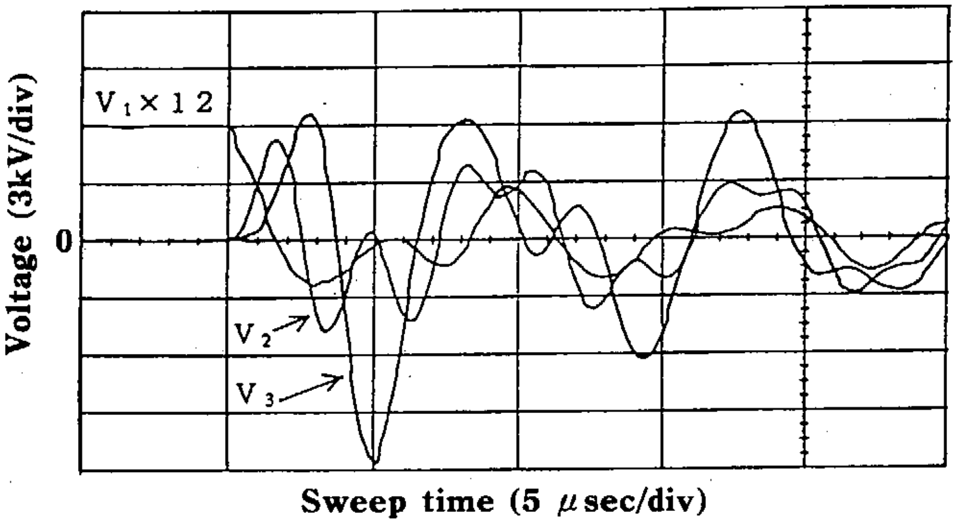

a) experiment

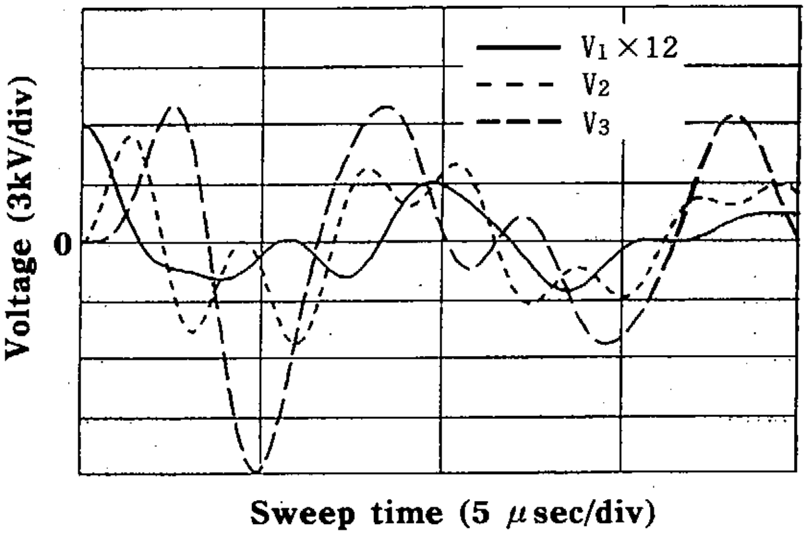

b) simulation

Fig.5.Typical waveforms for triple–resonance operations.

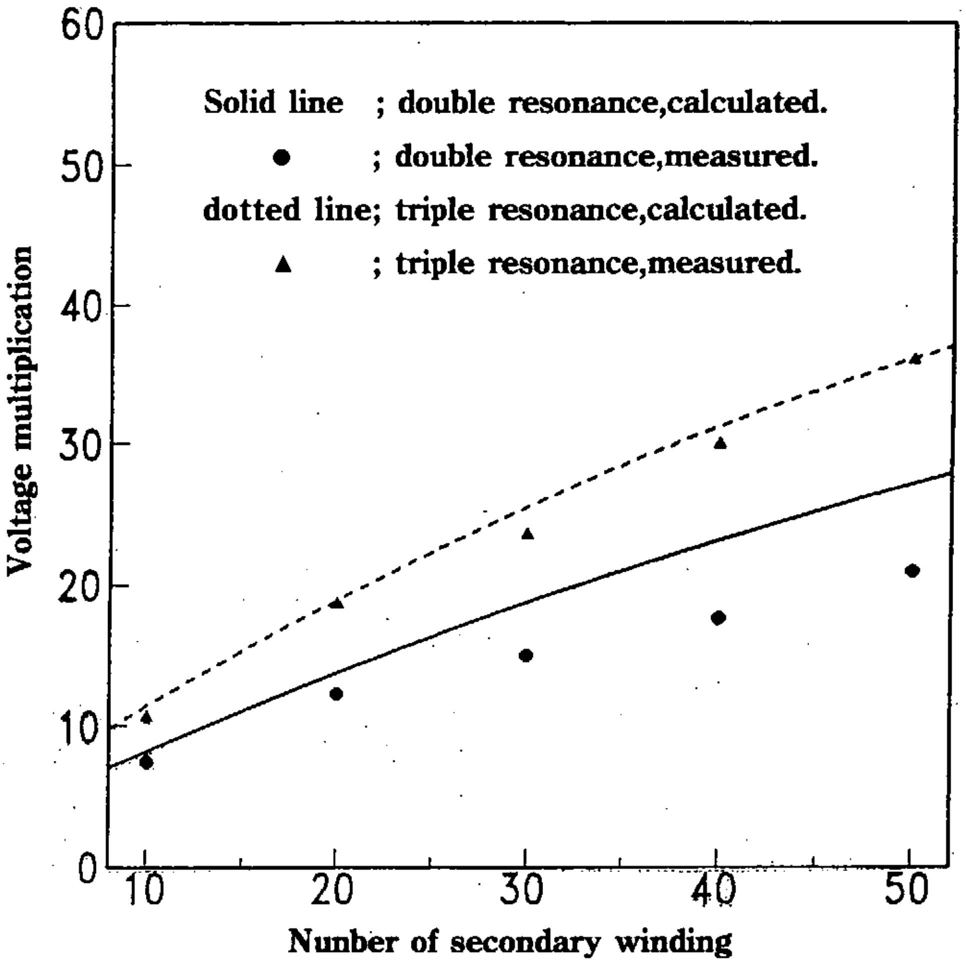

Fig.6. Voltage multiplication vs. turn ratio.

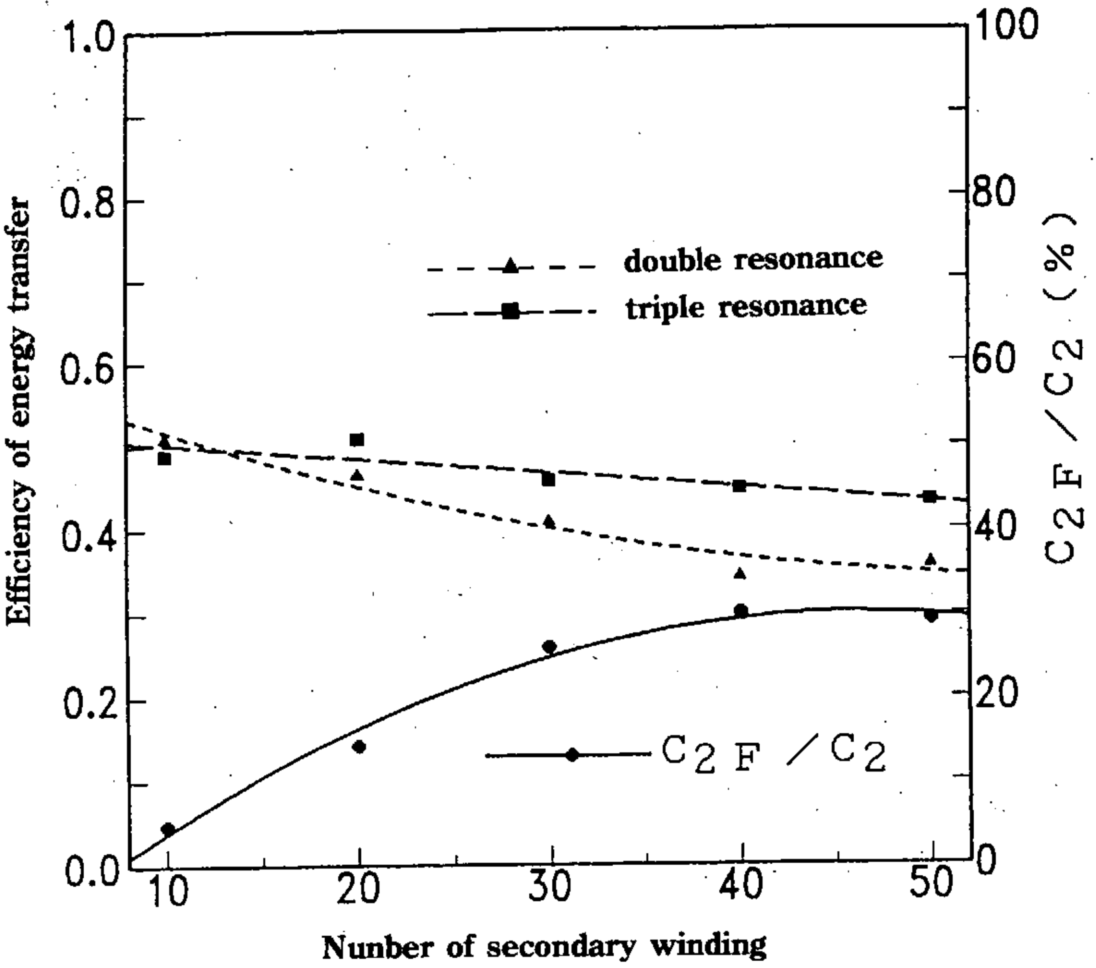

Fig.7. Efficiency of energy transfer vs. turn ratio.

Development of Inductive Energy Storage Pulsed Power Generator with Output of MV Class

K. Hasegawa, H. Akiyama, S. Katsuki, S. Maeda,
F. Kinoshita*, and H. Kuribayashi*

Department of Electrical Engineering and Computer Science,
Kumamoto University, Kumamoto 860, Japan
**Kyusyu Electric Power Co.,Inc., Fukuoka 815, Japan*

ABSTRACT

The research to generate the output voltage of MV class has been done by using an inductive energy storage pulsed power generator. An exploding thin copper wire in air is used as an opening switch. The maximum output voltage, which is calculated from the current waveform reached 24 MV.

1. INTRODUCTION

The pulsed power technologies have been studied prosperously in the world [1]-[5]. The pulsed power has many fields of applications, for example, the impulse test, the generation of charged particle beam, the pollution control, the production of the high temperature, high density plasma, and so on.

The pulsed power generator with an inductive energy storage system can be designed lightly, compactly, and cheaply in comparison with a capacitive energy storage system, though the development of the perfect opening switch is necessary [6][7]. We made the inductive energy storage pulsed power generator ASO- I and ASO-II [8][9]. The ASO-II generated the output voltage of 220 kV with the charging voltage of 25 kV. The development of the pulsed power generator with the output of MV class is important. Here, an inductive energy storage pulsed power generator with the output of MV class is studied.

2. EXPERIMENTAL APPARATUS AND METHOD

Fig.1 shows the equivalent circuit of the pulsed power generator. The generator consists of the capacitors as a primary energy source, triggered gap switches, the energy storage coil, and the opening switch. The primary energy source is the Marx bank which consisting of 10 stages, each of which contains two capacitors of 0.5 μ F connected in a series. The total capacitance, the maximum voltage, and the maximum stored energy are 0.025 μ F, 1 MV and 12.5 kJ, respectively. Three kinds of energy storage coils with 1.27 mH, 0.67 mH, and 2.3 mH are used. The opening switch is the thin copper wire with 0.03 mm in diameter. The fuse is set in air. The charging voltages of the capacitor, that is, the output voltage of the marx bank, are 80 kV, 240 kV, and 400 kV. The fuse length is changed from 20 to 400 cm.

The discharge current of the capacitor is measured by Rogowski coil. The output voltage Vout is calculated by the following equation,

$$\mathrm{Vout} = L\,(dI/dt) \qquad (1).$$

Here, L is a total inductance of the Marx bank and the energy storage coil. The value of L are 1.5 mH, 0.78 mH, and 3.3 mH.

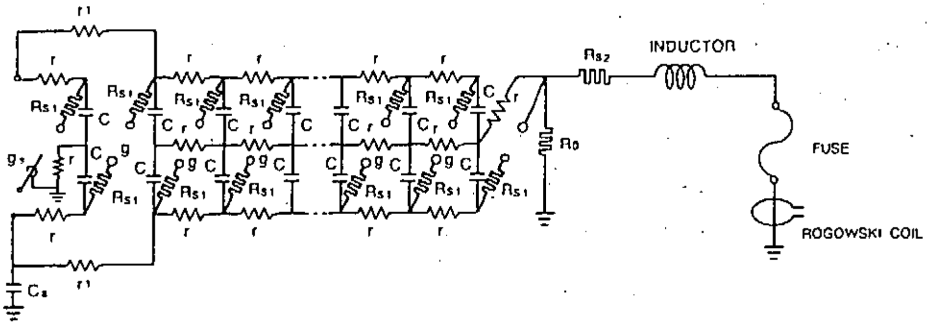

$R_{s1}=10\,\Omega\ (\times 20)$ $C=0.5\,\mu F$

$R_{s2}=120\,\Omega$ $C_{all}=0.025\,\mu F$

Fig.1. The equivalent circuit of the pulsed power generator.

3. EXPERIMENTAL RESULTS AND DISCUSSIONS

Fig.2 (a) shows the typical waveform of the current flowing through the energy storage coil. The charging voltage of the capacitor is 240 kV. The inductance of the energy storage coil is 1.5 mH. The number, diameter, and length of the fuse are 1, 0.03 mm, 60 cm, respectively. The current is interrupted at about 2.5 μ sec, and then the restrike occurs. Fig.2 (b) shows the waveform of the output voltage calculated from the Fig.2 (a) using eq. (1). The maximum output voltage of 12.4 MV is achieved.

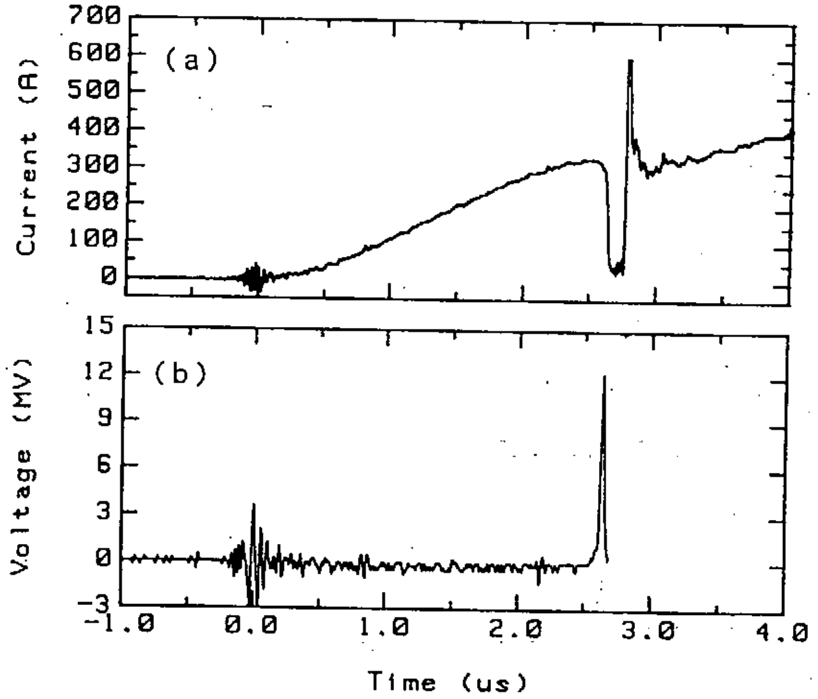

Fig.2. Typical waveforms of the current flowing through the energy storage coil (a), and the calculated output voltage (b).

Fig.3 shows the current waveforms by changing the fuse length. The fuse lengths are 20 cm, 50 cm, 100 cm, 150 cm, 200 cm, 250 cm, 300 cm, 350 cm, and 400 cm in Figs.3 (a)~(i), respectively. The charging voltage of the capacitor is 240 kV, and the inductance of the energy storage coil is 1.5 mH. The restrike occurs before the current becomes zero in the case of short fuse. These phenomena are caused by the breakdown of the vaporized copper wire, and the breakdown voltage is in direct propotion to the fuse length. The current interruption occurs slowly in the case of long fuse.

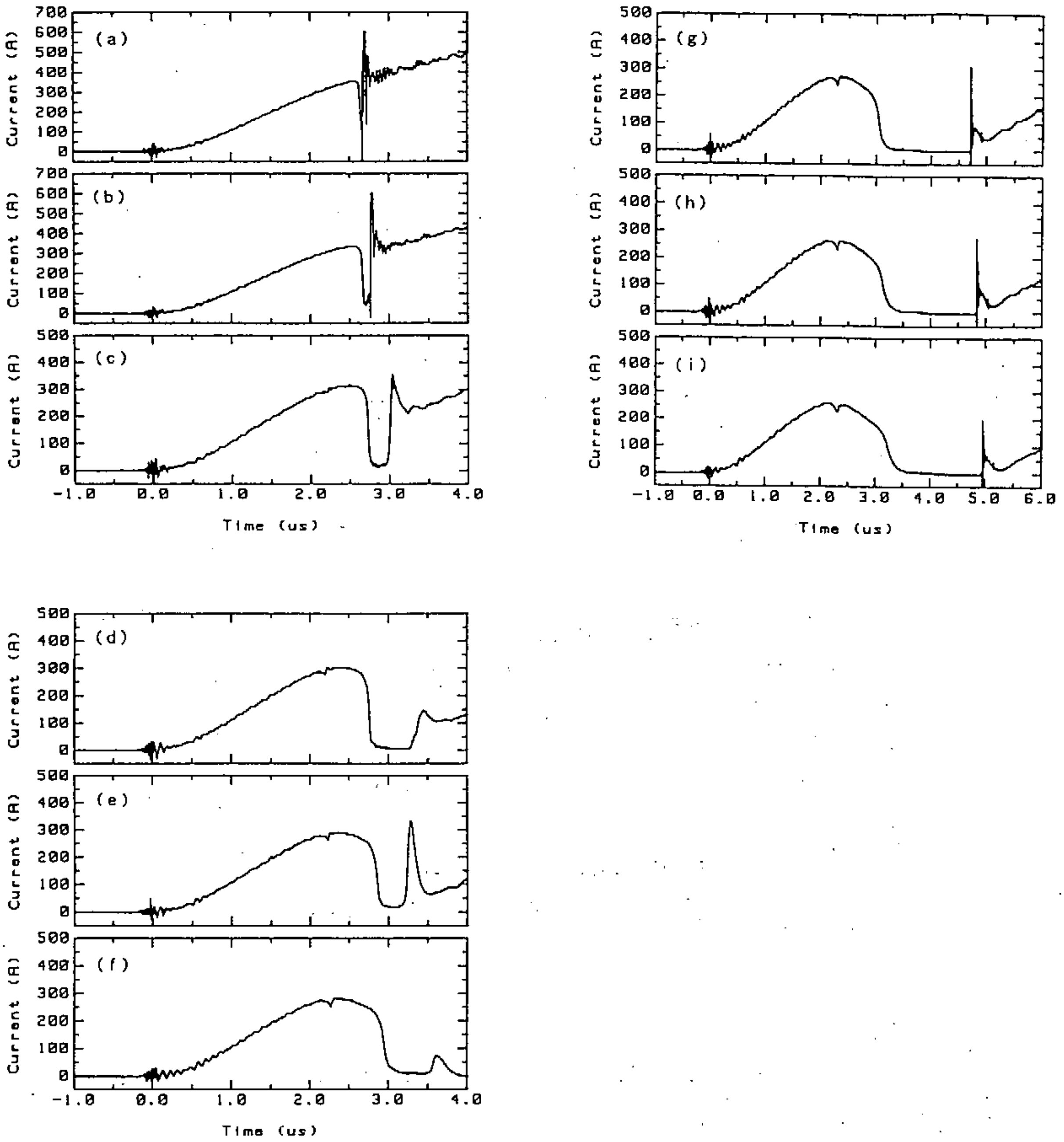

Figs.3. The current waveforms for different fuse lengths.

Fig.4 shows the current waveforms for different charging voltages of the capacitor, 80 kV, 240 kV, and 400 kV. The inductance of the energy storage coil is 1.5 mH, and the fuse length is 60 cm. In the case of small charging voltage of the capacitor, the value of the current is small, and the opening time of the fuse is long. The supplied energy into the fuse is not enough in this case.

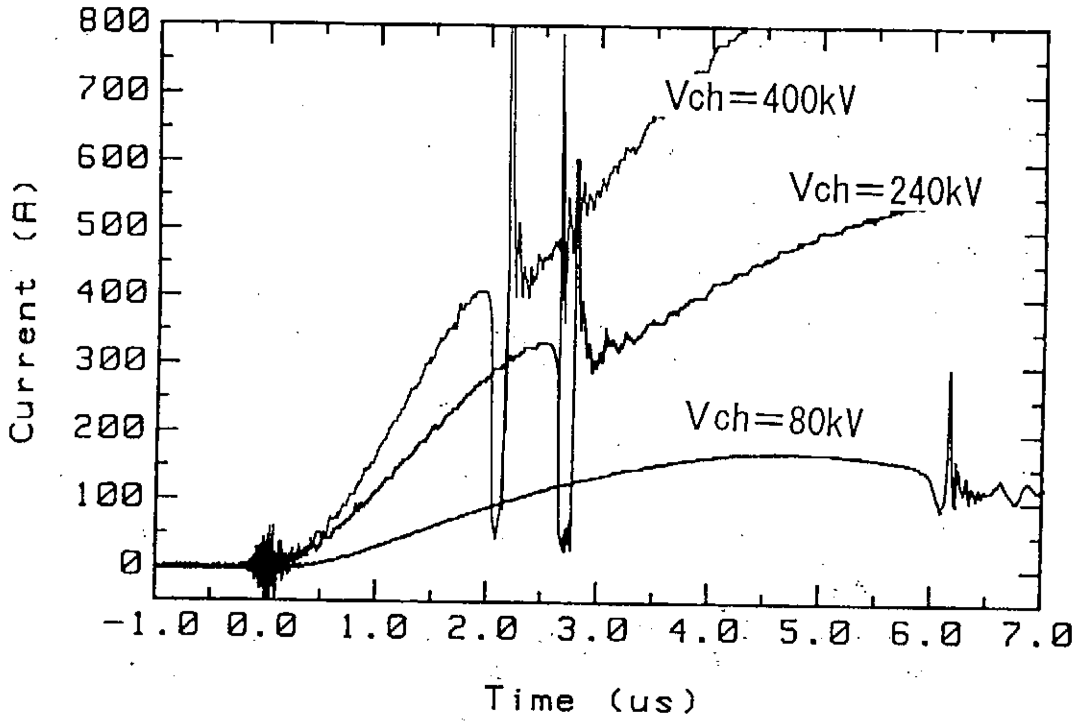

Fig.4. The current waveforms for different charging voltages of the capacitor.

Fig.5 shows the relation between the output voltage and the fuse length. The inductance of the energy storage coil is 1.5 mH. The charging voltage of the capacitor is 80 kV, 240 kV, and 400 kV. The more we supply the energy into the fuse, the more the peak of the output voltage become large.

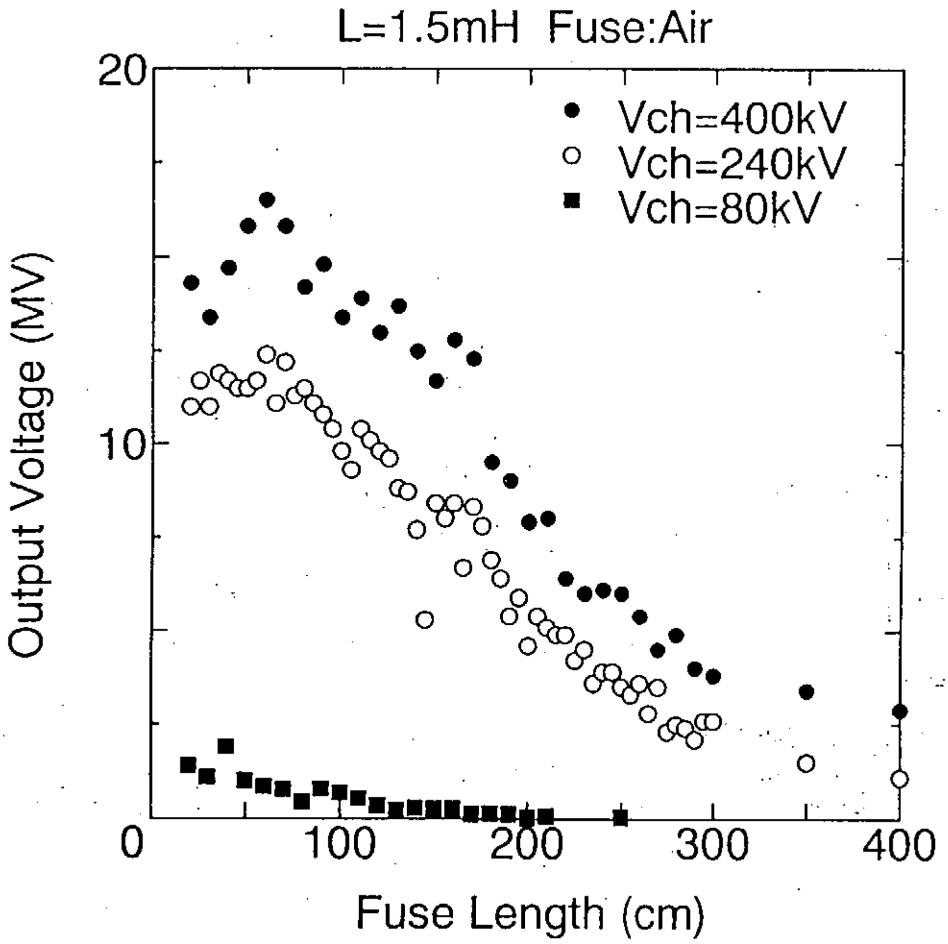

Fig.5. Dependence of the output voltage on the fuse length for different charging voltages.

4. CONCLUSIONS

We have studied whether the inductive energy storage pulsed power generator is able to generate the output voltage of MV class. The maximum output voltage, which is calculated from the current waveform, reached 24 MV.

5. REFERENCES

[1] T. Vijayan and V. K. Rohatgi, " Characteristics of Exploding-Wire Plasmas ", IEEE Trans. Plasma Sci., PS-13, 4 (1985).

[2] I. M. Vitkovitsky and V. E. Scherrer, " Recovery characteristic of exploding wire fuses in air and vacuum ", J. Appl. Phys. 52, 4 (1981).

[3] J. Salge, U. Braunsberger, and U. Schwarz, " CIRCUIT BREAKING BY EXPLODING WIRES IN MAGNETIC ENERGY STORAGE SYSTEMS ", energy storage, compression, and switching Vol.1, PLENUM PUBLISHING CORPORATION

[4] V. P. Kovalev, A. I. Kormilitsyn, A. V. Lunchinskii, V. I. Martynov, and I. A.Pekhterev, " IGUR-1 -an electron accelerator using an inductive energy storage and exploding wires ", Sov. Phys. Tech. Phys. 26, 9 (1981).

[5] J. M. Wilson, " PBFA- II ENERGY STORAGE SYSTEM PERFORMANCE AND ORERATION ", 6th IEEE PULSED POWER CONFERENCE, (1987).

[6] A. Guenther, M. Kristiansen, and T. Martin, " OPENING SWITCHES ", ADVANCES IN PULSED POWER TECHNOLOGY Vol.1, PLENUM PUBLISHING CORPORATION, (1987).

[7] L. Veron, B. Etlicher, A. S. Chuvatin, C. Rouille, and J. Stephan, " Experimental Investigation on a Long-Conduction Time-Plasma Opening Switch and its Application on a 0.1 TW Generator for Prepulse Suppression ", IEEE Trans. Plasma Sci., Vol. 21, 5 (1993).

[8] N. Shimomura, H. Akiyama, S. Maeda, " Compact Pulsed Power Generator by an Inductive Energy Storage System With Two-Staged Opening Switches ", IEEE Trans.Plasma Sci., Vol.19, 6 (1991).

[9] C. Grabowski, H. Akiyama, T. Seki, S. Katsuki, S. Maeda, " The Behavior of Parallel Wire Fuses as Opening Switches ", Memoirs of the Faculty of Engineering, Kumamoto University, Vol. 37, 3 (1992).

Characteristics of High Current Pulsed Arc Discharge

K. Masugata, M. Yoshida, T. Suzuki, and K. Yatsui
Nagaoka University of Technology,
Nagaoka, Niigata 940-21 Japan

abstract

Characteristics of high current pulsed arc discharge has been investigated to develop a high efficiency, highly repetitive pulse power switch. The energy transfer efficiency and the recovery of breakdown voltage has been evaluated by using charge transfer circuit. The energy transfer efficiency is found to be much higher when using hydrogen as a operation gas than that when using SF_6. The recovery time to obtain a 50 % of initial breakdown voltage are evaluated to be 0.5 ms, 2 ms, and 3 ms for H_2, SF_6 and air, respectively. From the measurement, energy transfer efficiency and repetition rate of the switch is found to be extremely improved by using H_2. To understand the mechanism of arc discharge, dynamic behavior has been observed. The arc radius is observed to increase with a supersonic velocity. The volume of hot gas remaining after the discharge is fund to be much smaller for H_2, as compared with that for SF_6. From time resolved measurement of arc resistance, the duration of high resistance phase is $\approx$ 100 ns for H_2 and is much shorter than that for SF_6.

1. Introduction

Pulse power technology has a wide area of applications such as the generation of high power particle beams, X-ray, or gas laser excitation [1,2]. For these applications, it is very important to develop a highly repetitive system to obtain a higher average power. Conventionally, a large number of discharge gap switches have been utilized in a pulse power system. SF_6 or air has usually been used as a operation gas [1,2]. However, since such a switches take a long time for the recovery of breakdown voltage, it is difficult to obtain a highly repetitive operation in such a system[3]. Recently, magnetic switches has been utilized with thyristor or thyratron to obtain a highly repetitive operation. In those system, single switch of thyristor or thyratron is utilized with a multi-stage magnetic pulse compressor. More than 5 kHz of repetition rate has been obtained in those systems [4]. However, due to the limitation of switching current in thyrisotor or thyratron, those combination seems to be applicable only for a small system.

Since the upper limit of switching current for the discharge gap switch is extremely high, the combination of high speed recovery gap switch with magnetic pulse compressor seems to be a good choice to develop a high-power, high-repetition system. Pressurized hydrogen gap switch seems to be a hopeful candidate for those system [5]. In this paper the characteristics of hydrogen gap switch is described in comparison with those with other gas.

2. Electrical Characteristics of Hydrogen Gap Switch

Electrical characteristics of pressurized gas gap switch has been investigated The gap switch used in the experiment is the field distortion type and it consists of a pair of main electrodes and a mid plate for trigger pulse injection. The main electrodes are made of copper-tungsten alloy and have a hemispherical shape with radius of curvature = 8 mm. The gap length between the main electrodes and a mid plate are 4 mm, namely total gap length (*d*) = 8 mm. In the experiment, middle voltage of the main electrodes is applied to the mid plate.

2.1 Self-Breakdown Voltage

Figure 1 shows the dependence of breakdown voltage (V_{BS}) of the gap on the filling pressure of gas. H_2, SF_6, and N_2 have been utilized as filling gas. As seen in the figure, V_{BS} almost linearly increases with increasing filling pressure. The values of V_{BS} for H_2 gas is found to be about half or 1/6 of that for N_2 or SF_6, respectively. For H_2, minimum switching voltage when trigger pulse of 50 kV is applied to the mid plate is also shown in the figure. From the data we see that operation range of charging voltage for the gap switch is from 50 kV to 100 kV when it is filled by 10 atm of H_2.

2.2 Recovery of Breakdown Voltage

Figure 2 shows the experimental circuit to evaluate the recovery characteristics of breakdown voltage. Two switches (SW_1, SW_2) with same dimension and characteristics has been utilized in the experiment. The gap switches are filled to the pressure corresponding to $V_{BS} = 50$ kV, that is ≈ 5 atm for H_2, ≈ 2 atm for N_2 and ≈ 1 atm for SF_6. The charging voltage of two capacitors (C_1 and C_2) connected to each switches are charged up to 35 kV (70 % of V_{BS}) in advance to the shot. The operation of the circuit is as follows: At first, SW_1 is triggered and C_1 is discharged. After the interval of T_d, SW_2 is triggered and observes the output voltage. The voltage of recovery (V_{RE}) is defined as the breakdown voltage of SW_1 at T_d after the breakdown. The value of V_{RE} is evaluated from the peak of output voltage when $V_{ch} \geq V_{RE} \geq \sqrt{2}V_{ch}$ and from the shoulder in the rising phase of output voltage when $V_{RE} \leq \sqrt{2}V_{ch}$.

Figure 3 shows the recovery characteristics of gap for each kinds of gas. From the figure we see that V_{RE} increases with increasing T_d. Time of 50 % recovery (τ_{R50}) where V_{RE} recover up to 50 % of V_{BS} is evaluated to be ≈ 0.5 ms, ≈ 2 ms, and ≈ 3 ms for H_2, SF_6 and N_2, respectively. From the experiment, we see that high repetition rate operation of more than 1 kHz is possible by using hydrogen gap switch.

2.3 Energy Transfer Efficiency

Energy transfer efficiency (η) has been evaluated in the captive energy transfer circuit. Figure 4 shows the circuit used for the evaluation. In the experiment, total gap length (*d*) of the switch is reduced up to 4 mm to reduce V_{BS} to operate the switch in a self-breakdown mode (operate without triggering). Here, η is defined as

$$\eta = \frac{(1/2) \cdot C_0 \cdot V_{ch}^2}{(1/2) \cdot C_1 \cdot V_{C_1 \max}^2}, \tag{1}$$

where and V_{C1max} are the charging voltage of C_0 and the peak value of the charging waveform of C_1 (V_{C1}), respectively. In the experiment, V_{C1} is evaluated by integrating the current (*i*) measured by a Rogowski coil. The parameter of the circuit elements are as follows:

$C_0 = C_1 = 100$ nF, $L_0 \approx 400$ nH, R_0 (wire resistance) $\approx 0.01\Omega$.

In the experiment, voltage of power supply is slowly increased until the switch is self-broken. Consequently, charging voltage (V_{ch}) is the function of filling pressure.

Figure 5 shows the energy transfer efficiency for each kinds of gas ported against V_{ch}. For SF_6, η decreases with increasing charging voltage and the efficiency at V_{ch} = 40 kV is low value of ≈ 70 %. In contrast to the case, for H_2 and N_2 , the efficiency increases with increasing charging voltage. The efficiency for H_2 and N_2 at $V_{ch} \approx 40$ kV are observed to be ≈ 90 % and ≈ 85 % respectively. From the experiment we see that η has a strong dependence on the operation gas. For H_2, the energy loss is very low as compared to those for SF_6 or N_2, which are conventionally utilized in the gap switch.

3. Dynamics of High Current Arc Discharge

The process of high current arc discharge is considered to be as follows:

1. After the application of electric field, thin plasma channel is initiated by a streamer discharge (initiation phase).
2. Once the channel is produced, current begin to flow and heat the channel. The heating reduces the resistance of the channel, which help the rise of current. Rapid increase of current enhance the heat up of the channel. Since the initial gas density of the channel is high, heat up of the channel produces a high pressure in the order of hundred atm. Due to the high internal pressure, arc plasma rapidly expand and produce a strong shock wave (high resistance phase).
3. In several hundred ns after the start of discharge, the temperature of plasma reaches a stable value and arc resistance decreases. (low resistance phase)
4. Plasma expansion continues for typically in the order of ten µs even after the termination of arc current since plasma pressure is still higher than the environment. Expansion process after the termination of current is considered to be adiabatic.
5. After reaching to the pressure equilibrium, arc plasma (hot gas) slowly cooled down and recover the breakdown voltage. (recovery phase)

However, the detail of the process is not yet understood. To clarify the process, we have observed time-resolvedly the arc discharge. In the experiment C-R discharge circuit is utilized as shown in Fig. 6 to damp the ringing current. To observe the full length of arc, a simple gap (without a mid plate electrode) of gap length = 5 mm is utilized in the experiment. The discharge is done under the self-breakdown mode. Filling pressures of the gap are changed for each gas to fix the discharge voltage.

4.1 Observation of Arc Plasma

Figure 7 shows the photographs of arc discharge in H_2 and SF_6 taken by a image converter camera. As seen in the figure, in both case, arc plasma rapidly expand and the radius of arc plasma exceed 1 mm in 400 ns. Comparing two cases, brightness of the arc is high and uniform in SF_6, whereas brightness in the center part of the arc is lower in H_2. Moreover, distortion in the arc column is seen in the case of H_2, which seems to be due to the hydrodynamic instability.

Figure 8 shows the arc radius evaluated from Fig. 7 plotted with discharge current waveform. As seen in the figures, expansion velocity tend to decrease with increasing t. In spite of the difference of mass density of the environment (0.34 Kg/m^3 for H_2 and

3.9 Kg/m^3 for SF_6) difference of the radius is not so large. The arc radius, expansion velocity, and mach number (M) evaluated from the figures are summarized in Table I.

Table I Dimension of arc plasma.

		$t \approx 200$ ns		$t \approx 600$ ns	
Gas	Pressure (atm)	Arc radius (mm)	Expansion velocity (m/s)	Arc radius (mm)	Expansion velocity (m/s)
H_2	0.6	4.2	2000 (M=1.6)	6.4	1000 (M=0.8)
N_2	1.8	3.6	1700 (M=5.1)	5.5	800 (M=2.4)
SF_6	3.8	3.4	1500 (M=10.1)	5.6	1300 (M=8.7)

4.2 Observation of Hot Gas Remaining after the Discharge

After the discharge of gap, hot gas heated by the discharge remains in the gap. Since that the density of gas is inversely proportional to the temperature of gas and that breakdown field is almost proportional to the gas density, existence of hot gas reduce the breakdown voltage. To clarify the mechanism of the recovery of breakdown voltage, we have observed the behavior of hot gas by using a shadowgraph technique. In the experiment, CW argon laser has been utilized as the light source with a image converter camera.

Figure 9 shows the example images of shadowgraph. In the photograph, we find a expanding shock wave and the hot gas column (density perturbation) in the behind of the shock wave. Figure 10 shows the position of shock front with a radius of hot gas. Since the sound velocity is much higher in H_2, the velocity of shock wave in H_2 is much higher than in SF_6. The radius of remaining hot gas are found to be ≈ 12 mm and ≈ 22 mm for H_2 and SF_6 respectively. The small volume of remaining hot gas in H_2 seems to reduce the cooling time and make possible the quick recovery of breakdown voltage.

4.3 Evaluation of Arc Resistance

Figure 11 shows the arc resistance (R_a) and current waveform for H_2 and SF_6 discharge. Here R_a is evaluated by the equation (2)

$$R_a = -\frac{d}{dt}\left(\frac{1}{2}C_0 \cdot V_c^2 + \frac{1}{2}L \cdot i^2\right)\cdot\frac{1}{i} - R_0. \qquad (2)$$

Here, V_c is the voltage of capacitance and R_0 is the resistance of damping resistance. In both case, arc resistance rapidly decreases in the rising phase of arc current (high resistance phase) and reaches to a constant value (low resistance phase). For the case of SF_6, high resistance phase continues for 200 ns, whereas ≈ 100 ns for H_2. The resistance of low resistance phase (resistance at the timing of peak current) is evaluated to be ≈ 0.2 Ω and ≈ 0.3 Ω for H_2 and SF_6, respectively.

The energy loss in the gap ($P_{\rm loss}$) is described as

$$P_{loss} = i^2 \cdot R_{arc}. \qquad (3)$$

By integrating $P_{\rm loss}$ we can obtain a energy loss in a shot. The value obtained is 20 J and 28 J for H_2 and SF_6, respectively. Since the initial energy stored in the capacitor is 109 J, the efficiency is evaluated to be 82 % and 74 % for H_2 and SF_6, respectively.

From the evaluation we see that, by using H_2 as a operation gas, the duration of high resistance phase and the resistance in the low resistance phase is reduce, which contribute to reduce the energy loss in the gap.

4 Conclusion

The characteristics of high current pulse arc discharge has been investigated to develop a high efficiency, highly repetitive pulse power switch. The energy transfer efficiency and the recovery of breakdown voltage has been evaluated by using charge transfer circuit. The energy transfer efficiency is found to be much higher when using H_2 as a operation gas as compared with that for SF_6. The recovery time to obtain 50 % of initial breakdown voltage are measured to be 0.5 ms, 2 ms, and 3 ms for H_2, SF_6 and air, respectively. From the measurement, energy transfer efficiency and repetition rate of the switch is found to be extremely improved by using H_2. To understand the mechanism of arc discharge, the grow up process of arc has been evaluated. The radius of arc plasma rapidly expand and it exceed 1 mm in 400 ns. The volume of hot gas remaining after the discharge is fund to be much smaller in H_2 arc, which enable the quick recovery of breakdown voltage. From the time resolved measurement of arc resistance, duration of *high resistance phase* and the resistance of *low resistance phase* for H_2 are found to have a very values of ≈ 100 ns 0.2 Ω, respectively, which enhance the efficiency of hydrogen gap switch.

Reference

1) J. A. Nation: Particle accelerators **10**, 1, (1979).
2) J. C. Martin: Proceedings of IEEE **80**, 934 (1992).
3) M. T. Buttram and R. S. Clark: Particle beam fusion progress report SAND-79-1944, 157 (1970).
4) D. S. Prono, D. Barrett, et al: Proc. 7th Int'l Conf.on High Power Particle Beams, Karlsruhe, **vol. II**, 214 (1980).
5) S. L. Moran and L. W. Hardesty; IEEE Trans. Electron Device, **38**, 726 (1991).

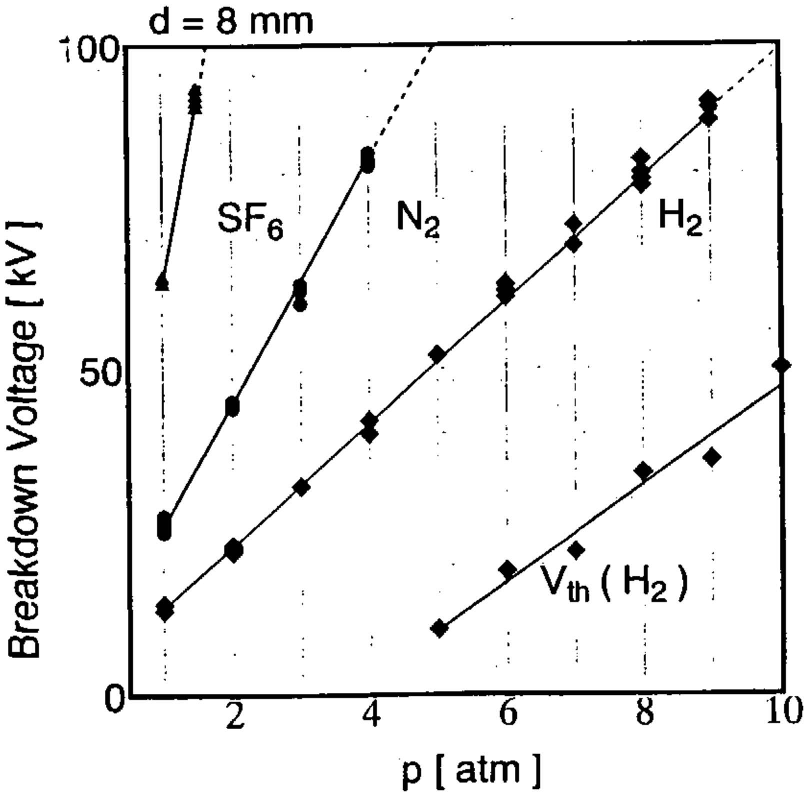

Figure 1 Breakdown voltage (V_{BS}) of the gap for the operation gas of H_2, air, or SF_6. The minimum trigger able voltage for H_2 is also plotted in the figure.

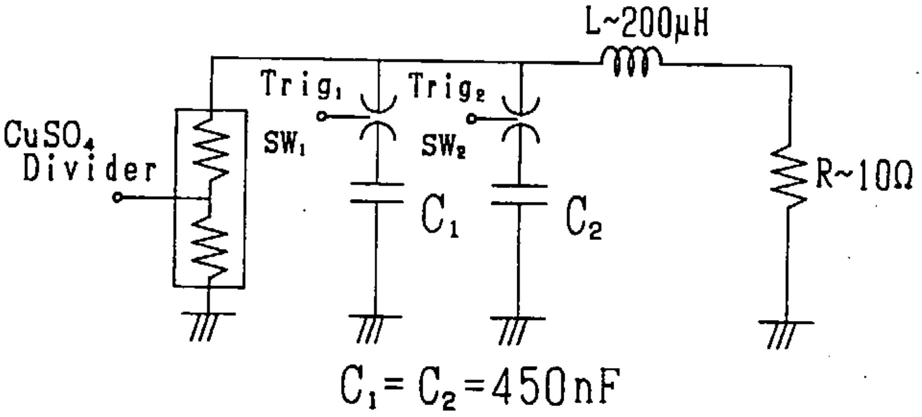

Figure 2 Experimental circuit to evaluate the recovery of breakdown voltage (V_{RE}).

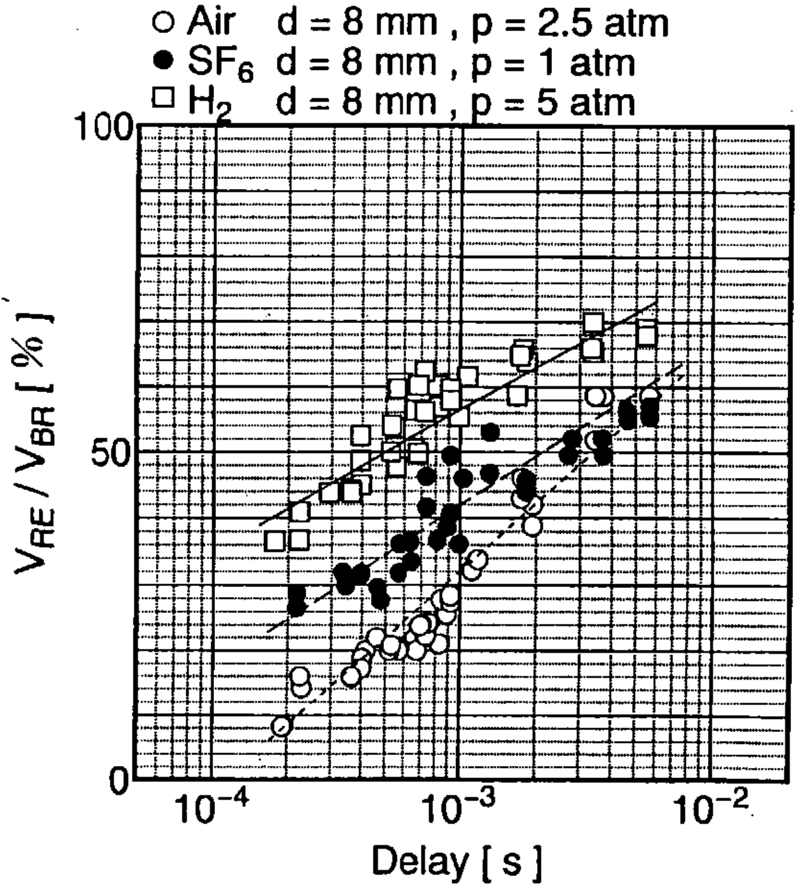

Figure 3 Recovery characteristics of discharge gap filled by a operation gas of H_2, air, or SF_6.

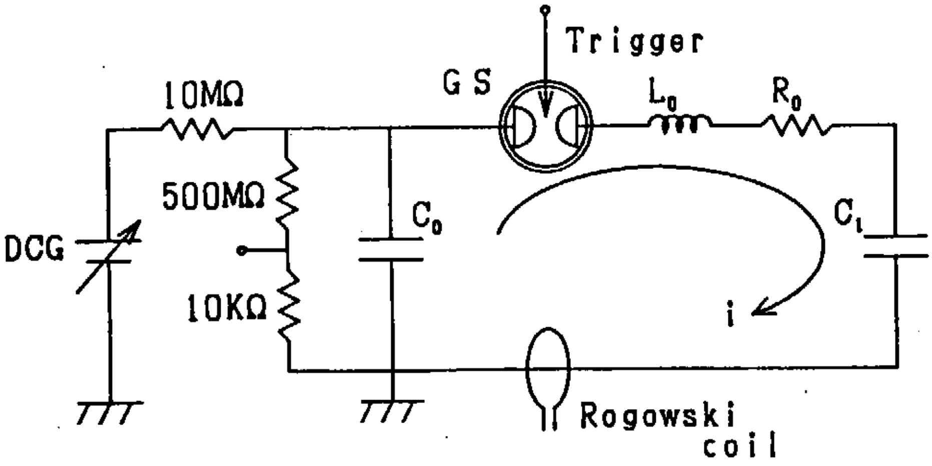

Figure 4 Experimental circuit to evaluate energy transfer efficiency.

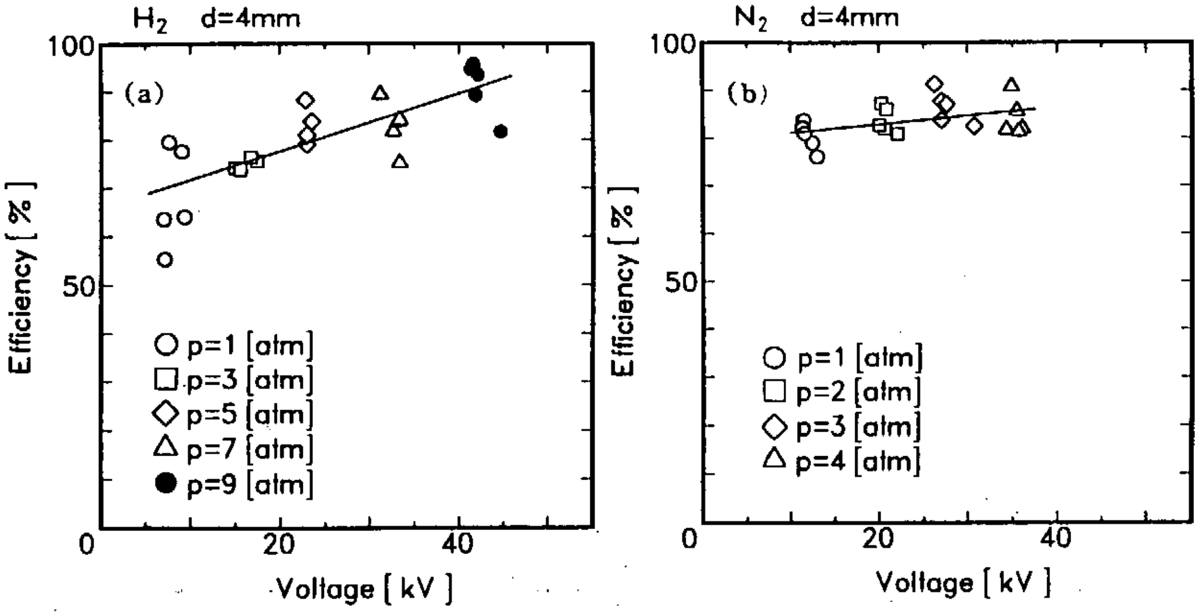

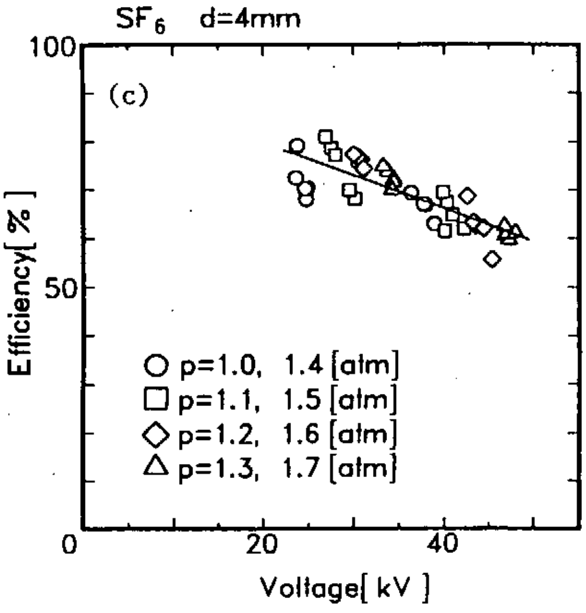

Figure 5 Energy transfer efficiency for (a) H_2, (b) N_2 and (c) SF_6, plotted against charging voltage.

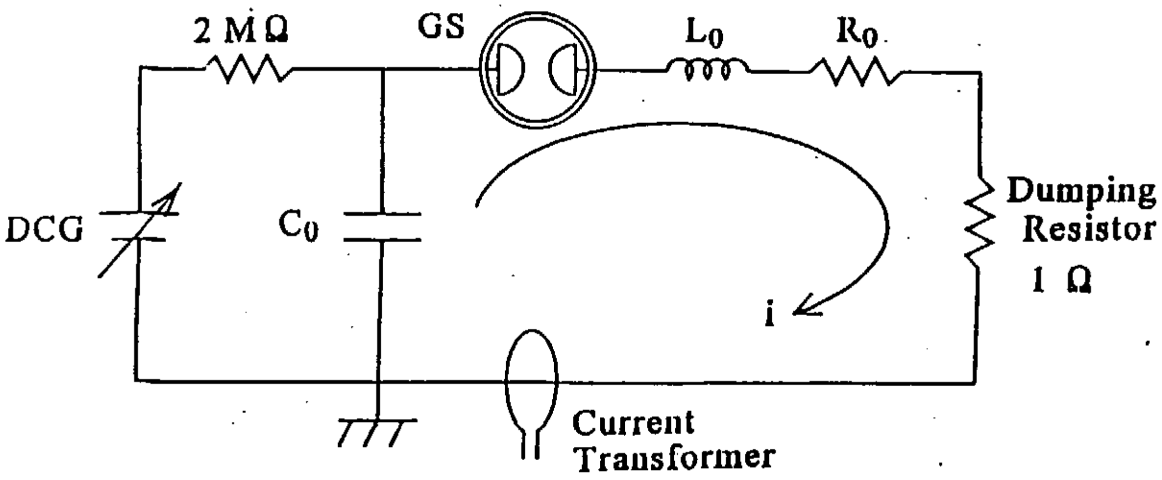

Figure 6 Experimental circuit to evaluate the dynamic behavior of arc discharge.

H_2 (3.8 atm)

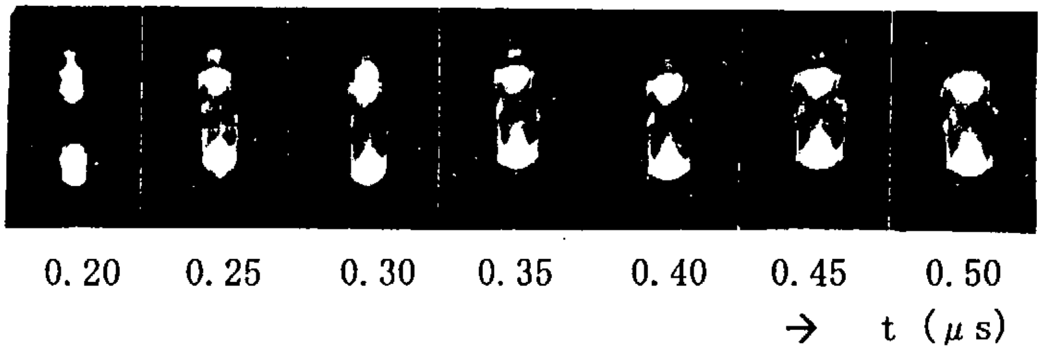

SF_6 (0.6 atm)

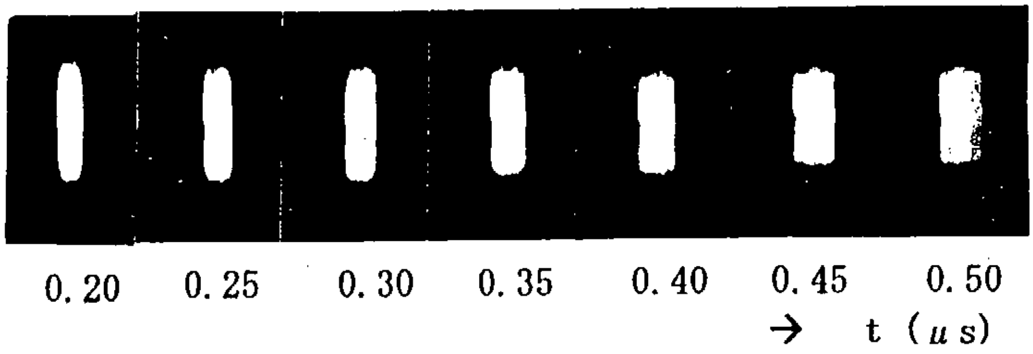

Figure 7 Photographs of arc discharge in H_2 and SF_6 taken by a image converter camera.

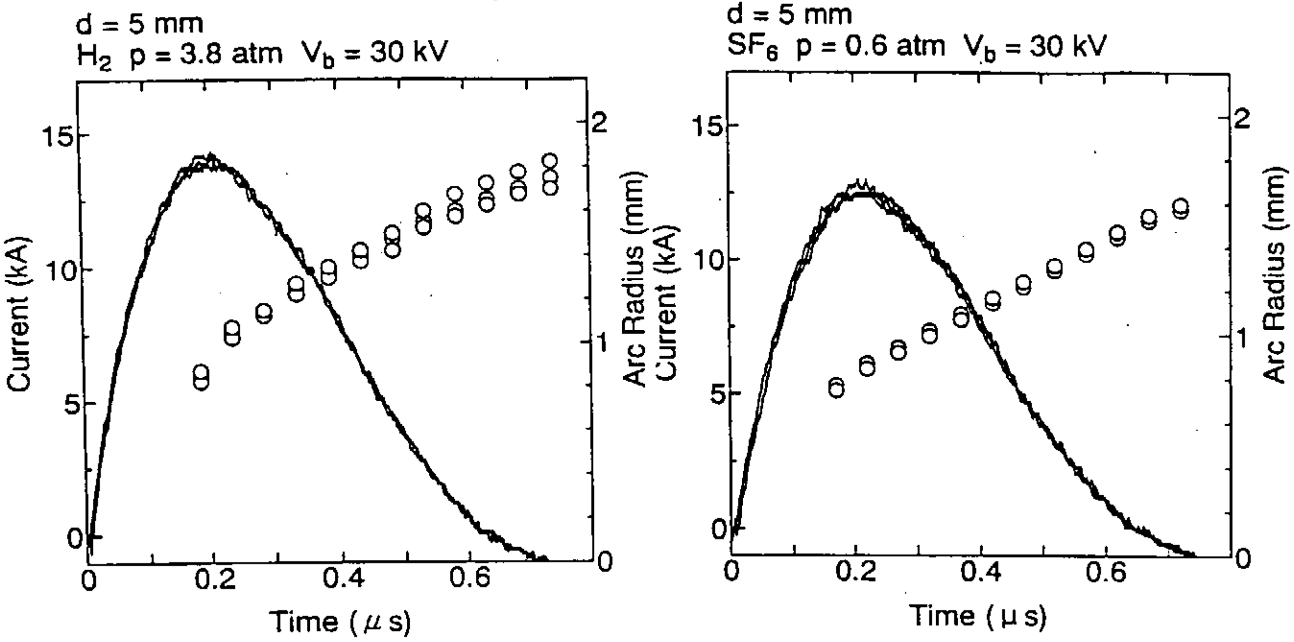

Figure 8 Time variation of arc radius evaluated from Fig. 7 for filling gas of (a) H_2, and (b) SF_6.

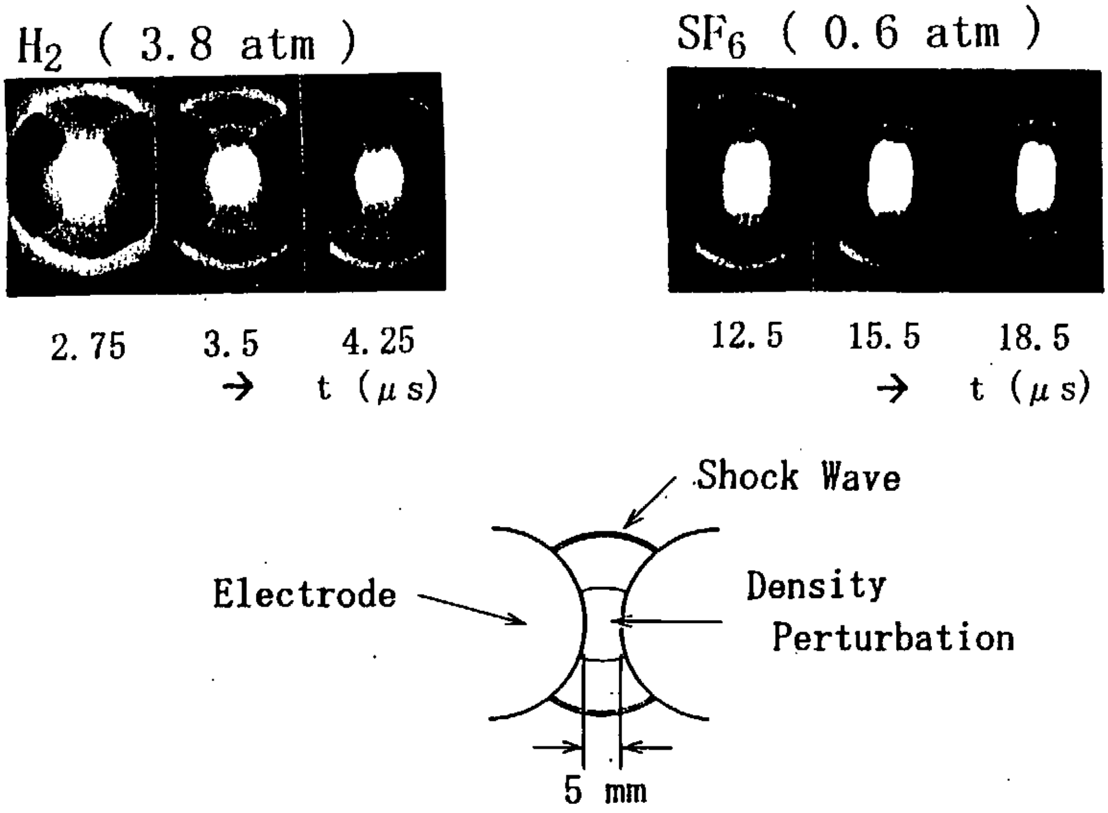

Figure 9 Examples of the image of shadowgraph for the filling gas of H_2 and SF_6.

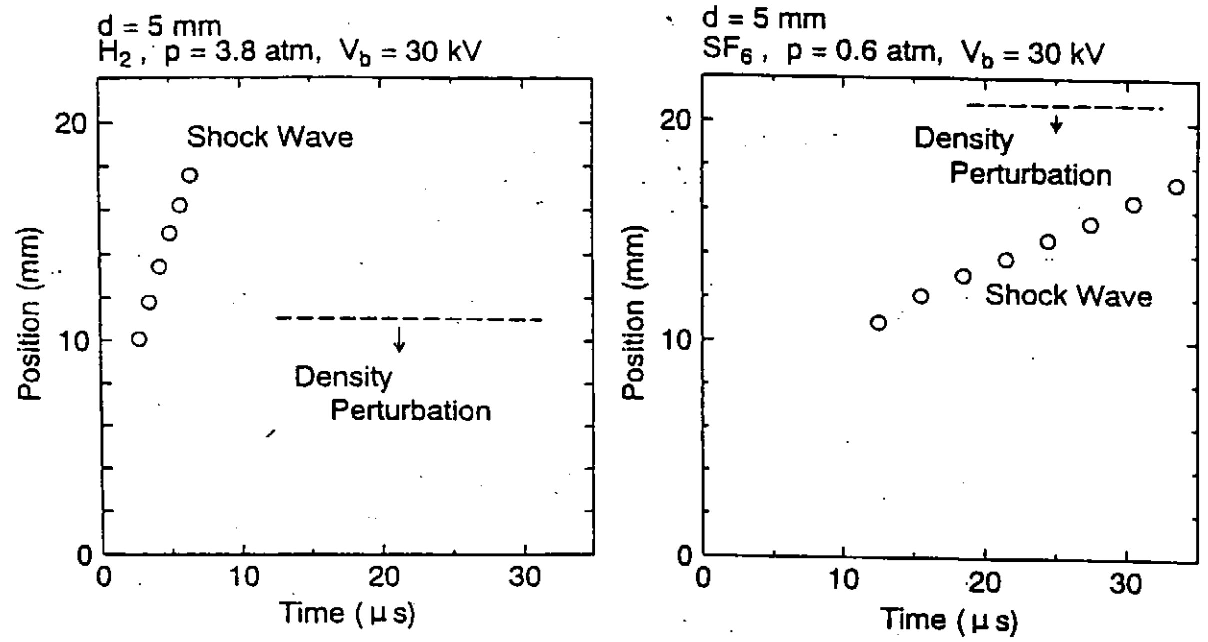

Figure 10 Time variation of the position of shock front with a radius of remained hot gas for filling gas of (a) H_2, and (b) SF_6.

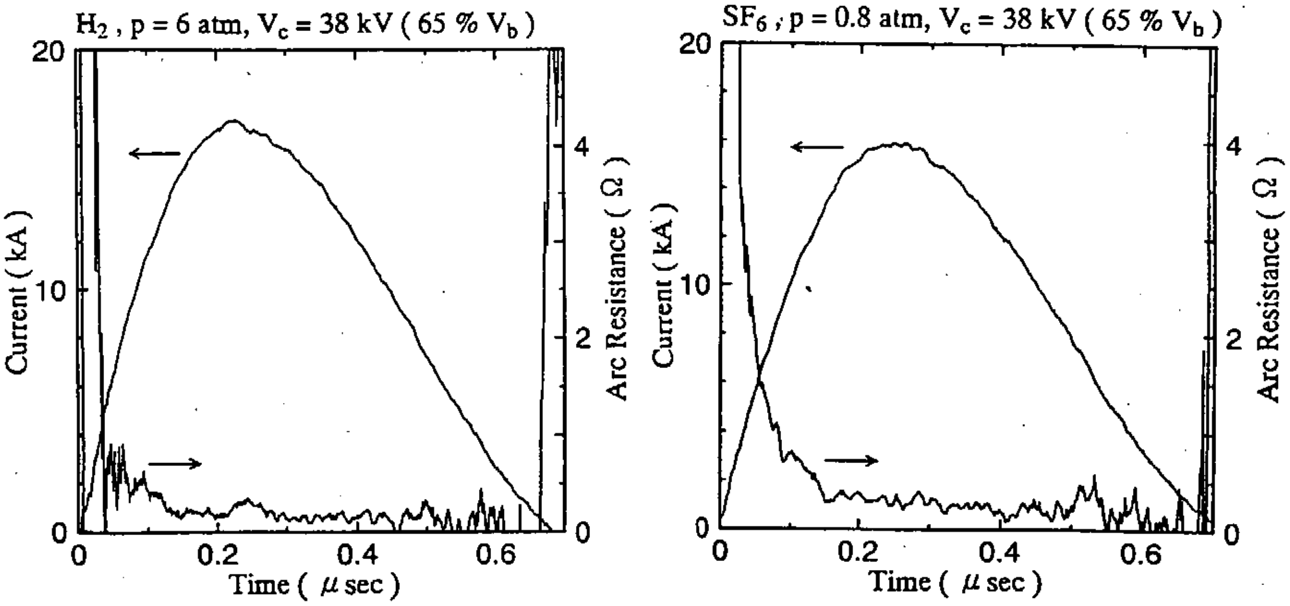

Figure 11 Arc resistance (R_a) and current wave form for the discharge in (a) H_2 and (b) SF_6.

POWER FLOW IN A RESISTIVE MICRO-MITL

Kazuhiko HORIOKA, Kazuki HIRAOKA,
Mitsuo NAKAJIMA and Takayuki AOKI

Department of Energy Sciences, Tokyo Institute of Technology
Nagatsuta 4259, Midori-ku Yokohama, Japan 226

ABSTRACT

In order to create high energy density plasmas, a new scheme is proposed which utilizes the Magnetically Insulated Transmission Line (MITL) concept. In the scheme, an electromagnetic (EM) power pulse is geometrically concentrated in vacuum to a micro-cylinder load through an impedance matched, tapered micro-MITL. The energy of high density EM wave is directly converted to thermal energy by resistive heating on the surface of micro-MITL. The power flow on the EM field through space charge dominated vacuum transmission line is discussed.

1. INTRODUCTION

The production of high energy density plasmas requires more than TWO/cm^2 power density on a tiny load. Although they can be created by intense beams of high power lasers or pulse power accelerators [1], conversion efficiency of the total system is relatively low and the produced plasma volume is rather small.

Fig.1 shows a schematic diagram of the typical pulse power generator. As has been discussed[2], the power density P of TEM-EM wave in vacuum can be expressed as follows,

$$P = Pt / A = | S | = E^2 / Z_0$$

where S is the Poynting vector, E is the electric field, Z_0 is the vacuum wave impedance (377 Ω), Pt shows the EM total power, and A denotes the cross sectional area of the transmission line. Generally the maximum electric field is the order of 0.2MV at most, for the water, the oil, and the vacuum-interface region of pulse power generators. So, the maximum power flux produced from conventional pulse power generator is the order of 10^8 W/cm^2 at vest. As shown in the above equation, one solution to avoid this limitation is spatial focusing of the EM energy in vacuum transmission lines [3,4,5].

Because of large electric field in the vacuum gap, the transportable power density in the vacuum transmission line region is also limited. Electric field stresses in the range of 0.2MV/cm cause field emission of electrons from conductors in vacuum. When the load current exceed the critical value, the self magnetic field of the power flow itself can insulate the electron motion across the high voltage gap. Hence, a creation of the high energy density plasmas with pulsed power generators is not possible without the MITL concept [6-9].

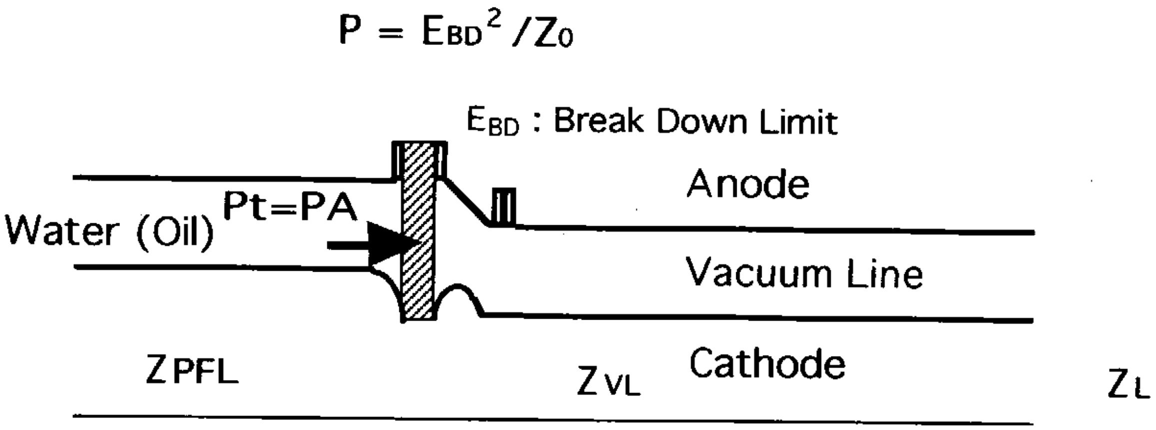

Fig.1 Schematic Diagram of the Power Flow in Conventional Pulse Power Generators

2. PRINCIPLE OF RESISTIVE MICRO-MITL CONCEPT

In order to increase the conversion efficiency and scale size of the plasma, we propose the micro-MITL concept which directly transform the EM energy to the one of plasma load. The EM power of 10^8 W/cm^2 density level is concentrated to TWO/cm^2 level with geometrical compression in a coaxially tapered vacuum line.

Fig.2 illustrates the concept of the micro-MITL. An EM power pulse produced by the conventional pulse power generator, is geometrically compressed in the vacuum transmission line section. Because in the micro-cylinder (load) region, the effective resistivity gradually increase, the high density power pulse is directly transformed to the thermal energy of the plasma load by resistive dissipation of the EM energy. At the end of the line, there is a load section where the EM wave is converted to plasma load. The hydrodynamic motion of the plasma is suppressed by the self magnetic field and the radiation energy of the plasma is confined with high-Z anode surface.

For stationary power flow condition, the single particle description of electrons predicts the critical current; Ic for the magnetic insulation. It can be written as [2],

$$Ic = (V/Zo)((\gamma+1)/(\gamma-1))^{1/2} = I_{\alpha}(\gamma^2-1)^{1/2} g$$

with

$$\gamma_0 = 1 + (eV)/(m_0c^2) = (1-\beta^2)^{-1/2}$$

where I_{α} is the Alfven current (8500A), g is the geometrical factor (=$(\ln(ri/ro))^{-1}$ for coax). Needless to say, the above criterion is not self-consistent, because the effect of space charge and the drifting electron current has not been accounted.

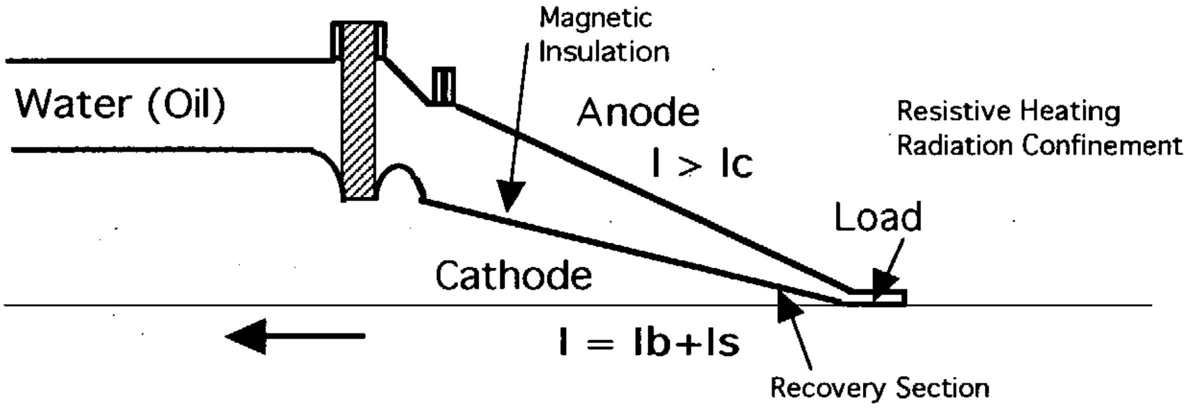

Fig.2 Schematic Diagram of Magnetically Insulated Tapered Transmission Line

If we use laminar flow model; i.e., electrons move in straight trajectories, self-consistent analytical solutions for the ratio of the space charge and the conduction current is expressed as follows [2],

$$I = g((m_0c^2/e)(2\pi/\mu_0 c))\gamma_m[\ln[\gamma_m+(\gamma_m^2-1)^{1/2}]+(\gamma_0-\gamma_m)/(\gamma_m^2-1))^{1/2}]$$

where

$$\gamma_{o,m} = 1+(eV_{o,m})/(m_oc^2) \qquad 1<\gamma_m<\gamma_0 \qquad I/Ib = \gamma_m$$

Here I is the anode current, V_m is the potential at the edge of the electron sheath, Ib is the conduction current at the cathode (cathode current) and γ_m is the ratio of total (anode) current and conduction current.

At the end of the tapered section, the enhanced electric field expected to become 10^7V/cm level. Thus, the MITLs have a high percent of space charge flow adjacent to the cathode.

The deposition energy; Ed on the cathode surface due to resistive heating is written as,

$$Ed = \int Ib^2 \cdot \eta_e \, dt$$

where η_e is the effective resistivity of the cathode surface. Recovery of the current in this sheath at the input of the load section is essential for the efficient conversion of wave energy to the plasma load.

In summary, the spatial contraction of the E-M energy with magnetic insulation, the resistive energy input and the radiation confinement with the surface of outer electrode are the essences of this scheme.

3. Equivalent Circuit Analysis for Space Charge Dominated MITL

If the EM power is transported through impedance mismatched line, the coupling efficiency between the pulse power generator and the plasma load is degraded by the reflection of EM wave. The equivalent circuit models of the MITLs are attractive for the design of the structures and the estimation of coupling efficiency of the MITLs to the load. In order to optimize the transport efficiency of the power pulse, we are developing an equivalent circuit analysis of zero-dimensional level. An appropriate model of power flows in vacuum which is dominated by the presence of the space charge in the gap is essential for the proper modeling of the equivalent circuit analysis. In the zero-dimensional model, we assume stationary flow condition ($\tau C \gg 1$), where C is the speed of light, τ is the rise time of the pulse power and l is the characteristic length of the structure. One unit of the equivalent circuit is shown schematically in Fig.3, where R is the effective resistance of the electrode. In the figure, Li and Ci show the effective inductance and the capacitance of the space charge dominated vacuum line. A self-consistent modeling of these factors in the equivalent circuit analysis is the critical issue for the power flow analysis.

We must take into account of the next factors for the proper modeling of the power flow.

(1) analytical expression of the ratio of space charge and conduction current
(2) recovery process of the space charge current
(3) effective value of the wall resistivity

4. Expected Set-up for Proof-of-principle Experiments

A schematic diagram of the expected experimental set-up is shown in Fig.4. A pulse power of 10^{11}W level from the LIMAY generator [4] is transported through carefully designed vacuum line section to a micro-cylinder load. The E-M power is gradually concentrated by the geometrical contraction of the tapered vacuum line. At the end of the transmission line, there are recovery section and the load section, where the E-M energy is converted to thermal energy of the plasma by resistive heating with conduction current. For the effective heating of the load, the space charge current is recovered to the conduction one at the end of the transport section. All of the transmission line structure is designed by the equivalent circuit calculations so as to maximize the coupling efficiency.

The front formation of the MITL power flow is schematically shown in Fig.5, where D shows the displacement current. When the high voltage pulse is applied to the MITL, an EM front (EM-shock wave) propagates. In addition to the displacement current, there is leak current in the front region until the self magnetic field is sufficiently high to insulate the field emitted electrons. The plasma formation on the anode surface, negative ions on the cathode[10], and the instability of space charge flow of electrons also bring about the current leaks or the gap closure. These factors limit the transportable power density.

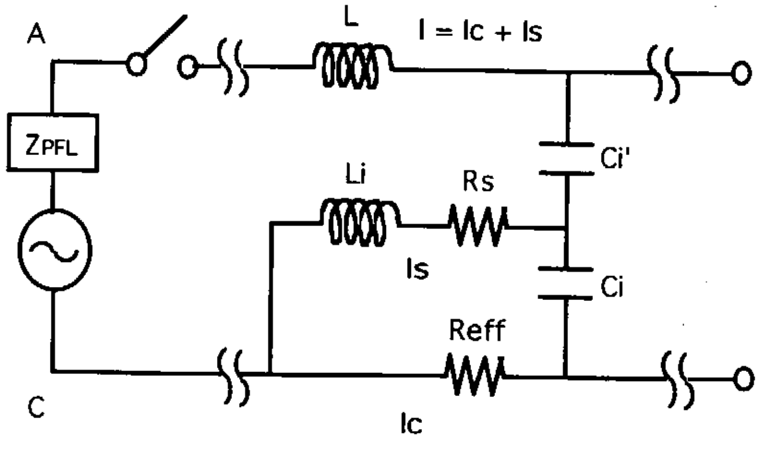

Fig.3 One Mesh of Equivalent Circuit Model

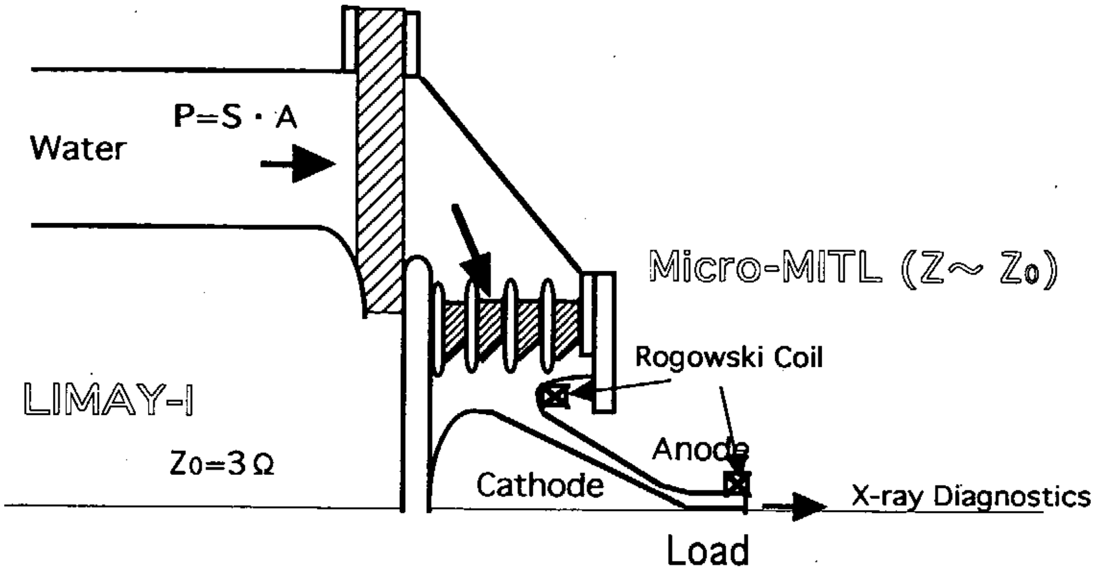

Fig.4 Schematic Diagram of Expected Setup for Proof-of-principle Experiments

The input and output currents, the ratio of space charge and conduction current, and the leak current are monitored by the Rogowskii coils. The important issues of the experimental study are the power transport in the space charge dominated vacuum line, current losses in the transition region, the recovery process of space charge current and the plasma formation on the electrode surface.

5. CONCLUDING REMARKS

We have proposed a new scheme for direct energy input from fast power pulse to a plasma load with cylindrical structure. The electro-magnetic power transports, direct energy input of it to small cylindrical loads with magnetic insulation, radiation trapping by the outer electrode, and recovery of the space charge electron flow at inlet region of the load are the essence of the proposed scheme.

In order to estimate the potentiality of the method and the efficiency of resistive energy dissipation, an equivalent circuit model has been developed, which includes the space charge current flow self-consistently.

The limit of power density must be set by anode plasma formation, negative ions closing the gap and other gap closure mechanisms. A proof-of-principle experiment and the equivalent circuit calculation for the evaluation of the scheme potentiality is under development now.

Further studies of power transport analysis through tiny vacuum lines and the experimental confirmation will reveal the potentiality of this concept.

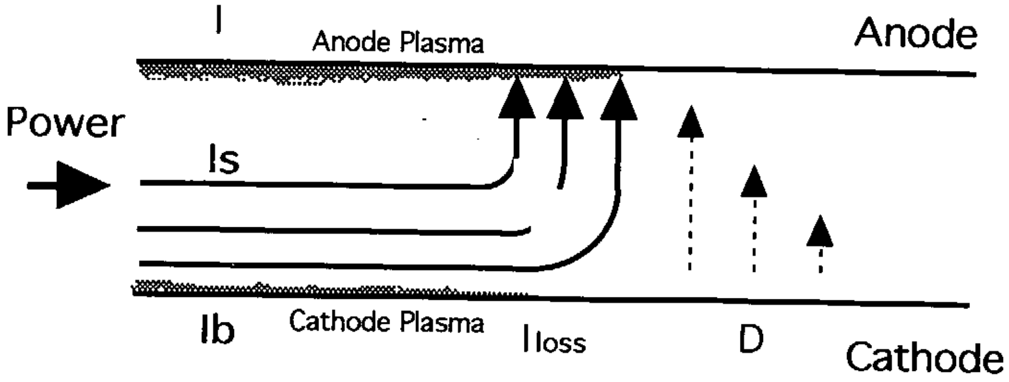

Fig.5 Front of Magnetically Insulated Electro-Magnetic Power Flow

Acknowledgement

We would like to express our thanks to Prof.Teruhiko Tazima of National Institute for Fusion Science for permission to transfer the LIMAY pulse power generator in our campus..

REFERENCES

[1] J.P.Quintenz et. al.; IEEE Proc., Vol.80, No.6, p.971 (1992)
[2] M.S.Di Capua; IEEE Transaction on Plasma Science, Vol.PS-11, No.3, P.205 (1983)
[3] A.Mohri, K.Ikuta and T.Tazima ; Jap. J. Appl. Phys., Vol.22, p.1582 (1983)
[4] M.Sato, J.Mizui, H.Yonezu and T.Tazima; Jap. J. Appl. Phys., 25, p.601 (1986)
[5] K.Yatsui ; Laser and Particle Beams, Vol.7, p.733 (1989)
[6] J.M.Creedon; J. Appl. Phys., Vol.48, No.3 , p.1070 (1977)
[7] J.P.VanDevender; J. Appl. Phys., Vol.50, No.6 (1979)
[8] M.S.Di Capua and D.G.Pellinen; J.Appl. Phys., 50(5), p.3713 (1979)
[9] J.T.Crow and G.D.Peterson; IEEE Transaction on Plasma Science; PS-11, No.3, p.219 (1983)
[10] R.W.Stinnet, M.A.Palmer, R.B.Spielman and R.Bengtson; IEEE Transaction on Plasma Science, PS-11, No.3 (1983)

Numerical Study of Coaxial Double Z-pinch for Resonant Photopumping X-ray Laser

T. Aoki, K. Horioka and M. Ogawa

Department of Energy Sciences, Tokyo Institute of Technology,
4259 Nagatsuta, Midori-ku, Yokohama 226, Japan

Abstract

Implosion dynamics of a coaxial double z-pinch is studied numerically for Na-Ne (sodium-neon) resonant photopumping x-ray laser. A one-dimensional MHD simulation code has been developed to understand the required plasma parameters. When the outer Na plasma implodes, the initially-applied magnetic field is compressed even inside the central Ne plasma. Effective photocoupling is achieved, however, the induced azimuthal current heats the Ne plasma up to several 100 eV. In order to prevent the Ne plasma from being compressed, a new structure with a solid mesh layer between Na and Ne plasma. This layer is optically thin, and the compressed field is screened within the skin depth. The numerical simulation shows that the new structure is suitable for the photopumping x-ray laser scheme.

§1. Introduction

The generation of a soft x-ray laser has been achieved by using plasmas driven by short-pulse optical lasers. In both electron impact excitation scheme[1-4] and recombination scheme[5,6], gains of soft x-ray laser were observed. A large gain coefficient of LiIII Ly-α was obtained by optical-field-induced ionization of ultrashort-pulse laser.[7] Recently population inversion of Na-Ne (sodium-neon) resonant photopumping scheme has been demonstrated with use of dense z-pinch plasma driven by pulsed-power.[8] In comparison with the case of laser-produced plasma, major advantages to use pulsed-power driven plasma are higher overall efficiency and larger total x-ray laser energy with use of less expensive driver. Characteristics of pulsed-power driver are longer pulse duration are large total energy. The radiative decay rate between the upper u and the lower l lasing levels is Einstein's A coefficient, $A_{ul} = 6.6\times10^{15}\lambda^{-2} f_{ul}(g_l/g_u)$, where the notations f_{ul} and λ are oscillator strength and wave length in the unit of Å, respectively. When we consider a x-ray laser of wave length $\lambda = 100$Å, we have

$A_{ul} \approx 6.6 \times 10^{10}$ (sec^{-1}), assuming a typical value of $f_{ul}(g_l / g_u) \approx 0.1$. On the other hands, the duration time of pulsed-power driver is at shortest 10 nsec, so that it is necessary to use lasing scheme of steady pumping. One of them is the electron collisional excitation pumping. Fast capillary discharges for this scheme have been studied, and J=0-1 gain of $\mathrm{Ar_{IX}}$ was reported recently,9) however, the scaling to shorter wave length is unknown because of the limitation of the current density and instabilities in the capillary plasma. Another candidate is the resonant photopumping and has large potential to generate shorter wave length x-ray laser with relatively high efficiency. During the last decade, this scheme has been studied theoretically and experimentally.10-13) The strong radiation produced by dense z-pinch plasma has possibilities to pump the lasant plasma. The demonstration8) used the radiation from the $1s^2$-$1s2p$ $^1P_1$ transition at 11.00027 Å in He-like Na. The $1s^2$-$1s4p$ $^1P_1$ transition at 11.0003 Å in He-like Ne was resonantly photoexcited. Electron and ion collisions transfer a large fraction of the excited $4p$ singlet population to the $4d$ and $4f$ levels. The highest gain is predicted to be $1s3d$ $^1D_2$-$1s4f$ $^1F_3$ transition at 231 Å. Generation of intense Na pump line needs a high-density ($>10^{19}$ ions cm^{-3}), high-temperature (> 300 eV) Na plasma.11) The Ne lasant plasma, however, needs to be a lower density ($\approx 10^{18}$ ions cm^{-3}) and temperature (< 100 eV) in order to maximize the population of Ne ions in the He-like ground state and minimize collisional excitation of lower lasing level.10) The Na wire array is imploded by a peak current of 10 MA in an electrical pulse with a peak power of 20 TW and a 40 nsec FWHM (full width at half-maximum). The radiation energy of 6 kJ was obtained at the Na pump line in a pulse with a peak power of 200 GW and a 20-nsec FWHM.

Recently a coaxial double z-pinch for the Al-Mg (Aluminum-Magnesium) resonant photopump laser scheme was proposed as shown in Fig.1.14) In this scheme, an axial magnetic field B_Z is applied initially in a coaxial plasma column. The annular Al plasma is imploded by the current from pulsed power generator. Concentric with the Al plasma, a lasant Mg plasma is produced on the axis. The Al plasma compresses both the B_Z field and the Mg plasma. The compressed B_Z field serves to separate the Al and Mg plasmas and to stabilize the Mg plasma. The advantage of the configuration is the high coupling efficiency for photopumping with a short separation distance (less than 1 mm) between the two plasmas.

In this article, we study the coaxial double z-pinch implosion for Na-Ne resonant photopump x-ray laser with less driving current. By using one-dimensional (1-D) MHD simulation, we examine the compatibility of the diverge condition that the Na plasma has high density and temperature and the lasant Ne plasma keeps relatively low density and low temperature. In the next section, we estimate plasma parameters of z-pinch plasma implosion by using a simple model. The 1-D MHD simulation is carried out for a more realistic conditions in section 3. We propose an improved structure of the double z-pinch in section 4. Summary is given in section 5.

§2. Estimation for Implosion Dynamics

We first study a simple model to know the basic parameters of a z-pinch implosion; the implosion time and the minimum pinch radius. The plasma column is assumed to have a outer radius of R, initially. The implosion dynamics in the cylindrical geometry is employed by the following continuity equation, momentum equation, and adiabatic relation,

$$M_p = 2\pi \int_0^R \rho r dr, \tag{1}$$

$$\rho\left(\frac{\partial u}{\partial t} + u\frac{\partial u}{\partial r}\right) = J_\theta B_z - J_z B_\theta - \frac{\partial P}{\partial r}, \tag{2}$$

$$\frac{P}{\rho^\gamma} = const. \tag{3}$$

Here M_p is the total mass of the plasma per unit length, and ρ is mass density, u is radial velocity, P is pressure, and γ is adiabatic index. For simplicity, thermal conduction and Joule heating are ignored. The notation J and B mean current density and magnetic field, respectively. Without dissipation, we have frozen-in field condition for B_z from the Maxwell equations,

$$\frac{B_z}{\rho} = const. \tag{4}$$

Given the total current I from the pulsed-power driver, the strength of the azimuthal magnetic field B_θ (R) at the outer radius is expressed as

$$B_\theta(R) = \frac{\mu_0 I}{2\pi R}. \tag{5}$$

Furthermore, we assume that the velocity profile is proportional to the radius, and all of the physical variables have self-similar profiles in the radial direction. We introduce a normalized radius $\xi = r / R(t)$, $0 \le \xi \le 1$, and normalized quantities η, Π, ϕ, and φ;

$$u = \xi dR(t)/dt, \quad \rho = \rho_0(t)\eta(\xi), \quad P = P_0(t)\Pi(\xi), \tag{6}$$

$$B_\theta = B_{\theta 0}(t)\phi(\xi), \quad B_z = B_{z0}(t)\varphi(\xi).$$

The boundary conditions are $\Pi(0) = 1$, $\Pi(1) = 0$, $\phi(0) = 0$, $\phi(1) = 1$, $\varphi(0) = 1$, $\varphi(1) = 0$.

Substituting the variables of eq.(6) into eq.(2), we have

$$\rho_0(t)\frac{d^2R(t)}{dt^2}\cdot\xi\eta(\xi) = -\frac{B_{z0}(t)^2}{2\mu_0 R(t)}\cdot\frac{\partial\varphi^2}{\partial\xi} - \frac{B_{\theta 0}(t)^2}{\mu_0 R(t)}\cdot\phi\frac{\partial\xi\phi}{\partial\xi} - \frac{P_0(t)}{R(t)}\cdot\frac{\partial\Pi}{\partial\xi}. \tag{7}$$

Integrating eq.(7) from ξ=0 to 1, and using the above boundary conditions, we obtain

$$\frac{M_p}{2\pi R(t)^2}\frac{d^2R(t)}{dt^2} = \frac{B_{z0}(t)^2}{2\mu_0 R(t)} - \frac{B_{\theta 0}(t)^2}{2\mu_0 R(t)}\beta + \frac{P_0(t)}{R(t)}, \tag{8}$$

where $\beta = 2\int_0^1 \phi\frac{\partial\xi\phi}{\partial\xi}d\xi$. It is clear that β takes a value of $1 < \beta < 2$, and $\beta \approx 4/3$ for $\phi(\xi)\approx\xi$. The axial and azimuthal magnetic fields and the pressure can be expressed in terms of their initial values,

$$B_{z0}(t) = B_{z0}(0)\frac{\rho_0(t)}{\rho_0(0)} = B_{z0}(0)\frac{R(0)^2}{R(t)^2}, \tag{9}$$

$$B_{\theta 0}(t) = \frac{\mu_0 I}{2\pi R(0)}\cdot\frac{R(0)}{R(t)} = B_{\theta 0}(0)\frac{R(0)}{R(t)}, \tag{10}$$

$$P_0(t) = P_0(0)\frac{\rho_0(t)^\gamma}{\rho_0(0)^\gamma} = P_0(0)\frac{R(0)^{\gamma 2}}{R(t)^{\gamma 2}}. \tag{11}$$

Substituting eq.(5), eq.(9) and eq.(10) into eq.(8), we have

$$\frac{d^2R(t)}{dt^2} = \frac{B_{z0}(0)^2}{\mu_0\rho_s}\cdot\frac{R(0)^2}{R(t)^3} - \frac{B_{\theta 0}(0)^2}{\mu_0\rho_s}\cdot\frac{\beta}{R(t)} + \frac{P_0(0)}{\rho_s}\cdot\frac{R(0)^{2\gamma}}{R(t)^{2\gamma+1}}, \tag{12}$$

where $\rho_s = M_p/\pi R(0)^2$. Multiplying $dR(t)/dt$ on both sides of eq.(12) and integrating over the time, we have

$$\frac{1}{2}\left|\frac{dR(t)}{dt}\right|^2 = \frac{B_{z0}(0)^2}{2\mu_0\rho_s}\cdot\left(\frac{R(0)^2}{R(t)^2}-1\right) - \frac{B_{\theta 0}(0)^2\beta}{\mu_0\rho_s}\cdot\ln\left(\frac{R(t)}{R(0)}\right) + \frac{P_0(0)}{2\gamma\rho_s}\cdot\left(\frac{R(0)^{2\gamma}}{R(t)^{2\gamma}}-1\right). \tag{13}$$

Here the initial condition of $\dot{R}(0) = 0$ is used.

In order to determine the trajectory of the outer radius R, we have to integrate eq.(12) over the time once again. However, the implosion time t_c can be easily estimated in the following approximation. In general pinch dynamics, the $j_\theta B_z$ term and the pressure gradient term on the right-hand side of eq.(13), which are acting outward forces, become dominant only when R reaches a small radius. By integration without the second and third terms, we have

$$t_c = \frac{1}{\sqrt{\frac{B_{\theta 0}(0)^2\beta}{\mu_0\rho_s}}}\int_0^{R(0)}\frac{dR(t)}{\sqrt{\ln\frac{R(t)}{R(0)}}} = 1.253\frac{R(0)}{\sqrt{\frac{B_{\theta 0}(0)^2\beta}{\mu_0\rho_s}}} = 1.253R(0)\sqrt{\frac{4\pi M_p}{\mu_0 I^2\beta}}. \tag{14}$$

The minimum radius of the plasma column is also derived without integrating eq.(13). When the plasma column has reached the minimum radius, the $j_z B_\theta$ force balances with the pressure gradient and the $j_\theta B_z$ force. In the case that the pressure gradient is dominant, the minimum radius $R_m = R(t_c)$ is determined by solving the following equation

$$\frac{B_{\theta 0}(0)^2 \beta}{\mu_0 \rho_s} \cdot \ln\left(\frac{R_m}{R(0)}\right) = \frac{P_0(0)}{2\gamma\rho_s} \cdot \left(\frac{R(0)^{2\gamma}}{R_m{}^{2\gamma}} - 1\right). \tag{15}$$

For $0.003 \le \frac{R_m}{R(0)} \le 0.2$, the relation $\ln\frac{R_m}{R(0)} \approx \left(\frac{R_m}{R(0)}\right)^\alpha$ $(-0.368 \le \alpha \le -0.3)$ holds good, and we obtain

$$R_m \approx R(0)\left(\frac{1}{2\gamma}\frac{\mu_0 P_0(0)}{B_{\theta 0}(0)^2 \beta}\right)^{1/3}. \tag{16}$$

When the $j_\theta B_z$ term is dominant near the minimum radius, the force balance between the Lorentz forces gives

$$R_m \approx R(0)\left(\frac{B_{z0}(0)^2}{2B_{\theta 0}(0)^2 \beta}\right)^{0.6}. \tag{17}$$

In Fig.2, the time histories of the plasma radius are shown. All of the lines are obtained by numerical integration of eq.(13). The notation (a) indicates the trajectory of the cold plasma without any external fields. The line (b) shows the case that the Lorentz force $j_\theta B_z$ is more dominant near the minimum radius than the pressure term. In the line (c), the thermal pressure gradient is dominant. In both the cases of (b) and (c), it is found that the times to reach the minimum radius are close to t_C. The minimum radius of the line (b) and (c) have good agreements with eq.(16) and eq.(17).

§3. Numerical Simulation

§3.1 Simulation Code

In order to study more realistic implosion, we have developed a 1-D MHD simulation code MULTI-Z which is based on MULTI7 code[15]. In the cylindrical geometry, the plasma dynamics is employed by the following equations,

$$\frac{\partial \rho}{\partial t} + \frac{1}{r}\frac{\partial r\rho u}{\partial r} = 0 , \tag{18}$$

$$\rho\left(\frac{\partial u}{\partial t} + u\frac{\partial u}{\partial r}\right) = j_\theta B_z - j_z B_\theta - \frac{\partial}{\partial r}\left(P_e + P_i\right) , \tag{19}$$

$$\rho\left(\frac{\partial e_e}{\partial t} + u\frac{\partial e_e}{\partial r}\right) = -P_e\frac{1}{r}\frac{\partial r u}{\partial r} + \frac{1}{r}\frac{\partial}{\partial r} r\kappa_e\frac{\partial T_e}{\partial r} + \frac{|j|^2}{\sigma} + S_{rad} , \tag{20}$$

$$\rho\left(\frac{\partial e_i}{\partial t}+u\frac{\partial e_i}{\partial r}\right)=-P_i\frac{1}{r}\frac{\partial ru}{\partial r}+\frac{1}{r}\frac{\partial}{\partial r}r\kappa_i\frac{\partial T_i}{\partial r}\ , \tag{21}$$

where κ is thermal conductivity and σ is electrical conductivity, respectively. The subscripts i and e indicate ion and electron. The notation S_{rad} is a radiation density coupling with radiation transport. For the electromagnetic field, we use the following Maxwell equations with Ohm's law,

$$\frac{1}{r}\frac{\partial}{\partial r}rB_\theta=\mu_0 j_z\ , \qquad \frac{\partial B_z}{\partial r}=-\mu_0 j_\theta\ , \tag{22}$$

$$\frac{\partial B_z}{\partial t}=-\frac{1}{r}\frac{\partial}{\partial r}rE_\theta\ , \qquad \frac{\partial B_\theta}{\partial t}=\frac{\partial E_z}{\partial r}\ , \tag{23}$$

$$\boldsymbol{j}=\sigma(\boldsymbol{E}+\boldsymbol{u}\times\boldsymbol{B})\ . \tag{24}$$

Two-temperature (or internal energy) and single-fluid model is suitable for z-pinch implosion. The electron and ion thermal pressures P_e, P_i are determined by the tabulated equation of state as functions of specific internal energy e_e, e_i and density ρ. For the charge state of the plasma ions and the radiation opacities, the same type of tabulated data are used. The tabulated thermal conductivity and electrical conductivity are also called in the code. The displacement current is neglected in the Maxwell equation (23), and we assume quasi-neutrality for dense z-pinch plasma with the time scale of 10-100 nsec. With respect to the multi-group radiation transport, the detail description was given in ref.(14). To solve the above equations numerically, a finite difference method is used, and Lagrangian scheme is adopted for the hydrodynamics. As the date tables mentioned above, the SESAME library$^{16)}$ is used.

§3.2 Simulation Results

By using the simulation code MULTI-Z, we study a coaxial double z-pinch implosion. In the initial state, it is assumed that the annular Na plasma has 1.3-cm outer radius and 0.9-cm inner radius. The inside Ne plasma with 0.4-cm radius is located at the coaxial center. The initial temperatures of both plasmas are assumed to be 2 eV, and the initial Na and Ne density is 3.5×10^{17} ions cm^{-3} and 1.5×10^{17} ions cm^{-3}, respectively. The implosion is driven by a 100-nsec sinusoidal current pulse with a peak current of 1 MA. The axial magnetic filed of 2 T is applied initially. The flow diagram of the implosion dynamics results in Fig.3. The coaxial plasma reaches the minimum radius at 83 nsec. It is found that the axial magnetic field serves to separate the two plasmas through the whole implosion and expansion processes. In the beginning, pulsed power driven current flows in the outer region of Na plasma. A strong shock wave is generated, and the shock speed and the implosion velocity are almost same. When the shock wave arrives at the inner surface of Na plasma at 50 nsec, Ne plasma starts to be compressed through the axial magnetic field. A shock wave driven by the Lorentz force $j_\theta B_z$ appears in Ne plasma and reaches the center at 77 nsec. The Ne plasma has less effect on the Na implosion dynamics, when the initial density of Ne plasma is lower than ions 10^{17} ions cm^{-3}. The electron density and electron temperature are given in Fig.4(a) and Fig.4(b), respectively. The regions indicated by the Lagrangian cell number 1-50 and 52-81 are Ne and Na plasma, respectively. At the maximum compression, the density and of 10^{20} ions cm^{-3} and the electron temperature of 300 eV are achieved in Na plasma. According to ref.11, the radiation temperature of 170 eV could be obtained for the pumping line. This radiation flux is estimated 27 GW per 1-cm axial length. Furthermore, the distance between Na and Ne plasma is reduced to 30 μm, and the photocoupling appears to be so efficient. The axial magnetic field increases up to more than 300 T at 80 nsec. The compression of the magnetic field depends strongly on the electrical conductivity. In our code, the electrical conductivity of SESAME library is used and confirmed the coincidence with Spizter formula at high temperature. An anomalous conductivity is a function of the parameter $\omega_c\tau_c = 10$, where ω_c is electron cycrotron frequency and τ_c is collision time, however, we do not have a sufficient formula over a wide range of the magnetic field. With the smaller conductivity, we have a smaller compression of the magnetic field and higher Joule heating. When we use 10 times smaller conductivity than the above simulation, we have 1.5 times the minimum radius.

The suitable Na plasma for emission of the pumping line was obtained, however, the central Ne plasma is compressed in association with the implosion of the outer Na plasma. Figure 4(b) shows that the first shock wave heats the Ne plasma to 100 eV. Inside the Ne plasma, the compression of the axial magnetic field causes to Joule heating of the induced azimuthal current. Although the adiabatic compression increases the density and temperature , the maximum temperature of Ne plasma is determined mainly by the Joule heating. At the maximum compression, the Ne density and temperature reaches 10^{19} ions cm^{-3} and 500 eV, respectively. These plasma parameters are apparently against the condition to minimize collisional process; a lower density ($\approx 10^{18}$ ions cm^{-3}) and temperature (< 100 eV). Even if we choose much lower Ne density initially, the maximum temperature increases more than the previous case. In the above configuration of the double z-pinch, the strong Na plasma implosion breaks the suitable plasma condition for the photopumping scheme.

§4. Proposal of structure with mesh layer

In order to achieve both the requirements for the Na plasma and the Ne plasma, we improve the double z-pinch structure. Our proposal is to insert a solid metal mesh layer between the Na and the Ne plasma as shown in Fig.5. We expect that this layer will work to exclude the compressed axial field penetrating into the Ne plasma. We choose the thickness in terms of eq.(10), in order that the implosion time τ_{mesh} is much longer than the implosion time of Na layer of 100 nsec. The solid metal has enough electrical conductivity at room temperature. The mesh structure works to screen the compressed magnetic field, and should be transparent for the pumping line from Na plasma.

The improved structure is investigated by using the simulation code MULTI-Z again. In the simulation, we insert Al mesh layer with 100-μm thickness and 1-mm radius. The initial densities of Na and Ne plasma are both 10^{18} ions cm^{-3}. Initially, the inner radius and the outer radius of Na plasma are 0.8 cm and 1.1 cm, respectively. The Ne plasma is filled inside the mesh layer. The drive current has 80-nsec pulse width, and the other conditions are same as those of the simulation in the previous section.

The simulation result shows that the mesh layer completely screens the penetration of the axial magnetic field. The flow diagram of the pinch plasma is shown in Fig.6. The solid aluminum has a skin depth for 100-nsec pulse is 0.1 mm at room temperature. It is found that the inside Ne plasma reminds undisturbed through the whole implosion process, and most of Al layer is still same position after the maximum compression time. Before 40 nsec, the Na plasma pinch is almost same as the simulation result without the mesh layer. The density and the electron temperature reach 10^{20} ions cm^{-3} and 600 eV at the peak, according to the perspective view of the electron density and the electron temperature of Na plasma, shown in Fig.7(a) and Fig.7(b). These conditions are desirable for the emission of the pumping line with enough strength. The improved structure appears to be quite reasonable for Na-Ne photopumping scheme.

§5. Summary

The 1-D MHD simulation for the double z-pinch implosion scheme shows that the inner plasma is too much heated and compressed, and is not desirable for the photopumping x-ray laser scheme. We propose the new structure with the solid mesh layer between two plasmas. It appears that the aluminum mesh with 100-μm thickness works well and has enough mass and electrical conductivity to screen the inner plasma from the implosion motion of the outer plasma. The maximum temperature and density of the Na plasma depend on the electrical conductivity and it reminds unknown parameter in the simulation. It should be compared with experiments. The instabilities are also important factor to achieve high density compression, and two- or three-dimensional simulations are required in the next stage.

Acknowledgment

We would like to thank Dr. Meyer-ter-Vehn and Dr. Ramis for giving the code MULTI and many useful information in using it on the workstation.

References

1) D.L.Matthews, et al.: Phys. Rev. Lett. 54 (1985) 110
2) M.D.Rosen, et al.: Phys. Rev. Lett. 54 (1985) 106
3) B.J.MacGowan, et al.: Phys. Rev. Lett. 59 (1987) 2157
4) Y.Kato, et al.: Proc. SPIE 1551 (1991) 56
5) S.Suchewer, et al.: Phys. Rev. Lett. 55 (1985) 1753
6) C.Chenais-Provics, et al.: Phys. Rev. Lett. 59 (1987) 2161
7) Y.Nagata, et al.: Phys. Rev. Lett. 71 (1993) 3774
8) J.L.Porter, et al.: Phys. Rev. Lett. **68** (1992) 796
9) J.J.Rocca, et al.: Phys. Rev. A 47 (1993) 1299
10) J.P.Apruzese and J.Davis, and K.G.Whitney: J. Appl. Phys. 53 (1982) 4020
11) J.P.Apruzese and J.Davis: Phys. Rev. A 31 (1985) 2976
12) F.C.Young, et al.: J. Appl. Phys. 69 (1991) 7520
13) C.Deeney, et al.: Appl. Phys. Lett. 58 (1991) 1021
14) N. Qi and D.A. Hammer: J. Appl. Phys. **74** (1993) 4303.
15) R.Ramis, R.Schmalz and J. Meyer-ter-Vehn: Comp Phys. Comm. 49 (1988) 475
16) B.I.Bennet et al.: Los Alamos report LA-7130 (1978)

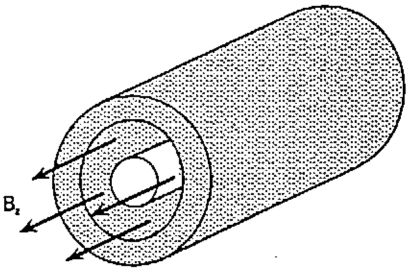

Fig.1 Schematic view of the coaxial double z-pinch configuration. The axial magnetic field is applied to both the annular Na plasma and the center Ne plasma.

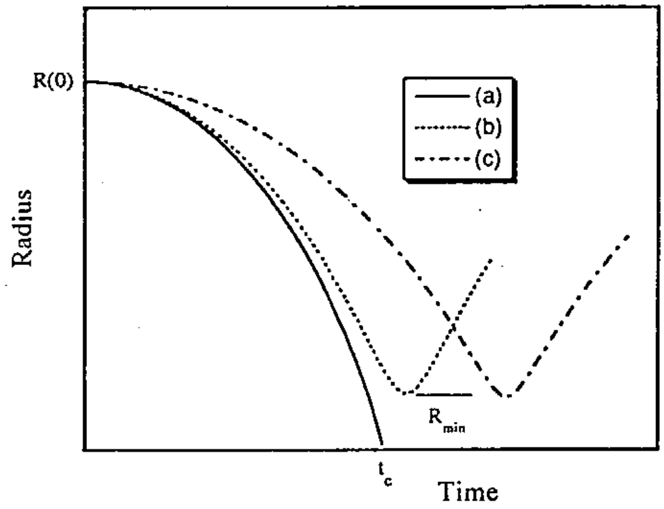

Fig.2 Trajectory of the outer radius of plasma column, showing (a) the case of the cold plasma, (b) $j_\theta B_z >> \partial P/\partial r$ and (c) the case of $\partial P/\partial r >> j_\theta B_z$.

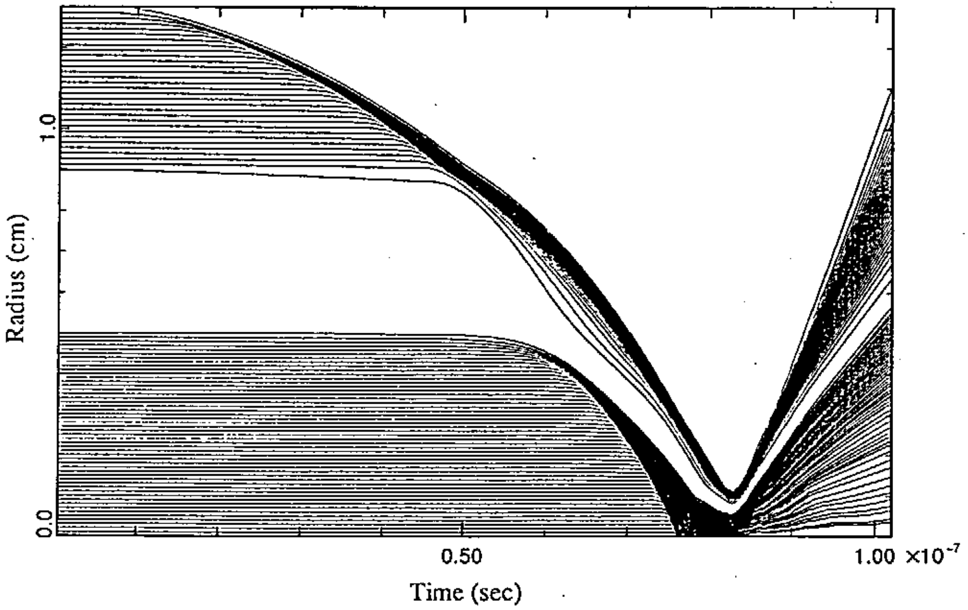

Fig.3 Flow diagram of the implosion dynamics. The current driven by pulsed power is a sinusoidal wave form with the peak of 1 MA and 100-nsec pulse.

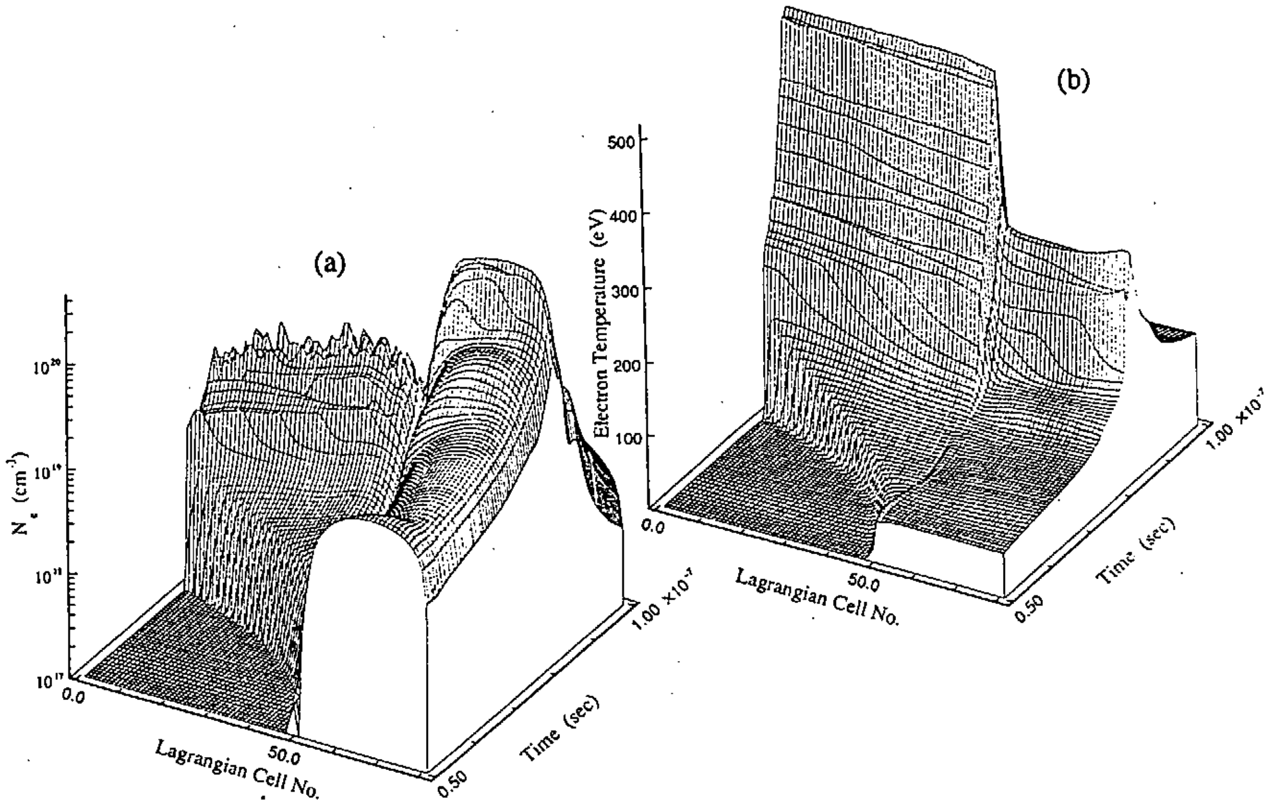

Fig.4 Perspective views of (a) the electron number density and (b) the electron temperature. The Na and Ne plasmas occupy the Lagrangian cell number of 52-81 and 1-50, respectively.

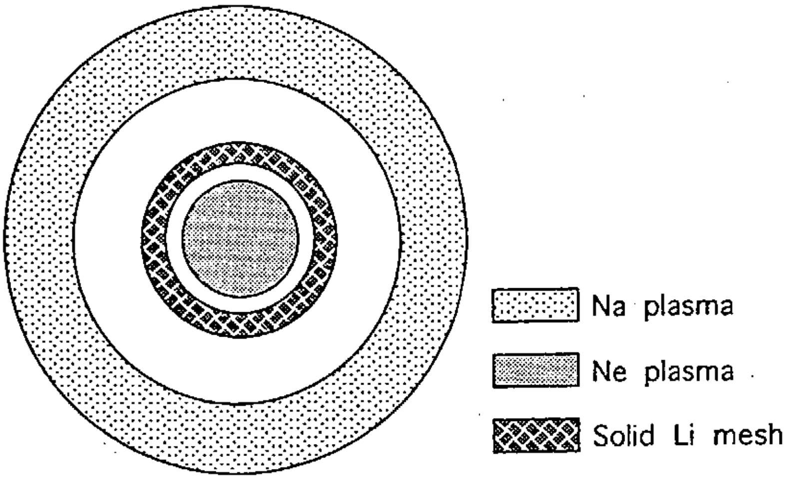

Fig.5 New structure of double z-pinch with solid mesh layer.

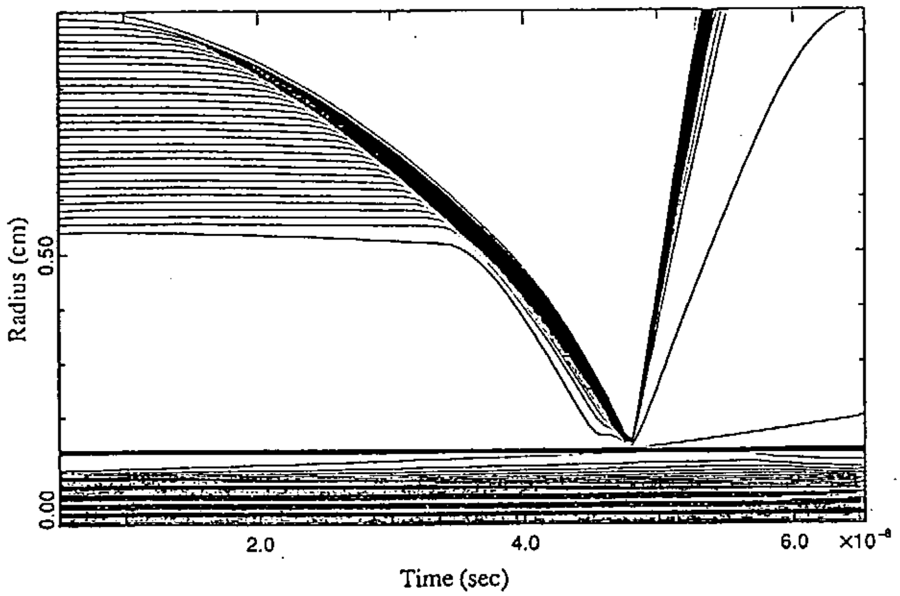

Fig.6 Flow diagram of pinch dynamics for the new structure.

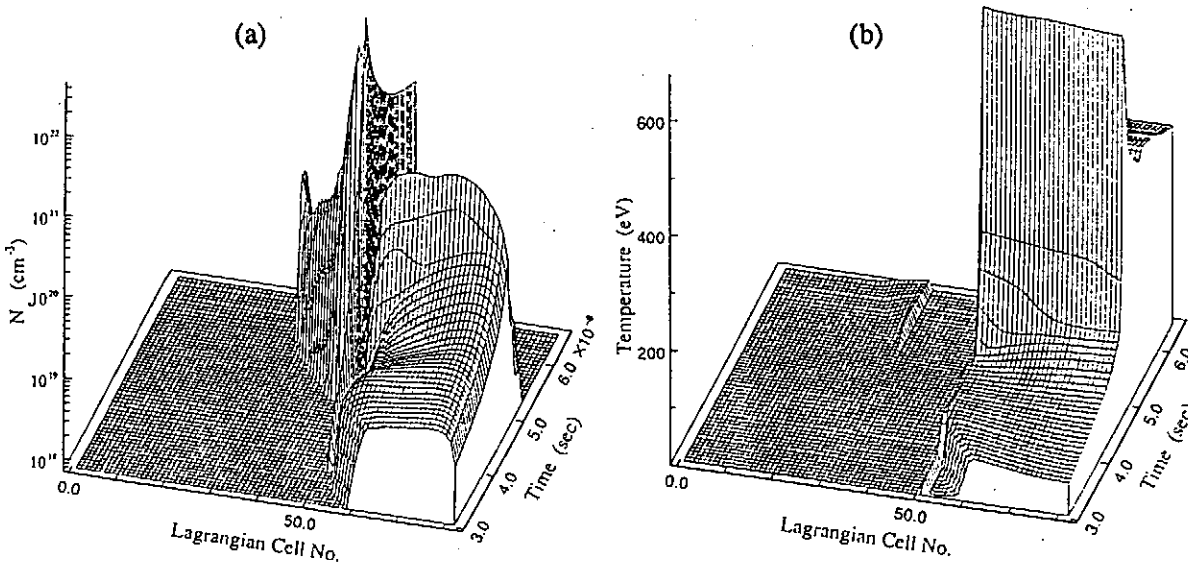

Fig.7 Perspective views of (a) the electron number density and (b) the electron temperature. The mesh layer is inserted within the region indicated by the Lagrangian cell number 31-50.

A time resolved 1D soft x–ray camera system for an impulsive source and its application to a plasma focus experiment

Takeshi Yanagidaira, Hiroshi Kurita, Takahisa Koshimizu, Jyun Mikami,
Toshikazu Yamamoto, Katsuji Shimoda and Katsumi Hirano

Department of Electronic Engineering, Gunma University
Kiryu, Gunma 376, Japan

Synopsis

A soft x–ray pinhole camera system for time–resolved, 1D measurement of an impulsive source whose energy is in the range from 1 keV to 20 keV is developed. The system is based on the filtered pinhole camera. The emission is detected by scintillator–photomultiplier combination. The spatial and the temporal resolution of this system are 1.3 mm and 5.2 nS, respectively. The absolute sensitivity of the channel is $\sim 4.2 \times 10^{-20}$ A/{photons/mrad ^{2} •s}. This system was successfully used to obtain the time evolution of the soft x–ray source generated with a plasma focus device with a gas–puffed target.

§ 1 Introduction

The soft x–rays generated by a dense plasma has considerable interest in fields such as the micro lithography for LSI manufacturing, the soft x–ray microscopy and the soft laser exitation. The emission of the soft x–rays is closely correlated with the plasma dynamics, and so the measurement of those emission is also important to explain the heating mechanism of the dense plasma.

For the plasma behavior time-integrated observations have been extensively carried out. However, few authors have been tried for the time resolved measurement. In a few papers, the time evolution of the soft x-ray source produced with a plasma focus has been reported. [1)]

The x-ray streak camera has been commercially supplied. However, it is sometimes hard to obtain because of its high price. Moreover it is difficult to measure intensity of the soft x-rays with linearity.

In this paper, we intend to construct a time resolved 1D soft x-ray camera system which is based on a filtered pinhole camera and to examine the characteristics such as spectral response, temporal- and spatial resolution.

§ 2 Experimental

2-1 General description of the system

The soft x-ray imaging system consists of a filtered pinhole camera for the soft x-rays and a detector which enables to make a temporal-and spatial resolved measurement. The detector is composed of an soft x-ray sensitive scintillator plate, slits, a bundled fiber optics and photomultiplier tubes. The schematic diagram of the detection system is shown in Fig. 1. A pinhole image of the soft x-ray source is made on the scintillator through a pinhole and foil filters which block the visible light also emitted from the source. The visible image generated by the soft x-rays on the scintillator plate is divided into six pieces by the six slits and the bundled six channel optical fiber which are arrayed in parpendecular to the electrode axis. Each channel of the optical signals is led to the photomultipliers (Hamamatsu Photonics H1161) and recorded in the storage oscilloscope (Hewlett Packard 54542A). The storaged signals are processed for suitable purpose such as scaling and deconvolution.

A soft X–ray pinhole camera with a quantitative image acquisition system is developed for soft X–ray image observation with time resolution. [2] A pinhole image of the X–ray source is made on the MCP through a pinhole and Be and Ag foil filters (25 μ m and 1 μ m in thickness, respectively) which prevent the visible light also emitted from the source. The spectral response of the MCP system is described in a previous paper. The combination of the filters and the MCP gives a pass band between 1.8 keV and 3.4 keV, which accepts Ar K–lines.

The advantage of this system is that the 1D x–ray image can be continuously recorded as it were a streak camera.

2–2 Spectral response

The spectral response of the detection system is determined by the passband of the filters and the characteristics and thickness of the scintillator plate. In this experiment, the source is imaged on to the plastic scintillator NE142 with thickness of 200 μ m through the pinhole of 0.1 mm in diameter and combination filter of Be and Ag whose thickness are 25 μ m and 1 μ m, respectively. The magnification of the image is 1/3. The calculated spectral response of this system is shown in Fig. 2. The effective passband of the system between 2.5 keV and 3.5 keV accepts Ar K–shell radiation.

2–3 Spatial resolution

The x–ray source and the detector system is illustrated in Fig. 3a). The arrayed slits perpendicular to the electrode axis allows to resolve spatially in the axial direction. However, the signal from the each channel is spatially integrated in the radial direction. The overall spatial resolution of each channel is determined by the diameter of the pinhole, the magnification of the image on the scintillator, the thickness of the scintillator and the width of the slit. In this case, estimation of the spatial resolution is usually carried out using the point spread function (PSF) as a figure-of-merit.[3] In this system, PSF is calculated as shown in Fig. 3b). Therefore, it is seen that the visible light through the slit is calculated as a function of the source location as shown in Fig. 4. The view field of each channel can be considered to be FWHM of the function. For L1 = 441 mm, L2 = 147 mm, d = 0.1 mm, t = 0.2 mm, and w = 0.1mm, FWHM is estimated to be 1.3mm.

2–4 Temporal resolution

There are several origin to limit the temporal dispersion in this system. They include the decay time of the scintillator, the response of the photomultiplier, the dispersion of the fiber–optic, and the response of the transmission line. A measurement of the impulse response of this system was made with a TEA N_2 laser (< 1 nS FWHM). The light was exposed removing the pinhole and filter of the system. The impulse response was ~ 5.2 nS (FWHM) and was in agreement with a predicted value of ~ 5 nS. It is considered that the decay time of the scintillator (2.5 nS) and the response of the photomultiplier (rise time ~ 3 nS) are dominant factors for the temporal resolution. Differences of the transit time of each channel were observed to be less than 2 nS(max.).

2–5 Dynamic range

Outputs from each channel were calibrated absolutely by means of the quantitative pinhole camera with a pulsed, soft x–ray source at plasma focus device. The absolute value of the calibration is 4.2×10^{-20} [I/{photons/mrad^2 •s}] at a bias voltage of 1650 V which I in Ampere is the output current of the photomultiplier.

The lower limit is determined by the quantization error of the oscilloscope and the dark count of the photomultiplier. The oscilloscope used in this experiment can accurately resolve 1.25 mV, including its own noise. This gives the lower detection limit of 1.7×10^{14}

photons/{mrad ^{2} •s}. On the other hand, the occurrence of the dark count larger than 1 mV which should affect measurements is negligible (< 100 counts/s) at room temperature.

The saturation effect of photomultiplier (−10 % at the output current of 50 mA) limits the linear response of the system up to 1.2×10^{18} photons/{mrad ^{2} •s}.

2–6 Soft x–ray source and monitor system

A Mather type plasma focus device with a squirrel cage outer electrode was employed to produce a high energy density plasma. The diameters of coaxial are 50 and 100 mm. The lengths of outer–and inner electrode were 230 and 280 mm, respectively. The condenser bank consisted of 28 × 1.56 μ F, 80 kV capacitors. The device is usually operated at the bank voltage of 50 kV and a gas pressure of 6 Torr hydrogen. However, to obtain intense soft x–ray emission argon was puffed with a fast acting valve through the inner electrode immediately before each discharge. When the bank is operated at 50 kV, the current in the plasma column was 0.8 MA at its peak approximately.

The soft x–ray pulse is monitored with an x–ray pin diode with the same foil filters as the pinhole camera. The view field of the diode contains the whole pinched plasma. The alignment of the diagnostic tools is shown in Fig. 5.

§ 3 Performance of the system

Examples of the experimental results obtained with the system is shown in Figs. 6a) and 6b). It was observed that there were two types of the soft x–ray sources. In Fig. 6a), a pinhole picture of hot spots, which are highly localized intense soft x–ray sources, are recognized. Six photomultiplier signals are shown in Fig. 6b). This indicates that the hot spots near the electrode face appear in the earlier phase and are successively generated toward the electrode axis. The "propagation velocity" was estimated to be 2 × 10 ^{7} cm/s. On the other hand, a filamentry soft x-ray source was observed in the example as shown in Fig. 7a). There are no time difference between the upper and lower ends as recognized from Fig. 7b).

The time of appearance of the hot spots which is observed in a lot of discharges is shown in Fig. 8 as the function of distance from the electrode face. Similar results were obtained by authors. 4) The system which we developed is suffient in temporal and spatial resolution for determining the time of hot spots appearance.

References

1 J. M. Bayley, G. Decker, W. Kies, M. Malzig, F. Muller, P. Rowekamp, J. Westheide and Y. V. Sidelnikov: J. Appl. Phys. 69 (1991) 613

2 Y. Takahama, J. Du, T. Yanagidaira and K. Hirano: Rev. Sci. Instrum. 65 (1994) 2508

3 D. L. Fehl, R. J. Leeper, J. R. Lee, M. A. Hedemann, W. A. Styger, B. R. Sujka, D. E. Hebron, S. J. Robischon and B. P. Peyton: Rev. Sci. Instrum. 65 (1994) 1935

4 H. Schmidt, D. Schulz and P. Antsiferov: AIP Conf. Proc. 299 DENSE Z-PINCHES, London, 1993 (AIP Press, New York, 1994) p. 348

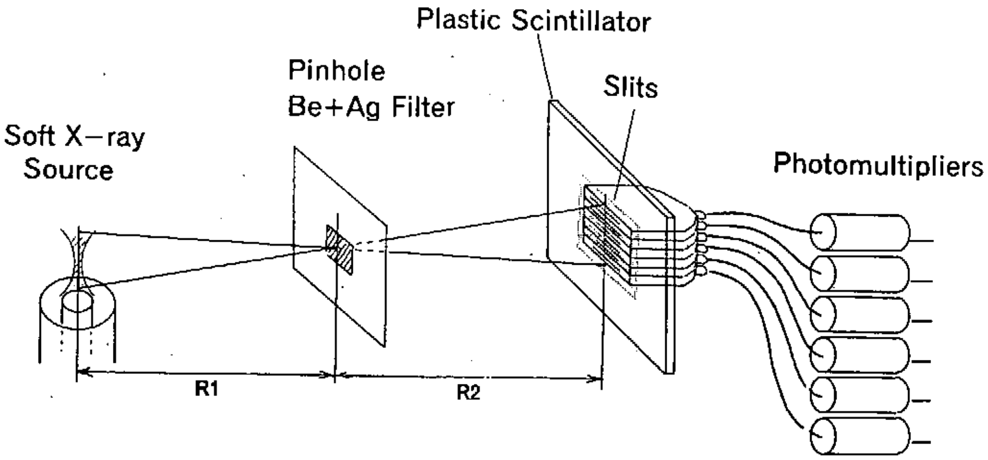

L1=441 mm, L2=147 mm (L2/L1=0.33)
Be filter 25 μ m
Ag filter 1 μ m
Diameter of Pinhole d=0.1mm
Thickness of Plastic scintillator t=0.2mm
Slit width w=0.1mm

Fig.1 Schematic diagram of detection system.

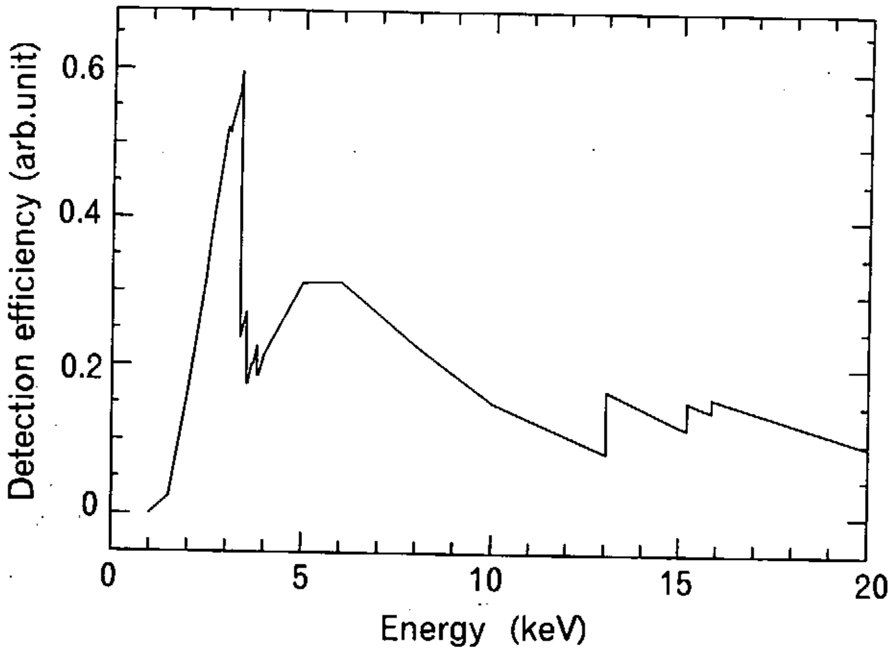

Fig.2 Calculated spectral response.

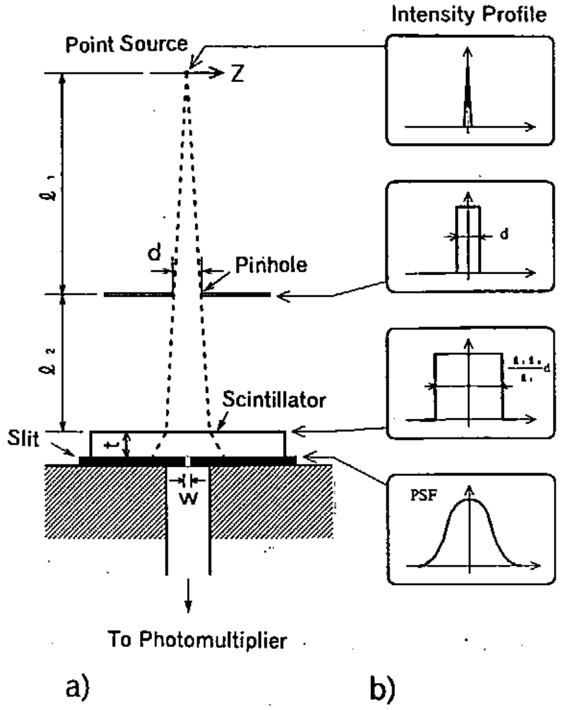

a) b)

Fig.3 Calculation of spatial resolution.

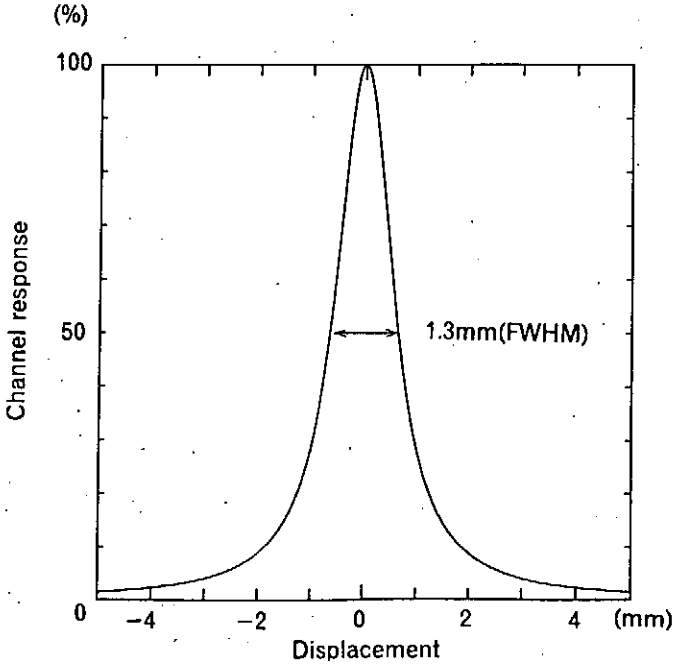

Fig.4 Channel response as a function of source location.

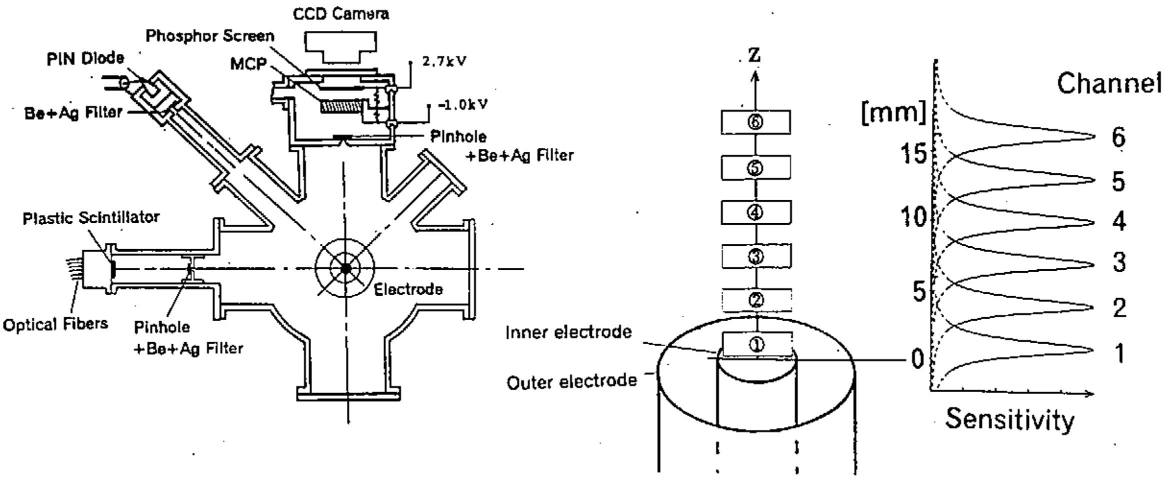

View field of each channel .

Fig.5 Alignment of the diagnostic tools.

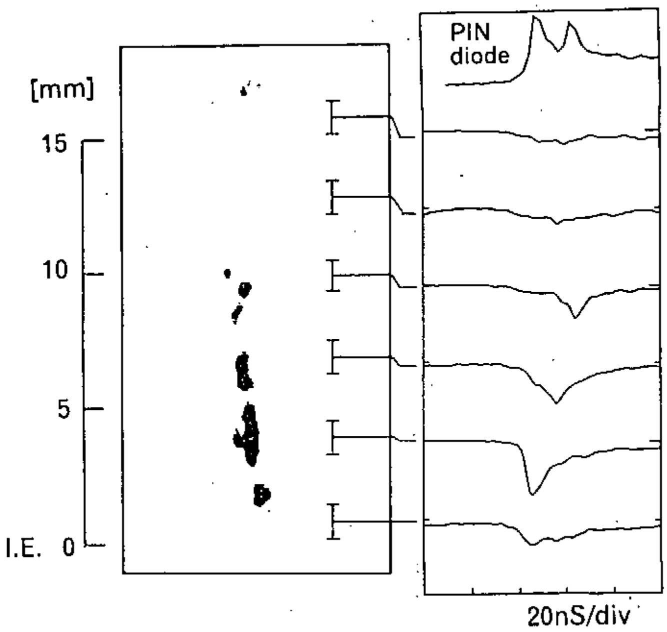

a) Pinhole image b) Photomultiplier signals

Fig. 6 Example of the pinhole image together with the oscilloscope traces showing the time history of the x-ray emission. Several hot spots are observed.

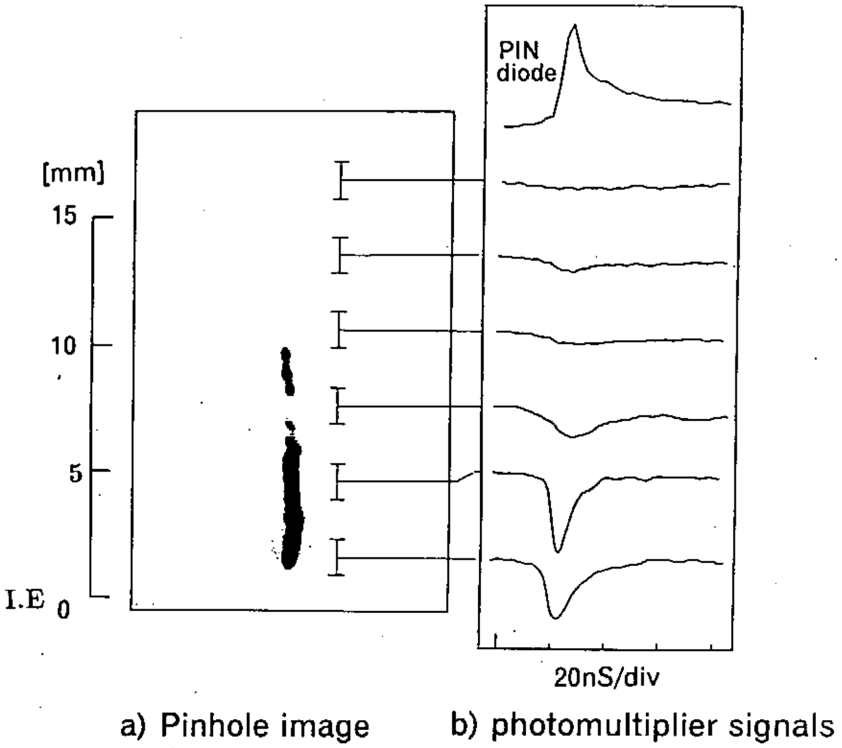

a) Pinhole image b) photomultiplier signals

Fig.7 Example of a filamentry shaped source.

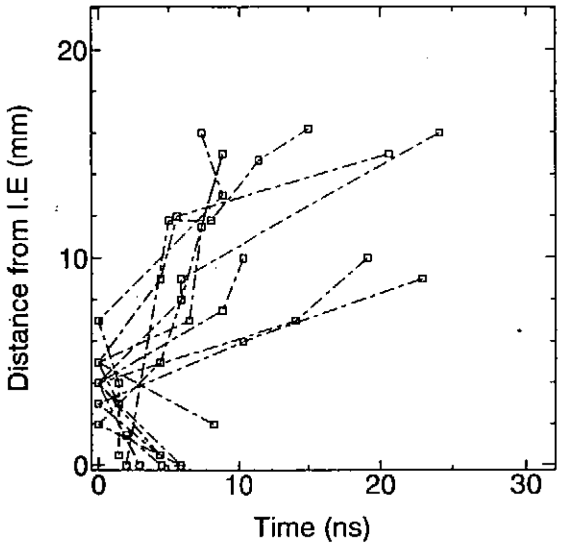

Fig.8 Time of appearance of the hot spots as a function of distance from the electrode face.

Hot Spots Characterization in Gas Puffed Z-Pinch Experiment

Jian Du, Hiroyuki Oba, Tetsuya Ohata, Yoshio Takahama, Katsuji Shimoda
and Katsumi Hirano
Department of Electronic Engineering, Gunma University
Kiryu, Gunma 376, Japan

Synopsis

Soft X-rays generated with a gas puff pinch device is characterized using a pinhole camera which enables a quantitative intensity measurement, a Bragg imaging spectrometer and a X-ray diode. A line density of neutral Ar gas N = 8.1 × 10^{17} atoms/cm (M = 5.5 × 10^{-5} g/cm) was formed between the electrodes with an interferometric observation. The soft X-rays were emitted for about 10 ns in the early stage of the plasma column formation. Highly localized and intense soft X-ray sources, hot spots were observed in the pinch plasma. The emitted energy was estimated to be 50 ± 15 J/4 π str, for Ar K-line. The reproducibility of the X-ray emission are displayed.

§ 1 Introduction

The gas puff pinch plasma has received considerable attention because of its high energy conversion efficiency into the soft X-ray radiation.[1, 2] Moreover, H, He and Li-like ions of high atomic number gases are easily produced with reasonable reproducibility in that plasma, and so it is possible to obtain intense line emission in the soft X-ray range. Wavelength of the soft X-ray can be chosen by changing the puffed gas. The pinched plasma acquires interest in soft X-ray sources of the X-ray microlithography, the X-ray microscopy for live and biological specimenes and the driver of the soft X-ray laser excitation.[3~9]

Various proposals have been made to explain mechanism of the soft X-ray emission in the z-pinch, but still it is not well understood. In this paper, we intend to characterize the soft X-ray source, so called the hot spot, in the pinched plasma which usually appears as a series of highly localized intense soft X-ray emitting regions.[10] Quantitative measurement of the soft X-ray intensity has been carried out, for example, using a calorimeter with unsatisfied accuracy so far. In this paper an intensity measurement of the soft X-ray spots is made using a pinhole camera system with which a quantitative measurement is possible.[11] Reproducibility of the soft X–ray emission in the gas puff pinch, which is frequently claimed without definite evidence is discussed.

§ 2 Apparatus

A schematic diagram of the gas puff z pinch system is shown in Fig. 1. The gas valve is typically operated at a pressure of 5 atm of argon. The iron hammer is accelerated along the stem by an electromagnetic force generated by a coil which consists of 300 turns of 66 mm diameter copper wire and is energized by a 330 μ F capacitor charged to 1 kV. The valve is opened by an impact of the hammer at the stem end. The working gas is puffed with the fast valve through 8 De Lavor nozzles which are located around a circumference of 46mm in diameter. The density of the puffed gas was measured by a Mach–Zehnder interferometer in which a ruby laser is employed as the light source.

The capacitor bank for the gas puff pinch discharge consists of 18 × 2.2 μ F, 30 kV capacitors. Each capacitor is switched by a pressurized spark gap. Gas is injected from an array of nozzles which are made on the circumference 4.0 mm in diameter. The delay time between the valve open and the fire of the spark gaps is chosen to obtain the maximum intensity of the soft X–ray. The discharge current were measured with a Rogowski coil. The current and its ringing frequency are 470 kA and 120 kHz when the bank is charged at 20 kV.

For diagnosis for the pinched plasma several tools are used such as a pinhole camera, a crystal spectrometer, X–ray diode and an image converter camera in streak mode for visible light.

A Bragg imaging spectrometer is employed to obtain a monochromatic image of the soft X–ray source in the pinched plasma. The spectrometer makes it possible to produce a monochromatic soft X–ray image without influence of position fluctuation of the X–ray sources from shot to shot. A flat RAP (rubidium acid phthalate) crystal whose 2d length is 26.12 Å is employed. The resolution power of the spectrometer is ~ 1000 around 4 Å which corresponds to the argon K–lines. The soft X–ray image is recorded on a film, Kodak TRI–X.

A soft X–ray pinhole camera with a quantitative image acquisition system is developed for soft X–ray image observation with time resolution.[12] A pinhole image of the X–ray source is made on the MCP through a pinhole and Be and Ag foil filters (25 μ m and 1 μ m in thickness, respectively) which prevent the visible light also emitted from the source. The spectral response of the MCP system is described in a previous paper.[13] The combination of the filters and the MCP gives a pass band between 3.7 and 7 Å, which accepts Ar K-lines. The photoelectrons produced by the X-rays on the MCP are multiplied by the MCP and accelerated onto the phosphor screen to produce an image of the visible light. The visible image formed on the phosphor screen is registered in an image memory board in 8 bits through a CCD camera. A preferable data processing, such as the 3-D display, is possible by using a personal computer.

The electrons, which are emitted from the MCP and carrying image information, are measured as the phosphor screen current simultaneously. This allows not only to obtain a quantitative relationship between intensity of visible image and the electron number, but also to carry out an effective time resolved observation. Therefore, We can evaluate number of the photons which pass through the pinhole after taking absorption by the metal foils into account.

The soft X-rays are monitored with a window removed PIN diode which is coupled with a set of filter (25 μ m Be and 1 μ m Ag). The viewing field of the diode is limited by a collimator to only the plasma produced by the discharge. The calculated response of the filtered PIN diode, the MCP-filter combination which is used as the detector in the pinhole camera, and the Be-Ag combination filter are shown in Fig. 2. It is recognized that the pinhole camera is not sensitive for the wavelength longer than 7 Å. When the combined filter of Be (25 μ m) and Ag (1 μ m) is adapted the soft X-ray output window for exposure of the photoresist, hard X-rays whose wavelength are shorter than about 2 Å might pass througth the window.

The dynamic behavior of the plasma was also monitored by an image converter camera in streak mode of the visible emitted light. The alignment of the diagnostic tools is shown in Fig. 3.

§ 3 Experimental Results

3-1 Ar gas puff

The fringe shift by the gas puff is shown in Fig. 4. Usually spatial distribution of physical quantities such as the spatial distribution of the gas density are derived by the Abel inversion of the shifted fringes. However the shift in our case is limited to nearly one fringe at the start of the z-discharge, and so we calculated only the mean density in the center region of interferogram as pointed for the arrows in Fig. 4.

If we assume d is the thickness of the gas shell, the fringe shift is given as

$$S(x) = \frac{2}{\lambda}\int_0^d \{\mu(x) - 1\}dx$$

where μ (x) is the refractive index of the puffed Ar, and S(x) ≈ 1 in this experiment. The refractive index is given as

$$\mu(x) = 1 + A(1 + B\lambda^{-2})\frac{n(x)}{n_s}$$

where n_s and n(x) are the neutral gas density at the standard and an arbitrary pressure, A and B are constants determined by the gas. If we assume the spatial distribution of the gas to be

$$n(x) = n_0 \sin\left(\frac{\pi}{d}x\right)$$

we obtain

$$n_0 = \lambda\frac{n_s}{A(1 + B\lambda^{-2})}\frac{1}{\int_0^d \sin\left(\frac{\pi}{d}x\right)dx}$$

When we substitute wavelength of Ruby laser, 694.3 nm and $A = 27.9 \times 10^{-5}$ and $B = 5.6 \times 10^{-11}$ for Ar, we obtain $n_s = 2.6875 \times 10^{19}$ cm^{-3}, d = 0.4 cm which is estimated by the interferogram, we obtain $n_0 = 1.5 \times 10^{-5}$ g/cm^3. Therefore, we obtain the mass per unit length, $M = 5.5 \times 10^{-5}$ g/cm or $N = 8.1 \times 10^{17}$ particles/cm. This values roughly agree with those of Ref. 14.

3-2 Plasma behavior and soft X-ray emission

Typical examples of the discharge current, the streak photograph and the soft X-ray signal obtained by the PIN diode are shown in Fig 5. The current dip coincides with the maximum compression of the plasma column and the first peak of the soft X-ray signal. The plenum pressure and the delay time between the valve opening and the start of the z-discharge are adjusted to obtain a high emission of the soft X-ray.

The pinch velocity of the plasma is ~ 7×10^6 cm/s immediately before the maximum compression. The minimum radius of the plasma is less than 1 mm which typically continues for ~ 100 ns. The plasma column is decayed by instabilities seems to be m = 2 type. Several soft X–ray pulses are observed with the PIN diode. The first one was detected at the maximum compression as mentioned above and second pulse appeared in ~ 20 ns after the first one.

3–3 Soft X–ray source and spectrum

More than 100 shots of the soft X–ray image, the phosphor current and, X–ray spectrogram were collected by a simultaneous measurement. An example is shown in Figs. 6 (a) and (b) which are the simultaneously taken pinhole image and spectrograph. Four hot spots (intensity X–ray emitting region) are recognized along the electrode axis in this figure. The number of the hot spots are varied from shot to shot. Ten spots were observed at maximum.

The number of the pinhole images obtained in the spectrometer taken with the pinhole camera does not always correspond to that taken with the spectral analyzed image. However the images taken by the pinhole camera completely agree with the image formed by the spectral lines as shown in Fig. 6(b). Therefore, it can be concluded that the hot spots obtained with the pinhole camera consist of the Ar spectral lines near 4 Å .

Three lines are obviously recognized in the spectral analyzed images whose wavelengths are measured to be 3.944 ± 0.004 Å , 3.968 ± 0.004 Å , 3.990 ± 0.004 Å . It is understood each line corresponds to the resonance line (3.948 Å $1s^2-1s2p\ ^1P_1$), the intercombination (3.966 Å $1s^2-1s2p\ ^3P_1$) and Ar XVII the group of dielectronic satellite lines[15] .

The intensity of the spots observed by the pinhole camera can be quantitatively displayed after data processing which is described in Ref. 11.

In general, photographic film is known to exhibit reciprocity failure for exposure time shorter than 1ms. The validity of applying the results obtained with a continuous X–ray source to those obtain pulsed X–rays has to be checked. However, the reciprocity failure is ignored for the lack of alternation method in this experiment.

Figure 7(a) and (b) show the cases in which the hot spots were recorded in different shots. The pinhole image and the spectral analyzed image were taken in the same shot simultaneously. It is recognized that the pinhole images and the spectral images appeared at the same location on the electrode axis. This also suggests that the hot spot consist of the spectral lines near 4 Å as mentioned above.

3-4 The soft X-ray output and reproducibility

For the typical 20 shots the soft X-ray out puts around 4 Å into 4 π steradian around are tabulated in Table 1 with I_0, Δ I, the time up to the maximum compression and number of the hot spots. It was recognized that the hot spots from 1 to 7 appeared shot to shot. However, it was not found any correlation between the numbers of hot spots and the total output of the soft X-rays.

The average output of the soft X-rays was 50 ± 15 J/4 π str. We also evaluated the X-ray intensity to be 10 ± 3 mJ/cm ^{2} at output window which mounted on the electrode axis and at 20 cm from the electrode face. This value is quite sufficient to obtain enough exposure of photoresist for the microlithography.

Reference

1) P. G. Burkhalter, J. Shiloh, A. Fisher and Robert D. Cowan: J. Appl. Phys. **50** (1979) 453.
2) G. Nave, C. D. Challes, A. E. Dangor and J. G. Lunney: J. Appl. Phys. **65** (1989) 3385.
3) Y. Kato, I. Ochiai, Y. Watanabe and S. Murayma: J. Vac. Sci. Technol. **B6** (1988) 195.
4) J. Bailey, Y. Ettinger, A. Fisher and R. Feder: Appl. Phys. Lett. **40** (1982) 33.
5) N. P. Economou and D. C. Flanders: J. Vac. Sci. Technol. **19** (1981) 868.
6) J. S Pearlman and J. C. Riordan: J. Vac. Sci. Technol. **19** (1981) 1190.
7) R. Feder, J. S. Pearlman, J. C. Riordan and J. L. Costa: J. Microscopy. **135** (1984) 347.
8) R. Feder, V. Banton, D. Sayre, J. Costa, M.Baldini and B. Kim: Science. **227** (1985) 63.
9) S. Maxon, P. Hagelstein, K. Reed and J. Scofield: J. Appl. Phys. **57** (1985) 971.
10) K. Hirano, N. Hisatome, T. Yamamoto and K. Shimoda: Rev. Sci. Instrum. **65** (1994) 3761.
11) Y. Takahama, J. Du, T. Yanagidaira and K. Hirano: Rev. Sci. Instrum. **65** (1994) 2505.
12) K. Hirano, Y. Takahama, M. Han and T. Yanagidaira: J. Phys. Soc. Jpn. **63** (1994) 365.
13) W. Parkes, R. Gott and K. A. Pounda: IEEE Trans. Nucl. Sci. **NS-17** (1970) 360.
14) A. E. Robson: Phys. Fluids. **B3** (1991) 1461.
15) N. J. Peacock, R. J. Speer and M. G. Hobby: J. Phys. B:**2** (1969) 798.

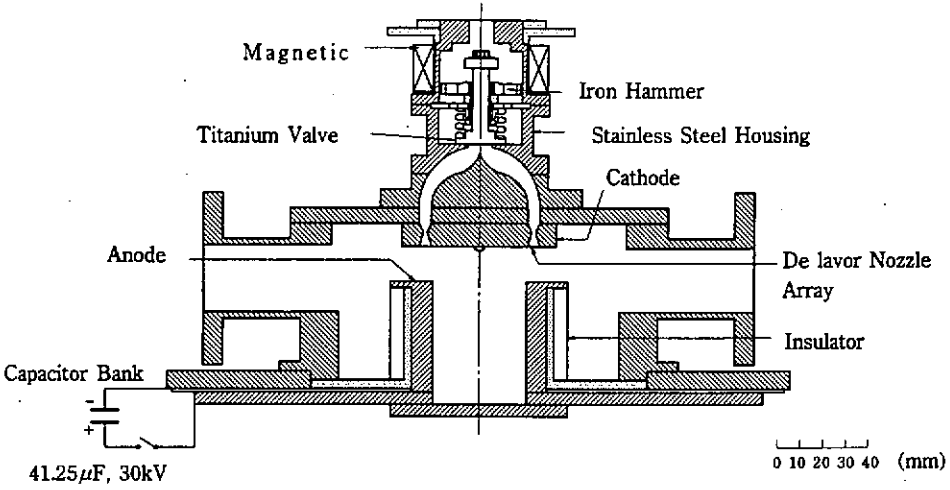

Fig. 1 Cross sectional view of the gas puff pinch device

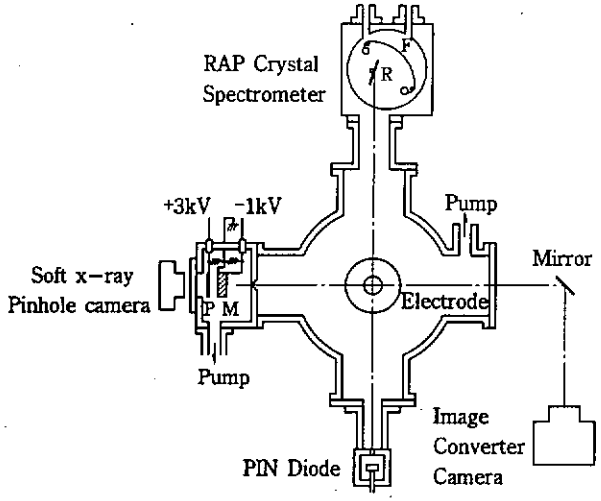

Fig. 3 Schematic diagram of the diagnostic tools

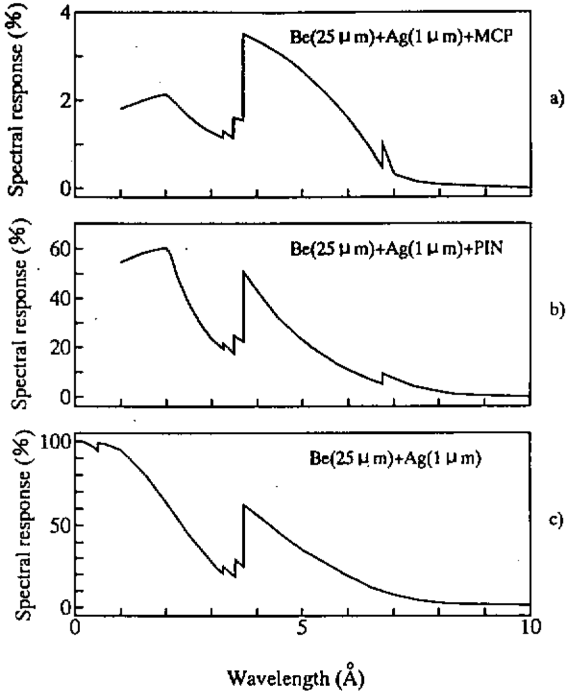

Fig.2 Spectral response of the pinhole camera a), the filtered X-ray PIN diode b) and the output window for the soft X-ray c)

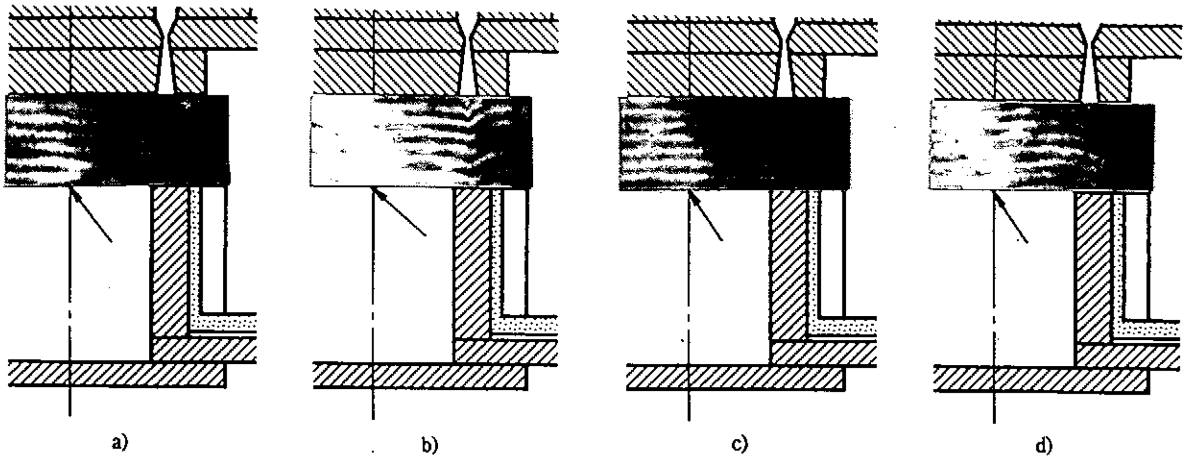

Fig.4 Interferograms of puffed neutral argon and the electrodes. The interferograms are taken at 3.7ms a), 4.0ms b), 4.3ms c) and 5.1ms d) after the start of valve current.

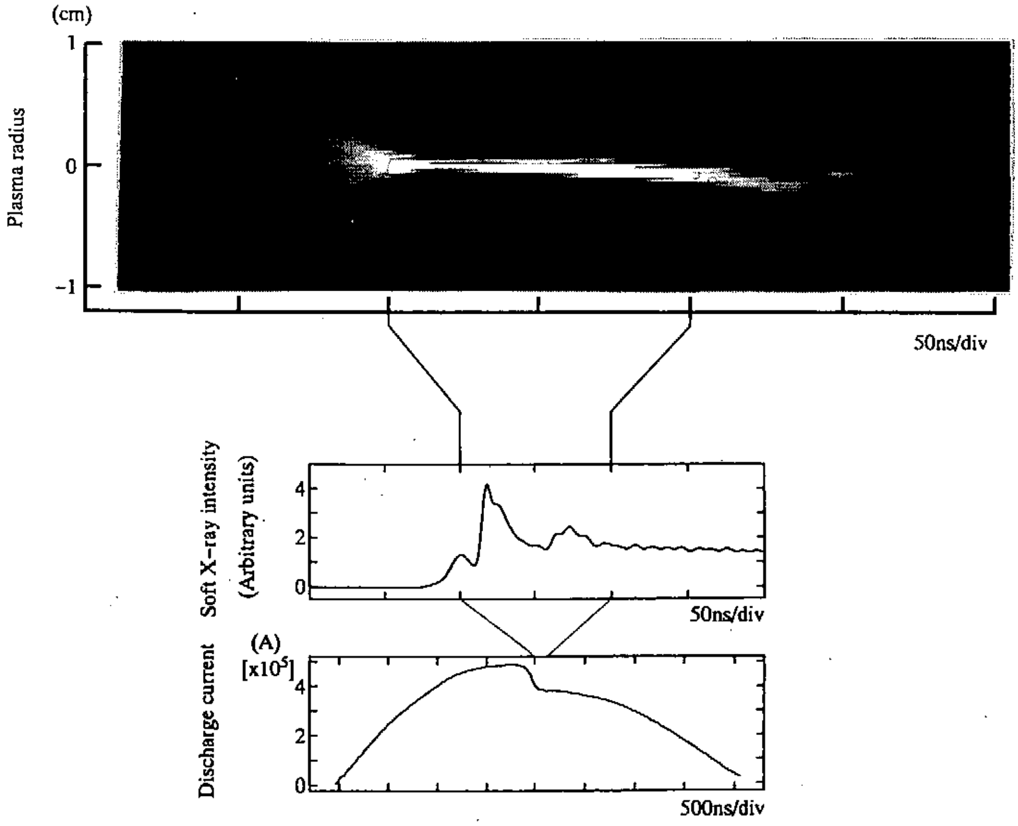

Fig.5 Time correlation between the plasma behavior, the soft X-ray emission and the discharge current

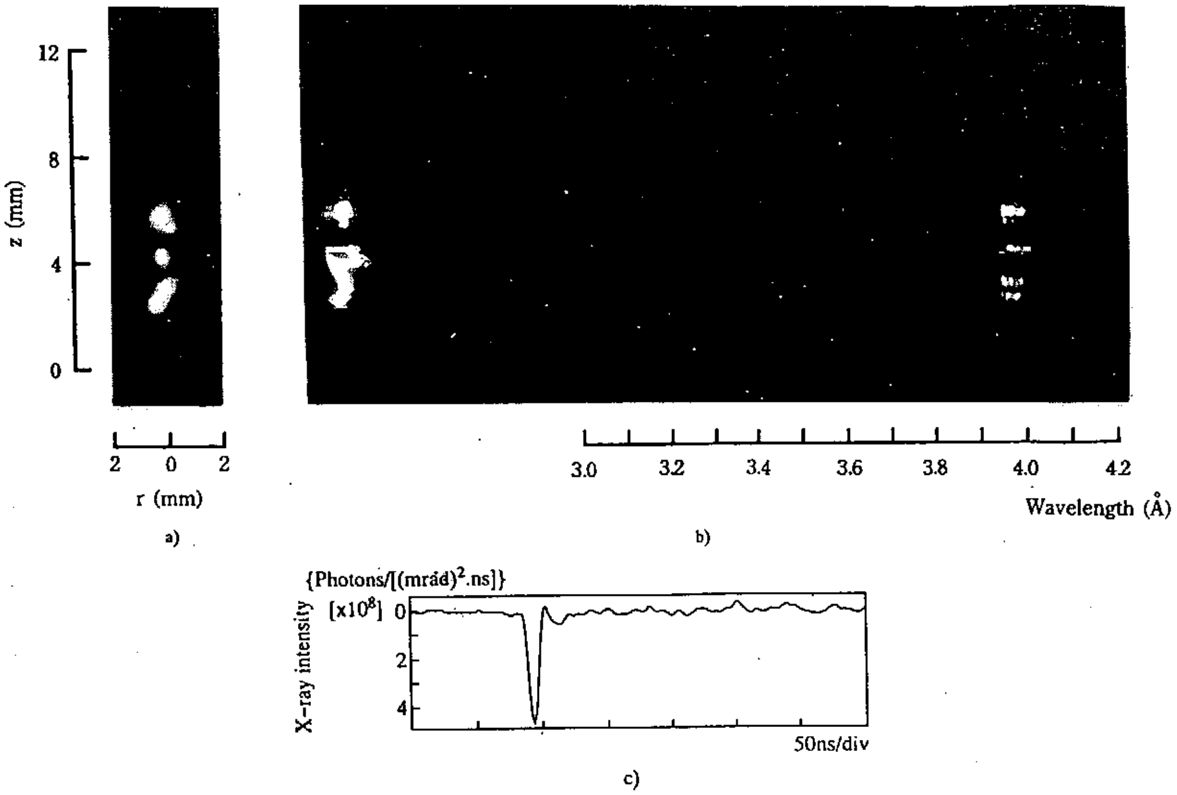

Fig.6 Examples of the hot spots. Hot spots observed simultaneously with the pinhole camera a), the imaging spectrometer b). Soft X-ray intensity obtained from the phosphor current c).

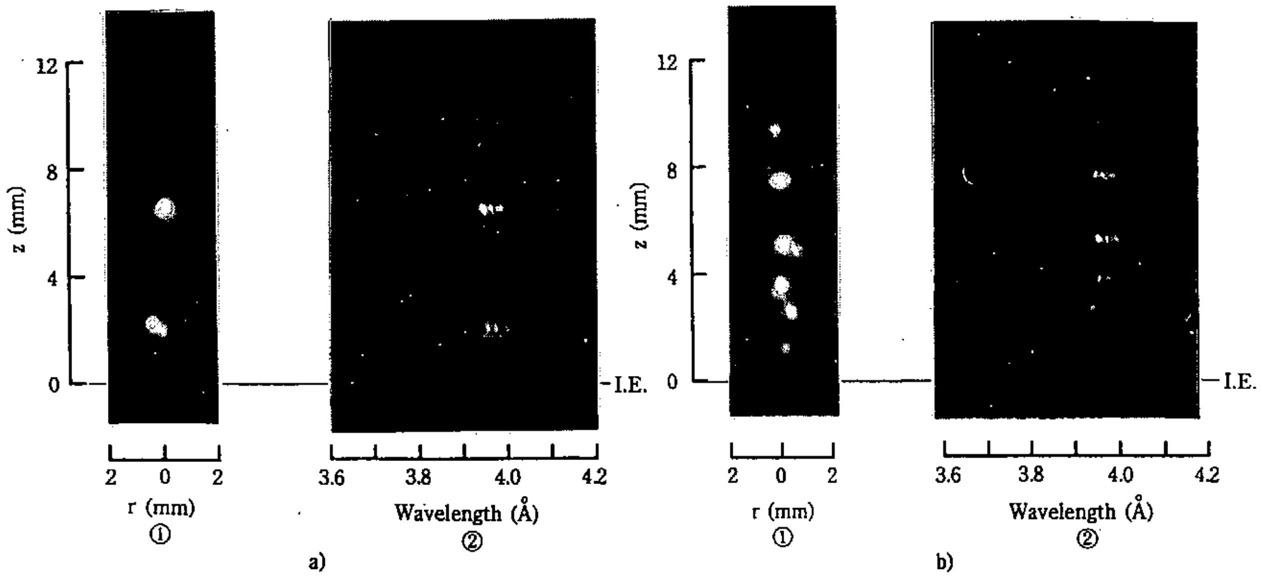

Fig. 7 Examples of the hot spots.

The pinhole image ① and the spectral analyzed images ② are simultaneously taken.

Table I Examples of the shot-to-shot variation of the intensity of Ar K line

Shot No.	Emission in 4π Str. (J)	Intensity at $L = 200$ mm on the electrode axis (mJ/cm^2)	τ_0 (μs)	I_0 (kA)	ΔI (kA)	$\Delta I/I_0$	Number of hot spot
226	32	6	1.82	467	117	0.25	3
228	36	7	1.82	490	69	0.14	2
232	48	9	1.88	490	69	0.14	2
240	67	12	1.88	490	93	0.19	3
255	46	8	1.88	444	70	0.16	2
256	32	6	1.94	444	70	0.16	3
259	74	14	1.76	467	70	0.15	7
264	47	9	1.82	467	46	0.10	1
268	54	10	1.84	467	46	0.10	3
270	65	12	1.80	467	93	0.20	2
272	79	15	1.80	514	93	0.18	5
279	90	17	1.72	490	46	0.09	4
284	51	9	1.74	514	70	0.14	2
285	54	10	1.88	444	47	0.11	2
287	53	10	1.58	467	46	0.10	2
300	51	9	1.88	467	117	0.25	2
305	62	11	1.72	514	70	0.14	2
306	46	8	1.90	467	70	0.15	3
308	52	10	2.08	421	93	0.22	2
329	46	9	1.74	467	70	0.15	3
Average	54	10	1.82	473	73	0.16	3
Standard deviation	15	3	0.10	25	22	0.05	

Enhanced stability and increased soft x-ray generation in a dense plasma focus by additional high z gas puff

Hiroyuki Kitaoka, Atsushi Sakurai, Atsushi Nonaka, Toshikazu Yamamoto,
Katsuji Shimoda and Katsumi Hirano

Department of Electronic Engineering, Gunma University
Kiryu, Gunma 376, Japan

Synopsis

A plasma focus device with a fast acting valve is designed for additional high z gas puff and is succesfully operated to produce intense soft x-rays. Using the fast acting valve, high z gas is injected to the pinch region just before the discharge to decouple the initial phase for the current sheath formation from the pinch formation phase. Quantitative measurement of soft x-ray intensity and the observation of the plasma behavior were carried out simultaneously for the additional gas puff discharge and the conventional gas embedded discharge. Experimental results show the enhancement of the plasma stability and the soft x-ray emission in two order of the intensity.

§ 1 Introduction

Soft x-ray sources with high brightness and small size are required for x-ray spectroscopy, high density lithography [1)] for the electronic device manufacture, x-ray microscope [2)] and x-ray laser pumping. [3)] The soft x-rays which suit to those purposes are successfully produced in the high energy density plasma by the z pinch devices including the plasma focus. Some of the purposes are satisfied with the SOR (synchrotron orbital radiation). However, this source is at disadvantage because of its cost performance in some cases.

To generate an intense soft x-ray, the pulse power generators are sometimes employed as the power supply to obtain a rapid rising current. In the plasma focus experiment, the plasma is carrying a heavy current at the beginning of the radial collapse already. This means that a rapid rising current is applied the collapsing plasma column at the beginning of the collapse plasma in the plasma focus.

When high z materials are admixed into hydrogen or deuterium which are normally employed in the z pinch experiment, the soft x-ray emission comes from very small region known as the hot spots or micropinches. [4)] A strongly collapsed plasma produces intense emission of soft x-rays. However, the strong collapse occurs in a narrow region of the percentage of admixed gas and the discharge voltage. This fact is brought by an in suficient current sheath formation and its poor acceleration which are essential for the strong collapse.

To avoid this difficulty, a high z gas to generate the soft x-rays is injected with a fast acting valve through the inner electrode to the pinch region just before each discharge. This makes possible to decouple the initial phase for the current sheath formation and the final phase for pinch formation. The high z gas for the additional puffing can be chosen for desirable wavelength of the soft x-rays. The intensity of soft x-rays in the discharge with additional high z gas puff was higher than that of the gas embedded discharge. In this paper, difference of the two operation mode was investigated quantitatively.

§ 2. Apparatus

A Mather type plasma focus device with a squirrel cage outer electrode was employed to produce a high energy density plasma. A cross sectional view of the plasma focus device is shown in Fig. 1. The diameters of coaxial electrodes are 50 and 100 mm. The lengths of outer-and inner electrode were 230 and 280 mm, respectively. The condenser bank consisted of 28 × 1.56 μ F, 80 kV capacitors. The device is enabled to operate in the gas embedded mode (mode 1) and high z gas puff mode (mode 2). However, to obtain much more soft x-ray emission argon was puffed with a fast acting valve through the inner electrode before each discharge. When the bank is operated at 45 kV, the current in the plasma column was 0.8 MA at its peak approximately.

For diagnosis several tools are used such as a pinhole camera, a crystal spectrometer, x-ray diode and an image converter camera in streak mode for visible light.

A Bragg imaging spectrometer 5) is employed to obtain a monochromatic image of the soft x-ray source in the pinched plasma. The spectrometer make it possible to produce a monochromatic soft x-ray image without influence of fluctuation from shot to shot. A flat RAP (rubidium acid phthalate) crystal whose 2d length is 26.12 Å is employed. The resolution power of the spectrometer is ~ 1000 around 4 Å which corresponds to the argon K-lines. The soft x-ray image is recorded on a film, Kodak TRI-X.

A soft x-ray pinhole camera with a quantitative image acquisition system 6) has been developed for soft x-ray image observation with time resolution. A pinhole image of the x-ray source is made on the MCP through a pinhole and Be and Ag foil filters (25 μ m and 1 μ m in thickness, respectively) which prevent the visible light also emitted from the source. The spectral response of the MCP system is described in a previous paper. 6) The combination of the filters and the MCP gives a pass band between 3.7 and 7 Å , which accepts Ar K-lines.

The photoelectrons produced by the x-rays on the MCP are multiplied by the MCP and accelerated onto the phosphor screen to produce an image of the visible light appears. The visible image is registered in an image memory board in 8 bits through a CCD camera. A preferable data processing, such as the 3D display, is possible by using a personal computer.

The electrons, which are emitted from the MCP and carrying image information, are measured as the phosphor screen current simultaneously. This allows not only to obtain a quantitative relationship between intensity of visible image and the electron number, but also to carry out an effective time resolved observation. Therefore, we can evaluate number of photons which pass through the pinhole after taking absorption by metal foil into account.

The response of the filtered PIN diode and the MCP-filter combination which is used as the detector in the pinhole camera are calculated. When the combined filter of Be(25 μ m) and Ag(1 μ m) is adapted to the soft x-ray out window, hard x-rays whose wavelength are shorter than about 2 Å might passed through the window.

The soft x-rays are monitored with a window removed PIN diode which is coupled with a set of filter (25 μ m Be and 1 μ m Ag). The viewing field of the diode is limited by a collimator to only the plasma produced by the discharge. The dynamic behavior was also monitored by an image converter camera in streak mode.

A Mach-Zehnder Interferometer in which a N_2 laser was used as a light source was employed to obtain the spatial distribution of electrons.
The alignment of the diagnostic tools is shown in Fig. 2.

§ 3 Experimental results and discussion

3-1 Stability enhancement and hot spots formation

Plasma behavior and hot spots are simultaneously observed for the cases of the mixed gas embedded (mode 1) and the additional gas puffed operation (mode 2). Typical results are shows in Figs. 3 a) and b). It is obviously seen from the streak photographs ① in Fig. 3 that the life time of the pinched plasma with the additional gas puffing is much longer that of the gas embedded mode. It can be pointed that the high z plasma compressed by the hydrogen current sheath is enhanced its stability.

In the previous paper we developed a method to describe the phosphor current as the absolute intensity of the soft x-ray intensity. The phosphor current in the mode 2 is 20 times higher than the mode 1 as shown in Fig. 3 ②. However, almost the same pulse widths are observed for the both modes.

It is shown in Fig 3 ③ that a lot of hot spots whose diameters are less than 1 mm appeared on the electrode axis in mode 2, whereas only one or two spots were observed in the mode 2. After the image processing for the 3D display using the pinhole camera system we obtain Fig. 3 ④. An absolute unit for the vertical axis is given with the system.

For the x-ray microscope and micro lithography it is desired that the x-ray source is generated at a fixed location from shot to shot. We can estimate the x-ray emission in the axial direction using Fig. 3 ④. Calculated results for operation mode 1 and 2 are shown in Fig. 4. We recognize that the photon number which are emitted to the axial direction in the mode 2 is one order higher than that of the mode 1.

3–2 Plasma dynamics

A time correlation between soft x–ray emission and the macroscopic plasma behavior which were obtained with the Mach–Zehnder interferometer is shown in Fig. 5. The HWHM of the soft x–ray pulse is ~ 10 ns. It is recognized that the soft x–ray emission begins at the maximum compression of the plasma column. The emission continued until the plasma column disrupted by growth of the $m = 0$ instabilities.

Figure 6 shows the relation between the interferogram of the plasma column a) and the location of the hot spots b) in the mode 2 (taken in the shot of Fig. 5 ⑤). It is seen that the strongly constricted part of the plasma column in a) which is pointed by ① is identical with one of the hot spots ①' in b) in their location. The locations of the hot spots except ①' did not correspond to the constricted part. This ascribed to the exposure time of the pinhole camera system. Whereas the hot spots generated for nearly 10 ns, the pulse width of N_2 laser which is used as the light source of the interferometer is less than 1 ns.

The hot spot were also observed with the time integrated spectrometer as shown in Fig. 6 c). We recognize that each location of the hot spots on the electrode axis is identical with each spectral analyzed image in c). This means the soft x–rays emitted from the hot spots consist of Ar K lines near 3.499 A.

References

1 J. S. Pearlman and J. C. Riordan: J. Vac. Sci. Technol. 19 (1981) 1190.

2 R. Feder, J. S. Pearlman, J. C. Riordan and J. L. Costa: J. Microscopy 135 (1984) 347.

3 J. L. Porter, R. B. Spielman, M. K. Matzen, E. J. McGuire, L. E. Ruggles and M. F. Vargas: Phys. Rev. Lett. 68 (1992) 796.

4 R. Lebert, A. Engel, K. Gäbel, D. Rothweiler, E. Förster and W. Neff: *Dense z–Pinches Third International Conference* eds. M. Haines and A. Knight (AIP Press, New York, 1993) p. 324.

5 K. Hirano, N. Hisatome, T. Yamamoto and K. Shimoda: Rev. Sci. Instrum. 65 (1994) 3761.

6 Y. Takahama, J. Du, T. Yanagidaira and K. Hirano: Rev. Sci. Instrum. 65 (1994) 2505.

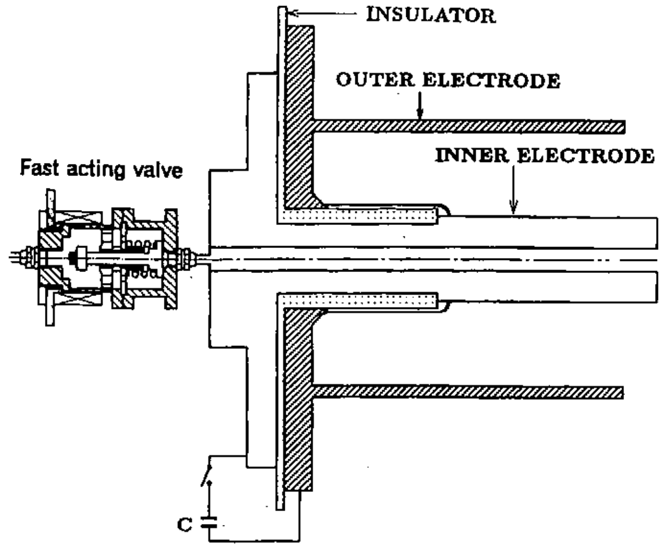

Fig. 1 Cross sectional view of the plasma focus device with a additional gas puff

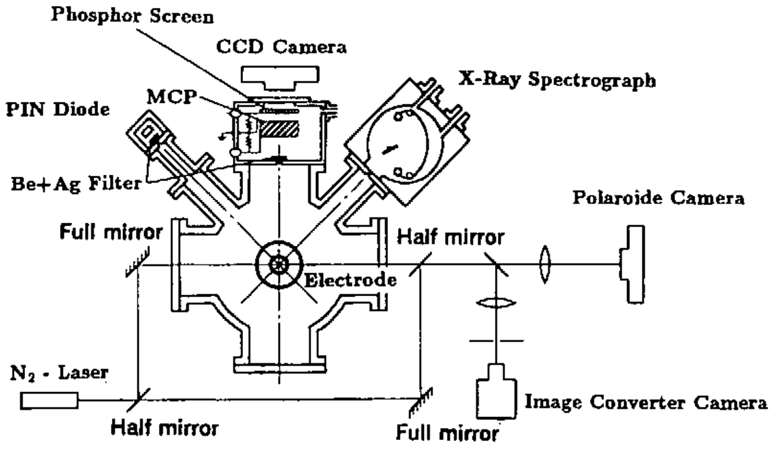

Fig. 2 Alignment of diagnostic tools

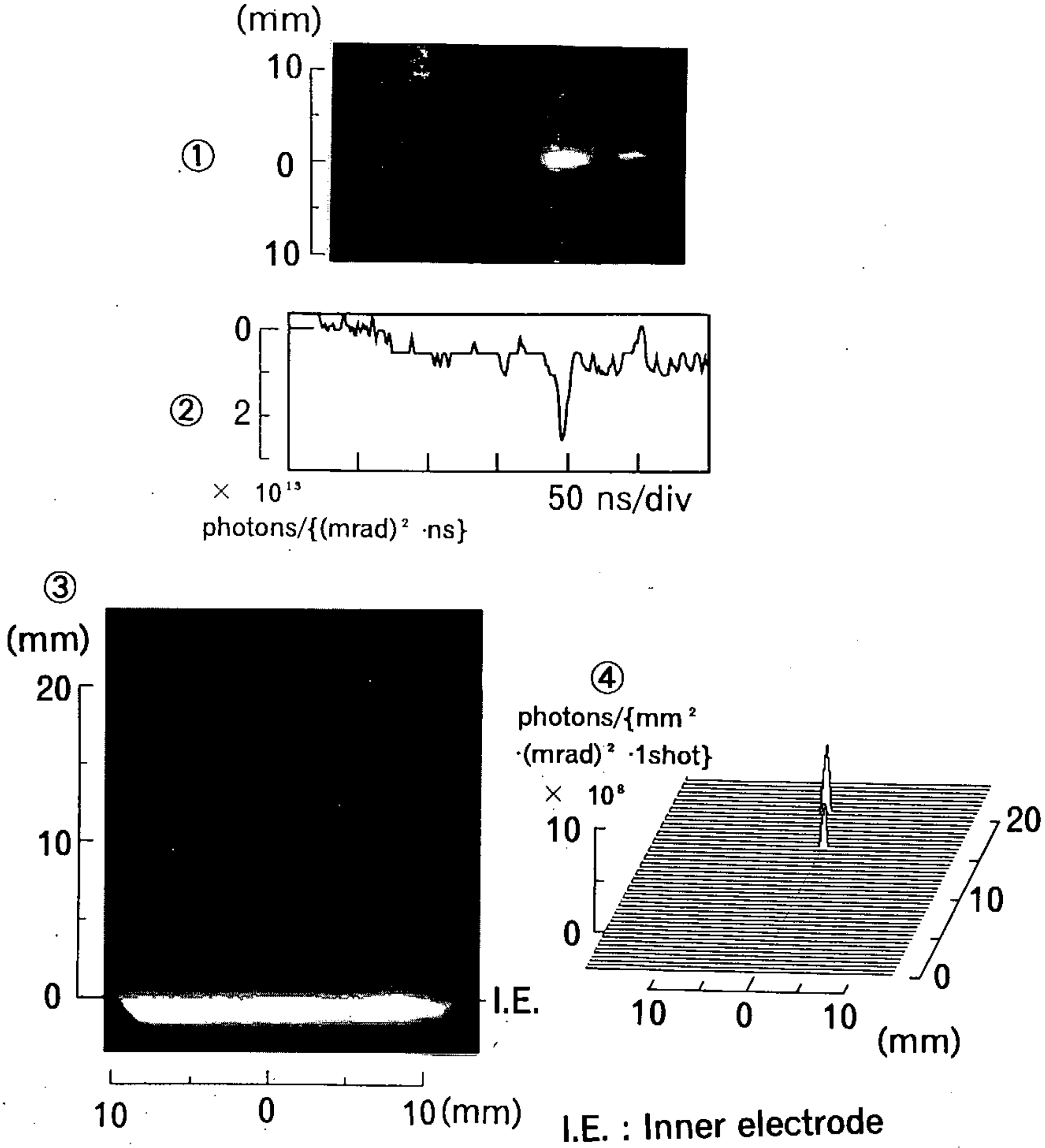

Fig. 3 Correlation between the macroscopic behavior of the plasma

a) The mixed gas embedded

① Streak photograph

② Phosphor current

③ Time integrated soft x-ray pinhole image

④ Spatial distribution of intensity in 3D display

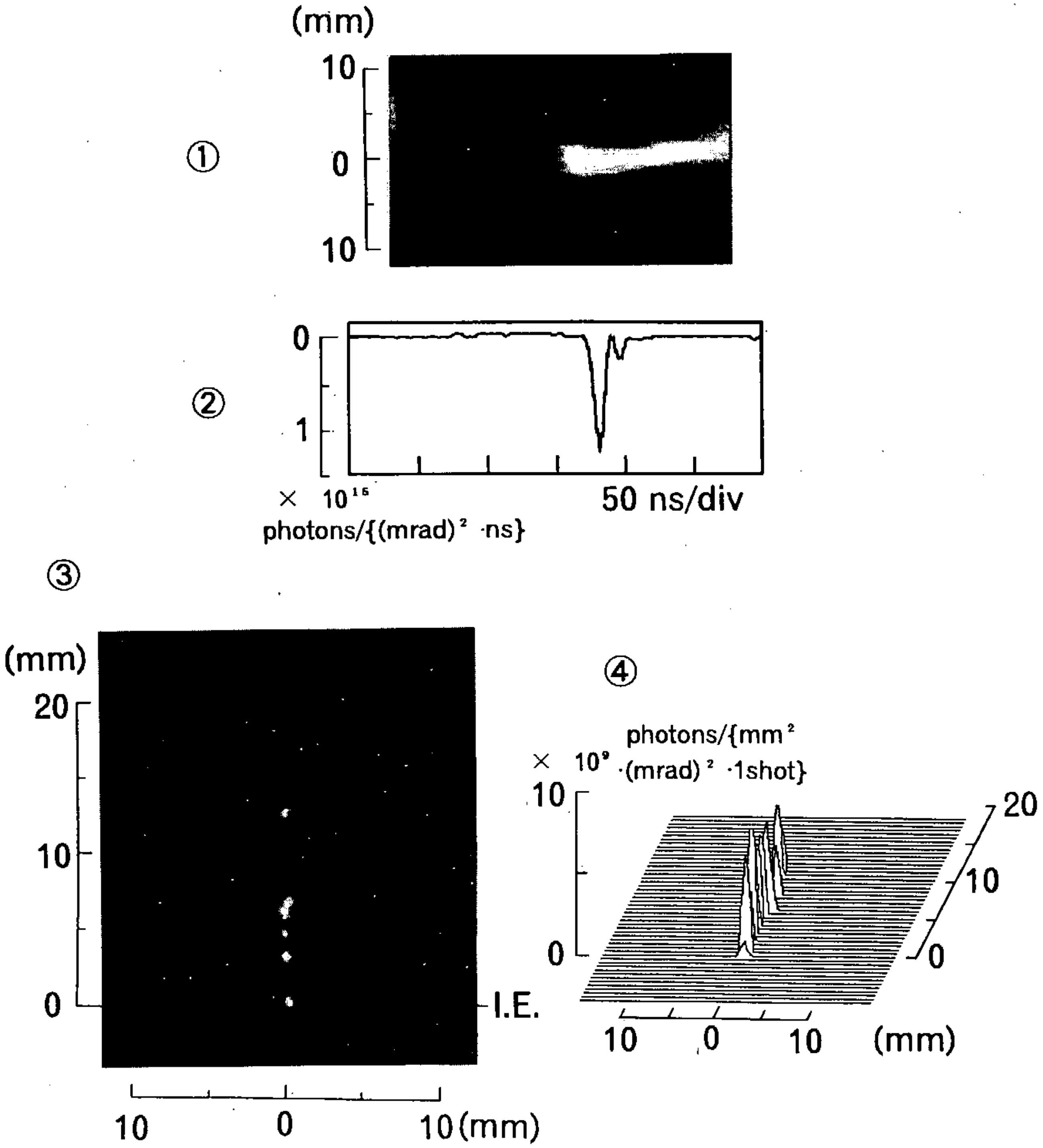

Fig. 3 b) The additional gas puffed

① Streak photograph
② Phosphor current
③ Time integrated soft x–ray pinhole image
④ Spatial distribution of intensity in 3D display

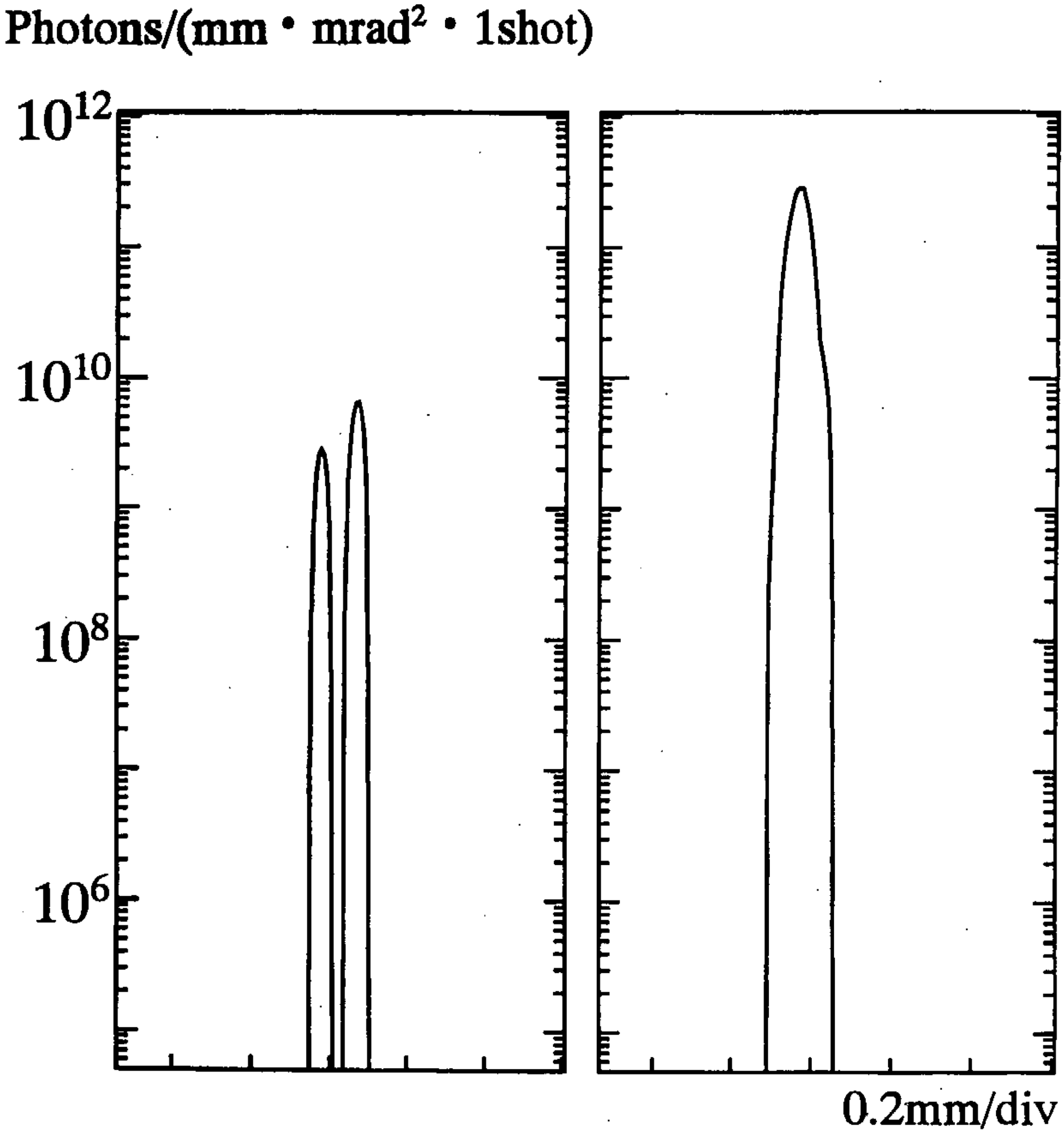

a) b)

Fig. 4 Estimation of the soft x−ray emission in the axial direction
a) The mixed gas embedded
b) The additional gas puffed

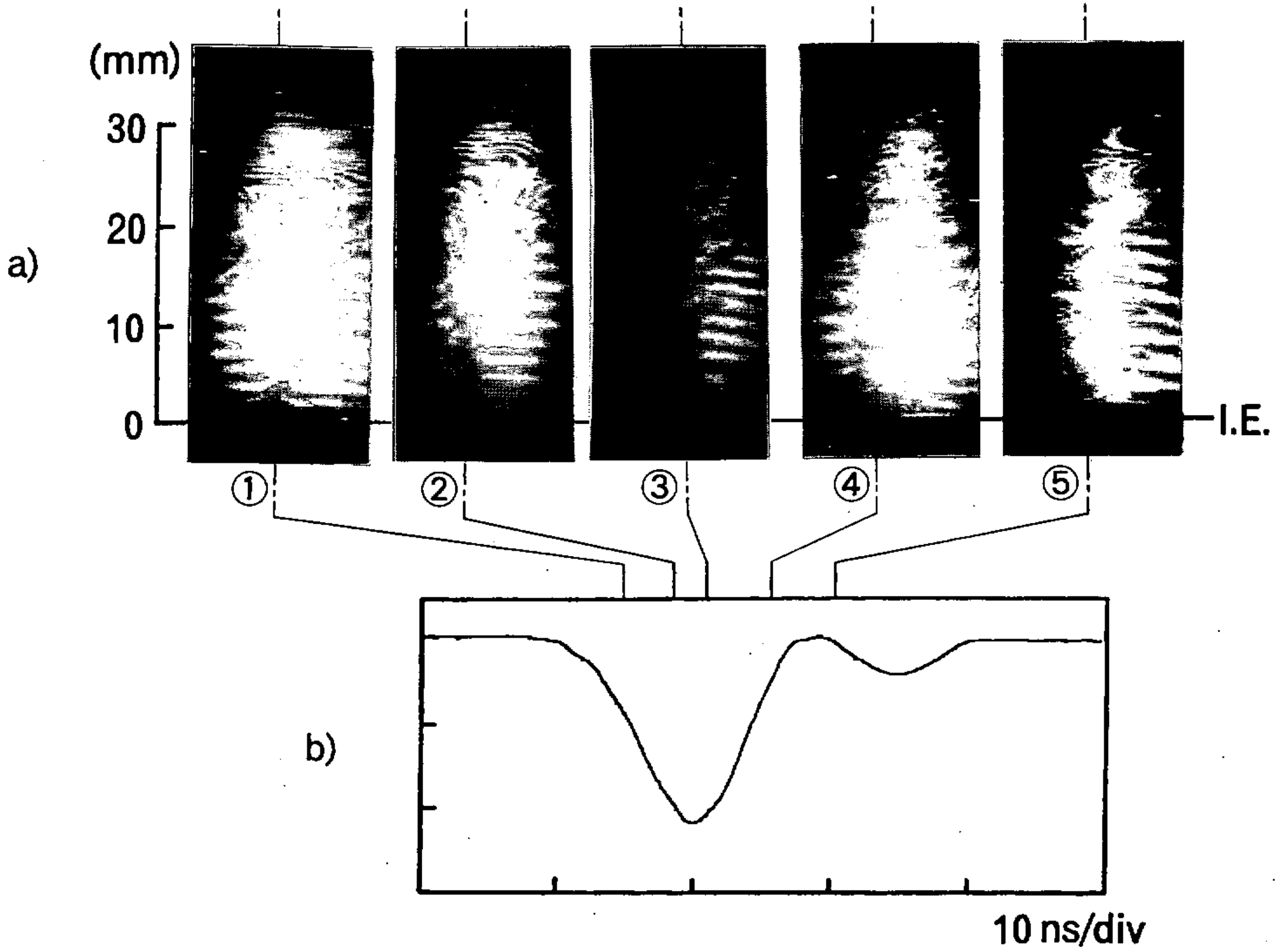

Fig. 5 Macroscopic plasma behavior
a) Mach−Zehnder interferogram
b) Phosphor current
I.E. : Inner electrode

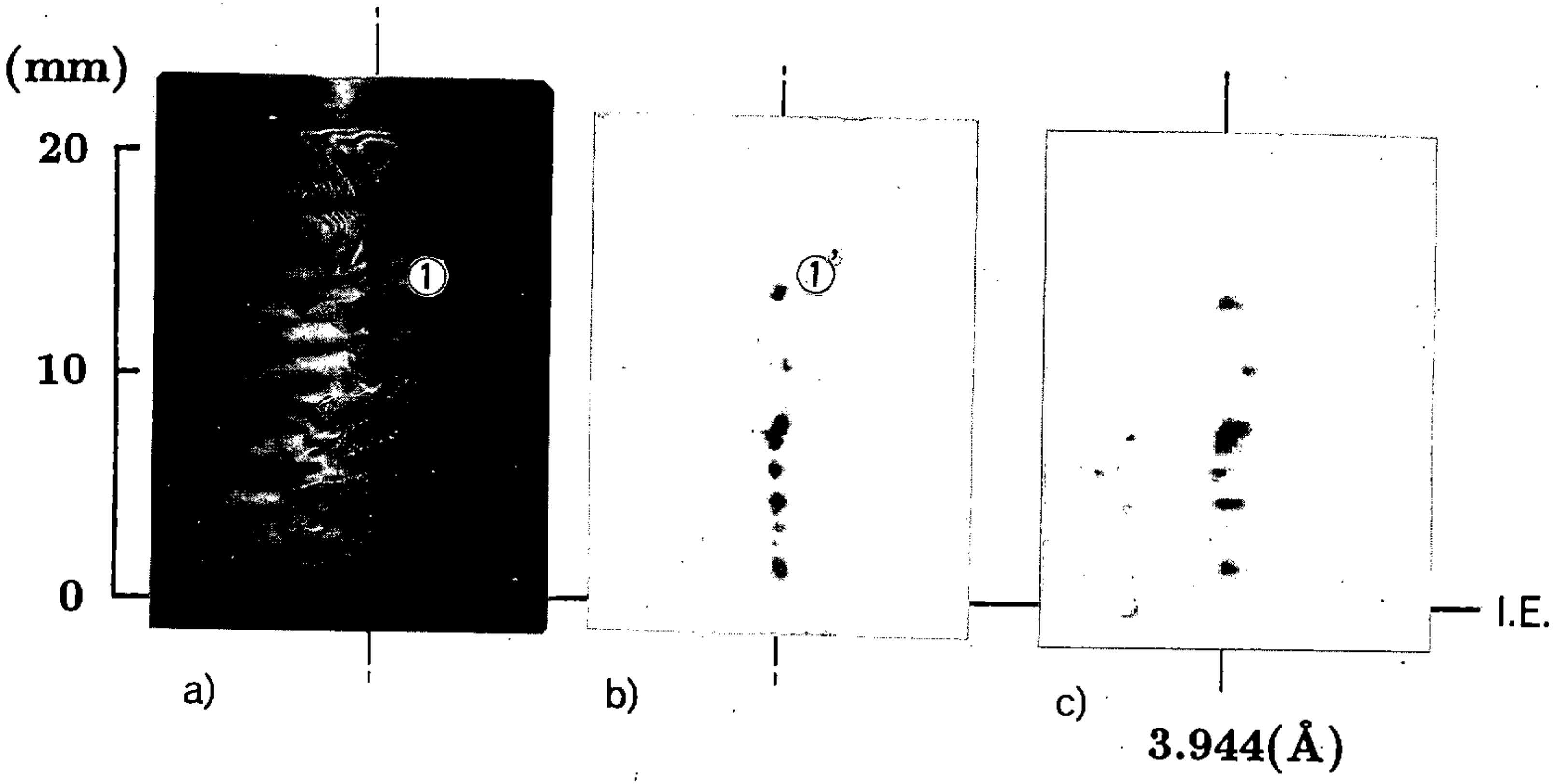

Fig. 6 Relation between the interferogram of the plasma

a) Mach−Zehnder interferogram
b) Time integrated soft x−ray pinhole image
c) Spectral analyzed image
I.E. : Inner electrode

Metal Vapor Puff Z-pinch Plasma and 1D MHD simulation

Kenji Arai, Seizo Furuya, Eiji Goto, Ken Hanazawa, and Shozo Ishii

Department of Electrical and Electronic Engineering
Tokyo Institute of Technology

Abstract

A novel method of creating high energy density plasmas is examined. This method uses pre-discharge to produce and inject metal vapor between Z-pinch electrodes from nozzles. The investigations on two types of metal vapor injection schemes are carried out. The vacuum discharge scheme cannot supply sufficient vapor for Z-pinch because little mass of the metal is vaporized in the module. The wire exploding scheme enhances the mass of injected vapor. We have created Z-pinch by employing a wire exploding scheme and observed the pinch dynamics and radiation of soft X-ray. One-dimensional MHD simulation has been carried out to obtain the details of temporal and spatial evolution of the Z-pinch.

1 Introduction

Z-pinch plasma can easily create high energy density plasma, and is concerned to use for efficient soft X-ray sources of soft X-ray lithography. Annular plasmas such as gas puff Z-pinch are enabled to get intense soft X-ray radiation by adjusting initial radius and line density properly [1, 2]. Gas puff Z-pinch has the advantage of high repetition rate operation. Since puffing material must be gaseous state, metallic elements are not applicable in gas puff Z-pinch.

The necessity of using metallic elements is the following.

- If it is possible to make many kinds of atom into plasma, a greater number of spectral lines emitted from the plasma can be obtained, and increase the number of line emission to get.
- For optical pumping soft X-ray laser, e.g., NaX-NeIX photocoupling [3] and AlXI-MgIX photocoupling [4], metal plasmas such as sodium, magnesium and aluminum are required.

The wire array Z-pinch is conventional method to create annular metal plasma. However, this type Z-pinch requires complicated handling process to fabricate multiple wire arrays. High repetition rate operation is impossible.

To overcome these problems on creating of metal plasma, we had proposed novel Z-pinch named *metal vapor puff Z-pinch* [5]. This method uses pre-discharge with a small capacitor to make metal into vapor to be injected between Z-pinch electrodes. In this report, we made experiments two types of method to produce metal vapor, *vacuum discharge scheme* and *wire exploding scheme*. The former uses vacuum arc to vaporize electrode, and the latter uses vaporization of metal wire by large current. We used aluminum for vacuum discharge type and copper for wire exploding type and compared those two methods.

Numerical analysis with MULTI-Z (1D MHD code) is also performed to estimate temperature and density of metal vapor puff Z-pinch plasma.

2 Experimental Setup

The Z-pinch plasma is powered by a capacitor bank of 27μF, *main-bank*, charged up to 20kV. The stored energy for main discharge is 5.4kJ. We also use a 4.45μF capacitor named *pre-bank* charged up to 20kV (890J) for metal vapor production. Main discharge starts several μs after the initiation of the pre-bank discharge.

The experimental setup shown in Fig. 1 consists of a discharge chamber and metal vapor producing module. Main discharge electrodes are equipped on the top of the module, and return current flows through the chamber. Anode is the upper electrode made of copper mesh. The cathode is the lower one which has nozzles for metal vapor puffing. In this experiment, nozzles are arranged in a circle of 20mm in radius and the electrode separation is 18mm.

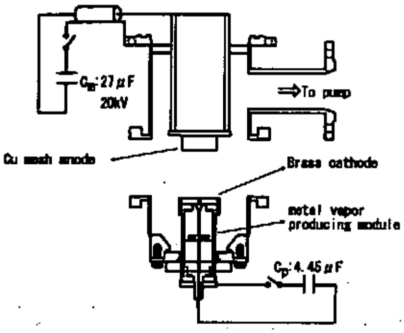

Figure 1: Schematic of Z-pinch generator.

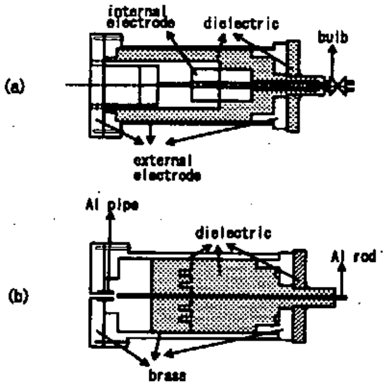

Figure 2: Metal vapor producing module.
(a). vacuum discharge type
(b). wire exploding type

The discharge vessel has four windows, two of witch are used for observing plasma behaviors. The vessel is evacuated about to 5 $\times 10^{-5}$ Torr by an oil-diffusion pump.

Each capacitor bank is switched by a trigatron type gap switch. These switches are triggered by a thyristor pulser output of which voltage is stepped up by a pulse transformer. Each thyristor pulser is controlled by a light signal transmitted through an optical fiber from delay pulser. The delay pulser can generate pulses with the arbitrary delay time between two pulses. Using this triggering system the main-bank discharge is able to start several μs after the pre-bank discharge. Hence generate side and control side are well separated electrically.

We have examined injection characteristics on two types of metal vapor producing scheme, vacuum discharge scheme (Fig. 2 (a)) and wire exploding scheme (Fig. 2 (b)). Both schemes use the pre-bank discharge. The former employs vacuum arc that makes electrodes vaporized. The latter uses metal wire which will be vaporized by huge current discharge. We use aluminum electrodes for the vacuum discharge scheme and copper wire for the wire exploding scheme.

Injected vapor and Z-pinch plasma are measured by the framing camera (HADLAND PHOTONICS: Imacon 792), which has 40ns exposure time and 160ns interframe time. An image intensifier is used with camera for observation of the injected vapor because the emitted light intensity is so weak. On the other hand, ND filters are placed in front of the camera for measurement of Z-pinch plasma because of too strong light from the plasma. We also use an X-ray diode (XRD) and an X-ray pinhole camera to measure temporal and spatial evolution of soft X-ray radiation from Z-pinch plasma. Since the former consists of an Al cathode and a 2μm-thick Mylar foil, its sensitivity for X-ray energy has two peaks at 284eV and 532eV. The latter has a 300μm-diameter pinhole with a 5μm-thick Be filter which can transmit soft X-ray of photon energy above 400eV photon energy. Soft X-ray images are recorded on Fuji NEOPAN 400 PRESTO film.

3 Simulation Models

To simulate the implosion of metal vapor puff Z-pinch plasma, we employed the MHD code, MULTI-Z. The basic algorithm of MULTI-Z is based on MULTI [6] and has been modified drastically for the application to Z-pinch by Aoki [7]. MULTI-Z is a code to solve two-fluid MHD equations in one-dimensional Lagrangian frame. The SESAME tabular equation of state is used to determine temperatures, average charge states, and specific heats from densities and specific energies.

Since we neglected the discharge circuit equation, the sinusoidal discharge current with the peak current of 300kA in 2μs has been assumed.

4 Results

4.1 The vapor injection of vacuum discharge scheme

Metal vapor produced by vacuum discharge scheme is injected from a single nozzle located at the center of the main-discharge electrode. Fig. 3 shows the pre-discharge current waveform (a) and the framing photographs (b) of the injected aluminum vapor. The exposure timings are shown in (a). The vapor is injected almost steadily without large diffusion after the fourth frame that is taken at 3μs after the beginning of the pre-discharge. Hence, the main-discharge is fired at this time to create dense metal vapor Z-pinch.

The main-discharge current and the framing photo of plasma are shown in Fig. 4. The exposure timings are also shown in (a).

Since bright images of the electrodes are evident, it is difficult to recognize in the figure that the main-discharge has been developed from the injected vapor. The plasma medium is brass of the main-discharge electrodes rather than the injected aluminum vapor.

The reason of this result is originated from the fact that the quantity of injected vapor is not enough to create the pinch plasma.

4.2 Metal vapor puff Z-pinch by wire exploding

We have surveyed various method to create larger mass vapor and reached a conclusion that wire exploding method is suitable for the purpose. We use 100μm-diameter copper wire. The density per unit length of the wire is 0.7mg/cm which is evaluated to be an appropriate mass density to have the maximum pinch at the current peak. We can expect to obtain much vapor to be injected. We have tried arrayed nozzles to form annular vapor profile. With this profile the pinch effect is enhanced. Sixteen nozzles of 2.0mm-diameter are located at the cathode on a circle of 2.0cm radius to form the arrayed profile.

The annular metal vapor is produced by wire explosion powered by pre-discharge and is injected between the main-discharge electrodes. Fig. 5 shows the main-discharge current waveform, the framing photographs of the Z-pinch. These results show that the plasma pinches at the third frame that is taken at 1.3μs after the beginning of the discharge. The peak of soft X-ray signal detected by the X-ray diode is observed at the same time.

The spatial profile of the soft X-ray emission taken by the X-ray pinhole camera is shown in Fig. 6. This photograph is a time-integrated picture of one shot. It shows that soft X-ray is radiated from four spots.

We set the initial condition to 0.7mg/cm for the density per unit length and 2.0cm for the annular array radius to obtain the maximum pinch at the current peak. However, the results in Fig. 5 show that the plasma pinches earlier. This is because that not all the mass of the exploding wire has not been injected.

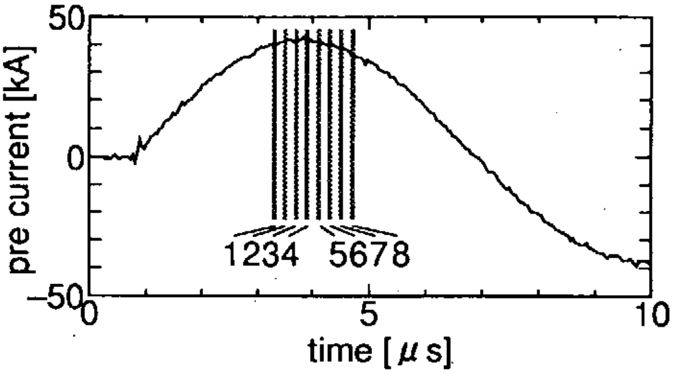

(a) Pre-discharge current and frame timing

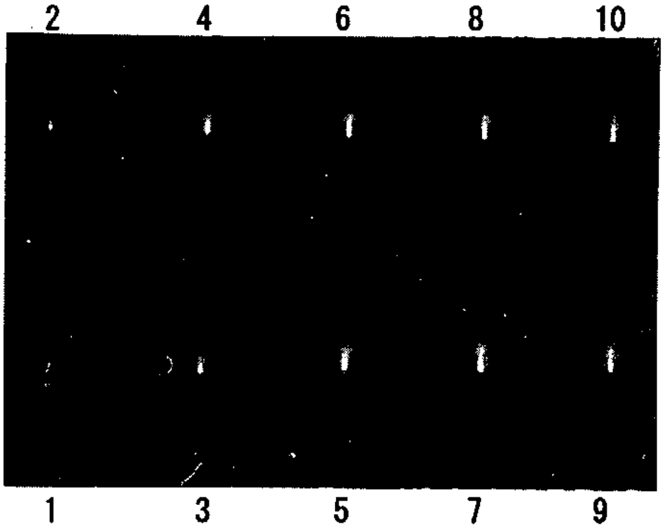

(b) Framing photograph

Figure 3: Framing photograph of injected vapor

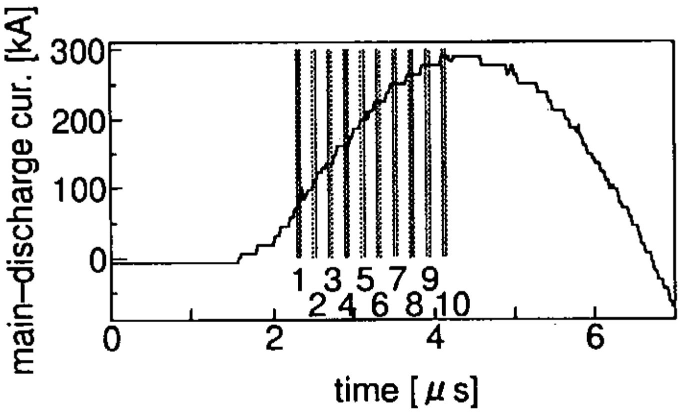

(a) Main-discharge current and framing timing

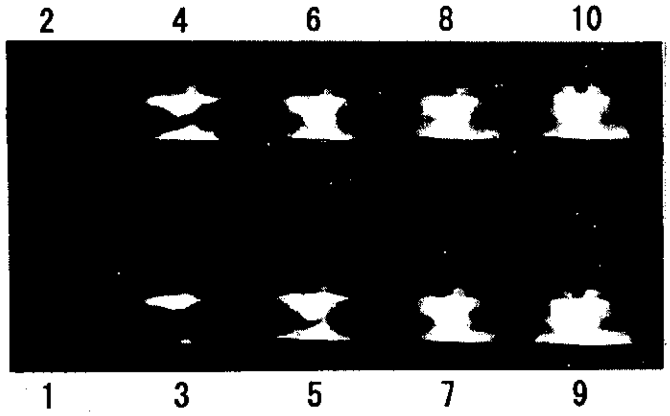

(b) Framing photograph

Figure 4: Results of measurement of Al Z-pinch plasma injected vapor by vacuum discharge scheme

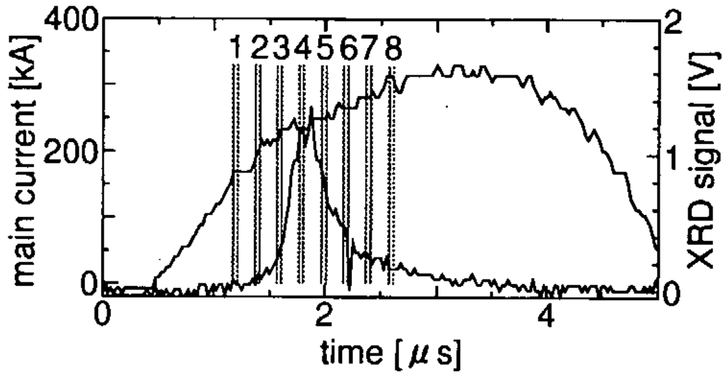

(a) Main discharge current, framing timing, and XRD signal

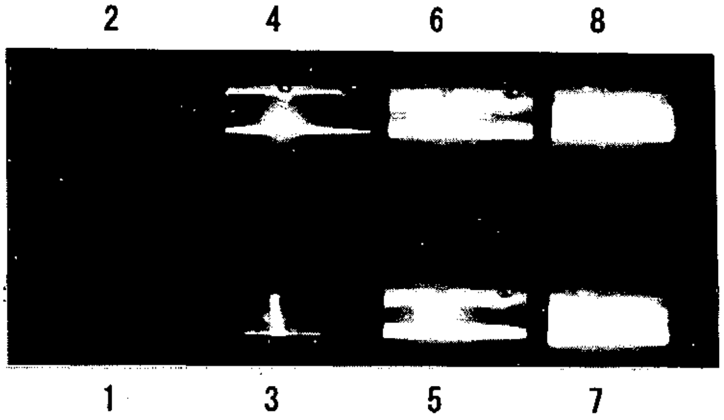

(b) Framing photograph

Figure 5: Results of measurement of Cu Z-pinch plasma injected vapor by vacuum discharge scheme

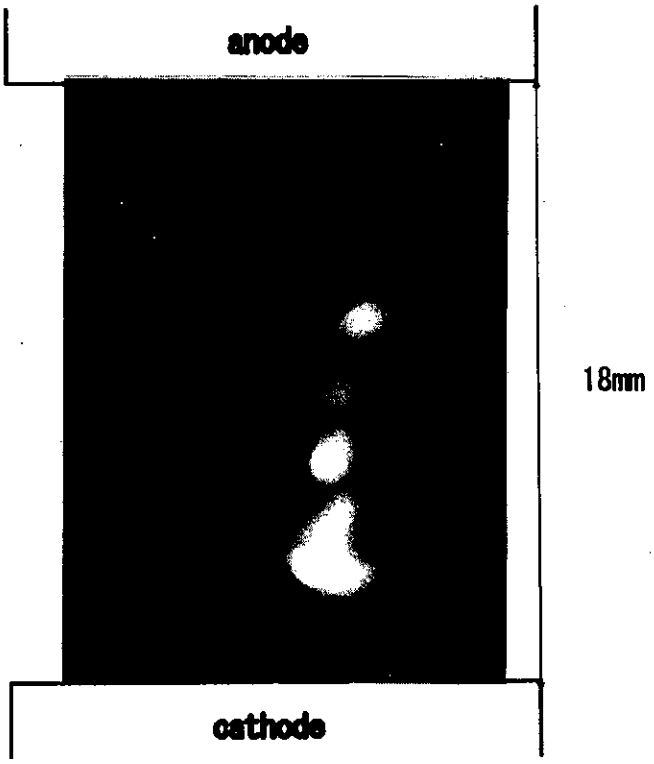

Figure 6: Soft X-ray image by X-ray pinhole camera from Cu Z-pinch plasma

4.3 Results of 1D MHD calculation

Since our metal vapor puff Z-pinch experiments are at infant stage, MHD simulation is important to estimate temporal and spatial evolution of many kinds of plasma parameters, namely, electron number density, electron temperature, ion temperature, and so on. We have evaluated the initial parameters by using a simple calculation with the slug model for the annular plasma to pinch at the current peak.

One dimensional MHD simulation is carried out to estimate approximate temperature and density of annular copper plasma. Fig. 7 shows the initial density profile which has the peak at 1.5cm of radius and the integrated mass per unit length of 0.5mg/cm.

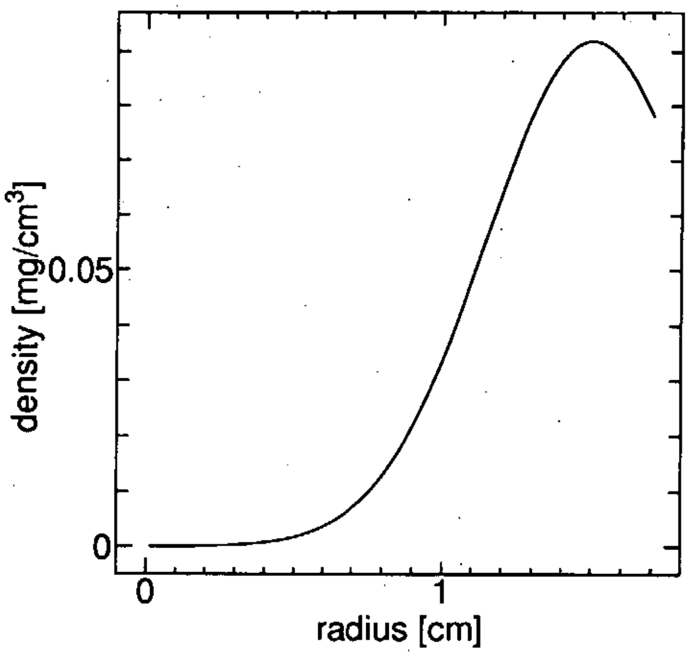

Figure 7: Initial density profile for simulation.

The results of the simulation are shown in Fig. 8. Fig. 8 (a) is a flow diagram that represents the temporal evolution of Lagrangian cells. It shows that the plasma column is pinched around 2μs which corresponds to the time of current peak. Fig. 8 (b) and (c) show the spatial and temporal evolution of mass density and electron number density respectively. The scale of spatial axis of Fig. 8 (b), (c) is not the radius but the Lagrangian cell number. It is estimated that the peak mass density is about 0.5mg/cm^3, that means, 4.7×10^{18}cm^{-3}. The maximum electron temperature of about 20eV has been obtained.

5 Conclusion

The metal vapor puff Z-pinch is investigated with experimentally and theoretically.

The vacuum discharge scheme cannot supply sufficient vapor for Z-pinch because little mass of the metal is vaporized in the module. The wire exploding scheme enhances the mass of injected vapor which establishes Z-pinch implosion. We also examined the pinch dynamics of the metal vapor puff Z-pinch plasma. The spatial profile of the soft X-ray emission taken by the X-ray pinhole camera shows that soft X-ray is radiated from four spots.

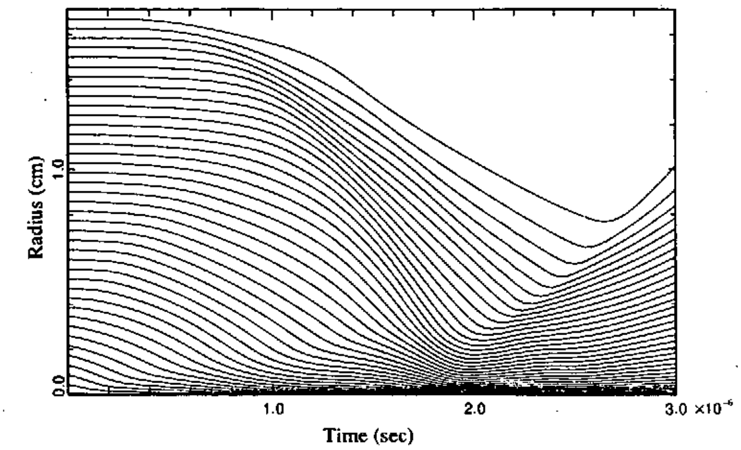

(a) Flow diagram

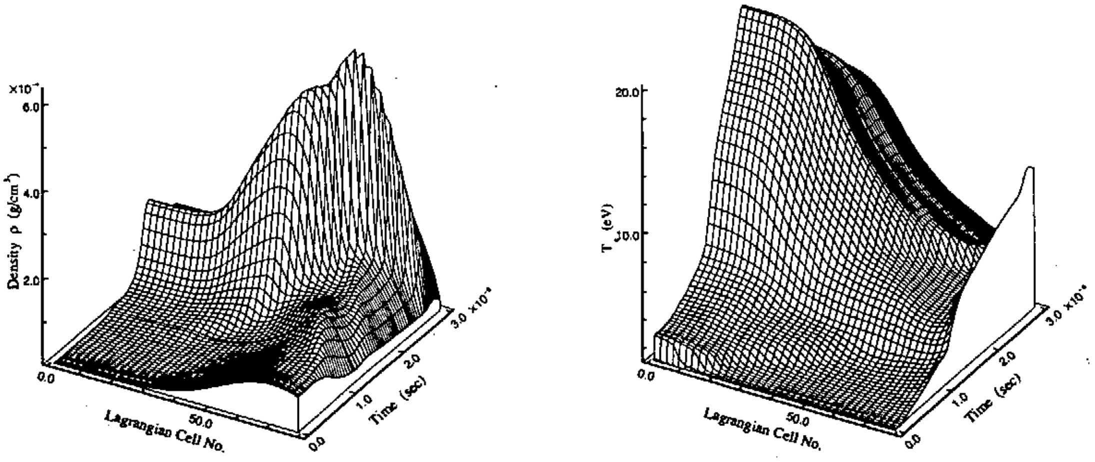

(b) Mass density variation (c) Electron temperature variation

Figure 8: Results of simulation of Cu Z-pinch by MULTI-Z.

We also carried out the simulation of annular copper vapor puff Z-pinch plasma with MULTI-Z, one-dimensional MHD Lagrangian code. The ion number density and electron temperature reach $4.7 \times 10^{18}\mathrm{cm}^{-3}$ and 20eV respectively when the plasma is imploded on the axis.

Acknowledgments

The authors wish to acknowledge the help and advice from Takayuki Aoki, Department of Energy Sciences, Tokyo Institute of Technology.

References

[1] C.Deeney, P.D.LePell, B.H.Failor, J.S.Meachum, S.Wong, J.W.Thornhill, K.G.Whitney, and M.C.Coulter, J. Appl. Phys. vol.75 pp.2781 (1994)

[2] M.Krishnan, C.Deeney, T.Nash, P.D.LePell, and K.Childers, AIP Conf. Proc. 195 DENCE Z-PINCHES pp.17 (1989)

[3] J.L.Porter, R.B.Spielman, M.K.Matzen, E.J.McGuire, L.E.Ruggles, M.F.Vargas, J.P.Apruzese, R.W.Clark, and J.Davis, Phys. Rev. Lett. vol.68 pp.796

[4] Mahadevan Krishnan and James Trebes, Appl. Phys. Lett vol.45 pp.189 (1984)

[5] Y.Hoshina, T.Suzuki, K.Arai, Q.P.Ai, and S.Ishii, NIFS-PROC-14 pp.89 (1993)

[6] R.Ramis, R.Schmalz, and J.Meyer-Ter-Vehn, Comp. Phys. Commun. vol.49 pp.475 (1988)

[7] T.Aoki, This symposium.

Creation and Measurements of Fine Particles Z-pinch plasma

Qing-Pin Ai, Daiju Itagaki, Osamu Tsuboi and Shozo Ishii

Tokyo Institute of Technology

Abstract

Recent interest in applications of intense soft X-ray and UV radiation has resulted in a new scheme of creating high energy density Plasmas. Z-pinch plasma was produced using copper fine particles of $1\mu m$ in diameter. The scheme is superior in high repetition rate and in high initial mass density. It is possible to control the plasma point that radiate intense soft X-ray, because the initial mass distribution has non-uniformity along the axis. The particles are accelerated by pulsed electrostatic field that is applied between the electrodes located beneath the main electrodes. The particles' behavior in the accelerating phase has been measured by means of He-Ne laser light scattering. The plasma currents are measured by Rogowski coils. The dynamic behaviors of the fine particles Z-pinch plasma in the implosion phase is observed by an image converter camera.

1 Introduction

Until now, Z-pinch plasma materials are divided into gas and solid, for example puffing gas, solid fiber, and solid thin film liner. Z-pinches easily producing high density and high temperature plasma open up various applications. Intense X-ray radiation from Z-pinch plasma is applied to X-ray laser and intense X-ray source for lithography in semiconductor processing. Spectral characteristics of soft X-ray and UV radiation from gas-puff Z-pinch have been investigated by many authors. The advantages of the gas-puff Z-pinch are high repetitive and reproducible operation. X-ray intensity and emission characteristics depend strongly on the initial gas profile and the injection timing. On the other hand, fiber pinches or imploding liner compression can create high density plasmas. However, it is difficult to set the plasma materials in the proper position between the main electrodes.

In this paper we report the Z-pinch by solid fine particle's injection that has both advantages of high repetition rate operation and high initial mass density. The principle of the system is similar to that of gas-puff pinch. Fine particles are accelerated and injected from a small nozzle. Since the injecting system is controlled electrically, the medium is injected faster than by the gas-puff system based on the mechanical control. The material of fine particles can be not only metal but also dielectric and its composite. The degree of freedom in choosing the wavelength range of soft X-ray radiation becomes so large. It is expected to have various applications of intense soft X-ray and UV source, and thin film deposition of materials with the high melting point. It is possible to control the plasma point that can radiate intense soft X-ray when the mass, the injected particle's size, and the injected velocity are chosen properly.

Physics of fine particles has been studied in surface science and in astrophysics. For example, surface disposition in thin film technology, and space dust and complex phenomena in astrophysical plasmas.

2 Experimental Setup

The concept of experimental setup is shown schematically in Figure 1.

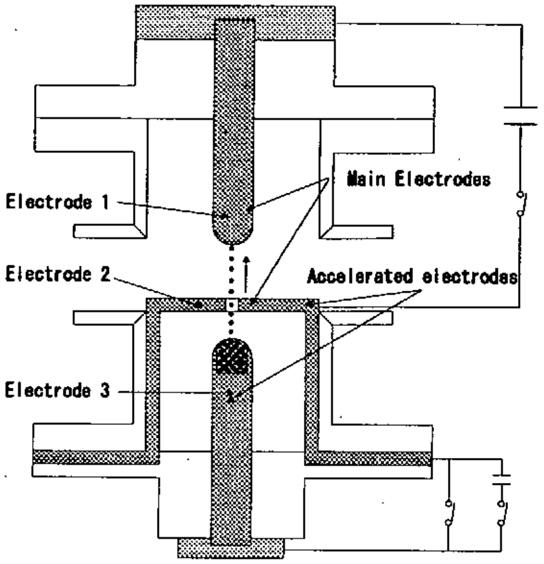

Accelerated Capacitor : C=0.441uF , V=12~15kV
Main Capacitor : C=4.45uF , V=15~20kV

Figure 1: The experimental setup of fine particles Z-pinch

The fine particle is accelerated by pulsed electrostatic field. This method requires only a simple apparatus with easy operation. The setup is made with three electrodes: the electrode 1 and 2 are made for main discharge with separation of 10mm, and the electrode 2 and 3 is for particles acceleration. The fine particles are injected through a small nozzle drilled at the center of the electrode 2. The nozzle size is 2mm in diameter. The vacuum chamber made of stainless steel is evacuated by a rotary pump and an oil-diffusion pump, the operating pressure is $0.5 \sim 3.0 \times 10^{-5}$Torr. There are three windows in the radial direction viewing the center of the chamber. X-ray and Visible radiation are detected through these windows.

Spherical copper particles of 1μm in diameter have been put on the top surface of the electrode 3. When high voltage pulse is applied between the accelerated electrodes, particles are charged to the same polarity as that of electrode 3. Fine particles are accelerated by the discharge of a capacitor of 0.441μF charged to $12 \sim 15$kV. The accelerating pulse has a square waveform with the pulse width of 3ms. The accelerated particles behaviors have been observed with optical measurement by He-Ne laser scattering.

The main discharge is powered by a capacitor bank of 4.45μF charged to $15 \sim 20$kV. The main discharge current and voltage are measured by Rogowski coils and resistive voltage divider respectfully. The pinch characteristics are diagnosed by streak photography viewing through the acrylic window in the radial direction.

3 Measurements and Results

Injected fine particles' behaviors in open air are measured with laser scattering method. The principal of measurements is shown in Figure 2. One can observe injected fine particles that can be made visible by using He-Ne laser illumination.

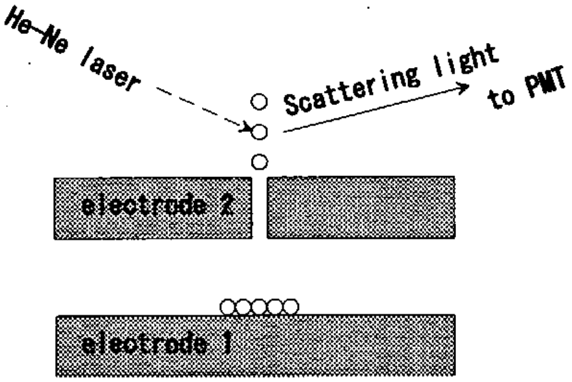

Figure 2: Injected fine particles' measurements in the air

Injected fine particle's photo in the vacuum is shown in Figure 3. The incidence laser is also reflected by electrodes and chamber glass windows.

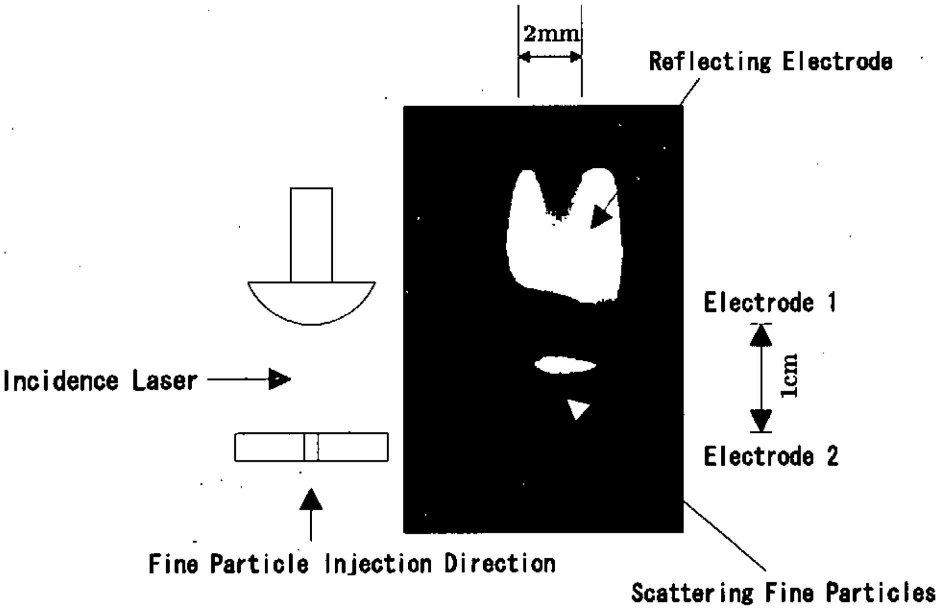

Figure 3: Injected fine particles open photo

In order to avoid the undesirable reflected light, we have used the optical system with lens and filter to bring the scattering fine particles to a focal point. The principal of measurements is shown in Figure 4.

The temporal behaviors in the accelerating phase have been observed by photomultiplier tube, where theirs waveforms are shown in Figure 5.

In the atmospheric condition, the motions of fine particles are influenced so largely by damping force and humidity that the masses of injected fine particles are very small and the particle's

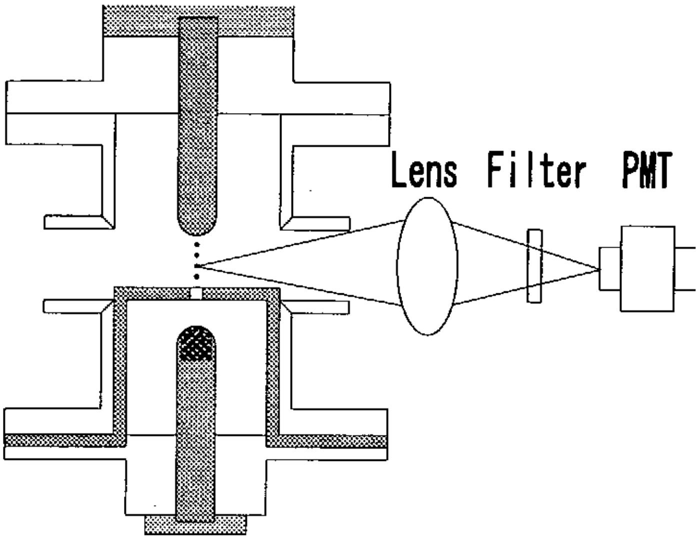

Figure 4: Injected fine particles' measurements in the vacuum

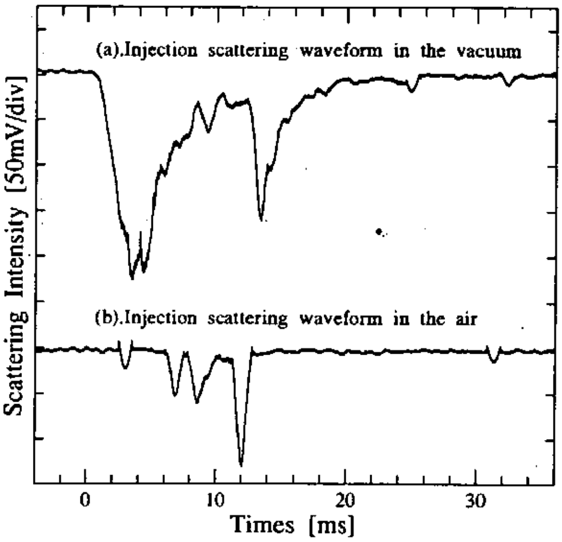

Figure 5: Scattering waveform of fine particle's injection

velocity is slow. On the other hand, the injected mass much larger and the velocity is fast enough in the vacuum. The initial line mass density is similar to that of fiber pinches.

Typical waveforms of the main discharge current and voltage are shown in Figure 6. The peak value of the discharge current is about 40kA,and a half period is 7μsec. The maximum charging voltage is 20kV. The initiation of the voltage falling down occurs simultaneously with the current rising. The plasma current is small as a result of several limitation in experimental condition. However, because of the initial mass density has non-uniformity along the axis, the visible light is emitted at several localized spots.

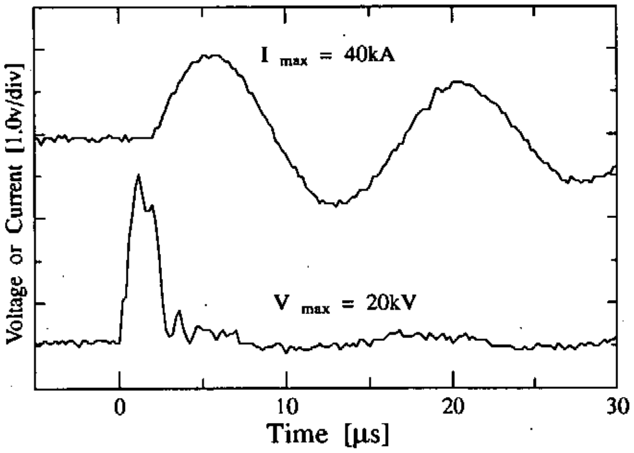

Figure 6: Main discharge current and voltage waveforms in the vacuum

The visible lights in streak photographs are shown in Figure 7. Plasma radial compression appears during the current rise phase, the minimum compression time coincides with a small dip of plasma current trace. The streak speed is 100ns/mm with the exposure time of 7μsec.

The current and image converter camera trigger waveforms and streak photograph have been measured at the same time on the same shot, plasma radial mini-imploding evolution is observed. However, on the whole, plasma continues to explode. Plasma implosion has not been observed. This is because fine particles Z-pinch discharge is from solid state and the discharge current rising is slow .

4 Conclusion

High density and high energy density Z-pinch plasma was produced in a new way and its validity was shown. The electrostatic acceleration that we chose to supply the plasma material to Z-pinch chamber is superior to other ways in ease to control. It is possible to control the plasma point that radiates intense soft X-ray, because the initial mass is non-uniformity along the axis. The injected particles' behaviors have been measured by the He-Ne laser scattering light. The maximum plasma current are at most 40kA because of experimental condition, The dynamic behavior of fine particles plasmas in the contraction phase is shown by image converter camera. Plasma implosion has not been observed.

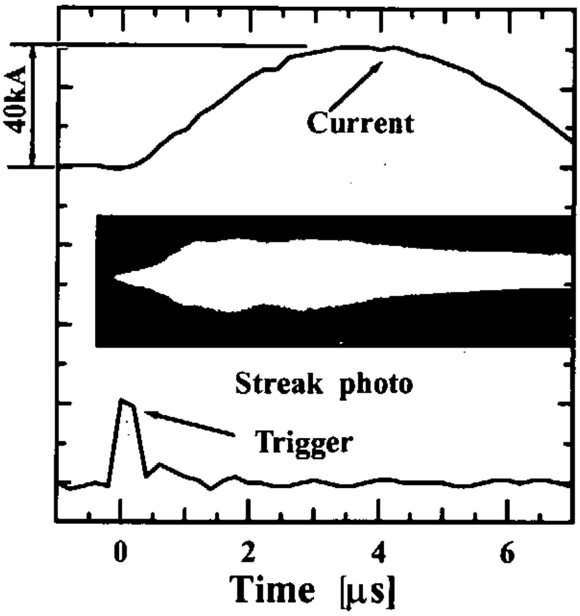

Figure 7: Streak photograph and main discharge current waveforms

References

[1] .Yokota: Purazuma kakuyugo gakkaisi(in Japanese), 6, 69, 1 (1993)

[2] .Shelton, C.D.Hendricrs, and R.F.Wuerker: J.Appl.Physics, 31,7, (1960)

[3] .Takasugi et al.: American Institute of Physics (1994)

[4] .Hoshina et al.: NIFS-PROC-14 89 (1993)

[5] .Hoshide et al.: NIFS-PROC-18 107(1994)

[6] .Y.H.Cho: J.Appl.Phys., 2561,35,9 (1964)

AN EXPERIMENTAL STUDY OF PULSE BEAM-EXCITED STRONG LANGMUIR TURBULENCE

Ritoku Ando, Masaru Masuzaki, Hiroshi Morita[a],
Ken-ichi Kobayashi[a], Masayuki Yoshikawa,
Haruhisa Koguchi and Keiichi Kamada

Department of Physics, Faculty of Science, Kanazawa University
Kanazawa 920-11, Japan

Abstract

We have carried out experiments on interaction of an intense relativistic electron beam (IREB) with a plasma which is an interesting subject from a point of view of nonlinear phenomena. Due to the interaction broadband microwave pulse was radiated and the microwave power reached about 2 MW. For the radiation, the ratio of the beam and the plasma densities (n_b/n_p) *was an important parameter. We found that there was an optimum on* n_b/n_p *at which the power density in the observing window (18 - 40 GHz) was maximum. When the value of* n_b/n_p *was among 0.001~0.01, the radiated microwave was strong. This condition on* n_b/n_p *is very similar to the condition that the streaming instability is strong.*

1, Introduction

Several works were performed on the high power broadband microwave radiation from a plasma into which an intense relativistic electron beam (IREB) was injected, in connection with the type III solar radio-wave emission. Many theories and simulations[1)] have shown that a plasma becomes strong Langmuir turbulent state when a strong electron beam is injected into the plasma. Such a process as creation, collapse and burnout of Langmuir cavitons repeats itself in the strong Langmuir turbulent state. In one of our experiments concerning this phenomenon, extremely strong high frequency electric fields with $W \sim 1.1$ was observed, W being electric field energy density normalized by the plasma thermal energy density.[2,3)] Benford and Weatherall have proposed a model which explains the radiation by a beam electrons interacting with cavitons.[4)]

In the first experimental research on such radiation carried out at University of

California, Irvine, it was claimed that intensity of the microwave radiation increased with n_b/n_p, and that when the density ratio became in excess of 0.1~1, the spectrum became broad and the intensity became saturated.[5] In this paper we report existence of an optimum in n_b/n_p for the radiation. It was found experimentally that at the optimum n_b/n_p the power density was maximum in the observing window (18~40GHz).[6] We will discuss importance of n_b/n_p for intensification of the radiation.

2. Experiment

A modified Pulserad 110A (1.5MeV, 27kA, 30ns) was utilized as a source of an intense pulsed electron beam. No magnetic field was applied. The experimental setup is shown in figure 1. A 36 mm diam. carbon cathode and an anode of titanium foil of 20 μm thick were employed to generate the beam. A plasma was produced by two rail-type plasma-guns with carbon electrodes located at $z = 10$ cm, where z is the distance from the anode. Profile of n_p was measured by a static Langmuir probe. Change of n_p by the IREB was not measured. The beam density n_b was measured by two methods. An average beam density $<n_b>$ was estimated from the beam current measured by a Rogowski coil and the beam radius obtained by luminescence of a phosphor plate. Radial density profile was obtained by a Faraday cup array. These two results coincided with each other. Combination of n_p with the former provides $<n_b/n_p>$ and that with the latter does n_b/n_p as a function of the radius. An 18-40 GHz 5-channel spectrometer[6] was used to measure the spectra of both radially and axially radiated microwaves.

Radiation was observed only during the IREB pulse. The microwave was radiated into the direction of beam propagation more strongly than into the radial direction. The power density which was the sum of the output of 5 channels of the spectrometer was 20 kW/cm^2 for the forward direction and 0.5 kW/cm^2 for the radial direction at their maximum. These facts show that the microwave radiation was due to acceleration of IREB. Total power was estimated to be 2 MW. The spectrum of the microwave was broad in the observing frequency window. The peak frequency in the spectrum was about 3 times of the plasma frequency of the target plasma. Hereafter we call the power density [W/cm^2] which is sum of the outputs of 5 channels of spectrometer observed radially at $z = 17.5$ cm as P_t.

Figure 2(a) shows n_p on the axis of the chamber at z =17.5 cm as a function of time, τ, from the gun firing time. The beam was injected at τ. The n_b/n_p was able to be varied by changing τ. Figure 2 also shows dependencies of typical parameters observed at z =17.5 cm on τ; (a) n_p and n_b, (b) the beam current and the beam diameter (D_b), (c) $<n_b/n_p>$ and (d) Pt. The $<n_b/n_p>$ decreased as n_p increased and it had a minimum value 0.001 around τ ≈ 10 μs, and then as n_p decreased it increased to an order of 1. Both microwave radiations into the forward direction and the radial direction had the same dependence on τ. As shown in figure 2(d), P_t has two peaks in this experiment. At τ 's corresponding to these peaks, $<n_b/n_p>$ ≈ 0.01.

For a check of the radial profile of n_b/n_p, thickness of the anode foil (t) was taken as a variable. Figure 3 shows radial distributions of n_b/n_p when the radiation was maximum for the thin foil case (15 μm) and for the thick foil case (40 μm). Roughly D_b increased with t for all τ. As shown in figure 3, n_b was lower and n_p was also lower in the thick foil case than the thin foil case. The n_b/n_p value was kept almost constant in these cases. Whenever n_b/n_p took a value of 0.001~0.01 in any place in the observed area, an intense microwave radiation was observed.

Figure 4 shows τ dependences of P_t obtained with t =15 μm and 40 μm foils. A dip on the dependence appeared more distinctly on the middle τ region for the thick foil case than the thin foil case. Figure 5 shows the dependences of beam current and average P_t at τ = 10~20 μs and 25~30 μs on the thickness of the anode foil. These τ's corresponded to the dip and the second peak of P_t. The beam current did not change appreciably with t, but P_t decreased strongly(P_t is plotted in logarithm in figure 5(b)). The change of P_t for the dip was more remarkable than that for the peaks.

3. Discussion

These behavior of P_t may be explained due to the coupling between the beam and the plasma predicted by the streaming instability[7]. The instability is well known as an important energy transfer mechanism from beam to plasma and an underlying phenomena of the strong Langmuir turbulence. The theory suggests a saturation of the instability at S =0.45. Here S , the strength parameter, is given by $S = \beta_0^2 \gamma_0 (n_b/2n_p)^{1/3}$. In our experiment ($\gamma_0$=4), S =0.45 corresponds to n_b/n_p =0.03. Also qualitative behavior of P_t as a function of foil thickness is very similar to that of the instability[8]. Under the foil scattering, the coupling efficiency of the instability can decrease quite rapidly as n_b/n_p decreases.

4. Summary

An optimum condition existed for a broadband microwave radiation in our experiment in which n_b are fixed while n_p was varied. The electron density ratio of beam and plasma (n_b/n_p) was a dominant factor on an intensity of the radiation. The optimum value of n_b/n_p was in the range between 0.001~0.01 in our experiments. Beam scattering by anode foil reduce the radiation intensity. And its scattering effect become quite serious as n_b/n_p decreases from the optimum n_b/n_p value. These behaviors are very similar to those of the streaming instability, which is considered as an underlying phenomena of the turbulence.

Acknowledgement

Part of this work was supported by a Grant-in-Aid for Scientific Research from the Ministry of Education, Science and Culture.

References

(a) Present address : Hitachi Corporation, Japan.

(1) For example, P.A.Robinson and D.L.Newman, Phys. Fluids B2 (1990) 3120, and references therein.

(2) M.Yoshikawa, et al. Jpn. J. Appl. Phys. 32 (1993) 969.

(3) M.Yoshikawa, et al. J.Phys. Soc. Jpn 63 (1994) 3303.

(4) G.Benford and J. C. Weatherall, Phys Fluids B 4 (1992) 4111.

(5) K.G.Kato, et al. Phys. Fluids 26 (1983) 3636.

(6) M.Masuzaki, et al. 1993, Proceedings of the 9th International Conference on High-Power Beams, vol.2, pp.1227-1232.

(7) Lester E.Thode, Phy. Fluids. 19 (1976) 306.

(8) Lester E.Thode, Phy. Fluids. 19 (1976) 831.

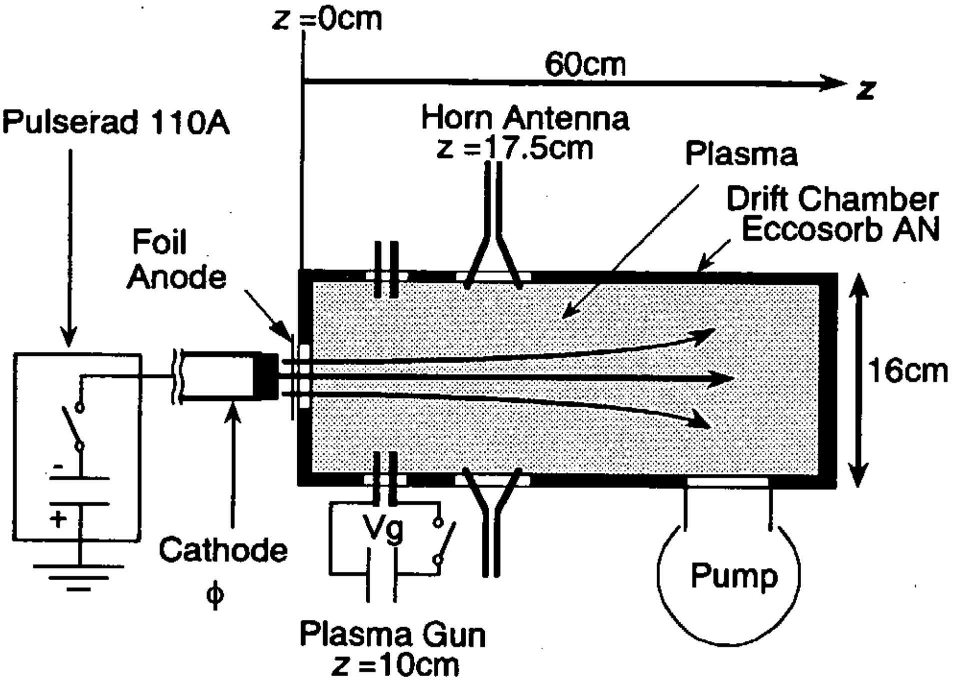

Fig.1 Experimental setup.

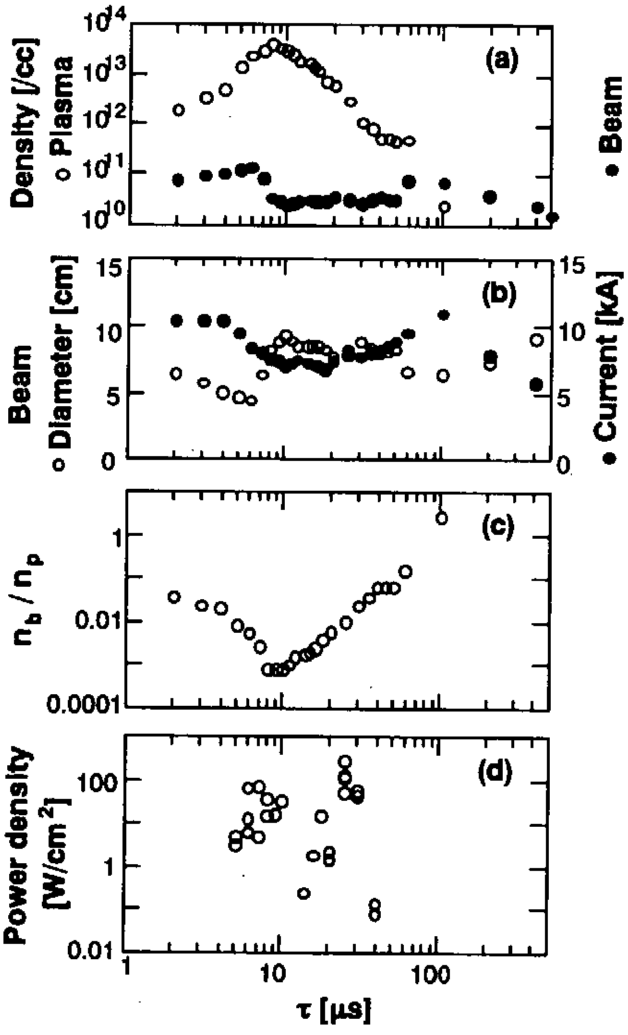

Fig.2 Relationship between parameters. ϕ = 36 mm, V_g= 2.8 kV, t = 20 μm.

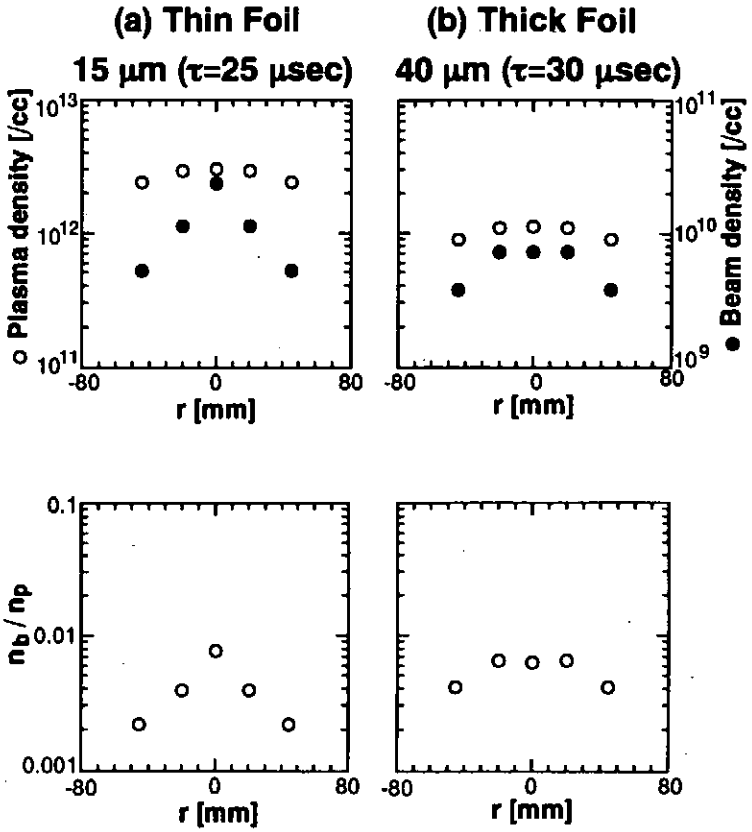

Fig.3 Intensity of the radiation (P_t) versus $<n_b/n_p>$.

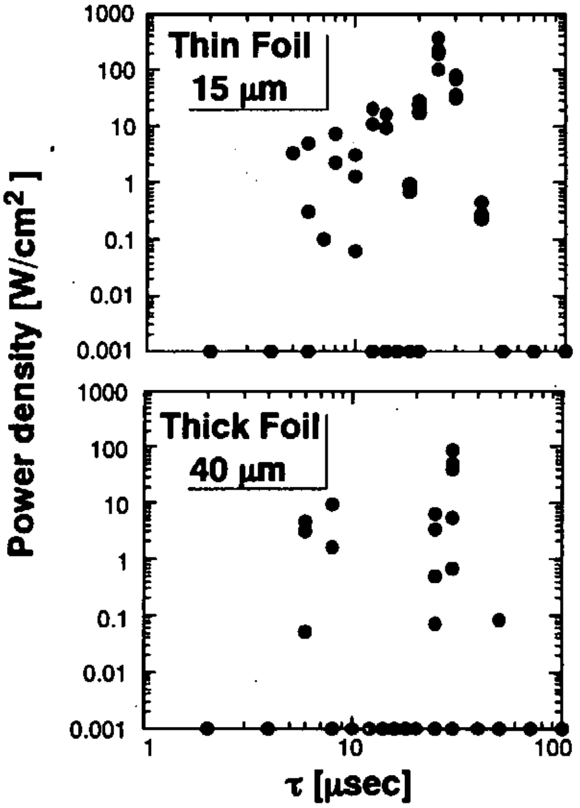

Fig.4 τ dependences of P_t obtained with thin and thick foils. (t =15 μm and 40 μm)

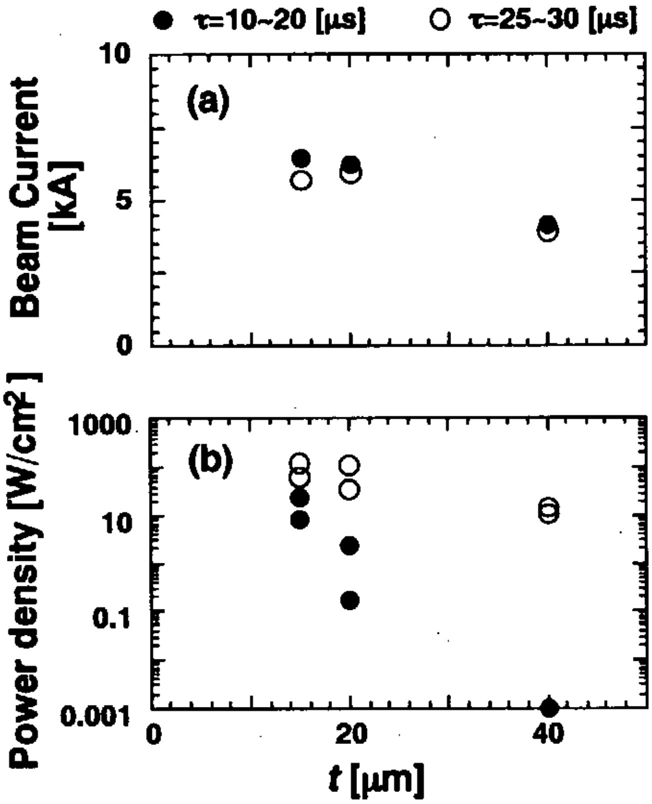

Fig.5 Beam current and microwave intensity versus thickness of anode foil (t) measured at z =17.5 cm. Open circles and closed circles correspond to the data of τ = 25~30 μs and τ = 10~20 μs respectively.

An X-Band Gyro-BWO Experiment with an Intense Relativistic Electron Beam

Keiichi Kamada, Hisayosi Igarasi, Kouichi Nawashiro[a],
Sunao Kawasaki*), Ritoku Ando and Masaru Masuzaki

Department of Physics, Faculty of Science, Kanazawa University
Kanazawa 920-11, JAPAN

*) Department of Physics, Faculty of Science, Saitama University
Saitama 338 , JAPAN

a) Present address: Nissin Electric Co. ltd. Ukyou-ku Kyoto 615

Abstract

A gyrotron backward-wave oscillator (gyro-BWO) was operated and it was magnetically tuned over the frequency range 9-13 GHz. An intense relativistic electron beam (450 keV, 300 A , 10 ns) was injected into an X-band rectangular wave guide immersed in an axial uniform magnetic field (up to 1T, 1 m long). In order to narrow the frequency spectrum of generated microwave in a shot, an aluminum foil was used to peel off the lower energy part of the beam. The power of the radiated microwave was estimated to be 1MW.

1. Introduction

Among high-power millimeter wave sources which utilize an intense relativistic electron beam (IREB), a gyrotron backward-wave oscillator (gyro-BWO) has such advantages as described below. (1) As only a simple waveguide is necessary to operate a gyro-BWO, power and beam handling can be much easier than those for a conventional backward-wave oscillator which requires a periodic structure. As a gyro-BWO results from an absolute instability,[1)] spatial feedback mechanism by a resonant cavity is not necessary. (2) The radiated frequency may be continuously tunable over frequency range above the cutoff frequency of the waveguide only by changing the strength of the magnetic field and/or the beam energy. (3) Compared to other electron cyclotron resonance devices, a gyro-BWO is relatively insensitive to the beam energy spread. This insensitivity to the beam energy spread allows the use of a low quality electron beam, for example, emitted from an explosive cathode using a conventional pulse line which has wide energy spread due to the time-varying impedance of the diode. (4) Theoretically high efficiency over 30% is predicted by using a modified magnetic field.[2-4)]

There are a few experimental reports on a gyro-BWO.[5-7)] They used a cylindrical waveguide and a long-pulse beam. In this paper, we report preliminary experimental results of an X-band gyro-BWO with a short-pulse IREB using a rectangular waveguide. At the first stage of our experiment, microwave radiation with wide X-band frequency range was obtained, so that it was difficult to analyze the mechanism of the oscillation. By utilizing an aluminum foil to reduce the energy spread of the IREB, the relationship between the radiated microwave frequency and the strength of the magnetic field was clarified and it showed good agreement with the calculated one which was derived from the model proposed by Parker et al.[1)]

2. Experimental Apparatus

A schematic diagram of the experiment is shown in Fig.1. A Pulserad 105A (Physics International) which utilized a conventional Blumlein line was used as a beam source in our experiment. A 650 kV, 16 kA, 10 ns pulse was available to a matched load. An axially uniform long-pulsed magnetic field (4-10 kG) was applied, by a solenoid coil 90 cm long, from the diode to the downstream side of beam propagation. Along the axis of the solenoid coil, an X-band rectangular waveguide with a length of 1.5 m long was located.

A stainless steel pipe with a diameter of 8 mm was used as a cathode. A 35 mm thick carbon cylindrical disk with a 11 mm diam. aperture on the center was used as a hollow anode. The anode and cathode spacing was 5 mm. The peak voltage of -450 keV was applied to the cathode. The peak diode current was 10 kA. Through the 11 mm diam. aperture, an electron beam of about 300 A was injected into the waveguide. The beam propagated along the magnetic field and diverged to the waveguide wall at the exit of the solenoid.

Microwaves radiated in the magnetic field were received by a horn located just behind the Lucite vacuum window at the end of the waveguides. A 100m X-band dispersive line was utilized to observe the overall frequency range of the radiated microwaves. The microwaves were monitored by crystal detectors at the entrance and at the exit end of the dispersive line. Microwave frequency was calculated from the time for the wave to pass through the dispersive line. A variable attenuator was used in the entrance branch. Waveguides of 1 m long with higher cutoff frequencies than that of X-band were used as high pass filters to observe higher frequency components of the radiated microwaves. The total output power of the microwaves was estimated by the output of the crystal detector taking into account of the attenuation factor of the variable attenuator which was calibrated by a low power oscillator.

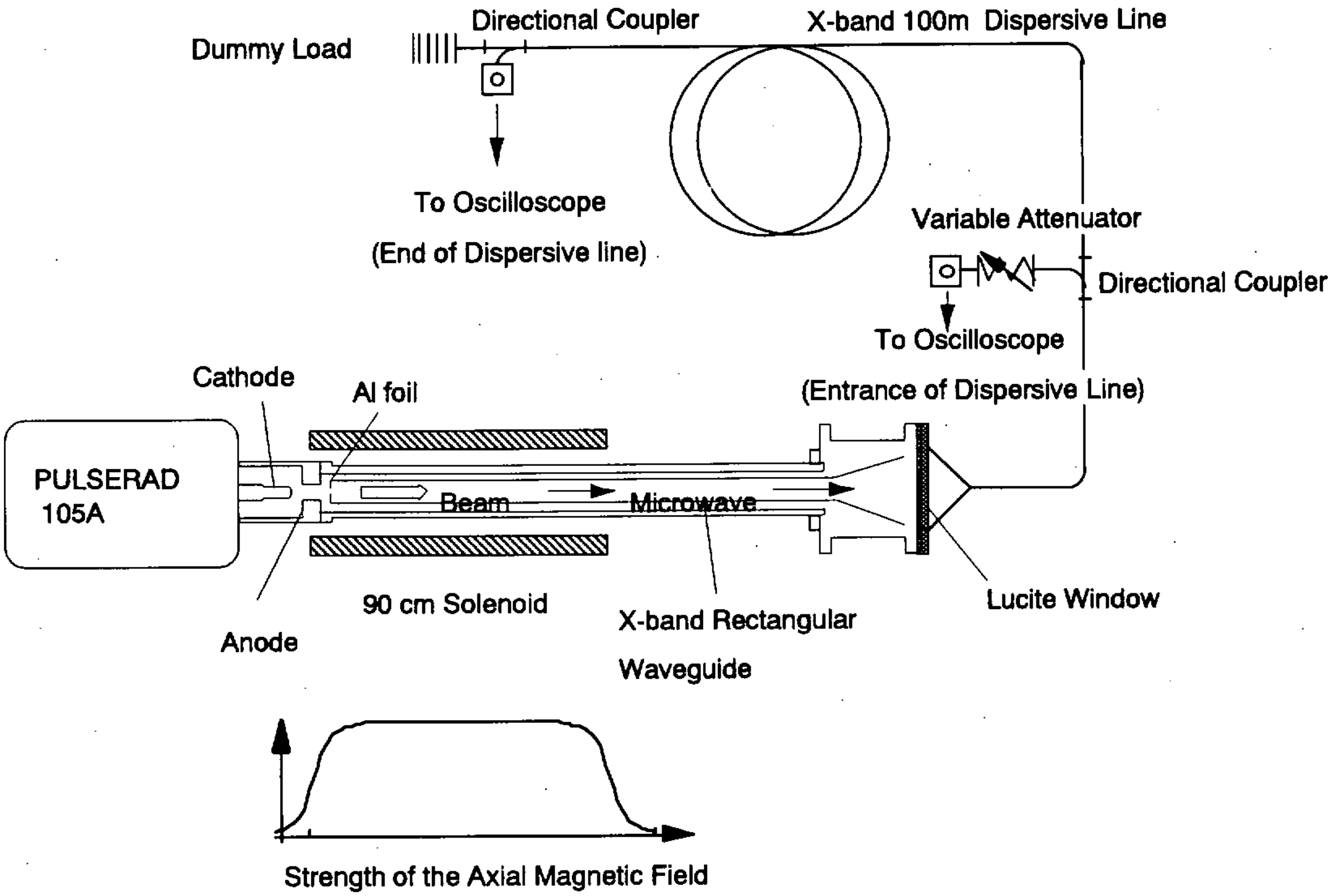

Fig. 1 Experimental configulration

3. Experimental Results.

Typical pulse forms of diode voltage, diode current and beam current are shown in Fig. 2 . The beam current propagated without loss through the magnetic field. The energies of beam electrons corresponded to the diode voltages at their emission times. The beam electrons were emitted in wide energy range, so that the spectrum of the microwave radiation was broad and had many peaks (Fig. 3a) . Especially, the reflected diode voltage and current due to the mismatch between the diode and pulse line impedances brought about additional radiation. It was difficult to identify their frequencies in our long dispersive line system. To clear the phenomena, a 45 μm thick aluminum foil was used to peel off the lower energy part of the beam. The stopping power of a 45 μm thick aluminum foil was evaluated to be 100 keV and the energy loss for a 450 keV electron was estimated to be 30 keV. As shown in Fig.2, the beam current emitted after the main pulse was reduced by the foil. With a 45 μm aluminum foil, only the microwave radiation due to the main pulse of the diode voltage was observed as shown in Fig. 3b .

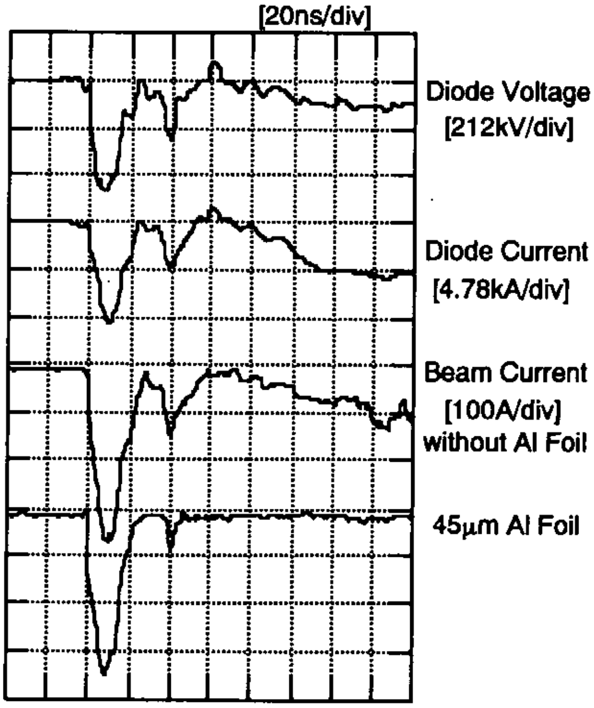

Fig. 2. Typical pulse forms

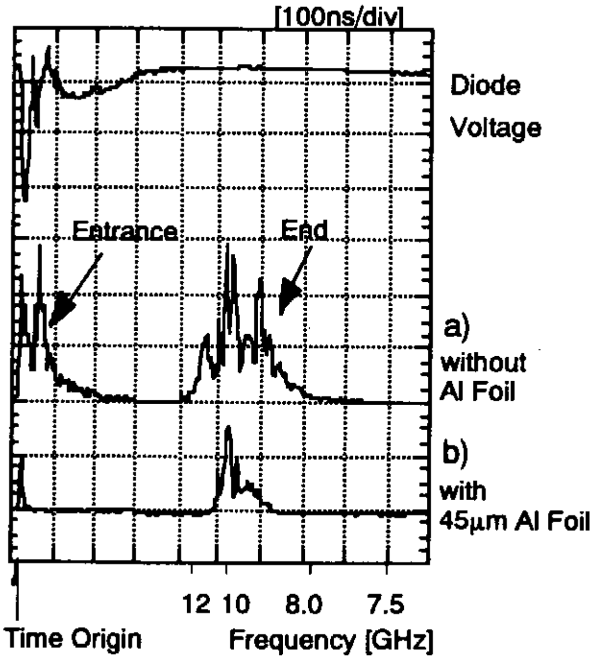

Fig. 3. Microwave signals with(a) and without(b) aluminum foil.

The frequency was evaluated by the time of flight through the 100 m dispersive line. The dispersed microwave signals show some discrete peaks on the broad spectrum. Frequencies of the peaks are plotted in Fig.4 as a function of the strength of magnetic field. The larger radius of the open circles corresponds to the higher peak of the signal. The frequency increased as the strength of the magnetic field increased. The frequency above 18 GHz was not accurate because of the resolution of our system, and besides, the higher frequency than 22 GHz was not observed by using the waveguide with higher cutoff frequency than X-band frequency.

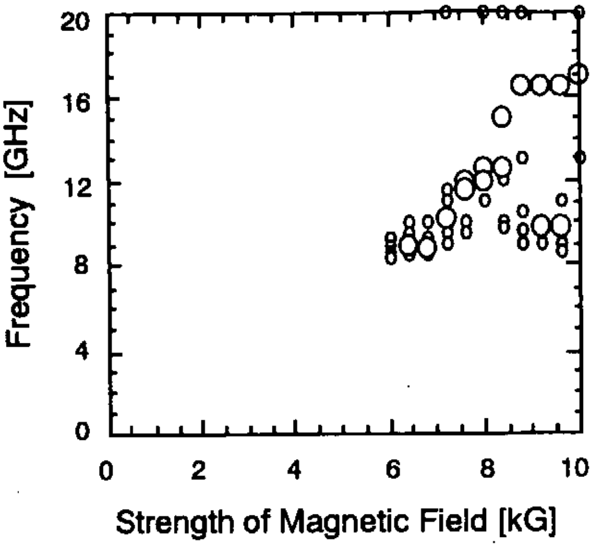

Fig. 4. The radiated frequency vs the strength of the magnetic field.

The total radiated microwave power was roughly estimated to be 1MW. The power increased as the beam current increased from 100 A to 350 A. There was no indication of saturation of the microwave output power.

To examine the effect of the interaction region length, a bent waveguide was inserted. The beam hit the wall at the bent and the microwave propagated through the

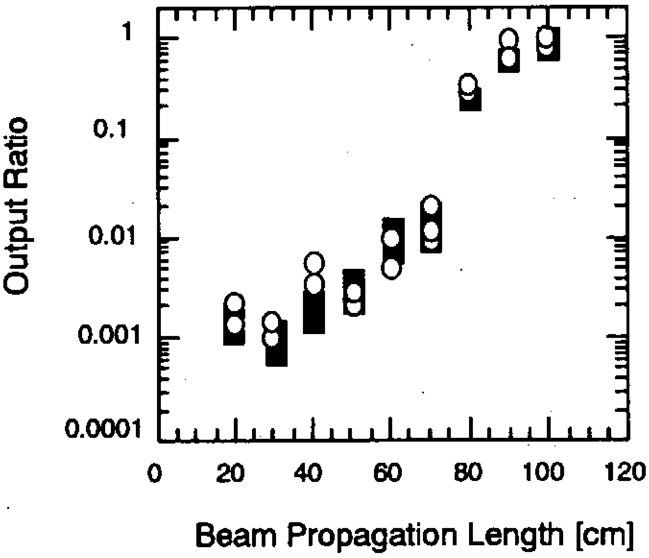

Fig. 5. The output power of radiated microwave increased as the length of beam propagation increased.

bent. The position of the bent waveguide was changed. The frequency spectrum of the microwave did not depend on the position of the bent waveguide. As shown in Fig. 5 , the microwave output power increased as the length of the beam propagation increased.

4. Discussions

Following Parker et al.[1], we derived a dispersion relation from the linearized Maxwell-Vlasov equations based on a model of an electron cyclotron maser with a cylindrical electron beam passing through a rectangular waveguide. The beam energy and the velocity ratio ($v_\perp / v_\parallel$) were taken into account as delta functions. The dispersion relation is expressed with Bessel functions as below.

$$\frac{\omega^2}{c^2} - k_z^2 - k_c^2 = - \frac{1}{c^2} \frac{N_0 e^2}{ab\varepsilon_0 m_0} \frac{1}{\gamma} \sum_{s=-\infty}^{\infty} \left(A_{S1} \frac{\omega^2 - c^2 k_z^2}{\Delta\omega_s^2} + A_{S2} \frac{\omega - v_z k_z}{\Delta\omega_s} + A_{S3} \frac{s\Omega_0}{\Delta\omega_s \gamma} \right)$$

where

$$\Delta\omega_s = \omega - v_z k_z - \frac{s\Omega_0}{\gamma} \ , \ A_{s1} = (1 + (-1)^{n+s} J_0(2 R_G)) \frac{v_\perp^2}{c^2} J_s' (R_L)^2$$

$$A_{s2} = 1 - \frac{s^2}{R_L^2} (1 + (-1)^{n+s} J_0(2 R_G)) \, 2 R_L J_s' (R_L) J_s(R_L)$$

$$A_{s3} = (-1)^{n+s} J_0(2 R_G)) \, 2 R_L J_s' (R_L) J_s(R_L)$$

$$R_L = \frac{\gamma \, v_\perp}{\Omega_0} \ , \quad R_G = r_G k_c \ , \quad \Omega_0 = \frac{e B_g}{m_0} \ , \quad k_c = \frac{n\pi}{a} \ .$$

Here, the crosssection of the waveguide is a rectangulr a × b, the strength of the magnetic field is represented by Bg, the radius of the beam is r_G, ω is the angular frequency, k_c and k_z are the cutoff and the axial wave number, respectively, N_0 is the number of electrons per unit length, $m_0$is the mass of electron, e is the electric charge unit, and ε_0 is the permitivity of vacuum.

To derive the numerical values from the dispersion equation, we put the velocity ratio to be 0.3 because the axial beam velocity was calculated to be more than 0.5 c, where c is the speed of light, by the time of flight method with a Faraday cup. The waveguide mode is TE_{10}. In Fig. 6, the calculated (filled symbols) and experimental (open circles) values are plotted vs the strength of the magnetic field. Below 5 kG, the lower and upper frequency of filled symbols at the same field strength indicate the backward and forward-wave interaction, respectively. Above 5 kG, the frequencies of the forward-wave interaction are over 20 GHz, and the radiated microwave with the frequency over 22 GHz was not observed experimentally. As shown in this figure, the dominant component of the observed microwave is identified to be due to the backward-wave interaction between the fast beam cyclotron wave and the TE_{10} waveguide mode. The beam energy components of about 100-400 keV are responsible for the radiation. About the output power dependence upon the beam current, the experimantal result agrees with this model qualitatively.

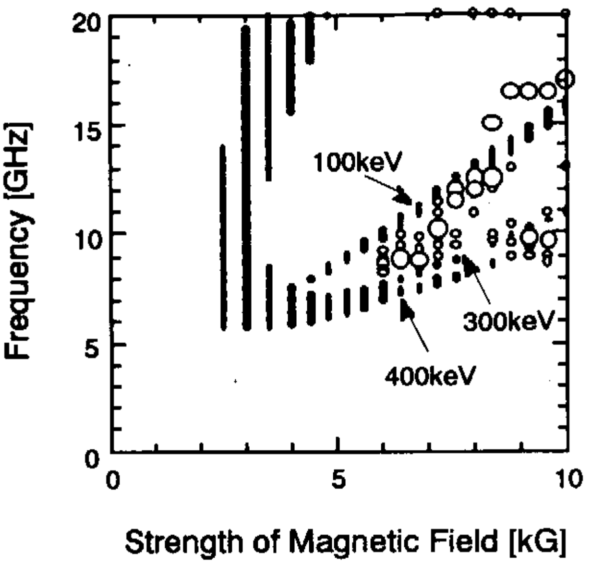

Fig.6. The experimental results (open circles) and derived values from the dispersion relation (filled symbols).

More precise discussion requires more information about beam characteristics and more realistic treatment of the theoretical model. We continue to study unsolved problems described below. (1) Although the diode voltage and the beam current showed smooth continuous changes in time, discrete peaks in the frequency spectrum were observed. We coild not point out which parameter of the beam is most sensitive to the power of the microwave radiation. (2) The microwave from forward-wave interaction was not observed, though its calculated growth rate was comparable to that of the backward-wave interaction. (3) The increase of output power with the increase of beam propagation length is not considered theoretically yet.

5. Conclusion

In conclusion, the gyro-BWO with a short pulse intense relativistic electron beam can be a simple useful device for generating tunable, high-power X-band wavelength radiation. Without aluminum foil, broadly tunable radiation with wide frequency spectrum in X-band is available. Although the efficiency for microwave production reported here are low, our experiments suggest that the propagation length could be important parameters in order to increase the efficiency.

References

1) S.Y.Park et al., Int. J. Electrons, 57,1109 (1984)
2) A.K.Ganguly and S.Ahn : Appl. Phys. Lett. 54, 514 (1989)
3) A. T. Lin : Phys. Rev. A 46, R4516 (1992)
4) A.T.Lin and C.C.Lin : Phys. Fluids B5, 2314 (1993)
5) S.Y.Park,R.H.Kyser et al , IEEE Trans Plasma Sci.,18,321 (1990)
6) M.E.Conde et al: Phys. Fluids B, 5, 1934 (1993)
7) C.S.Kou et al: Phys. Rev. Lett., 70, 924 (1993)

Cascaded High-T_c Bulk Superconductor Lenses (Supertrons) for Intense Electron Beams

Akihito OHSHIMA, Hidenori MATSUZAWA, Yasuyuki MIZUTANI,
Kazuhiro SHOJI, Eizoh IKAWA, Yukio CHINO and Shinji SUGANOMATA
Faculty of Engineering, Yamanashi University, Kofu 400

Abstract

The two-stage tubular lenses (Supertrons) focused and transported intense electron beams (~2 kA, ~340 keV, ~10 ns) over the range of lens separation of ~17 mm or less. In this range the second lens focused the electron beams having an angle of incidence with the axis of the lens less than a critical value of ~34°. The first and second lenses were 40 and 13 mm long, respectively, with an inner diameter of 20 mm and a wall thickness of ~1.5 mm. The lenses were made from Bi-based powder-pressed materials. Neon gas was introduced into the diode gap and into the bore of the lenses at pressures of 0.1 Torr order. The experimental results suggest that adjacent lenses ought to be positioned closer than the value of their inner diameter and are each long enough in axial direction if they are longer than their radii.

1. Introduction

We have proposed and demonstrated[1,2] high-critical-temperature (T_c) bulk superconductor lenses (Supertrons) for charged particle beams. Their principle is as follows: When we inject charged particle beams, *e. g.* electron beams, into high-T_c superconductor tubes (Supertrons), the tubes confine and compress the azimuthal self-magnetic field of the beams into their bore by the Meissner effect. As a consequence, the enhanced field focuses the beams themselves. When the lens tubes are bent, electron beams will propagate[3,4] along their curved axes as laser beams do along optical fibers.

For the operation of a single lens, we have already evaluated lenses made from Y-, Bi-, and Tl-based powder-pressed, and Y-based melt-processed materials by observing[1] radial profiles of focused electron beams and by changing2) their operation temperatures. Out of the high-T_C superconductors, Bi-based powder-pressed materials were best suitable to lenses for pulsed electron beams. This is because the materials intrinsically satisfy a ferrite-core model2) of the lenses.

As an example of cascaded lenses, we previously reported an electron-beam guide5) for induction linear accelerators. In this example, two Bi-based lenses were operated in series. Voltage pulses applied between them accelerated electron beams. These beams traveled a 155-mm-long second lens through a 20 mm bore. If we intend only to transport electron beams, a single long lens or cascaded short lenses are to be used, and no accelerating voltages will be necessary among the lenses.

In this article, we prepared two-stage cascaded lenses6) to which no accelerating voltage was applied, and observed focusing and transporting of electron beams with the second-stage lens. The experimental results provided fundamental criteria for cascading the lenses. The array of the passive lenses manifested the utility of a novel lens system of Supertrons.

Figure 1 shows schematic arrangements of two lenses and envelopes of electron beams focused with the lenses. Such axicentered

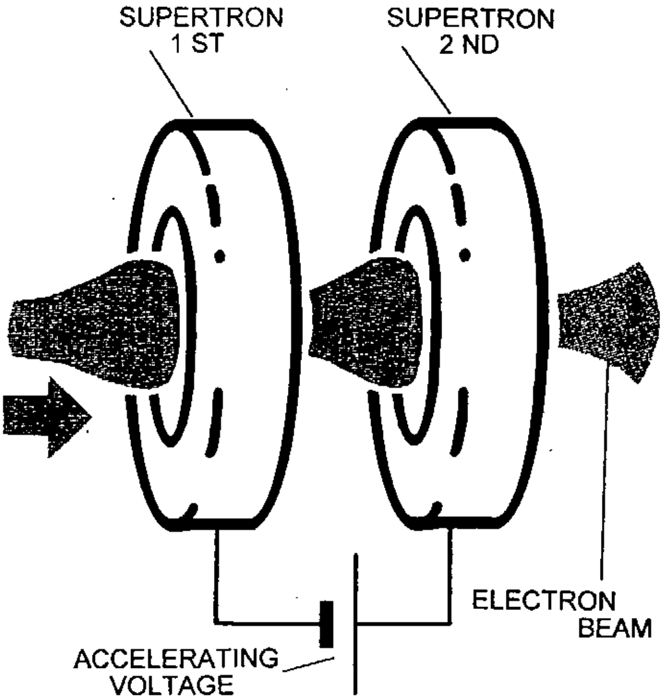

Fig. 1. Cascaded lenses and electron-beam profiles. In the present work, no accelerating voltage is applied.

arrangements of lenses are compared to an array of glass-made optical lenses. Hence, if the lenses guide electron beams efficiently, then the method of the same treatment will be extended to periodic focusing channels of more than two-stages.

2. Experimental Setup

Figure 2 schematically shows the experimental setup for the two-stage Supertrons. Energetic primary electrons (~340 keV, ~2 kA, ~10 ns) were field emitted from the cathode by applying high-voltage pulses across the diode gap, which consisted of a velvet-backed cathode and a tapered cylindrical anode. The anode also played a role of the first stage of the cascaded lenses. The second lens was located downstream of the first with a separation of 6 - 20 mm. These lenses were suspended and grounded with perforated stainless-steel plates of 1 mm thickness. The lenses were prepared by cold-isostatic-pressing Bi-based superconductor powder into configurations of the lenses designed and by sintering these lens tubes in air for 100 h at 850 °C. The lenses thus shaped were fastened onto the inner surfaces of copper-made heat sinks with electrically conducting epoxy resin. Liquid nitrogen cooled the lenses via the heat sinks down to ~90 K or less. The first and second

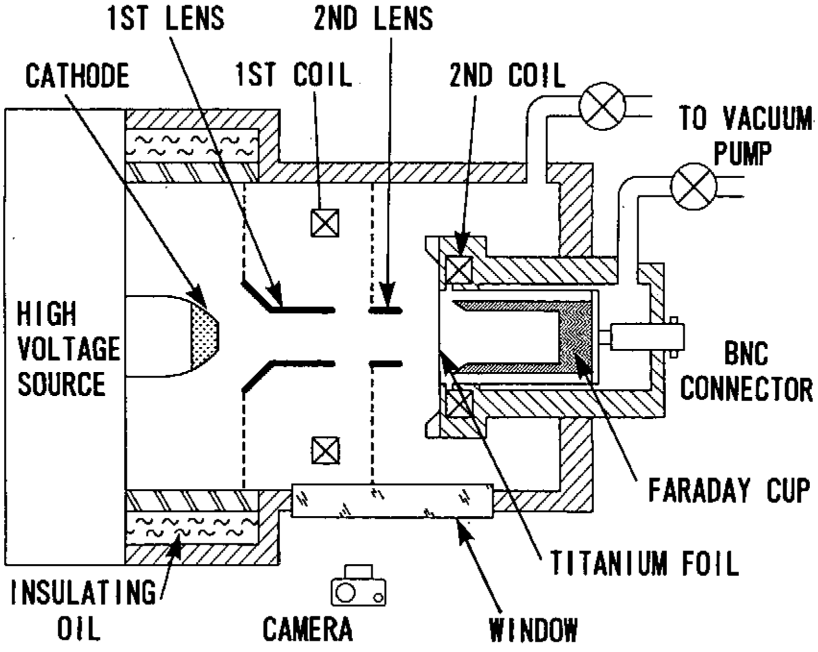

Fig. 2. Schematic of experimental setup.

lenses were 40 and 13 mm long, respectively, with an inner diameter (aperture) of 20 mm. The lens wall was ~1.5 mm thick. To know radial profiles of focused electron beams, graphite-made apertures were set at the entrance or exit of the second lens. The apertures had through-holes of 1 - 15 mm diameter.

To easily focus electron beams with the lenses, we introduced neon gases of 0.1 Torr order into the diode chamber7) and into the bore of the lenses.8) We chose neon gas because it has the lowest thermal conductivity among the gases that do not liquefy at liquid nitrogen temperature. We once tried nitrogen gas, but lenses were much damaged. Since then neon gas has been used.

The chamber enclosing the lenses had a viewing window of a 15-mm-thick plastic plate. A sheet of metal mesh behind the window prevented the window from electrically charging up. Through the window we took open-shutter photographs of spatial distribution of the light emission from neon gases. Two self-integrating Rogowski coils were each positioned at the exits of the lenses. The second Rogowski coil was downstream of a 20-μm-thick titanium (Ti) foil and was kept at pressures of $\sim 10^{-4}$ Torr. The Ti foil transmits only electrons of energies of higher than 60 keV,9) and absorbs other lower-energy electrons. Thus the Faraday cup detected correct currents of primary electron beams. The Faraday cup had a 26-mm-diameter aperture, and its entrance was 5 mm downstream of the Ti foil. The Ti foil was always placed 15 mm downstream of the position at which we wanted to know the electron currents, because of the space necessary to mount the Faraday cup. Hence, the distance between the second-lens exit and Ti foil was 15 mm. The second Rogowski coil and Faraday cup were fixed each other and were movable together in the axial direction. Time evolutions of outputs of the Rogowski coils were displayed on high-speed waveform digitizers (Tektronix SCD 1000, 1 GHz).

3. Experimental Results and Discussions

Figure 3 presents open-shutter photographs of light emission from 0.18-Torr Ne gases at the exits of the lenses. The two lenses were 15 mm apart from edge to edge. On the left-hand side of the photographs, electron beams emerge from the superconducting first lens.

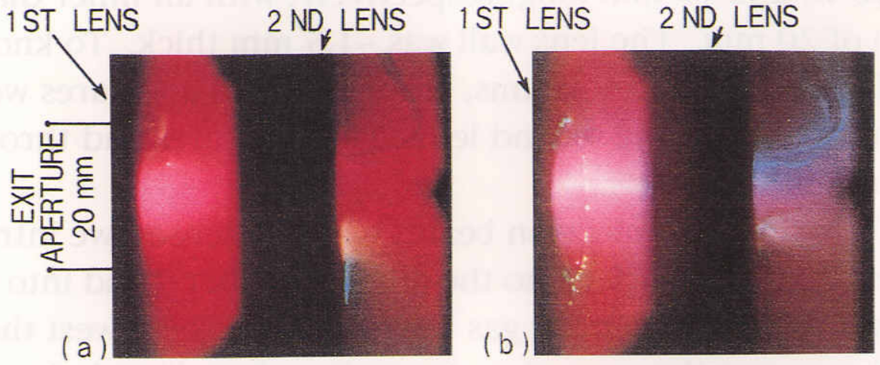

Fig. 3. Open-shutter photographs of light emission from neon gases which were excited with electron beams. (a) Only the first lens was superconducting. (b) Both the first and second lenses were superconducting: Glorious trace of focused electron beams is recognizable at the exit of the superconducting second lens.

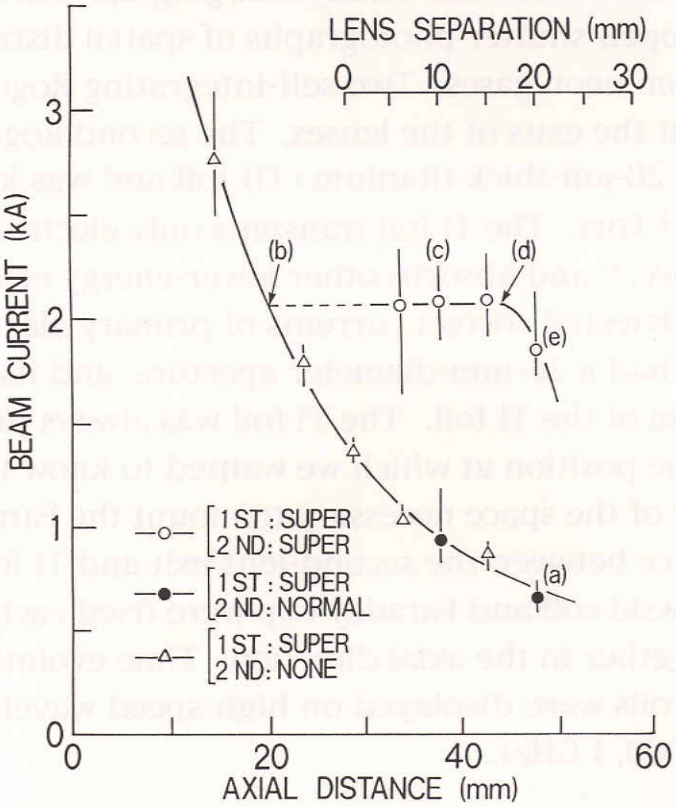

Fig. 4. Electron currents detected with Faraday cup as a function of axial distance from first-lens exit to Ti foil in front of Faraday cup. Triangles are for the operation of only superconducting first lens. Open circles are for both the two lenses being superconducting. Solid circles are for the combination of the superconducting first lens and normal conducting second lens. Separations between the two lenses are read on the top abscissa. Marks (a) - (e) indicate the lens arrangements (a) - (e) in Fig. 5.

The black areas in the central regions of Fig. 3 are the shadow of the second lens. The second lens was normal conducting in Fig. 3(a), whereas it was superconducting in Fig. 3(b). In Fig. 3(b), a focused electron beam exit the second lens and forms its glorious trace. In Fig. 3(a), however, no trace is recognizable at the second-lens exit. A thermocouple was glued onto the upper edge of exit of the second lens.

Figure 4 shows electron currents which the Faraday cup detected as a function of axial distance d from the exit of the first lens to the Ti foil. The triangle points are for the operation of only the superconducting first lens. The currents decreased proportional to $d^{-1.3}$, not to d^{-2}. This is because electron beams concentrated about the lens axis and the Faraday cup detected near-axis flows of the beams. The vertical lines through the data points indicate ranges of the maximum and minimum values for the operation of more than ten shots. The open circles are for the superconducting lenses cascaded with a separation of 6 - 20 mm. In Fig. 4, the shortest separation of 6 mm, read on the top abscissa, corresponds to the axial distance of 34 mm on the bottom abscissa. For the separation of less than ~17 mm , the second lens focused electron currents of an identical value ~2 kA, independently of the separation distance. This fact suggests that the second lens exclusively focused such electron beams that exited the first lens into a cone having the critical apex angle which the second-lens aperture subtended as an angle of acceptable incidence. Beyond that range of the separation, the focused electron currents decreased. The lenses had an inner diameter of 20 mm. Therefore, as rough criteria for cascading Supertrons, we can say that lens separations ought to be shorter than the value of the inner diameter of the lenses and that lenses work properly if they are longer in axial length than the value of their radii.

The solid circles in Fig. 4 are for the combination of the superconducting first lens and normal conducting second lens. From the geometrical ray tracing of electron trajectories (Fig. 5(a)), we inferred that the normal conducting second lens, if working as only an aperture, intercepted no electron currents which the Faraday cup would collect. In addition, both the triangle and solid circle points in Fig. 4 lie on an approximated single line. These facts mean that the normal conducting second lens exhibited no focusing effect on the electron beams.

From the experimental results in Fig. 4 we derived electron beam trajectories as in Fig. 5. The indications (a) - (e) in Fig. 4 correspond to the lens arragements of Figs. 5(a) - (e), respectively. Both the second lens and beam spots at the entrance and exit of it were drawn to scale based on the results in Fig. 4. The beam spot sizes at the exit of the first lens were depicted using the previous experimental results.1) The envelopes were approximated by straight lines connecting the beam spots. Accordingly, the envelopes will, in truth, behave more smoothly as in Fig. 1, instead of the angular ones in Fig. 5. As mentioned above, the electron currents focused were constant ~2 kA for the lens separation less than ~17 mm. To collect this current with the Faraday cup for the operation of a single first lens, the Ti foil along with the Faraday cup should be at the axial distance of ~19 mm as derived from the intersection of the open-triangle and -circle lines, indicated by the mark (b) in Fig. 4. Figure 5 (b) indicates the lens arrangement and electron beam profiles for this fundamental case. The emerging beams made a critical half-apex-angle θ_c of ~34° with the axes of the lenses. While the lens separation was increased up to the upper limit (~17 mm, Fig. 5 (d)) through 10 mm (Fig. 5 (c)), the second lens focused all the electron beams having an angle of incidence less than the critical one. For the separation ~17 mm, the envelopes having the critical apex angle struck nearly the edge of entrance of the second lens. For the further increased separation

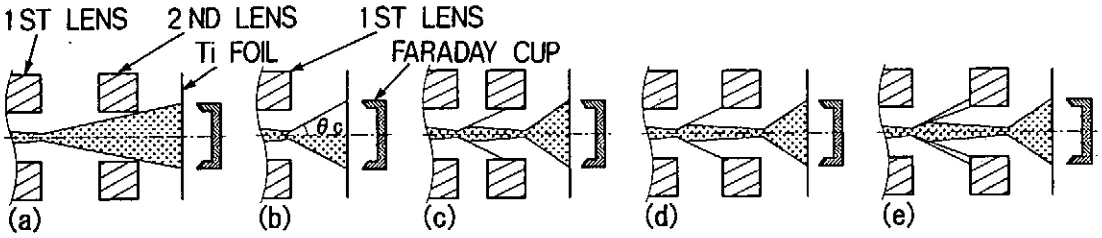

Fig. 5. Envelopes of electron trajectories inferred from experimental results in Fig. 4. The lenses and beam spots at the entrance and exit of them are all drawn to scale. (a) The normal conducting second lens which acts as only an aperture intercepts no electron currents incident on the Faraday cup. Lens separation is 20 mm. (b) At the axial distance of 19 mm, Faraday cup detects the maximum electron currents which the second lens can focus for the range of lens separation less than ~17 mm. The arrangement defines a critical angle of incidence, θ_C. (c) Lens separation is 10 mm. (d) Lens separation is 17 mm. These two cases (c) and (d) are within the range of constant current focusing (~2 kA). (e) Lens separation (20 mm) is beyond the range of constant current focusing, and hence incident electron currents partially strike the entrance of the second lens.

of 20 mm beyond the upper limit (Fig. 5(e)), the outermost envelopes no longer of 20 mm beyond the upper limit (Fig. 5(e)), the outermost envelopes no longer entered the second lens. Therefore, the currents focused decreased as shown by the right-hand-end open circle point in FIg. 4. We have no reasonable explanation of the critical angle of incidence.

4. Conclusions

The cascaded lenses (Supertrons) transported intense electron beam currents ~2 kA in the range of their separation of less than ~17 mm. The transported currents declined when the lens separation exceeded the range. From the geometrical ray tracing of trajectories of electron beams, incident electron beams are focused and transported only when they enter the aperture of lenses with an angle of incidence less than a critical angle θ_c of ~34°. As approximate criteria for the arrangement of the lenses, we can say that lenses ought to be spaced closer than the value of their inner diameter (aperture) and that lenses function well enough if they are each longer in axial length than their radii. To establish definite criteria for designing cascaded lenses, we need to accumulate more experimental data. However, the criteria derived will be regarded as the first approximate standards.

In this article, liquid nitrogen cooled the lenses to 85 - 88 K. If they are cooled further to lower temperatures, the lenses may act sufficiently even for their prolonged separation and for their shortening in axial length. This is because, in the previous article,2) Bi-based powder-pressed lenses operated better with decreasing operation temperatures. Anyway, the obtained results indicate the utility of cascaded Supertrons.

References

1) For a review, see H. Matsuzawa: J. Appl. Phys. 74 (1993) R111 [Errata; 76 (1994) 624].

2) H. Matsuzawa, H. Kobayashi, H. Mochizuki, N. Yoneyama, A. Ohshima, S. Hirano, E. Mori, G. Horigome, Y. Ishida and Y. Chino: Jpn. J. Appl. Phys. 33 (1994) 2526 [Errata; 33 (1994) 4799].

3) H. Matsuzawa, Y. Ishibashi, T. Osada, K. Irikura, K. Okamoto, H. Wada, A. Mochizuki and T. Akitsu: Jpn. J. Appl. Phys. 29 (1990) 785.
4) H. Matsuzawa, Y. Ishibashi, M. Ariizumi and H. Saegusa: Appl. Phys. Lett. 59 (1991) 141.
5) H. Matsuzawa, H. Wada, S. Mori and T. Yamamoto: Jpn. J. Appl. Phys. 30 (1991) 2972.
6) A. Ohshima, Y. Mizutani and H. Matsuzawa: *Advances in Superconductivity VII*, eds. K. Yamafuji and T. Morishita (Springer, Tokyo, 1995) to be published.
7) H. Matsuzawa and T. Akitsu: J. Appl. Phys. 63 (1988) 4388.
8) P. A. Miller, J. B. Gerardo and J. W. Poukey: J. Appl. Phys. 43 (1972) 3001.
9) L. Pages, E. Bertel, H. Joffre and L. Sklavenitis: Atomic Data 4 (1972) 1.

Publication List of NIFS-PROC Series

NIFS-PROC-1 *U.S.-Japan on Comparison of Theoretical and Experimental Transport in Toroidal Systems Oct. 23-27, 1989* Mar. 1990

NIFS-PROC-2 *Structures in Confined Plasmas –Proceedings of Workshop of US-Japan Joint Institute for Fusion Theory Program–* ; Mar. 1990

NIFS-PROC-3 *Proceedings of the First International Toki Conference on Plasma Physics and Controlled Nuclear Fusion –Next Generation Experiments in Helical Systems– Dec. 4-7, 1989* Mar. 1990

NIFS-PROC-4 *Plasma Spectroscopy and Atomic Processes –Proceedings of the Workshop at Data & Planning Center in NIFS–*; Sep. 1990

NIFS-PROC-5 *Symposium on Development of Intensed Pulsed Particle Beams and Its Applications February 20 1990*; Oct. 1990

NIFS-PROC-6 *Proceedings of the Second International TOKI Conference on Plasma Physics and Controlled Nuclear Fusion , Nonlinear Phenomena in Fusion Plasmas -Theory and Computer Simulation-;* Apr. 1991

NIFS-PROC-7 *Proceedings of Workshop on Emissions from Heavy Current Carrying High Density Plasma and Diagnostics;* May 1991

NIFS-PROC-8 *Symposium on Development and Applications of Intense Pulsed Particle Beams, December 6 - 7, 1990*; June 1991

NIFS-PROC-9 *X-ray Radiation from Hot Dense Plasmas and Atomic Processes*; Oct. 1991

NIFS-PROC-10 *U.S.-Japan Workshop on "RF Heating and Current Drive in Confinement Systems Tokamaks" Nov. 18-21, 1991,* Jan. 1992

NIFS-PROC-11 *Plasma-Based and Novel Accelerators (Proceedings of Workshop on Plasma-Based and Novel Accelerators) Nagoya, Japan, Dec. 1991*; May 1992

NIFS-PROC-12 *Proceedings of Japan-U.S. Workshop P-196 on High Heat Flux Components and Plasma Surface Interactions for Next Devices*; Mar. 1993

NIFS-PROC-13	『NIFS　シンポジウム 「核燃焼プラズマの研究を考える－現状と今後の取り組み方」 1992 年 7月 15 日、核融合科学研究所　』 1993 年 7月 *NIFS Symposium* *"Toward the Research of Fusion Burning Plasmas -Present status and Future strategy-", 1992 July 15, National Institute for Fusion Science;* July 1993 (in Japanese)
NIFS-PROC-14	*Physics and Application of High Density Z-pinches,* July 1993
NIFS-PROC-15	岡本正雄、講義「プラズマ物理の基礎」 平成5年度　総合大学院大学 1994年　2月 *M. Okamoto,* *"Lecture Note on the Bases of Plasma Pysics"* *Graduate University for Advanced Studies* Feb. 1994 (in Japanese)
NIFS-PROC-16	代表者　河合良信 平成5年度　核融合科学研究所共同研究 研究会報告書 「プラズマ中のカオス現象」 *"Interdisciplinary Graduate School of Engineering Sciences"* *Report of the meeting on Chaotic Phenomena in Plasma* Apr. 1994 (in Japanese)
NIFS-PROC-17	平成5年度NIFSシンオジウム報告書 「核融合炉開発研究のアセスメント」 平成5年11月29日-30日　於　核融合科学研究所 *"Assessment of Fusion Reactor Development"* *Proceedings of NIFS Symposium held on November 29-30, 1993 at National Insitute for Fusion Science"* Apr. 1994 (in Japanese)
NIFS-PROC-18	*"Physics of High Energy Density Plasmas Produced by Pulsed Power"* June 1994
NIFS-PROC-19	K. Morita, N. Noda (Ed.), "*Proceedings of 2nd International Workshop on Tritium Effects in Plasma Facing Components at Nagoya University, Symposion Hall, May 19-20, 1994",* Aug. 1994
NIFS-PROC-20	研究代表者　阿部　勝憲　（東北大学・工学部） 所内世話人　野田信明 平成6年度　核融合科学研究所共同研究［研究会］ 「金属系高熱流束材料の開発と評価」成果報告書 K. Abe and N. Noda (Eds.),

	"Research and Development of Metallic Materials for Plasma Facing and High Heat Flux Components" Nov. 1994 (in Japanese)
NIFS-PROC-21	世話人：森田　健治（名大工学部）、金子　敏明（岡山理科大学理学部） 「境界プラズマと炉壁との相互作用に関する基礎過程の研究」 研究会報告 K. Morita (Nagoya Univ.), T. Kaneko (Okayama Univ. Science)(Eds.) *NIFS Joint Meeting "Plasma-Divertor Interactions" and "Fundamentals of Boundary Plasma-Wall Interactions" January 6-7, 1995 National Institute for Fusion Science* Mar. 1995 (in Japanese)
NIFS-PROC-22	代表者　河合　良信 プラズマ中のカオス現象 Y. Kawai, *Report of the Meeting on Chaotic Phenomena in Plasma,*1994 Apr. 1995 (in Japanese)
NIFS-PROC-23	K. Yatsui (Ed.), *New Applications of Pulsed, High-Energy Density Plasmas;* June 1995